JAERI-Review
2003-029

JP0350706

REVIEW OF JT-60U EXPERIMENTAL RESULTS IN 2001 AND 2002

November 2003

JT-60 Team

日本原子力研究所
Japan Atomic Energy Research Institute

本レポートは、日本原子力研究所が不定期に公刊している研究報告書です。
入手の問合わせは、日本原子力研究所研究情報部研究情報課（〒319-1195 茨城県那珂郡東海村）あて、お申し越し下さい。なお、このほかに財団法人原子力弘済会資料センター（〒319-1195 茨城県那珂郡東海村日本原子力研究所内）で複写による実費頒布を行っております。

This report is issued irregularly.
Inquiries about availability of the reports should be addressed to Research Information Division, Department of Intellectual Resources, Japan Atomic Energy Research Institute, Tokai-mura, Naka-gun, Ibaraki-ken 〒319-1195, Japan.

© Japan Atomic Energy Research Institute, 2003

編集兼発行　日本原子力研究所

JAERI－Review 2003－029

Review of JT-60U Experimental Results in 2001 and 2002

JT-60 Team*

Department of Fusion Plasma Research and Department of Fusion Facility
Naka Fusion Research Establishment
Japan Atomic Energy Research Institute
Naka-machi, Naka-gun, Ibaraki-ken

(Received September 10, 2003)

The results from the JT-60U experiments in 2001 and 2002 are reviewed. A high poloidal beta (β_p) H-mode plasma with full non-inductive current drive was obtained at 1.8 MA, and the fusion triple product reached 3.1×10^{20} m^{-3} keV s. High normalized beta (β_N) around 2.7 was maintained for 7.4 s. Neoclassical tearing mode suppression by electron cyclotron current drive (ECCD) was accomplished using a real-time feedback control system, and improvement in β_N was obtained. In a reversed shear plasma, a high DT-equivalent fusion gain (> 0.8) was maintained for 0.55 s with a current hole. High confinement reversed shear plasmas where the electron temperature was higher than the ion temperature were obtained. A new operation scenario was established in which a plasma with high bootstrap current fraction and internal transport barriers (ITBs) was produced without using the OH coil. For physics studies of ITB formation, dedicated experiment was performed, in which the heating power was deliberately scanned. Accumulation of heavy impurity related to strong ITBs in reversed shear plasmas, and degradation of ITBs by electron cyclotron heating (ECH) in weak positive shear plasmas was found. In high β_p mode plasmas, Ar exhaust by ECH was obtained. Correlation between the particle and thermal diffusivities was observed in ITB plasmas with both negative and weak shear. As for the current hole, the mechanism was investigated in detail by accurate current profile measurement and ECCD. A new type of Alfvén eigenmode (Reversed shear Alfvén eigenmode) was proposed, and the observed frequency chirp was explained quite well. As for ECCD, the current drive efficiency was evaluated in a reactor-relevant high electron-temperature regime. In Ar-seeded H-mode plasmas with the outer strike point located on the divertor dome-top, high-power negative-ion-based neutral beam injection (N-NBI) extended the electron density regime to 0.95 Greenwald density keeping confinement enhancement factor over the ITER98(y, 2) scaling of 0.9. In H-mode plasmas, enhancement of the pedestal pressure was obtained with an increase of β_p in a high triangularity configuration. Dedicated measurement of edge localized

mode dynamics and scrape-off-layer plasma flow advanced the physics understanding. Hydrogen-isotope retention properties in the in-vessel materials were investigated. For the carbon divertor plates, it was found that erosion was dominant in the outer divertor and re-deposition was predominant in the inner divertor. Detritiation of the vacuum vessel was undertaken by glow discharge cleaning, electron cyclotron resonance discharge cleaning, and Taylor discharge cleaning. The above-mentioned achievements were much owing to improved performance of the heating systems, poloidal coil capability, diagnostics, etc. The negative-ion-based neutral beam (N-NB) and electron cyclotron (EC) heating power increased up to 6.2 MW and 3 MW, respectively.

Keywords:
Tokamak, JT-60U, High β_p H-mode Plasma, Reversed Shear Plasma, H-mode Plasma, Non-inductive Current Drive, Internal Transport Barrier, Current Hole, Impurity, Divertor, Diagnostics, Hydrogen-isotope, Negative-ion-based Neutral Beam, Electron Cyclotron Range of Frequency

※ JT-60 Team

H.Akasaka, N.Akino, K.Anno, M.Arai[1)], T.Arai, N.Asakura, N.Ashikawa[2)], M.Azumi, P.E.Bak[3)], M.Bakhtiari[4)], L.G.Bruskin[5)], A.V.Chankin[6)], C.Z.Cheng[7)], F.Cheng[8)], S.Chiba, N.Ebisawa, T.Fujii, T.Fujita, T.Fukuda[9)], A.Fukuyama[10)], H.Funaba[2)], A.Funahashi[11)], H.Furukawa[1)], M.Furukawa[4)], X.Gao[6)], N.N.Gorelenkov[7)], Y.Gotoh[1)], L.Grisham[7)], S.Haga[1)], K.Hamamatsu, T.Hamano[1)], T.Hatae, A.Hatayama[12)], N.Hayashi, T.Hayashi, S.Higashijima, N.Hikida[1)], K.W.Hill[7)], S.Hiranai, H.Hiratsuka, Y.Hirohata[13)], J.Hobirk[14)], A.Honda, M.Honda, T.Horikawa[1)], Y.Hoshi[1)], N.Hosogane, H.Hosoyama[1)], K.Iba[1)], H.Ichige, S.Ide, Y.Idomura, K.Igarashi[1)], K.Ikeda[2)], Y.Ikeda, S.Inagaki[2)], A.Inoue[1)], M.Isaka, A.Isayama, S.Ishida, K.Ishii[1)], Y.Ishii, M.Ishikawa[4)], K.Isobe[15)], K.Itami, S.Itoh[16)], T.Iwahashi[1)], K.Iwasaki[1)], I.Kachtchouk[17)], Y.Kagei[4)], K.Kajiwara[18)], E.Kajiyama[1)], Y.Kamada, D.Kamata[19)], A.Kaminaga, T.Kashiwabara[1)], K.Katayama[16)], M.Kawai, Y.Kawamata, Y.Kawano, M.Kazawa, H.Kikuchi[1)], K.Kikuchi[1)], M.Kikuchi, Y.Kishimoto, S.Kitamura, A.Kitsunezaki[20)], K.Kizu, S.Kobayashi[10)], H.Kodama[21)], K.Kodama, Y.Koide, S.Kokusen[1)], T.Kondoh, S. Konishi[10)], S.Konoshima, S.V.Konovalov[6)], G. J. Kramer[7)], A.V.Krasilnikov[17)], H.Kubo, Y.Kudoh, K.Kurihara, G.Kurita, M.Kuriyama, A.Kurumada[22)], Y.Kusama, N.Kusanagi[1)], L.L.Lao[18)], S.Lee[23)], G.Lei[8)], J.Li[6)], W.Li[8)], J.Manickam[7)], K.Masaki, H.Masui[1)], T.Matsuda[24)], M.Matsukawa, T.Matsumoto, M.Matsuyama[25)], Y.Matsuzawa[1)], K.Meguro[1)], O.Mitarai[26)], Yukitoshi Miura, Yushi Miura, N.Miya, A.Miyamoto[1)], K.Miyata[1)], N.Miyato[4)], J.Miyazawa[2)], Y.Miyo, K.Mogaki, Y.Morimoto[21)], A.Morioka, S.Moriyama, K.Nagasaki[10)], S.Nagaya, O.Naito, H.Nakamura[15)], Y.Nakamura, T.Nakano, M.Nakatsuka[9)], Y.Narushima[2)], R.Nazikian[7)], S.V.Neudatchin[27)], H.Ninomiya, M.Nishikawa[16)], N.Nishino[28)], T.Nishitani, T.Nishiyama, M.Noda[1)], N.Noda[2)], K.Noto[1)], T.Ohga, K.Ohshima[1)], A.Oikawa, T.Oikawa, M.Okabayashi[7)], J.Okano, K.Okano[29)], K.Okuno[21)], S.Omori, Y.Omori, H.Oohara[30)], T.Oshima, Y.Oya[31)], N.Oyama, T.Ozeki, G.Rewoldt[7)], S.Sakakibara[2)], Y.Sakamoto, A.Sakasai[32)], S.Sakata, T.Sakuma[1)], S.Sakurai, T.Sasajima, N.Sasaki[1)], F.Sato[1)], Minoru Sato, Mutsuki Sato[1)], K.Sawada[19)], M.Seimiya, H.Seki[1)], M.Seki, Y.Shibata[33)], K.Shimada, K.Shimizu, M.Shimizu, M.Shimono, K.Shinohara, S.Shinozaki, H.Shirai, S.Shiraiwa[31)], M.Shitomi[34)], M.Sueoka, A.Sugawara[1)], T.Sugie, M.Sugihara[32)], K.Sugiyama[33)], H.Sunaoshi, Masaei Suzuki[1)], Mitsuhiro Suzuki[1)], T.Suzuki, Y.Suzuki[4)], M.Takahashi[1)], S.Takano[1)], Y.Takase[31)], M.Takechi, N.Takei[35)], S.Takeji[36)], H.Takenaga, Y.Taki[1)], T.Takizuka, H.Tamai, T.Tanabe[33)], Y.Tanai[1)], S.Tanaka[10)], T.Taniguchi[31)], M.Terakado, T.Terakado, K.Tobita, K.Toi[2)], S.Tokuda, T.Totsuka, R.Toyokawa[1)], N.Tsubota[1)], K.Tsuchiya, T.Tsugita, Y.Tsukahara, T.Tuda, K.Uehara, T.Uehara[1)], Y.Uesugi[33)], N.Umeda, H.Urano[14)], K.Urata[1)], K.Ushigusa[37)], K.Usui, M.Wakatani[10)], S.Wang[5)], A.D.Whiteford[38)], G.A.Wurden[39)], H.Yagi[1)], J.Yagyu, H.Yamada[2)], T.Yamamoto, Y.Yamashita[1)], H.Yamazaki[1)], K.Yamazaki[2)], Y.Yang[8)], K.Yokokura, I.Yonekawa, Hidetoshi Yoshida, Hidetsugu Yoshida[9)]

1) Staff on loan
2) National Institute for Fusion Science, Japan
3) Ikast, Denmark
4) Post-Doctoral Fellow
5) Japan Society of the Promotion of Science Invitation Fellowship
6) JAERI Fellow
7) Princeton Plasma Physics Laboratory, USA
8) MEXT Science Exchange Program (former STA Exchanger)
9) Osaka University, Japan
10) Kyoto University, Japan
11) Kaihatsu Denki CO., LTD., Japan
12) Keio University, Japan
13) Hokkaido University, Japan
14) IPP Garching, Germany
15) Dept. of Fusion Engineering Research, Japan Atomic Energy Research Institute
16) Kyushu University, Japan
17) TRINITI, Russia
18) General Atomics, USA
19) Shinshu University, Japan
20) Research Organization for Information Science & Technology, Japan
21) Shizuoka University, Japan
22) Ibaraki University, Japan
23) High Energy Accelerator Research Organization, Japan
24) Information Systems Operating Division, Japan Atomic Energy Research Institute
25) Toyama University, Japan
26) Kyushu Tokai University, Japan
27) Kurchatov Institute, Russia
28) Hiroshima University, Japan
29) Central Research Institute of Electric Power Industry, Japan
30) Office of ITER Project Promotion, Japan Atomic Energy Research Institute
31) The University of Tokyo, Japan
32) Dept. of ITER Project, Japan Atomic Energy Research Institute
33) Nagoya University, Japan
34) Safety Division, Japan Atomic Energy Research Institute
35) Fellow of Advanced Science
36) Ehime University, Japan
37) Office of Planning, Japan Atomic Energy Research Institute
38) University of Strathclyde, UK
39) Los Alamos National Laboratory, USA

JT-60U実験結果のレビュー(2001年～2002年)

日本原子力研究所那珂研究所　炉心プラズマ研究部・核融合装置試験部

JT-60チーム※

(2003年9月10日　受理)

2001年及び2002年のJT-60U実験の結果をレビューする。高β_pHモードプラズマでは、プラズマ電流1.8 MAの完全非誘導電流駆動状態で核融合三重積3.1 × 10^{20} m^{-3} keV sを達成した。また、規格化ベータ値約2.7を7.4秒間維持した。電子サイクロトロン波電流駆動を用いた実時間帰還制御で新古典テアリングモードを抑制し、規格化ベータ値を改善した。負磁気シアプラズマでは、高い核融合エネルギー増倍率（$Q_{DT}^{eq} > 0.8$）を電流ホールを伴う状態で0.55秒間維持した。電子温度がイオン温度よりも高い状態で、高閉じ込めの負磁気シアプラズマを得た。内部輸送障壁を有する高自発電流割合の高性能プラズマを、中心ソレノイドコイルを用いない革新的運転シナリオによって生成した。内部輸送障壁の形成に関する物理研究のために、加熱パワーを詳細に変えた実験を行った。負磁気シアプラズマでは強い内部輸送障壁に伴う不純物の蓄積を、弱磁気シアプラズマでは電子サイクロトロン波加熱による内部輸送障壁の劣化を観測した。また、高β_pHモードプラズマでは、電子サイクロトロン波加熱によってArを排出することができた。負磁気シアラズマ及び弱磁気シアプラズマにおいて、内部輸送障壁における粒子拡散と熱拡散の関係を観測した。また、電流ホールについては、正確な電流分布測定と電子サイクロトロン波電流駆動を用いて、その機構を詳しく調べた。新たなアルフベン固有モード（負磁気シアアルフベン固有モード）を提唱し、実験で観測された揺動周波数の上昇を説明した。また、電子サイクロトロン波電流駆動については、核融合炉に相当する高電子温度領域で電流駆動効率を評価した。Ar入射のHモードプラズマでは、外側ストライク点をダイバータドームの頂上に置いた配位で、負イオン源中性粒子加熱を行うことによって、グリーンワルド密度の95%においてITER98(y,2)スケーリングの0.9倍の閉じ込め性能を実現した。Hモードプラズマに関しては、高三角度配位ではポロイダルベータ値の増加に伴って周辺ペデスタルの圧力が増加することを観測した。Hモードにおける周辺部不安定性（ELM)およびスクプレープオフ層におけるプラズマ流に関する詳細な測定を行い、その物理的理解を深めた。真空容器内材料における水素同位体の蓄積に関して研究を行った。炭素材ダイバータタイルは、外側ダイバータ部では損耗が、内側ダイバータでは再堆積が観測された。グロー放電洗浄、電子サイクロトロン共鳴放電洗浄、テイラー放電洗浄を用いて、真空容器のトリチウムの排出を行った。尚、上に述べた成果は、加熱装置、ポロイダルコイル、計測装置等の性能向上によるところが大きい。負イオン源中性粒子の加熱パワーは6.2 MWを、電子サイクロトロン波の加熱パワーは3 MWを達成した。

那珂研究所：〒311-0193　茨城県那珂郡那珂町向山 801-1

※ JT-60チーム

赤坂 博美，秋野 昇，安納 勝人，荒井 優[1)]，新井 貴，朝倉 伸幸，芦川 直子[2)]，安積 正史，P.E.Bak[3)]，M.Bakhtiari[4)]，L.G.Bruskin[5)]，A.V.Chankin[6)]，C.Z.Cheng[7)]，F.Cheng[8)]，千葉 真一，海老沢 昇，藤井 常幸，藤田 隆明，福田 武司[9)]，福山 淳[10)]，舟場 久芳[2)]，船橋 昭昌[11)]，古川 弘[1)]，古川 勝[4)]，X.Gao[6)]，N.N.Gorelenkov[7)]，後藤 純孝[1)]，L.Grisham[7)]，芳賀 三郎[1)]，濱松 清隆，濱野 隆[1)]，波多江 仰紀，畑山 明聖[12)]，林 伸彦，林 孝夫，東島 智，疋田 繁紀[1)]，K.W.Hill[7)]，平内 慎一，平塚 一，広畑 優子[13)]，J.Hobirk[14)]，本田 敦，本田 正男，堀川 豊彦[1)]，星 芳幸[1)]，細金 延幸，細山 博己[1)]，射場 克幸[1)]，市毛 尚志，井手 俊介，井戸村 泰宏，五十嵐 浩一[1)]，池田 勝則[2)]，池田 佳隆，稲垣 滋[2)]，井上 昭[1)]，井坂 正義，諫山 明彦，石田 真一，石井 和宏[1)]，石井 康友，石川 正男[4)]，磯部 兼嗣[15)]，伊丹 潔，伊藤 智之[16)]，岩橋 孝明[1)]，岩崎 慶太[1)]，I.Kachtchouk[17)]，影井 康弘[4)]，梶原 健[18)]，梶山 英一[1)]，鎌田 裕，鎌田 大[19)]，神永 敦嗣，柏原 庸央[1)]，片山 一成[16)]，河合 視己人，川俣 陽一，河野 康則，椛澤 稔，菊池 弘[1)]，菊池 勝美[1)]，菊池 満，岸本 泰明，北村 繁，狐崎 晶雄[20)]，木津 要，小林 進二[10)]，児玉 博[21)]，児玉 幸三，小出 芳彦，石仙 茂晴[1)]，近藤 貴，小西哲之[10)]，木島 滋，S.V.Konovalov[6)]，G. J. Kramer[7)]，A.V.Krasilnikov[17)]，久保 博孝，工藤 祐介，栗原 研一，栗田 源一，栗山 正明，車田 亮[22)]，草間 義紀，草薙 直人[1)]，L.L.Lao[18)]，李 成洙[23)]，G.Lei[8)]，J.Li[6)]，W.Li[8)]，J.Manickam[7)]，正木 圭，増井 浩史[1)]，松田 俊明[24)]，松川 誠，松本 太郎，松山 政夫[25)]，松沢 行洋[1)]，目黒 和美[1)]，御手洗 修[26)]，三浦 幸俊，三浦 友史，宮 直之，宮本 篤[1)]，宮田 克行[1)]，宮戸 直亮[4)]，宮澤 順一[2)]，三代 康彦，藻垣 和彦，森本 泰臣[21)]，森岡 篤彦，森山 伸一，長崎 百伸[10)]，永谷 進，内藤 磨，中村 博文[15)]，中村 幸治，仲野 友英，中塚 正大[9)]，成嶋 吉朗[2)]，R.Nazikian[7)]，S.V.Neudatchin[27)]，二宮 博正，西川 正史[16)]，西野 信博[28)]，西谷 健夫，西山 友和，野田 政明[1)]，野田 信明[2)]，能登 勝也[1)]，大賀 徳道，大島 克己[1)]，及川 晃，及川 聡洋，M.Okabayashi[7)]，岡野 潤，岡野 邦彦[29)]，奥野 健二[21)]，大森 俊造，大森 栄和，大原 比呂志[30)]，大島 貴幸，大矢 恭久[31)]，大山 直幸，小関 隆久，G.Rewoldt[7)]，榊原 悟[2)]，坂本 宜照，逆井 章[32)]，坂田 信也，佐久間 猛[1)]，櫻井 真治，笹島 唯之，佐々木 昇[1)]，佐藤 文明[1)]，佐藤 稔，佐藤 睦[1)]，澤田 圭司[19)]，清宮 宗孝，関 宏[1)]，関 正美，柴田 泰成[33)]，島田 勝弘，清水 勝宏，清水 正亜，下野 貢，篠原 孝司，篠崎 信一，白井 浩，白岩 俊一[31)]，蔀 守正[34)]，末岡 通治，菅原 章博[1)]，杉江 達夫，杉原 正芳[32)]，杉山 一慶[33)]，砂押 秀則，鈴木 昌栄[1)]，鈴木 光博[1)]，鈴木 隆博，鈴木 善雄[4)]，高橋 正己[1)]，高野 正二[1)]，高瀬 雄一[31)]，武智 学，武井 奈帆子[35)]，竹治 智[36)]，竹永 秀信，滝 義秋[1)]，滝塚 知典，玉井 広史，田辺 哲朗[33)]，棚井 豊[1)]，田中 茂利[10)]，谷口 智利[31)]，寺門 正之，寺門 恒久，飛田 健次，東井 和夫[2)]，徳田 伸二，戸塚 俊之，豊川 良治[1)]，坪田 直明[1)]，土屋 勝彦，次田 友宣，塚原 美光，津田 孝，上原 和也，上原 聡明[1)]，上杉 喜彦[33)]，梅田 尚孝，浦野 創[14)]，浦田 一宏[1)]，牛草 健吉[37)]，薄井 勝富，若谷 誠宏[10)]，S.Wang[5)]，A.D.Whiteford[38)]，

G.A.Wurden[39)]，八木　洋[1)]，柳生　純一，山田　弘司[2)]，山本　巧，山下　睦樹[1)]，山崎　晴幸[1)]，山崎　耕造[2)]，Y.Yang[8)]，横倉　賢治，米川　出，吉田　英俊，吉田　英次[9)]

1) 業務協力員
2) 核融合科学研究所
3) Ikast、デンマーク
4) 博士研究員
5) 日本学術振興会招聘フェロー（旧 STA フェローに相当）
6) 原研リサーチフェロー
7) プリンストンプラズマ 物理研究所、米国
8) MEXT 研究員交換プログラム（旧原子力交流制度研究員）
9) 大阪大学
10) 京都大学
11) 開発電気株式会社
12) 慶応大学
13) 北海道大学
14) マックスプランク研究所、ドイツ
15) 日本原子力研究所、核融合工学部
16) 九州大学
17) トリニティ、ロシア
18) ジェネラルアトミクス社、米国
19) 信州大学
20) 高度情報科学技術研究機構
21) 静岡大学
22) 茨城大学
23) 高エネルギー加速器研究機構
24) 日本原子力研究所、情報システム管理課
25) 富山大学
26) 九州東海大学
27) クルチャトフ研究所、ロシア
28) 広島大学
29) 電力中央研究所
30) 日本原子力研究所、ITER業務推進室
31) 東京大学
32) 日本原子力研究所、ITER開発室
33) 名古屋大学
34) 日本原子力研究所、安全管理課
35) 特別研究生
36) 愛媛大学
37) 日本原子力研究所、企画室
38) ストラスクライド大学、英国
39) ロスアラモス国立研究所、米国

This is a blank page.

Contents

1. Introduction
T. Fukuda, H. Kubo and Y. Kamada ····· 1

2. Overview of the Experimental Results
H. Kubo, T. Fukuda and Y. Kamada ····· 3

3. High Performance and Non-inductive Current Drive ····· 9
3.1 Extended Plasma Regimes of the High β_p ELMy H-mode with NNB Injection and Enhanced Capability of High Triangularity Operation
Y.Kamada et al. ····· 9
3.2 Achievement of a High Fusion Triple Product and Steady State Sustainment in High βp ELMy H-mode Discharges in JT-60U
A. Isayama et al. ····· 13
3.3 High Fusion Performance Experiments with Reversed Shear Plasmas
T. Fujita et al. ····· 14
3.4 LHCD on High Confinement Reversed Shear Plasmas at High Normalized Density and Low q Regime
S. Ide et al. ····· 18
3.5 Formation of ITB Extending to Larger Minor Radius in Reversed Shear Plasmas
S. Ide et al. ····· 22
3.6 Plasma Current Initiation and Ramp-up without Use of Ohmic Heating Center Solenoid and Formation of High Confinement Plasma
Y. Takase et al. ····· 26
3.7 Plasma Equilibrium and Confinement in a Tokamak with Nearly Zero Central Current Density in JT-60U
T. Fujita et al. ····· 27
3.8 Response of Current Hole to Error Fields and Current Drive
T. Fujita et al. ····· 28
3.9 Experimental Study on Physics of Electron Cyclotron Current Drive
T. Suzuki et al. ····· 32
3.10 Off-axis Current Drive with Neutral Beams
J. Hobirk et al. ····· 35

4. Transport in Core Plasmas ····· 39
4.1 Dependence of Ion Thermal Diffusivity on Heat Flux at the Internal Transport Barrier in JT-60U
Y. Sakamoto et al. ····· 39
4.2 Non-locality in Relation between Er Shear and Diffusivity at the Internal Transport Barrier
Y. Sakamoto et al. ····· 40
4.3 Impact of Electron Heating on ITB Plasmas
S. Ide et al. ····· 41
4.4 Studies on Electron ITB Formation Condition in JT-60U
T. Fukuda et al. ····· 42
4.5 Studies of Ion Internal Transport Barrier Formation Condition in Terms of Global Plasma Parameters
T. Suzuki et al. ····· 46
4.6 Dynamics and Interplay of L-H-L Transitions and ITB-events in Reversed Shear Plasmas with Internal Barriers in JT-60U
S.V. Neudatchin et al. ····· 51
4.7 Energy Confinement Scaling for Reversed-shear Plasmas with Internal Transport Barrier in JT-60U

T. Takizuka et al. ····· 52
4.8 Cold Pulse Propagation in the Vicinity of ITB on JT-60U
S. Inagaki et al. ····· 53
4.9 Relationship between Particle and Heat Transport in ITB Plasmas
H. Takenaga et al. ····· 57
4.10 Responses of Internal Transport Barrier to External Perturbations
H. Takenaga et al. ····· 58
4.11 Particle Transport during Electron Cyclotron Heating
H. Takenaga et al. ····· 62
4.12 Influence of the Maxwell Stress on the Zonal Flow Formation in JT-60U Reversed Shear Plasmas
T. Fukuda et al. ····· 66
4.13 Validation of the Asymmetric Pressure Perturbation Model for the Active Control of Sheared E × B Flow in Steady-state Burning Plasmas with ITB
T. Fukuda et al. ····· 67
4.14 Burning Plasma Simulation and Burn Control Trial in Reversed Shear Plasma
H. Takenaga et al. ····· 68
4.15 Perturbative Transport using Modulated ECH
A. Isayama et al. ····· 72

5. Improved Confinement at High Density and H-mode Pedestal ····· 75
5.1 Influence of Ar Puff on High Density ELMy H-mode Plasmas
N. Asakura et al. ····· 75
5.2 High Density and High Confinement ELMy H-mode Plasmas with Gas-puffing
H. Takenaga et al. ····· 79
5.3 Study of Pellet Injection Characteristics and Extension of Operation Region to High Density Using High-Field-Side Midplane Pellet Injection
H. Takenaga et al. ····· 83
5.4 Edge Pedestal Structure in Type I and Type II ELMy H-mode
Y.Kamada et al. ····· 87
5.5 Asymmetry of Collapse of Density Pedestal by Type I ELM on JT-60U
N. Oyama et al. ····· 88
5.6 Mechanism for Energy Loss by ELMs
A. V. Chankin et al. ····· 89
5.7 Studies on H-mode Transition using 2nd Harmonic X-mode ECH
N. Oyama et al. ····· 93

6. MHD Instability and High-energy Ions ····· 97
6.1 Real-time Stabilization of Neoclassical Tearing Mode
A. Isayama et al. ····· 97
6.2 Stabilization Effect of Early ECCD on Neoclassical Tearing Mode
K. Nagasaki et al. ····· 98
6.3 Effect of ECH/ECCD on Sawtooth Oscillations in NB-heated Plasmas in JT-60U
A. Isayama et al. ····· 99
6.4 Property of Alfven Eigenmode in JT-60U Reversed Shear and Weak Shear Plasmas
M. Takechi et al. ····· 100
6.5 Enhanced Beam Stopping Cross-section by Fast Ions Generated by N-NB
K. Okano et al. ····· 101

7. Disruption and Plasma Equilibrium ····· 102
7.1 Characterization of Axisymmetric Disruption Dynamics toward VDE Avoidance
Y. Nakamura et al. ····· 102
7.2 Fast Plasma Shutdown Scenarios in the JT-60U Tokamak Using Intense Mixed Gas

Puffing
M. Bakhtiari et al. ····· 105
7.3 A New Scheme of Plasma Shape Reconstruction Based on the CCS Method with the Axisymmetric Forward-problem Solution of Eddy Currents for the JT-60 Equilibrium Analyses
K. Kurihara et al. ····· 106

8. Impurities ····· 109
8.1 Effects of Electron Cyclotron Heating on Impurity Transport in ITB Plasmas
H. Takenaga et al. ····· 109
8.2 Estimation of Confinement Times for Central and Edge Fuelled Helium
H. Takenaga et al. ····· 110
8.3 Boronization Effects Using Deuterated-decaborane in JT-60U
T. Nakano et al. ····· 114
8.4 Estimation of the Density Ratio of Impurity Injected by Neutral Beam
T. Nakano et al. ····· 115

9. Divertor and SOL Plasmas ····· 116
9.1 SOL Plasma Flow and Influences on Divertor Plasma
N. Asakura et al. ····· 116
9.2 Fast Measurements of SOL Plasma Flow in ELMy H-mode Plasma
N. Asakura et al. ····· 119
9.3 Fast Measurement of Divertor Plasma in ELMy H-mode
N. Asakura et al. ····· 120
9.4 H_2 Molecule Spectroscopy in Divertor Plasmas
H. Kubo et al. ····· 124
9.5 2D Distribution of Divertor Radiation in JT-60U
S. Konoshima et al. ····· 128
9.6 Measurement of Ion Temperature in Divertor Plasmas
T. Nakano et al. ····· 129
9.7 Feedback Control of Divertor Plasma Density using Divertor Interferometer
H. Takenaga et al. ····· 131

10. Plasma Facing Materials and Detritiation ····· 135
10.1 Tritium Distribution in the Plasma-facing Wall of JT-60U
K. Masaki et al. ····· 135
10.2 The Depth Profiles of Deuterium and Hydrogen in Graphite Tiles Exposed to Deuterium Plasma Discharges of JT-60U
Y. Hirohata et al. ····· 136
10.3 Study of Chemical States of Graphite Tiles Exposed to Deuterium Plasma by XPS
Y. Oya et al. ····· 140
10.4 Erosion and Re-deposition on the Graphite and CFC Tiles used in the W-shaped Divertor
Y. Gotoh et al. ····· 144
10.5 Tritium Degassing Operation using Cleaning Discharges
S. Higashijima et al. ····· 145
10.6 Detritiation Characteristics by Glow Discharge Cleaning in JT-60U
H. Nakamura et al. ····· 149
10.7 Exhaust Gas Composition in Discharge Cleaning of JT-60U
T. Horikawa et al. ····· 153

11. Diagnostics ····· 157
11.1 Application of Nonlinear Optics for Drastic Improvement of YAG Laser Performance on JT-60U Thomson Scattering System

M. Nakatsuka et al. ····· 157
11.2 Double Pass Thomson Scattering Diagnostics using SBS Phase Conjugation Mirror in JT-60U
T. Hatae et al. ····· 161
11.3 Very High Electron Temperature Diagnostics using Combined Ruby and YAG Laser Thomson Scattering System in JT-60U
T. Hatae et al. ····· 165
11.4 First Application of Diamond Window for Infrared Laser Diagnostics in Fusion Plasmas
Y. Kawano et al. ····· 169
11.5 Heterodyne O-mode Reflectometer on the JT-60U Tokamak
N. Oyama et al. ····· 170
11.6 Singular Value Decomposition Analysis of Multichannel Electron Cyclotron Emission Signals of Tokamak Plasma
A. Isayama et al. ····· 171
11.7 Maximum Entropy Estimation of Electron Cyclotron Emission Spectra from Incomplete Interferograms in ELMy H-mode Tokamak Experiment
A. Isayama et al. ····· 172
11.8 Collective Thomson Scattering Based on CO_2 Laser for Ion Energy Spectrum Measurement in JT-60U
T. Kondoh et al. ····· 173
11.9 Spatial Profile Measurement Method of Absolute Detection Efficiency of the Infrared Heterodyne Receiver for the CO_2 Laser Collective Thomson Scattering System in JT-60U
S. Lee et al. ····· 174
11.10 Development of Advanced Collective Thomson Scattering for Impurity Concentration, Helium Ash Density and D/T Ratio Measurements
S. Lee et al. ····· 175
11.11 Collective Thomson Scattering Diagnostic for Fast Ion and Deuterium to Tritium Ratio Measurement in Open Magnetic Systems
S. Lee et al. ····· 176
11.12 Development of Fast Charge Exchange Recombination Spectroscopy using Interference Filter Method in JT-60U
S. Kobayashi et al. ····· 177
11.13 Remark on Apparent Increase in Ion Temperature in CXRS Measurement due to Large Velocity Gradient
Y. Koide ····· 178
11.14 Neutron Emission Profile Measurement on JT-60U
M. Ishikawa et al. ····· 182
11.15 Reciprocating Mach Probe System for High-Field-Side SOL Measurement
N. Asakura et al. ····· 183
11.16 Tritium and Gas Species Measurement System in JT-60U Exhaust Gas
A. Kaminaga et al. ····· 187

12. Heating Systems ····· 191
12.1 Improvement of Beam Performance in Negative-ion Based NBI System for JT-60U
N. Umeda et al. ····· 191
12.2 Operational Progress of the ECRF System in JT-60U
T. Fujii et al. ····· 192
12.3 Optimization of Polarization for ECRF System in JT-60U
S. Moriyama et al. ····· 195
12.4 Optimization of LHRF System for ECR Discharge Cleaning
M. Seki et al. ····· 196

Acknowledgments ····· 197

目次

1. 緒言
福田、久保、鎌田 …… 1

2. 実験結果概要
久保、福田、鎌田 …… 3

3. 高性能化と非誘導電流駆動 …… 9
3.1 高三角度運転の拡張と負イオン源NB入射による高β_pELMy Hモードプラズマ領域の拡大
鎌田 他 …… 9
3.2 JT-60Uの高βp ELMy Hモード放電における高核融合三重積と定常維持の達成
諫山 他 …… 13
3.3 負磁気シアプラズマによる高核融合性能実験
藤田 他 …… 14
3.4 高規格化密度、低q領域での高閉じ込め負磁気シアプラズマにおけるLHCD
井手 他 …… 18
3.5 負磁気シアプラズマにおける大きな小半径まで広がったITBの形成
井手 他 …… 22
3.6 センターソレノイドなしのプラズマ電流立ち上げと高閉じ込めプラズマの生成
高瀬 他 …… 26
3.7 JT-60Uにおける中心電流密度がほとんどゼロのトカマクのプラズマ平衡と閉じ込め
藤田 他 …… 27
3.8 誤差磁場および電流駆動に対する電流ホールの応答
藤田 他 …… 28
3.9 電子サイクロトロン電流駆動の物理についての実験にもとづく研究
鈴木 他 …… 32
3.10 中性粒子ビームによる周辺電流駆動
Hobirk 他 …… 35

4. コアプラズマにおける輸送 …… 39
4.1 JT-60U内部輸送障壁におけるイオン熱拡散係数の熱流速依存性
坂本 他 …… 39
4.2 内部輸送障壁での径電場シアと拡散係数の関係における非局所性
坂本 他 …… 40
4.3 ITBプラズマへの電子加熱の影響
井手 他 …… 41
4.4 JT-60Uにおける電子系内部輸送障壁形成条件の研究
福田 他 …… 42
4.5 巨視的プラズマパラメータの観点からのイオン内部輸送障壁形成条件の研究
鈴木 他 …… 46

4.6 JT-60U 中の内部障壁を持つ負磁気シアプラズマにおける L-H-L 遷移と ITB 事象の動的挙動と相互作用
Neudatchin 他 …… 51
4.7 JT-60U 中の内部輸送障壁を持つ負磁気シアプラズマのエネルギー閉じ込め比例則
滝塚 他 …… 52
4.8 JT-60U の ITB 近傍におけるコールドパルスの伝搬
稲垣 他 …… 53
4.9 内部輸送障壁を有するプラズマでの粒子輸送と熱輸送の関係
竹永 他 …… 57
4.10 外部摂動に対する内部輸送障壁の応答
竹永 他 …… 58
4.11 電子サイクロトロン加熱時の粒子輸送
竹永 他 …… 62
4.12 JT-60U 負磁気シア放電における帯状流の形成に関するマクスウェル応力の寄与
福田 他 …… 66
4.13 内部輸送障壁を伴う定常核燃焼プラズマにおける ＥＸＢ シア流の能動的制御を目的とした非対称圧力摂動効果の検証
福田 他 …… 67
4.14 負磁気シアプラズマにおける燃焼模擬と燃焼制御の試み
竹永 他 …… 68
4.15 変調 ECH を用いた摂動輸送
諫山 他 …… 72

5. 高密度閉じ込め改善とＨモードペデスタル …… 75
5.1 高密度ＥＬＭｙＨモードプラズマへのアルゴンガスパフの影響
朝倉 他 …… 75
5.2 ガスパフを用いた高閉じ込め ELMy H モードプラズマの高密度化
竹永 他 …… 79
5.3 内側ペレット入射を用いたペレット入射特性の研究と運転領域の高密度化
竹永 他 …… 83
5.4 Type I 及び Type II ELMy H モードにおける周辺ペデスタル構造
鎌田 他 …… 87
5.5 JT-60U における type I ELM による密度ペデスタル崩壊の非対称性
大山 他 …… 88
5.6 ELM によるエネルギー損失機構
Chankin 他 …… 89
5.7 Ｘモード２倍高調波加熱を用いたＨモード遷移の研究
大山 他 …… 93

6. MHD 不安定性と高エネルギーイオン …… 97
6.1 新古典テアリングモードの実時間安定化
諫山 他 …… 97
6.2 早期 ECCD の新古典テアリングモードに対する安定化効果
長崎 他 …… 98
6.3 JT-60U の NB 加熱プラズマにおける鋸歯状振動に対する ECH/ECCD の

効果
諫山　他 …… 99
6.4　JT-60U の負磁気シアおよび弱磁気シアプラズマにおけるアルフベン固有モードの特性
武智　他 …… 100
6.5　負イオンＮＢＩで生成された高速イオンによるビーム停止断面積の増大
岡野　他 …… 101

7. ディスラプションとプラズマ平衡 …… 102
7.1　VDE 回避に向けた軸対称ディスラプション挙動の特性評価
中村　他 …… 102
7.2　JT-60U トカマクにおける混合ガスパフを用いたプラズマの高速遮断シナリオ
Bakhtiari　他 …… 105
7.3　プラズマ形状再構築(逆問題)と軸対称渦電流(順問題)との順逆問題連成解法スキーム の新提案
栗原　他 …… 106

8. 不純物 …… 109
8.1　内部輸送障壁を有するプラズマでの電子サイクロトロン加熱の不純物輸送への影響
竹永　他 …… 109
8.2　中心供給及び周辺供給ヘリウムの閉じ込め時間の評価
竹永　他 …… 110
8.3　重水素化デカボランを用いたボロン化処理の効果
仲野　他 …… 114
8.4　中性粒子ビームによって入射される不純物量の評価
仲野　他 …… 115

9. ダイバータ・SOL プラズマ …… 116
9.1　境界層プラズマ流とダイバータプラズマへの影響
朝倉　他 …… 116
9.2　ＥＬＭｙＨモードプラズマにおける境界層プラズマ流の高速測定
朝倉　他 …… 119
9.3　ＥＬＭｙＨモードプラズマにおけるダイバータプラズマの高速測定
朝倉　他 …… 120
9.4　ダイバータプラズマの水素分子分光
久保　他 …… 124
9.5　JT-60U の二次元ダイバータ放射分布
木島　他 …… 128
9.6　ダイバータプラズマにおけるイオン温度測定
仲野　他 …… 129
9.7　ダイバータ干渉計を用いたダイバータ密度帰還制御
竹永　他 …… 131

10. プラズマ対向材料とトリチウム排出 …… 135
10.1　JT-60U プラズマ対向壁におけるトリチウム分布

正木　他 …… 135
10.2 JT-60U の重水素プラズマに曝された黒鉛タイル中の重水素および水素の深さ分布
広畑　他 …… 136
10.3 XPS による重水素プラズマに曝されたグラファイトタイルの化学状態に関する研究
大矢　他 …… 140
10.4 W型ダイバーターで使用された黒鉛およびＣＦＣタイル上の損耗・再堆積
後藤　他 …… 144
10.5 洗浄放電を用いたトリチウムガス出し運転
東島　他 …… 145
10.6 JT-60U グロー放電洗浄によるトリチウム除去挙動
中村　他 …… 149
10.7 JT-60U 放電洗浄における排ガス組成分析
堀川　他 …… 153

11. 計測装置 …… 157
11.1 JT-60U トムソン散乱測定装置における非線形光学素子を応用した YAG レー ザーの性能改善
中塚　他 …… 157
11.2 JT-60U における SBS 位相共役鏡を用いたダブルパストムソン散乱計測
波多江　他 …… 161
11.3 JT-60U のルビー及び YAG レーザートムソン散乱測定装置を組み合わせた高電子温度の診断
波多江　他 …… 165
11.4 赤外レーザを用いた核融合プラズマ診断における初めてのダイヤモンド窓の適用
河野　他 …… 169
11.5 JT-60U トカマクにおけるヘテロダイン型Ｏモード反射計
大山　他 …… 170
11.6 トカマクプラズマの電子サイクロトロン放射信号の特異値分解解析
諫山　他 …… 171
11.7 最大エントロピー法を用いた，ELMy H モードトカマク実験における不完全な干渉信号からの電子サイクロトロン放射スペクトルの推定
諫山　他 …… 172
11.8 JT-60U におけるイオンネルギースペクトル測定のための炭酸ガスレーザーを用いた協同トムソン散乱計測
近藤　他 …… 173
11.9 JT-60U における炭酸ガスレーザー協同トムソン散乱システム用赤外線ヘテロダインレシーバーの絶対検出効率の空間プロフィール測定法の開発
Lee　他 …… 174
11.10 不純物、ヘリウムと D/T 比測定のための先進協同トムソン散乱計測法の開発
Lee　他 …… 175
11.11 開放端系磁場閉込め装置の高速イオンならびに重水素トリチウム比測定のための協同トムソン散乱計測
Lee　他 …… 176
11.12 JT-60U におけるフィルター法を用いた高速荷電交換分光装置の開発

小林　他 …… 177
11.13 CXRSによるイオン温度測定に対するプラズマ回転速度勾配の影響
小出 …… 178
11.14 JT-60Uにおける中性子発生分布測定
石川　他 …… 182
11.15 高磁場側測定用可動マッハプローブ・システム
朝倉　他 …… 183
11.16 JT-60U排気中のトリチウム及びガス種測定システム
神永　他 …… 187

12. 加熱装置 …… 191
12.1　JT－60U用負イオンNBIのビーム性能の改善
梅田　他 …… 191
12.2　JT-60U ECRF装置の運転性能の進展
藤井　他 …… 192
12.3　JT-60Uにおける電子サイクロトロン波帯加熱装置の偏波最適化
森山　他 …… 195
12.4　ＥＣＲ放電洗浄を目的としたＬＨＲＦ加熱装置の最適化
関　他 …… 196

謝辞 …… 197

1. Introduction

During the years of 2001 and 02, the strenuous campaign has been performed in JT-60U, intended to further extend the achieved reactor-relevant performance, with emphasis on the sustainment of improved confinement, and deepen the knowledge in plasma science under the pervasive collaborative program mainly with Japanese universities. Accordingly, a large part of the campaign was devoted to the highly integrated performance experiment for the development of advanced tokamak with internal transport barrier (ITB), aimed at providing remarkable contributions to the establishment of steady-state advanced operation scenario in International Thermonuclear Experimental Reactor (ITER). Further improvement in confinement at high density and impurity transport in ITB plasmas have also been another initiative, in addition to the impact of strong electron heating. Furthermore, physics oriented issues, such as the electron ITB formation condition and perturbative transport studies, have been pushed forward strongly. As to the collaborative experiment with universities, the modeling in fusion plasmas and validation of the theoretical models have been emphasized. The active contribution to the International Tokamak Physics Activity (ITPA), which is aimed at producing a firm scientific basis for the fusion reactor, was also an important element. A broad range of urgent issues in tokamak physics is within the purview of ITPA, in addition to the diagnostics development, such as the transport modeling and confinement scaling, ITB physics, magnetohydrodynamic (MHD) stability and control, heating and current drive, steady-state operation, pedestal physics and divertor optimization. Furthermore, development of innovative plasma operation technique, namely the start up of plasma current without using the central solenoid, which enables the reduction of engineering constraints in a fusion reactor, was undertaken. In the later period of the 2002 campaign, exploratory investigation on the residual tritium removal has been undertaken, as the tritium retention in the vessel has been rigorously disputed in ITER.

It should be mentioned hereby that substantial achievements owe above all much to the significant progress in the performance of heating devices, such as electron cyclotron heating (ECH) and the negative-ion-based neutral beam injection (N-NBI), and extension of the poloidal coil capability which has enabled to increase the plasma triangularity (δ) at high plasma current. In addition, injection of multiple pellets from the high-field-side equatorial plane has been made possible, which in principle leads to the efficient fueling by the $E \times B$ drift. Namely, the N-NBI and ECH capabilities have been raised respectively up to 6.2 MW for 1.7 s and 3 MW for 2.7 s. The reduction in N-NBI beam divergence extended the pulse length to 10 seconds at 355 keV and 2.6 MW, whilst one 110 GHz gyrotron source was added in the 2002 campaign to increase the injected energy to 10 MJ i.e., 2.8 MW for 3.6 s. The consequence of these improvements in plasma performance is simple and straightforward, in terms of the enhanced current drive (CD) and profile control capabilities.

As a result, the leading position of JT-60U in fusion science was successfully maintained [1-4]. A high poloidal beta (β_p) H-mode plasma with full non-inductive current drive has been obtained at 1.8 MA and the fusion triple product reached 3.1×10^{20} keV·s·m^{-3}, and the high DT-equivalent fusion power gain (Q_{DT}^{eq}) of 0.8 was sustained for 0.55 s in a high performance plasma with a current hole. In addition, N-NB heating in an A_r seeded plasma extended the n_e/n_{GW} (n_e: electron density, n_{GW}: Greenwald density) range up to 0.95 with confinement enhancement factor HH_{y2} over the ITER98(y, 2) scaling of 0.9. The detailed descriptions of the achievements and developments as well as the results from the physics based programs are described in the following sections.

References

[1] Kubo, H. et al., Phys. Plasmas **9**, 2127 (2002).

[2] Fukuda, T. et al., Plasma Phys. Control. Fusion **44** ,39 (2002).

[3] Miura, Y. et al., Phys. Plasmas **10**, 1809 (2003).

[4] Fujita, T. et al., "Overview of JT-60U results toward high integrated performance in reactor-relevant regime", Proc. 19th IAEA Fusion Energy Conference, IAEA-CN-94/OV/1-3; Submitted to Nuclear Fusion.

2. Overview of the Experimental Results

High Performance and Non-inductive Current Drive

The extension of the full non-inductive CD regime to higher current has been pushed forwards by utilizing the increased N-NB power and increased poloidal coil capability for higher δ. As a result, the full non-inductive CD was achieved in a 1.8 MA high-β_p H-mode plasma discharge, and the fusion triple product reached 3.1×10^{20} keV·s·m^{-3}. In addition, with the improved capability, high values of normalized beta (β_N) around 2.7 were maintained for 7.4 s or 60 τ_E (τ_E: energy confinement time) at $\delta = 0.45$, whilst the quasi-steady beta values maintained for longer than $5\tau_E$ was raised to $\beta_N = 3.05$ by the increase of δ to 0.6. On the other hand, the sustainment of high performance reversed shear discharge has been undertaken. The DD neutron production rate of 4.6×10^{16}/s, $\beta_N = 1.6$, $\tau_E = 0.89$ s, H^{89} over the L-mode scaling of around 3.0 and $Q_{DT}^{eq} = 1.2$ were obtained at $I_p = 2.60$ MA and $q_{95} = 3.3$. The duration of high fusion-performance ($Q_{DT}^{eq} > 0.8$) was extended to 0.55 s. The improved confinement at high normalized density has also been demonstrated in full non-inductive CD reversed shear discharge, using the combination of lower hybrid current drive (LHCD) and NNBCD. Here, the ITB radius was expanded up to $\rho = 0.8$, and $HHy2 = 1.4$ was achieved at $n_e/n_{GW} = 0.8$.

The test related to the start up of plasma current (I_p) without using the central solenoid has been undertaken, which is aimed at not only improving the efficiency of the tokamak design but also reducing the engineering constraints in a fusion reactor. As a consequence, the plasma current initially raised by LHCD was increased with the help of flux input by the increased current in vertical field coils and the bootstrap current. A very high performance plasma was produced with $HH_{y2} = 1.6$, $\beta_p = 3.6$ and $\beta_N = 1.6$ at $I_p = 0.6$ MA. Here, both ITB and the edge transport barrier were accompanied. The safety factor (q) profile was inverted, and the current hole was confirmed.

Another issue of highlight is the observation of the equilibrium shape with nearly zero current density in the core or the "current hole" persisted stably for several seconds in a reversed shear plasma. Although the external current drive (CD) inside the current hole has been undertaken, no significant amount of change in the current density has been observed.

In ITER or demo reactors, off-axis ECCD in high-electron-density and high-electron-temperature plasmas is required. By optimizing the target current profile and EC wave deposition location, a stable high-electron-temperature plasma has been obtained where central electron temperature of nearly 21 keV was maintained for 0.8 s. It was found that the evaluated CD efficiency is lower than the result of the linearized calculation in the high electron temperature regime. Furthermore, effect of trapped electrons was also observed.

Transport in Core Plasmas

The physics studies of ITB formation, dedicated experiment has been performed, in which the heating power was deliberately scanned. In positive shear plasmas, there was a threshold heating power for formation of weak ITB, while no threshold power was found in reversed shear plasmas. In both of positive shear and reversed shear plasmas, the strong ITB was formed with bifurcation or a sudden drop in ion thermal diffusivity (χ_i) as a function of time or radial electric field (E_r) shear. Considering that the electron heating would be predominant in burning plasmas, intensive investigations on the electron heating of ITB plasmas have been carried out, where it has been found that very high confinement can be sustained in negative central shear plasmas with strong ITB. In weak shear plasmas, on the other hand, it was found that the barrier is deteriorated. In order to study the electron ITB physics, systematic investigation has been performed, in which the EC power was scanned mainly under the absence of ion ITB. As a result, it was found that the threshold heating power does not seem to exist, similar to the case of weak ion ITB. The electron ITB was formed in the negative shear region away from the location of the minimum safety factor (q_m), and it expands outward as the ion ITB is formed with an increased heating power. The possible correlation between R/L_{Te} (R: Major radius, $L_{Te} = - T_e / (dT_e/dr)$) and $s-\alpha$ ($\alpha = -q^2 R d\beta/dr$) was documented.

The confinement scaling of reversed shear plasmas with ITB has been investigated. It was thereby found that the stored energy inside the ITB radius does not have the heating power dependence, but strongly related to $\varepsilon\beta_p$ ($\varepsilon = r/R$). Also, the heat pulse propagation experiment has been performed, using pellet injection in ITB plasmas. It was thereby documented that the amplitude of cold pulse is enhanced at the ITB location and disappears inside, which is not consistent with the diffusive model. It has also been documented that the particle and thermal diffusivities are well correlated in ITB plasmas under both negative and weak shear in a wide range of χ_i, being $1<\chi_i/\chi_i^{NC}<10$ (χ_i^{NC}: ion thermal diffusivity calculated by the neoclassical transport model). The control of ITB is another issue of concern, in particular in burning plasmas, in which the plasma is in the autonomous state and the external heating power for the profile control is considerably lower than the alpha-heating power. Various approaches using impurity injection and perturbation with pellets, ECH and non-resonant field were performed. Reduction of density fluctuation and substantial improvement in confinement were observed, when the pellet was injected into reversed shear plasmas.

Improved Confinement at High Density and H-mode Pedestal

In the H-mode regime, important issues are to maintain high confinement at high density and to reduce the ELM (edge localized mode) heat load to the divertor target plates. In Ar-seeded H-mode plasmas, higher confinement is obtained at high density in comparison

with the no impurity-seeding cases. In JT-60U, a specific configuration with the outer strike point located on the dome-top, namely the "dome-top configuration," has been found to be effective to further enhance the confinement, where the giant ELMs disappear at high density, and the maximum ELM-induced heat load decreases to 1/3 - 1/5. In the 2002 campaigns, high-power N-NB injection extended the density regime to $n_e/n_{GW} = 0.95$ keeping HHy2 of 0.9 at the same time.

It is above all important to raise the pedestal pressure in order to enhance the global stability and confinement properties. It has been heuristically found in a pellet injected discharge that the pedestal pressure increased by a factor of 2-2.5 with total (or core) poloidal beta in high δ ($\delta = 0.45$) plasmas with either type I and type II ELMs. As a result, high confinement of $HH_{y2} = 1.1$ was achieved at $n_e/n_{GW} = 0.7$. The type II ELM regime has been extended to a lower q by increasing δ up to 0.6. In addition, the dynamics and poloidally asymmetric structure of the collapse at ELMs have been found by the combination of various diagnostics, such as the reflectometer and high resolution ECE. Furthermore, it was manifested that the ELM heat load is mainly carried by the convective transport, using the SOL (scrape off layer) Mach probes and infrared camera.

MHD Instability and High-energy Ions

For the sustainment of high β_N in a low collisionality regime, suppression of neoclassical tearing mode (NTM) is indispensable. A real-time "search and suppress" technique has been intensively developed for the efficient NTM control, where the location of the island center is evaluated using the electron temperature perturbations measured with ECE diagnostic and the injection angle of EC wave is determined so that the EC power is deposited right at the island center. It was observed that the 3/2 NTM intensity decreased gradually and completely stabilized. Accordingly, the value of β_N spontaneously was recovered from 1.5 to 1.7 without an increase of the total heating power, which indicates that the energy confinement was improved by the NTM suppression. The effectiveness of early ECCD has also been confirmed.

In support of the advanced operation scenario in ITER, the validation of a theoretical model, related to the reversed-shear-induced Alfvén eigenmode (RSAE) has been undertaken. It was documented that the strong dependence of RSAE frequency on the value of q_{min}, as well as the frequency-chirping feature is consistent with the theoretical model.

Disruption and Plasma Equilibrium

Extended database on disruptions aimed at consolidating the ITER engineering design has been compiled. In addition, features of vertical displacement events (VDEs) have been analyzed to the detail with emphasis on the current density profile and shaping. Furthermore, forced plasma termination schemes have been developed using the impurity gas

puff. In regard to the plasma equilibrium control, CCS (Cauchy conditioned surface) method has been established and made routinely available in the 2002 campaign, in which the effect of eddy current was studied for implementation in the code.

Impurities

Impurity reduction in high-confinement plasmas is considered as one of the important issues for the improvement of plasma performance. In the recent experimental campaign, apparent Ar exhaust from the inside of the ITB by ECH injection has been observed in high-β_p plasmas. In regard to the He exhaust characteristics, investigation of the particle confinement time for central and edge fuelled He suggested that He exhaust capability was limited not by the particle confinement in the main plasma but by pumping in the divertor region even in the high-confinement plasmas. By boronizing the vessel using (10-20) g of $B_{10}D_{14}$ every ~200 shots, the oxygen content in the main plasma has been kept below ~ 1%. By investigation of the D_α spectra from the NBs, it was suggested that (0.6-3)% of oxygen was included in the NBs.

Divertor and SOL Plasmas

Understanding of divertor and SOL plasmas has progressed by new observations and theoretical analyses. The Mach probe measurement at three different locations (the low-field-side midplane, X-point, and high-field-side SOL) accompanied by the UEDGE simulation has been extensively performed to document the SOL flow pattern and role of the plasma drifts on the SOL flow dynamics. During ELMs, the SOL flow has also been measured. The dynamics of the ELM heat and particle deposition have also been investigated, using the fast-sampling divertor Langmuir probes. As to recycling, the H_2 line emission profiles measured in attached divertor plasmas have been reproduced by the calculation that employs a neutral transport code with a collisional-radiative model. In the detached divertor plasma with a MARFE, deep penetration of H_2 molecules was observed. With respect to the radiative losses, it has been documented that radiative volume moved upward along the divertor legs from the vicinity of the divertor plates with an increase of density, being redistributed uniformly over the whole divertor region, and eventually condensed in a localized region (X-point MARFE). In addition, the ion temperature distribution in divertor plasmas has been investigated by analyzing Doppler profiles of C IV lines.

Plasma Facing Materials and Detritiation

Evaluation of tritium retention properties in in-vessel materials is important from a viewpoint of safety in the fusion reactor. Observation of tritium distribution retained in the plasma-facing wall indicated that the high-energy tritium produced by the DD nuclear reaction was lost by the ripple transport before its thermalization and implanted deeply into

the wall with high incident energy. On the other hand, by the secondary ion mass spectroscopy and X-ray photoelectron spectroscopy, it has been found that the profiles of hydrogen isotopes are related to the flux of ions and/or charge exchange neutrals, erosion and re-deposition, and tile temperature. It has been documented that the re-deposition process was dominant (the maximum thickness was ~60 μm) in the inner divertor, whereas the erosion was predominant (the maximum erosion depth was ~20 μm) in the outer divertor.

The detritiation of the vacuum vessel has also been undertaken by the glow discharge cleaning, electron cyclotron resonance discharge cleaning, and Taylor discharge cleaning using H_2, He and Ar. The H_2 glow discharge cleaning was the most effective for detritiation, and it was suggested that the isotope exchange reaction strongly contributed to the detritiation. The dominant chemical species of the removed tritium was hydrogen molecule (HT and DT), and the fractions of water vapor (HTO and DTO) and hydrocarbon were small.

Diagnostics

For the extended understandings of fusion plasmas, development of new diagnostic systems and improvement of existing diagnostics are indispensable. As to the YAG-laser Thomson scattering diagnostic, average laser output power of 205 W has been achieved at 50 Hz with total energy of 4.1 J, using a two-line YAG amplifier system with stimulated-Brillouin-scattering phase conjugation mirrors (SBS-PCM). A double-pass Thomson scattering method with SBS-PCM has also been applied for the first time, and the scattered light intensity increased by a factor of 1.6. In order to improve the resolution at high electron temperature (T_e > 15 keV), combining scheme of the YAG and the Ruby laser system, which extends the detection wavelength coverage, has been developed and it demonstrated its effectiveness. By the application of diamond windows to the infrared laser polarimeter, feasibility of the diamond vacuum window for optical diagnostics has been demonstrated. In addition to the X-mode system, a three-channel heterodyne O-mode reflectometer has been upgraded for measurement of density fluctuations not only at the ETB (edge transport barrier) region but also at the ITB region. For the ECE measurement, singular value decomposition scheme has been applied to ECE signals measured with the grating polychromator, and its usefulness has been demonstrated. The non-thermal emission pulses due to ELMs can induce large disturbance for interferograms observed with the Fourier transform spectrometer. From the incomplete Michelson interferograms, the radial profile of electron temperature has successfully been evaluated using the maximum entropy method. A collective Thomson scattering diagnostic system based on a pulsed CO_2 laser has been developed for the measurement of ion temperature and the energy spectrum of fast ions, and the commissioning of the system has been started. Here, a new effective method for the spatial profile measurement of absolute detection efficiency of an infrared heterodyne receiver has been developed. Furthermore, advanced techniques using collective Thomson scattering were

proposed for the measurement of impurity density and D/T density ratio. As to the ion temperature measurement, a filter method with three wavelength channels has been applied to CXRS (charge exchange recombination spectroscopy) diagnostics, aiming at the measurement of the ion temperature and rotation with a high time resolution. As a result, the time resolution of 0.8 ms was achieved. On the other hand, for CXRS diagnostics, possibility of apparent increase in measured ion temperature due to a large velocity gradient was investigated. With a Stilbene neutron detector, measurement of the neutron emission profile has become routinely available in JT-60U. In order to measure the Mach number profiles, electron temperature, electron density and floating potential in the inner divertor plasma, a reciprocating Mach probe system has been recently installed. In addition, in order to measure the tritium exhaust amount and chemical form of tritium in the exhaust gas during JT-60U operation, a tritium and chemical composition measurement system has been installed.

Heating Systems

The heating systems have been improved to enhance the plasma performance. In regard to the negative-ion based NBI system, the heat load to the NBI port limiter has been reduced by the improvement of the beam focusing, and long pulse (10 s) injection has been demonstrated at high beam power of 2.6 MW. As to the ECRF system, the highest injected power of 3 MW has been achieved by suppressing the parasitic oscillation in the gyrotrons. The feedback control of the poloidal injection angle of the EC beam has also been developed for the NTM stabilization. On the other hand, the 2GHz-LHRF system, long pulse (~ 45 min) and low power (30-40 kW) operation scheme has been optimized for the tritium removal experiment, where electron cyclotron resonance condition was adopted for the discharge cleaning.

3. High Performance and Non-inductive Current Drive

3.1 Extended Plasma Regimes of the High β_p ELMy H-mode with NNB Injection and Enhanced Capability of High Triangularity Operation

Y. Kamada, A.Isayama, H.Takenaga, T. Suzuki, T.Fujita,

Abstract. The high-β_p ELMy H mode plasma regime has been successfully expanded by utilizing improved capability of high triangularity operation, enhanced NNB injection performance and pellet injection. In the high I_p (=1.8MA) regime, the record value $n_D(0)\tau_E T_i(0)=3.1\times10^{20}m^{-3}skeV$ under the full non-inductive current drive condition was achieved in the reactor relevant condition, and the stored energy W_{dia} has been enhanced to 8.0MJ. At triangularity ~0.6, the β_N value sustainable sufficiently longer than the energy confinement time ($>5\tau_E$) has been increased up to 3.05 in the low q_{95}(<4) regime. In addition, JT-60U has extended the Grassy ELM regime to low q_{95} (<4).

1. Introduction

With the main aim of providing physics basis for ITER and the steady-state tokamak reactor, JT-60U has been optimizing operational concepts and extending discharge regimes toward simultaneous sustainment of high confinement, high β_N, high bootstrap fraction, full non-inductive current drive and efficient heat and particle exhaust utilizing variety of heating, current drive, torque input and particle control capabilities [1,2]. In the weak magnetic shear (high-β_p) ELMy H modes characterized by both internal (ITB) and edge transport barriers and high bootstrap current fractions f_{BS}, discharges have been sustained near the steady-state current profile solutions under full noninductive current drive [1]. After that, in 2001 and 2002, the high-β_p ELMy H mode plasma regime has been expanded further by utilizing improved capability of high triangularity operation, enhanced NNB injection performance and pellet injection. The new high triangularity operation allows us to produce higher triangularity at a given plasma current (for example δ=0.34 at I_p=1.8MA and δ=0.6 at I_p=1MA) or to sustain a medium δ for longer period (δ=0.45 for 8-9sec).

2. Enhanced plasma performance with full non-inductive current drive

In the high β_p ELMy H-mode regime, we have demonstrated a high fusion triple product $n_D(0)\tau_E T_i(0)=3.1\times10^{20}m^{-3}skeV$ under the full non-inductive current drive condition (see Sec.2.7 and [3]) (E39713, I_p=1.8MA, $B_t(0)$=4.09T, q_{95}=4.1, $n_D(0)=4.2\times10^{19}$m-3, τ_E=0.344s, $T_i(0)$=21.5keV, $T_e(0)$=10.5keV, H_{89PL}=2.53, HH_{y2}=1.22, W_{dia}=7.6MJ, β_N=2.40, β_p=1.73, f_{BS}=0.50 and f_{NBCD}=0.50, P_{rad}/P_{net}=0.54, n_e-bar=$4.0\times10^{19}m^{-3}$=0.42n_{GW}, Z_{eff}=3.0). The discharge waveforms and the profiles of T_i, T_e n_e and q are shown in Fig.1. In this discharge, we injected NNB for current drive and heating and EC for central electron heating.

The integrated performances of representative discharges in the high β_p ELMy H-mode regime are shown in Fig.2(a) (I_p=1.8MA:E39713, I_p=1.5MA:E36715[1], I_p=1MA:E21895[4]).The full scale for each axis represents one of the ITER steady-state operation design examples. In the high β_p H-mode regime, discharges satisfy the requirements for H_{Hy2},f_{BS} and f_{CD}. However, for density and radiation power, in particular, further improvement is needed. Figure 2 (b) shows the achieved full non-inductive discharge regime on the ν_e*(collisionality) - ρ_{pi}*(normalized poloidal gyroradius) plane. Since behavior of the

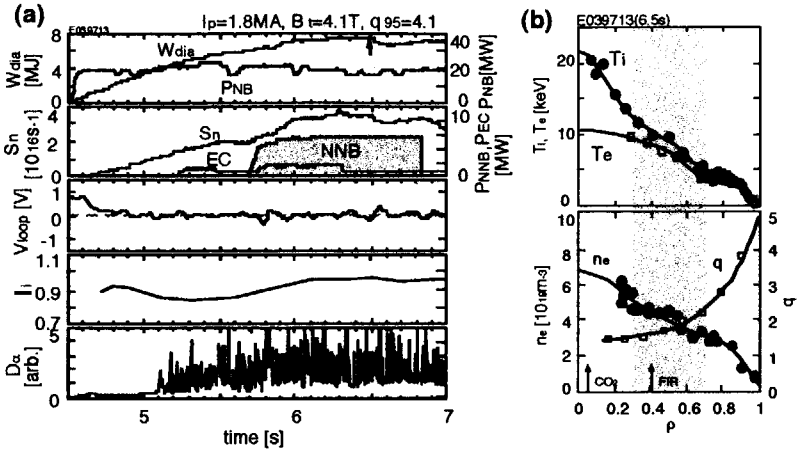

Fig.1: (a) Discharge waveforms and (b) temperature, density and safety factor profiles for E39713 (I_p=1.8MA, $B_t(0)$=4,1T, q_{95}=4.1, δ=0.34).

key physics processes, such as stability, transport and bootstrap current are determined by these non-dimensional parameters, it is necessary to demonstrate the required performances at sufficiently low values of ν_e^* and ρ_{pi}^* close to the reactor operational regimes. The JT-60U high-β_p full noninductive CD regime has accessed ν_e^*~0.01-0.02 and ρ_{pi}^*~0.06. These values are close to those for the ITER steady-state reference design; $\nu_e^* \sim \nu_e^{*ITER}$ and $\rho_{pi}^* \sim 3\ \rho_{pi}^{*ITER}$. In extending such high β_N regime to the reactor relevant regime with low-ν_e^* &ρ_{pi}^* regime, the key issue is stabilization of the neoclassical tearing mode (NTM) [5]. In the high-β_p ELMy H-mode regime at high I_p and B_t, we could successfully stabilize the NTM (m/n=3//2 and 2/1) by optimizing the combination of the current and the pressure profiles to reduce $\beta_p(L_q/L_p)$ around the rational surfaces [3], and the β_N value sustainable for much longer than τ_E (>5 τ_E) has been increased up to ~2.3 at $B_t(0)$=4.1T (Fig.2(c). Consequently, the fusion performance for the full non-inductive current drive regime has been improving towards the reactor relevant regime as shown in Fig.2(d).

In 2002, towards higher fusion performance, we have optimized the discharge

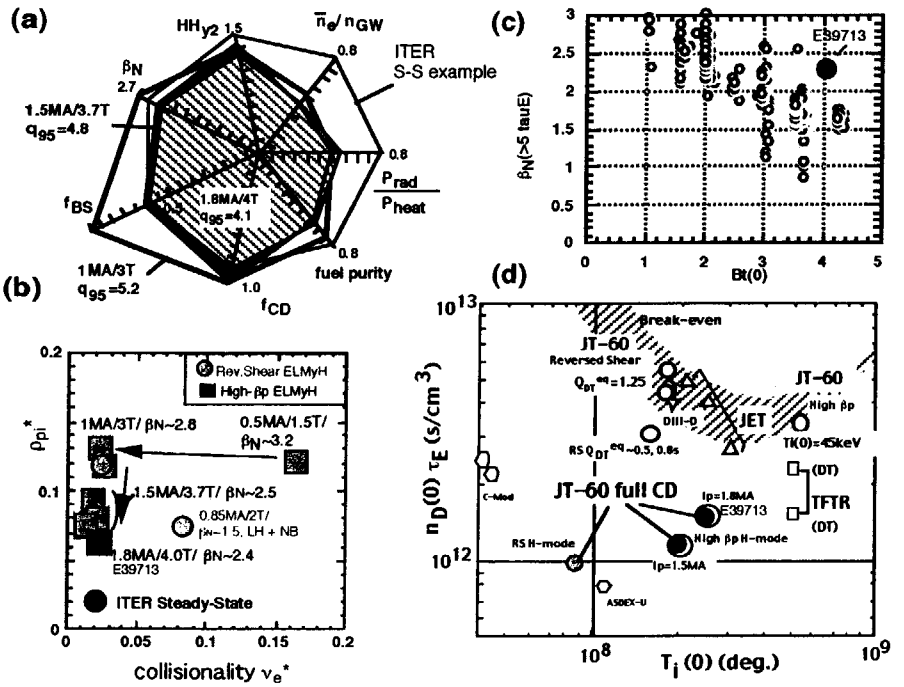

Fig.2: (a) Achieved integrated performance under full non-inductive current drive (High-β_p ELMy H-mode, I_p=1.0, 1.5 and 1.8MA). The full scale for each axis represents one of the ITER steady-state operation examples. (b) Operation regime of full noninductive CD at high β_N approaching the ITER regime in terms of ρ_{pi}^* and ν_e^*. (c) β_N value sustainable sufficiently longer than τ_E (>5τ_E) versus $B_t(0)$. The closed circle corresponds to E39713. (d) JT-60U full non-inductive CD performance on the $n_D(0)\tau_E$ - $T_i(0)$ plane.

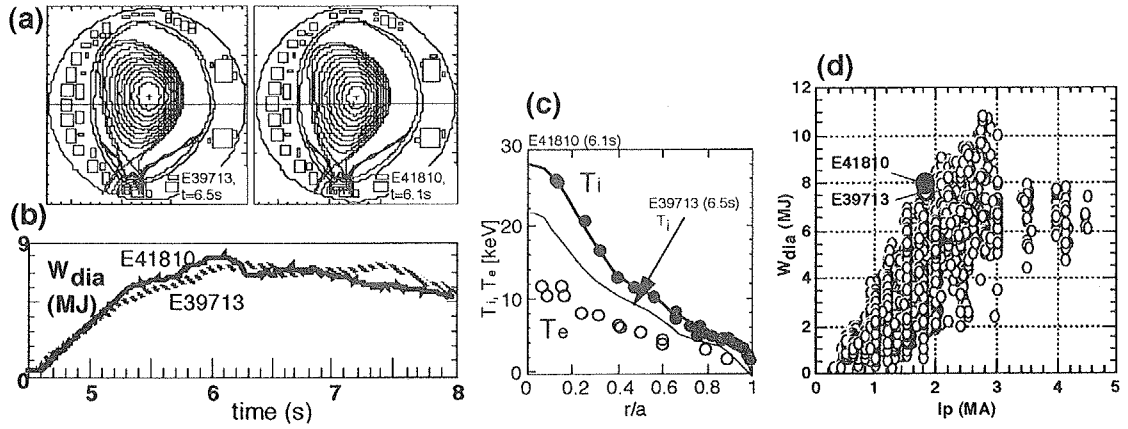

Fig.3: (a) Plasma poloidal cross sections for E39713(t=6.5s, I_p=1.8MA, $B_t(0)$=4.06T, q_{95}=4.09, R_p=3.24m, a=0.80m, κ=1.52, δ=0.34, V_p=56.5m^3) and E41810(t=6.1s, I_p=1.8MA, $B_t(0)$=4.08T, q_{95}=3.97, R_p=3.23m, a=0.76m, κ=1.58, δ=0.34, V_p=53.2m^3).(b) Time evolution of the plasma stored energy (W_{dia}) for E39713(dotted) and E41810 (solid). (c) Ion and electron temperature profiles for E41810 (t=6.1s). $T_i(r)$ for E39713 (6.5s) is also shown for comparison. (d) Summary of W_{dia} vs. I_p in JT-60U. Data for E39713 and E41810 are highlighted.

condition and achieved W_{dia}=8.0MJ (E41810) without NTMs at the same I_p=1.8MA and B_t=4.1T as E39713 (W_{dia}=7.6MJ). The main points are 1) reduction of the plasma volume from 56.5m^3 to 53.2m^3 for increasing the power density and, at the same time, 2) shifting the axis position vertically downwards by 4cm in order to broaden the central heating power from the perpendicularly injected NBs, and 3) increasing elongation from 1.52 to 1.58 with keeping the same triangularity of 0.34. The discharge cross section, waveform of W_{dia} and profiles of T_i and T_e are shown in Fig.3 for E41810 and E39713. The achieved W_{dia}=8.0MJ is the rechord value at I_p=1.8MA in JT-60U (Fig.3(d)).

3. Extended high beta regimes

With the improved capability of the high triangularity operation in JT-60U, at δ ~ 0.6 with the optimum pressure profile [6], the β_N value sustainable sufficiently longer than the energy confinement time (>5τ_E) has been increased up to 3.05 in the low q_{95}(<4) regime. The typical waveforms and the plasma shape for the high δ high-β_p ELMy H-mode discharge are

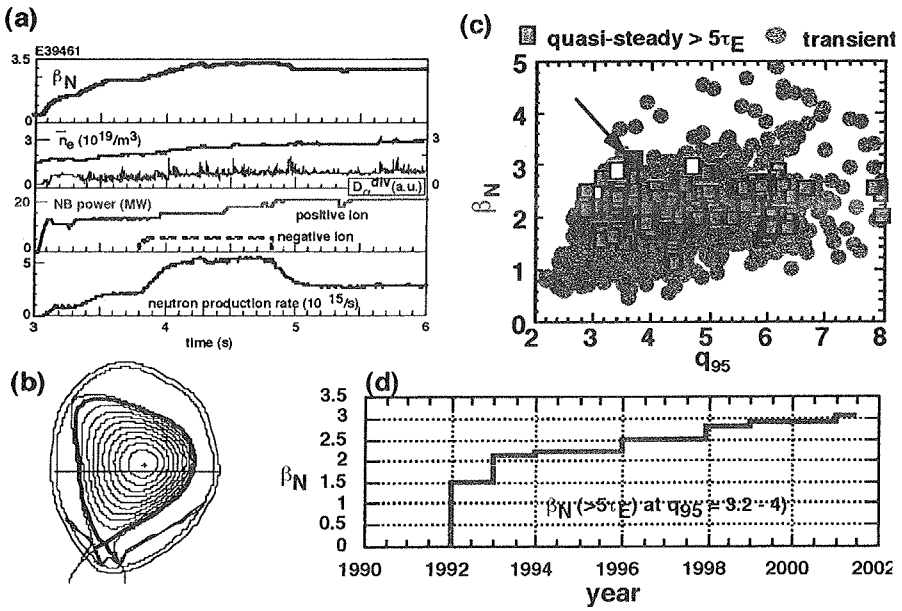

Fig.4: (a)&(b) Discharge waveforms and the plasma cross section for E39461 (I_p=1MA, $B_t(0)$=1.95T, q_{95}=3.68, R_p=3.44m, a=0.86m, κ=1.32, δ=0.57, V_p=60.2m^3, β_p=1.87, β_N=3.23). (c) Summary of β_N vs. q_{95} in JT-60U. Squares correspond to quasi-steady (sustained for >5τ_E) data. (d) Progress of β_N value sustainable sufficiently longer than the energy confinement time (>5τ_E) in the low q_{95} (<4) regime.

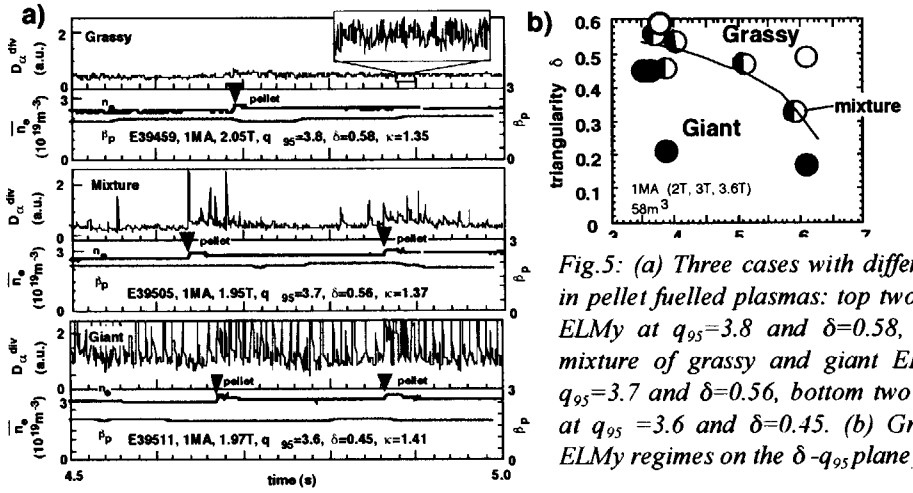

Fig.5: (a) Three cases with different behavior of ELMs in pellet fuelled plasmas: top two columns: pure grassy ELMy at q_{95}=3.8 and δ=0.58, middle two columns: mixture of grassy and giant ELMs at slightly lower q_{95}=3.7 and δ=0.56, bottom two columns: giant ELMy at q_{95} =3.6 and δ=0.45. (b) Grassy ELMy and giant ELMy regimes on the δ -q_{95} plane.

shown in Fig.4(a)&(b) (E39461, I_p=1MA, $B_t(0)$=1.95T, q_{95}=3.67). In this type II (grassy). ELMy discharge, NNB was injected for 1sec together with the high field side pellet injection, and β_N =3.0 - 3.25 was sustained for ~1sec with H_{89PL}~ 2.0, HH_{y2}~1.1 and β_p~1.9.)). Figure 4(c) summarizes β_N vs. q_{95} in JT-60U, where squares correspond to quasi-steady (sustained for >5τ_E) data. Progress of β_N (>5τ_E) in the low q_{95} (<4) regime is given in Fig.4(d). In addition, at δ~0.45, β_N=2.7 has been sustained for 7.4s determined by the hardware limitations. In this case, m/n=3/2 NTM was destabilized but the mode amplitude was saturated [3].

4. Expanded grassy ELMy regimes

Another benefit of the high δ shape is achievement of Grassy ELMs with small peak heat and particle load onto the divertor plates. One of the urgent issues for ITER is achievement of the small ELMs in the low safety factor (q_{95}<4) regime. JT-60U has reported [6] that the Grassy ELMs appear at high q_{95} and high δ, and , in addition, a high β_p value helps it. Utilizing the new high triangularity capability, JT-60U has successfully extended the Grassy ELM regime to low q_{95} (<4) (see also Sec.3.18). Figure 5(a) shows three cases at I_p=1MA. The top two columns show that a pure Grassy ELMy phase is sustained at q_{95}=3.8 and δ=0.58. However, if both q_{95} and δ are reduced slightly (q_{95}=3.7 and δ=0.56), mixture of grassy and giant ELMs is observed (middle two columns). And, at lower q_{95} (=3.6) and δ (=0.45), only Giant ELMs appear (bottom two columns). The grassy ELM regime is given on the q_{95}-δ plane in Fig.5(b). It should be noted that the high field side pellets were injected into these discharges. At insufficient δ and q_{95} (see the middle columns in Fig.5(a)), pellets seem to induce giant ELMs. However, if δ and q_{95} are sufficiently high (top two columns), pellets do not induce giant ELMs and the grassy ELMy phase can be sustained.

REFERENCES

[1] Y. Kamada, et al., Nucl. Fusion **41** (2001) 1311.
[2] Y. Kamada et al., Fusion Sci. Tech. **42** (2992) 185.
[3] A. Isayama et al., Proc. 19th IAEA Fusion Energy Conf, Lyon, 2002, IAEA-CN-94/EX/C2-2.
[4] Y.Kamada et al., in Plasma Physics and Controlled Nuclear Fusion Research 1994 (Proc. 15th Int. Conf. Seville), Vol. 1, IAEA, Vienna (1995) 651.
[5]. A. Isayama et al., Nucl. Fusion **41** (2001) 761.
[6] Y. Kamada et al., in Fusion Energy 1996 (Proc. 16th Int. Conf. Montreal) Vol. 1, IAEA, Vienna (1997) 247.
[7] Y. Kamada et al., **Plasma Phys. Control. Fusion 42 (5A) (2000) A247. (Grassy)**
[8] Y. Kamada et al., Plasma Phys. Control. Fusion **44** (5A) (2002) A279.

3.2 Achievement of a High Fusion Triple Product and Steady State Sustainment in High β_p ELMy H-mode Discharges in JT-60U [1]

A. Isayama, Y. Kamada, N. Hayashi, T. Suzuki, T. Oikawa, T. Fujita, H. Takenaga, K. Ushigusa, T. Ozeki, Y. Ikeda, N. Umeda, H. Yamada[1)], M. Isobe[1)], Y. Narushima[1)], K. Ikeda[1)], S. Sakakibara[1)] and K. Yamazaki[1)]

1) National Institute for Fusion Science

High β_p ELMy H-mode plama is characterized by a weak positive shear with the central safety factor above unity, and it is compatible with the standard operational scenario in ITER. In the optimization of the discharge scenario, important issues are (a) simultaneous achievement of high-beta and high-confinement with a high fraction of non-inductive driven current and (b) steady-state sustainment of the high performance plasma. After the improvement of the power supply for poloidal coils in 2001, even at high plasma current of I_p~1.8 MA, a high triangularity plasma (δ_x~0.3, where δ_x is the triangularity at the separatrix.) can be produced for 5 s, which is much longer than the typical energy confinement time (~0.2-0.3 s). In addition, improvement of the NNB injector increased the beam energy and injection power. In the plasma operation, destabilization of neoclassical tearing mode was successfully suppressed by tailoring the pressure and current profiles. In shot E39713, a high fusion triple product of 3.1×10^{20} m^{-3}·s·keV was obtained, which exceeds the previous record by as large as 50%. Results from the time-dependent transport code TOPICS show that the full noninductive current drive condition is surely satisfied, and that fractions of driven current by neutral beams, bootstrap current, and electron cyclotron wave are 48%, 50%, and 2%, respectively, close to those in the steady-state operation in ITER. The improvement of the power supply for the poloidal fields coil also enables sustainment of a plasma with δ_x~0.45 for 10 s, which also corresponds to the maximum pulse width of neutral beams in JT-60U. In shot E39706, an ELMy H-mode plasma with β_N~2.7 and β_p~1.5 has been sustained for 7.4 s, which corresponds to ~60τ_E (I_p=1 MA, B_t=1.8 T, q_{95}=3.4). The duration is determined only by the facility limit such as capacity of power supply and upper limit of injection duration of neutral beams.

References

[1] Isayama A, et al., Proc. 19th IAEA Fusion Energy Conference, IAEA-CN-94/EX/C2-2; submitted to Nuclear Fusion.

3.3 High Fusion Performance Experiments with Reversed Shear Plasmas

T. Fujita, Y. Kamada, S. Ide, Y. Sakamoto, T. Fukuda, H. Takenaga, S. Takeji, T. Nakano, T. Oikawa, T. Suzuki, M. Ishikawa, M. Takechi, N. Oyama, Y. Koide, Y. Kawano, T. Hatae, O. Naito, A. Isayama and the JT-60 team

1. Introduction

High current (I_p>~2.5MA) reversed shear experiments with a high elongation configuration was performed in 2001, aiming at a new record of DT-equivalent fusion gain (Q_{DT}^{eq}) and extension of duration of Q_{DT}^{eq} >1. The previous record of Q_{DT}^{eq} was 1.25, which was achieved in 1998 [1] and the longest duration of Q_{DT}^{eq} >1 was ~140 ms in the same discharge. To improve the fusion performance, impurity reduction, confinement improvement with pellet injection, H-mode transition, enlargement of ITB radius and NNB injection were attempted. The results of these trials are described below. In parallel with high performance experiments, physics studies on reversed shear plasmas including internal transport barriers (ITBs) [2], MHD stability and plasma disruption, were also intended and various data were obtained.

2. Experimental Results

2.1. Impurity reduction

The improvement of fuel purity or the reduction of impurity is very effective to enhance Q_{DT}^{eq}. In high performance reversed shear plasmas with Q_{DT}^{eq}~1, the typical value of Z_{eff} and n_D/n_e were 3.0-3.3 and 0.54-0.6, respectively. Reduction of Z_{eff} by 0.3 would result in ~15% enhancement of S_n and Q_{DT}^{eq} for the same values of other parameters (T_i, T_e, the plasma stored energy and the energy confinement time). The impurity reduction was attempted by lowering the wall temperature (T_{wall}), wall conditioning with boronization, deuterium pellet injection and gas puffing. In a preliminary experiment in May 2001, reversed shear plasmas were produced and compared with T_{wall} of ~280 °C, which was a standard case, and ~150 °C. High performance plasmas with Q_{DT}^{eq}~1 were also obtained with T_{wall} of 150 °C and no serious problems were encountered in the wall conditioning after the disruption. The impurity contents were measured in quasi-steady discharges with a 2.4 MA flat-top and with a larger plasma major radius for Thomson scattering measurement. Then, it was found that the value of Z_{eff} evaluated from Bremsstrahlung was reduced from 3.5 to 3.0 due to decrease of oxygen impurity content by lowering T_{wall}. According to this encouraging result, in the campaign in autumn, T_{wall} was fixed to 150 °C and boronization was carried out typically once per two weeks. As a result, the oxygen content was kept at a low level (~1%), but the carbon content stayed at ~4% and the neutron production rate S_n was not increased. Pellet injection and gas puffing were also attempted to improve the fuel purity, but no significant

increase in S_n was observed.

2.2. Confinement improvement with pellet injection and H-mode

The injection of pellets was attempted originally to improve the fuel purity by increasing the fuelling and to cause the H-mode transition by increasing the edge density. Though these effects were not obtained, it was observed that density fluctuation at the ITB layer was reduced and confinement was improved when pellets were injected at the current flat-top of 2.2 MA [3]. The density increased inside the ITB while T_i and T_e were almost unchanged after the pellet injection, which resulted in confinement improvement. The reduction of density fluctuation may be related to the increase in temperature gradients caused by cold pulse propagation induced by pellets. However, when pellets were injected during the current ramp-up phase with I_p >2.2 MA, no clear confinement improvement was observed, though reduction of magnetic and density fluctuations were obtained.

High current reversed shear plasmas with a high elongation configuration had usually an L-mode edge. If an H-mode edge could be combined with strong ITBs with large radii, enhanced confinement, beta limit and $Q_{DT}{}^{eq}$ would be expected. The loss power across the separatrix seems to be sufficient to cause an H-mode transition. The reason of no H-mode transition is considered too low edge densities in these discharges [4]. To increase the edge density and to trigger the H-mode transition, a strong gas puff of 10 Pam^3/s was attempted. Then, clear L to H transition, appearance of ELMs and formation of pedestal were observed, but the ITB radius became small and S_n was low. In this discharge, the dome-top configuration, where the outer hit point was located on the dome-top, was also employed since lower threshold power was observed with reduced X-point height [5]. On the other hand, in discharges with B_t = 3.73 T, which was lower than the standard value (4.05T), the L to H transition was sometimes observed without strong gas puffing, but the growth of pedestal was small and no improvement of performance was obtained.

2.3. Enlargement of ITB radius

Optimization of pressure and current profiles was attempted to enlarge the radii of q_{min} and ITB and improve the confinement. In usual reversed shear discharges, a divertor configuration is established ~0.3 s after the plasma start-up and NB was injected to form an ITB [1]. This scenario is effective to make large radii of ITB foot and q_{min} in JT-60U reversed shear discharges. To obtain a larger radius of q_{min} by retarding the current penetration, electron heating with ECRF wave was attempted, though its deposition location was off-axis, around the half radius, in 4 T discharges. However, collapses at q_{min}~4 was observed when ECRF heating was employed together with NB heating in a divertor discharge. Then, a new discharge scenario was attempted, in which a limiter configuration was kept for 0.8 s, or until 1 MA was reached, and ECRF was injected during the limiter configuration without NB

heating. With this scenario, the time with q_{min} ~3 was successfully passed through with higher bata (β_N~0.9) than in a standard scenario without ECRF (β_N~0.7), as shown in Fig. 1, and a larger radius of q_{min} was obtained. However, collapses at I_p ~ 2.2 MA (q_{min} ~ 2.4, q_{95} ~ 3.7) were frequently observed in this scenario. To suppress these collapses, it was required to reduce the ITB strength by reducing the central heating power and applying gas puffing.

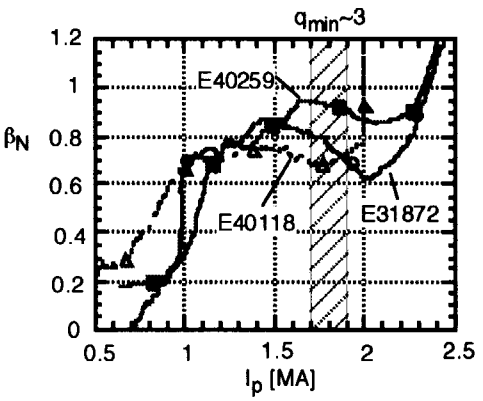

Fig. 1. β_N as a function of plasma current I_p in discharges with conventional scenario (E31872 and E40259) and with a new scenario (E40259).

In a shot E40259, which was obtained by using the above technique, the plasma was maintained for 0.3 s during a 2.6 MA flat-top and high performance was achieved. The waveforms and profiles of this discharge are shown in Fig. 2. The value of q_{min} at the collapse was 1.8 and slightly lower than usual values, which resulted in longer sustainment of this discharge than usual ones. The reason why this discharge was maintained into a lower q_{min} regime is not identified yet. The peak value of Q_{DT}^{eq} in this discharge was 1.24 and the duration of Q_{DT}^{eq}>1 was ~140 ms, both of which were close to or equal to the previous records. Other parameters are q_{95} = 3.3, W_{dia} = 8.3 MJ, S_n = 4.6x10^{16} n/s, β_N = 1.6, τ_E = 0.89 s, H_{89} = 3.0. The time-derivative of plasma stored energy, dW_{dia}/dt, was small and hence P_{DT}^{eq}/P_{NB}^{abs} reached 0.8. This is the highest value in JT-

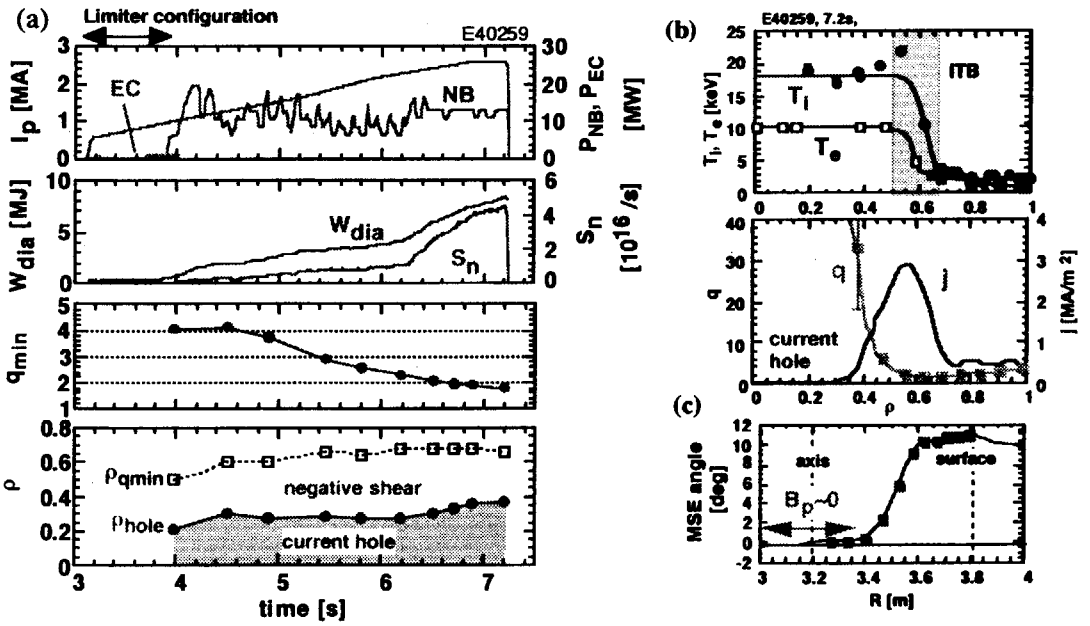

Fig. 2. A high performance reversed shear plasma E40259. (a) Time evolution of I_p, NB and EC power, plasma stored energy (W_{dia}), neutron production rate (S_n), q_{min} and normalized radii of current hole and q_{min}. (b) Radial profiles of T_i, T_e, q and j. (c) Profile of MSE polarization angle along the major radius.

60U. The duration of Q_{DT}^{eq}>0.8 reached 0.55 s and was extended from the previous value (0.35 s) as shown in Fig. 3. It is noted that the current hole [8] was established by ECRF heating and was maintained afterwards in this discharge as shown in Fig. 2. Hence it was confirmed that the current hole was compatible with a high I_p, low q, high performance plasma.

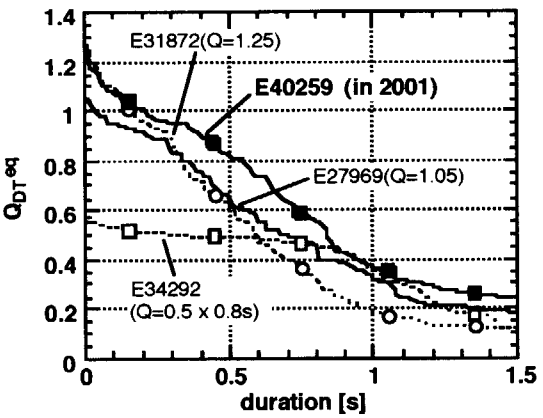

Fig. 3. Q_{DT}^{eq} as a function of its duration in typical reversed shear discharges; E27969 in which Q_{DT}^{eq}>1 was achieved for the first time in JT-60U [6], E31872 in which the highest value of Q_{DT}^{eq} was achieved [1], E34292 in which Q_{DT}^{eq}=0.5 was sustained for 0.5 s [7] and E40259 in 2001. Durations for Q_{DT}^{eq} =0.5-0.9 are longest in E40259.

2.4. NNB injection

Negative-ion based NB, NNB was injected into reversed shear plasmas aiming at control of magnetic shear in the central region, reduction of ripple-induced fast ion loss by replacing perpendicular NBs, improvement of stability by changing the pressure profile. Though the effects of the first two were unclear, improvement of stability was obtained. In a shot with NNB injection, Q_{DD} $=P_{DD}/P_{net}$ reached 6.0×10^{-3} and the record value of Q_{DD} (5.7×10^{-3}) was renewed. However, the fraction of fast ion component was large and Q_{DT}^{eq} remained 0.7.

3. Summary

High current reversed shear experiments were performed for achieving high values of DT-equivalent fusion gain, Q_{DT}^{eq}. Though the record value of Q_{DT}^{eq} was not renewed, extension of high fusion performance (Q_{DT}^{eq}>0.8 for 0.55 s) was obtained.

References

[1] Fujita, T., et al., Nucl. Fusion **39**, 1627 (1999).
[2] Sakamoto, Y., et al., in IAEA 2002, EX/P2-08, submitted to Nucl. Fusion.
[3] Takenaga, H., Oyama, N., et al., 4.10 in this review.
[4] Fukuda, T., et al., 3.7 in experimental review 2000.
[5] Tsuchiya, K., et al., 3.10 in experimental review 2000.
[6] Ishida, S., et al., Phys. Rev. Lett. **79**, 3917 (1997).
[7] Fujita, T., et al., Nucl. Fusion **41**, 180 (2002).
[8] Fujita, T., et al., Phys. Rev. Lett. **87**, 245001 (2001).

3.4 LHCD on High Confinement Reversed Shear Plasmas at High Normalized Density and Low q Regime

S. Ide, T. Fujita, Y. Kamada, Y. Sakamoto, T. Suzuki, M. Seki and the JT-60 team

1. Introduction

Toward realization of steady state fusion reactor, it is important to access non-inductive full current drive with high confinement at high normalized density with respect to the Greenwald density (n_{GW}), f_{GW}, in lower safety factor (q) regime. It has been demonstrated in a JT-60U reversed magnetic shear (RS) plasma that high confinement of $H_{H(98,y2)}$ (confinement improvement factor over the H-mode scaling) = 1.4 at high normalized density of 82% of n_{GW} is obtained under full non-inductive current drive [1, 2]. In the experiment, lower hybrid range of frequencies (LHRF) and negative ion-based neutral beam (N-NB) were employed as external current drivers together with higher bootstrap current fraction (f_{BS}) of 62%. However, the result was obtained at rather higher q regime (= 6.9), I_p = 0.9 MA and B_t = 2.5 T. For an economical operation of a commercial fusion reactor, the operational q regime should be lower than that; q ~ 3.5 - 4 would be required. In order to investigate high confinement and high density RS plasmas under full-current drive in lower q regime, it is tried to extend the operational regime towards higher plasma current (I_p). On raising I_p, it is also an important subject to investigate whether high confinement can be maintained at high normalized density, since the Greenwald density increases linearly with I_p.

2. Experimental Results

A configuration and discharge scenario are based on the discharge in which high confinement full current drive was achieved at high normalized density [1, 2]. A typical equilibrium is shown in Fig.1. Main change is on the plasma current; it is raised up to 1.5 MA (in the last campaign, I_p had been raised up to 1.1 MA). Accordingly the operational regime in q is shifted to lower q (q_{95} > ~ 4.8). In Fig.2 (a) shown is a plot of f_{GW} against I_p. The open squares correspond to discharges in the previous campaign, while open circles correspond to discharges in this campaign. It can be seen that quite high f_{GW} (~ 0.8) is achieved even at Ip ~ 1.5 MA. It should be noted that f_{GW} is evaluated with the

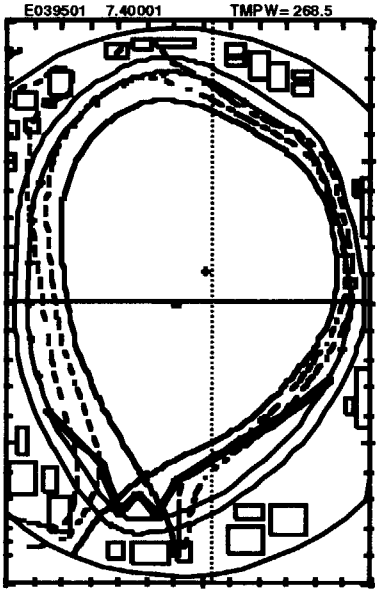

Fig.1. A typical equilibrium configuration, 1.5 MA/ 3.2 T. The dotted vertical chord indicates the line along which the line averaged density is evaluated.

density averaged along the vertical chord shown in the figure for simplicity. In Fig.2 (b) plotted is the confinement improvement factor over the L-mode scaling (H_{89p}) against f_{GW}, the symbols are used in the same manner as those in Fig.2 (a). As shown in the figure, confinement is similarly improved at this range of high f_{GW} both in the lower I_p discharges in the previous campaign and in the higher I_p discharges in this campaign. It should be noted that, in the evaluation the heating power 70% of the injected NB power is assumed to be absorbed. Non-absorbed fraction, the shine thorough, the ripple loses and the charge exchange loss, has been evaluated in some of large bore configuration discharges, I_p of from 0.85 to 1.5 MA, is rather closer to 40% or even higher. The absorption power of 70% is assumed to be safer side so as not to over estimate H_{89p}.

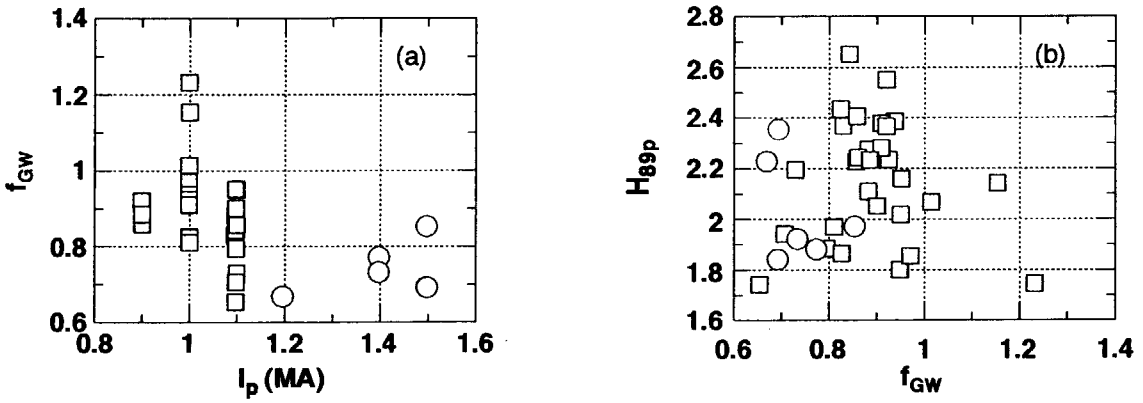

Fig.2. f_{GW} versus I_p (a) and H_{89p} versus f_{GW} (b). The open squares correspond to discharges in the previous campaign, while open circles correspond to discharges in this campaign.

Profiles of q, n_e, T_e and T_i are shown in Fig.3 for the case of H_{89p}~2.4 at f_{GW}~0.7. The high confinement could be attributed to the location of the ITB foot which is about 80% of the minor radius as show in the figure. Since the LH power was injected from 5.5 s to increase slowly, LHCD is expected to be still small at 5.9 s. Due to notching in the LHCD power, the location of q_{min} and thus the ITB location continued to shrink, and confinement was not maintained. It should be noted that at 5.9 s, f_{BS} is evaluated as 58%. Therefore the target plasma at this I_p regime is expected to potentially satisfy the original aim, that is full non-inductive current drive with high confinement at high normalized density.

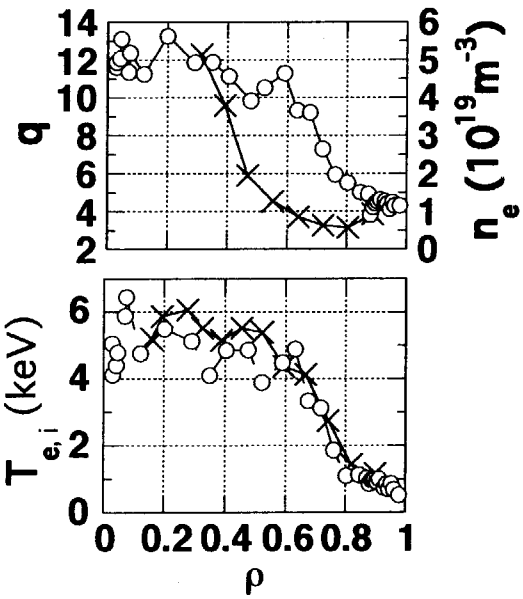

Fig.3. Profiles of q (crosses), n_e (open circles), T_e (crosses) and T_i (open circles) in E39501 at 5.9s, H_{89p} and f_{GW} are evaluated as 2.4 and 0.7 at 5.8s.

Current drive, however, had not been satisfactory pursued as expected, mainly because of the poor LHCD launcher performance and N-NB injection. One of the most successful discharges in this campaign is shown in Fig.4. As shown in the figure, the LHRF injection was successful up to ~ 6.5 s then notching started. Up to 6.5 s, the q and T_i profiles did not change drastically as shown in Fig.5. This might be attributed to the off-axis LHCD.

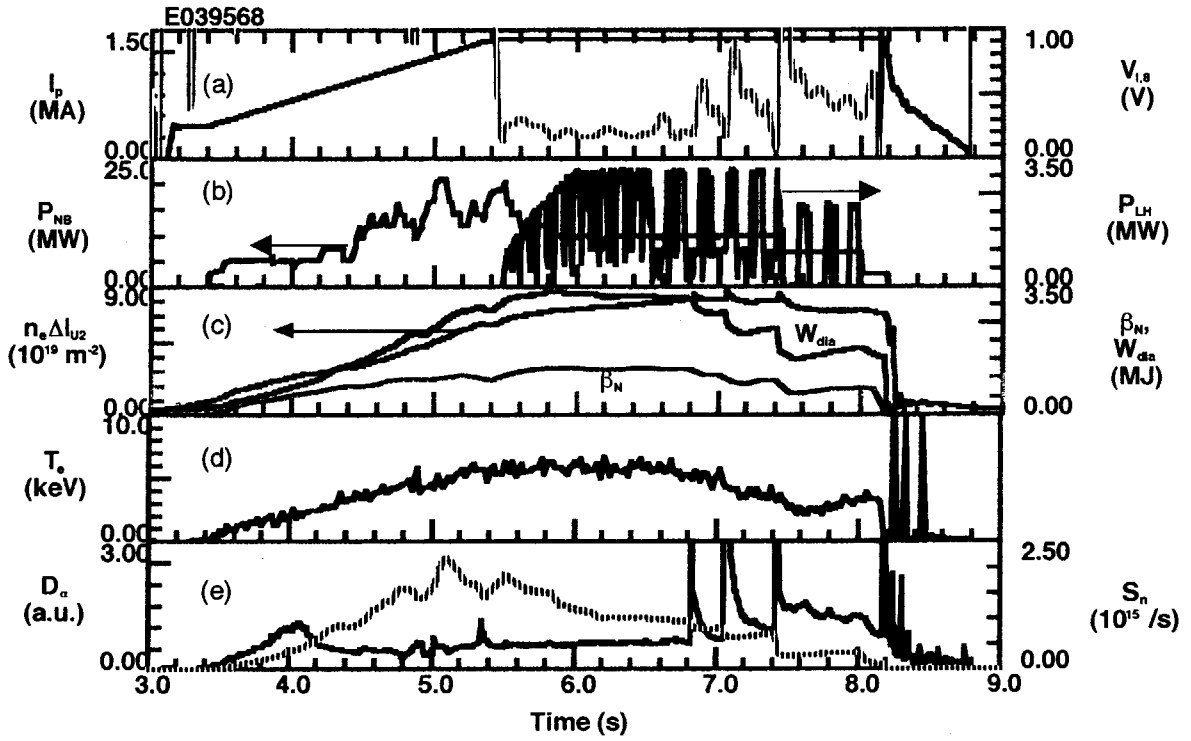

Fig.4. Typical waveforms in one of the most successful discharge, in which LHCD is injected into high confinement plasma (E39568). (a) The plasma current (solid line) and the surface loop voltage (dotted line). (b) The injected NB and LHRF powers. (c) The line integrated density, the stored energy and the normalized beta. (d) The electron temperature in the plasma central region. (e) The brightness of the deuterium alfa line (solid line) and the neutron yield (dotted line).

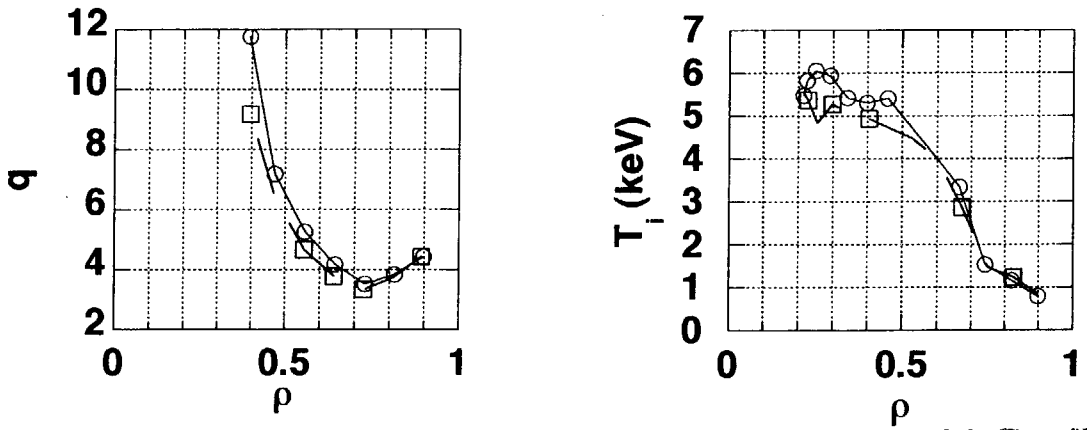

Fig.5.The safety factor profile at 5.95 (open circles) and 6.4 s (open squares) (a), and the Ti profile at 5.95 and 6.4 s (b) in E39568.

3. Summary

It had been tried to extend experimental regime of high confinement full-current drive with high bootstrap current fraction at high normalized density to higher plasma current regime by LHCD and N-NBCD. The target plasmas seem to posses potential to fulfill requirements, while non-inductive current drive had not been examined satisfactory due to hardware condition in limited operational time.

References

[1] Ide, S., et al., Plasma Phys. Controlled Fusion, **44**, A137 (2002).

[2] Ide, S., et al., Proc. of the 19th IAEA Fus. Energy Conf. Lyon, EX/C3-3 (2002).

3.5 Formation of ITB Extending to Larger Minor Radius in Reversed Shear Plasmas

S. Ide, T. Suzuki, Y. Sakamoto, H. Takenaga, T. Fujita, Y. Koide
and the JT-60 team

1. Introduction

An internal transport barrier (ITB) is one of the most important factors in steady state (SS) tokamak fusion reactor research. Since the stored energy is found to increase with expansion of the ITB extension in the minor radius [1], it would be beneficial to obtain an ITB at minor radius as large as possible. It has been observed that in JT-60U reversed magnetic shear (RS) plasmas, the ITB radius can be quite large. It is found that in certain cases the ITB radius can be about 90% of the minor radius in RS plasmas. In this section, such wide radius ITBs are discussed.

2. Experimental Results

Such a wide ITB was firstly confirmed in a target plasma for LHRS discharge. The toroidal field at R = 3.32 m was 3.45 T and the working gas was deuterium. The waveforms of the discharge are shown in Fig.1. As shown in the figures, the plasma was moved outward from 5.0 s during the I_p ramp-up phase and the plasma poloidal cross section was also expanded in order to form a large bore plasma which was compatible with the LHRF injection. The change in the plasma volume is from 70 m^3 at 5.0 s to 80 m^3 at 5.4 s. Although it is not clearly distinguished in the waveforms, the ITB was formed earlier in the discharge, around 4.0 s or even earlier. At 5.4 s, q_{eff} was 5.9, β_p and β_N were 1.1 and 1.3 respectively. As indicated in the waveform of the D_a line brightness, ELMs are coexisting. Profiles of the plasma

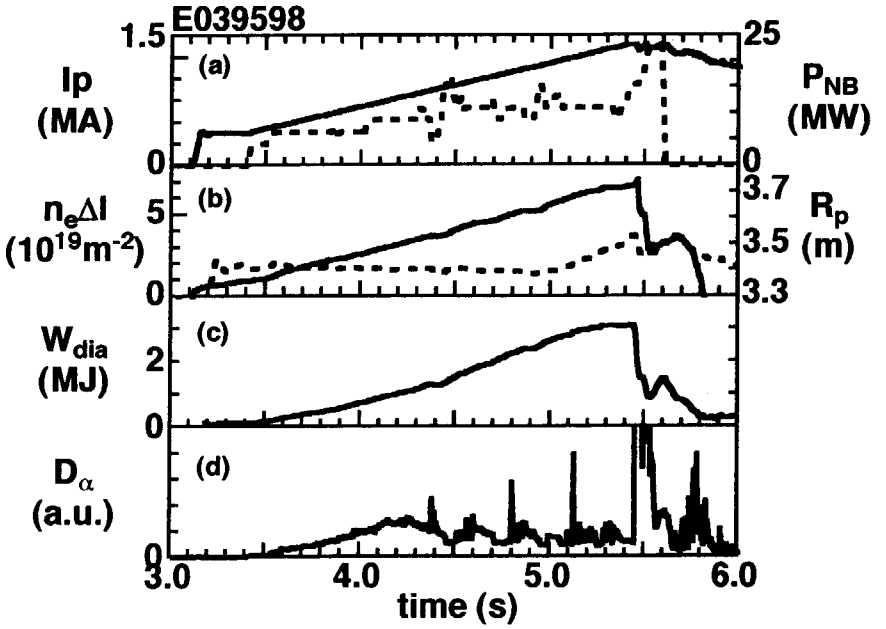

Fig.1. Waveforms; (a) the plasma current (solid line) and the NB power (dotted line), (b) the line integrated electron density (solid line) and the major radius (dotted line), (c) the stored energy and (d) the D_α line brightness.

parameters at 5.4 s are shown in Fig.2. As shown in the figure, the ITB foot point can be found at around 90% of the minor radius in T_e, T_i and n_e profiles. That location of the ITB feet is corresponding to the location of the minimum in the q profile (about 85% of the minor radius) as show in Fig.2. Although ELM activities are visible, the pedestal does not look clear in the profiles. The cross-sectional view of the plasma (E39598) at 5.4 s is shown in Fig.3.

The confinement improvement over the H-mode scaling is evaluated at 5.4 s as high as about 2.1. In the evaluation, 40% of the injected NB power is assumed to be lost.

So far such a wide ITB has ended up with disruption or a hard collapse. It has been observed not only in large bore plasmas but also in smaller bore plasmas. Moreover, it is observed both in deuterium and hydrogen discharges. Attained β_N is plotted in Fig.4 against the outermost major radius of the separatrix (R_{out}). It should be noted that the minor radius (a_p) is 1.0 - 1.1 m and the conducting wall is at about 4.65 m at the same height of the plasma center. That is a ratio of separatrix to the conducting wall

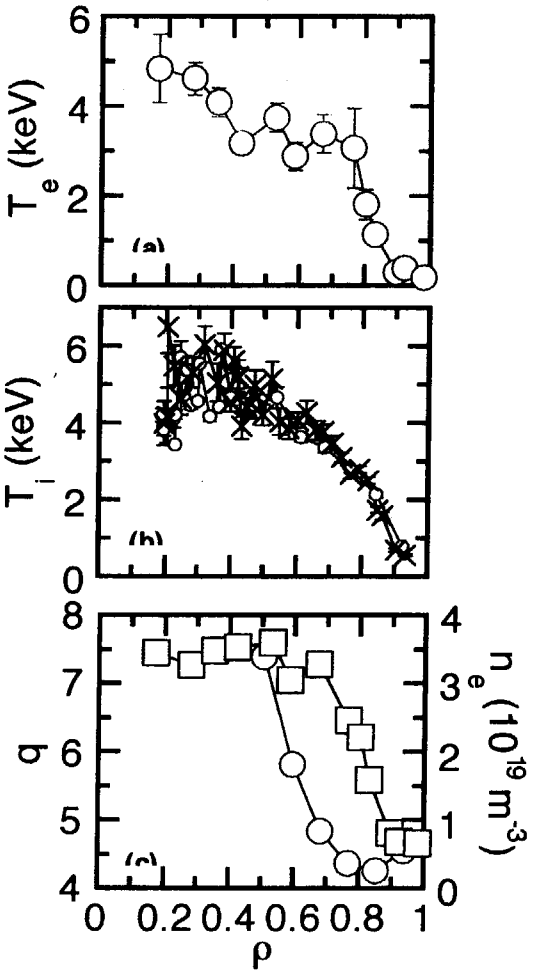

Fig.2. Profiles of plasma parameters in E39598 at 5.4 s. (a) The electron temperature profile measured by YAG Thomson scat. (b) The ion temperature profiles measured by the toroidal CXRS system (circles) and the poloidal CXRS system (crosses). (c) The safety factor profile (circles) and the electron density profile measured by YAG Thomson scat. (squares).

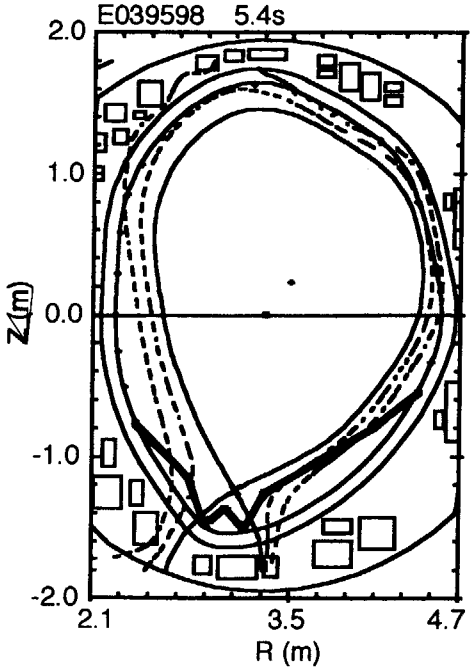

Fig.3. The poloidal cross-sectional view of the plasma E39598 at 5.4s when the profiles shown in Fig.2. are taken.

distance to the minor radius is about 1.2. In the figure, open circles correspond to ITBs with $\rho_{foot} \sim 0.9$ in deuterium discharges and an open diamond corresponds to that in a hydrogen discharge, while open square corresponds to an ITB with $\rho_{foot} \sim 0.8$. All the discharge but one indicated with square met disruption or hard collapse. It seems that the beta limit of such a wide ITB plasma is lower than that of smaller ITB radius discharges. It should be noted that beta limit in JT-60U usual RS ITB plasmas, whose ITB radius is 0.7a or smaller, is about 1.8 or higher. It also seems that as the plasma approaching to the outer wall the beta limit would increase. However, in order to confirm that more precise analysis and basically more discharges would be required. It would be noted that the plasma shown in Fig.s 2 and 3 is corresponding R_{out} =4.43 m in Fig.4.

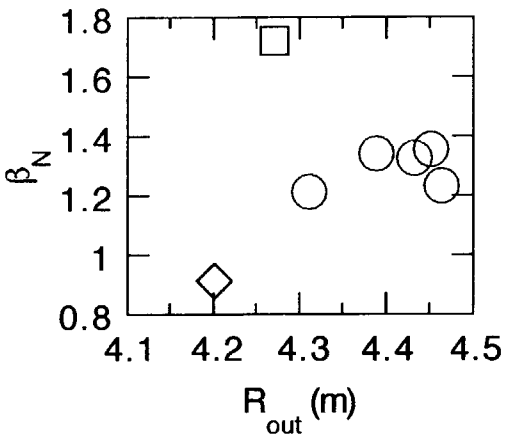

Fig.4. The attainable normalized beta against outermost major radius of the separatrix. Cases of ITB of $\rho_{foot} \sim 0.9$, deuterium (open circles) and hydrogen (open diamond), taken just before disruption or hard collapse. A case of ITB of $\rho_{foot} \sim 0.8$ in a deuterium discharge (open square), no disruption/collapse.

3. Discussion and Summary

It is confirmed that an ITB foot can expand as large as 90% of the minor radius. Since the foot location is found to be vicinity of the q minimum location as usual RS ITB plasmas, formation of large shear reversal area would be a key for the formation of such a wide ITB. Although the extent of the ITB is large, the confinement is not very high. This should be attributed to lower beta limit in these cases. The plasma meets disruption or collapse on the way to reach full confinement performance. So far observed, the attainable normalized beta limit in such a wide ITB plasmas is lower than that in smaller ITB radius ($\rho < 0.8$) plasmas. Although a poor pedestal, though ELM like activities are accompanied, might reduce the beta, the beta limit looks lower that that of even usual L-mode edge RS plasmas. Systematic stability analysis would be necessary for further investigation. A wide ITB is found to be formed both in large and small bore plasmas. However, the beta limit seems to be lower in smaller bore plasmas whose separatrix is farther away from the conducting wall. However, for final conclusion more systematic scan of wall-separatrix distance with precise measurement of the ITB location which also seems to affect the beta limit strongly would be required.

Reference

[1] Takizuka T., *et.al.*, Plasma Phys. Controlled Fusion **44**, A423 (2002).

3.6 Plasma Current Initiation and Ramp-up without Use of Ohmic Heating Center Solenoid and Formation of High Confinement Plasma [1]

Y. Takase,[1] S. Ide, S. Itoh,[2] O. Mitarai,[3] O. Naito, T. Ozeki, Y. Sakamoto, S. Shiraiwa,[1] T. Suzuki, S. Tanaka,[4] T. Taniguchi,[1] M. Aramasu,[1] T. Fujita, T. Fukuda, X. Gao,[5] M. Gryaznevich,[6] K. Hanada,[2] E. Jotaki,[2] Y. Kamada, T. Maekawa,[4] Y. Miura, K. Nakamura,[2] T. Nishi,[1] H. Tanaka,[4] K. Ushigusa, and the JT-60 Team

1) U. Tokyo, 2) Kyushu University, 3) Kyushu Tokai University, 4) Kyoto University, 5)Academia Sinica, P.R. China, 6) EURATOM/UKAEA Fusion Association, UK

An integrated scenario consisting of (1) a novel plasma start-up method using the vertical field (B_v) and shaping coils (VR and VT coils), (2) an intermediate noninductive ramp-up stage, and (3) a controlled transition to a high-density, bootstrap-dominated, high-confinement plasma has been demonstrated for the first time (Fig. 1). In these experiments the current in the F-coil (OH solenoid) was kept constant at zero. It was shown that I_p can be initiated in phase (1), even with a negative B_v (*i.e.*, in the direction opposite to that required for equilibrium), provided that there is a strong source of plasma (in this case provided by EC and LH). A plasma current of 0.2 MA was formed by induction provided by VR and VT coils (t = 2.1 to 2.25 s) during this phase. The VR coil current was ramped from 0, but the VT coil current was ramped from a negative current, providing additional poloidal flux and an appropriate B_v for equilibrium at the end of I_p ramp-up. A diverted configuration is formed at 2.5 s, and further ramp-up to 0.4 MA was achieved by a combination of electron heating and current drive by EC and LH waves.

When the current has become high enough to confine the injected beam ions, density was increased and NBI was started under stored energy feedback control. In addition to the noninductive current drive effect, I_p ramps up due to the flux provided by the B_v increase. Addition of NNBI contributes to further ramp-up by current drive and β_p increase. The plasma created by this technique had both internal and edge transport barriers, and had β_p = 3.6 ($\varepsilon\beta_p$ =1), β_N = 1.6 (marginally stable to the n =1 kink-ballooning mode), H_{H98y2} = 1.6 and $f_{BS} \geq 90\%$, at I_p = 0.6 MA and $\bar{n}_e = 0.5 n_{GW}$ (at t = 8.5 s). A current hole is formed from the LH ramp-up phase, and the q profile is deeply reversed, with q_{min} = 5.6 at r/a = 0.7 and q_{95} = 12.8.

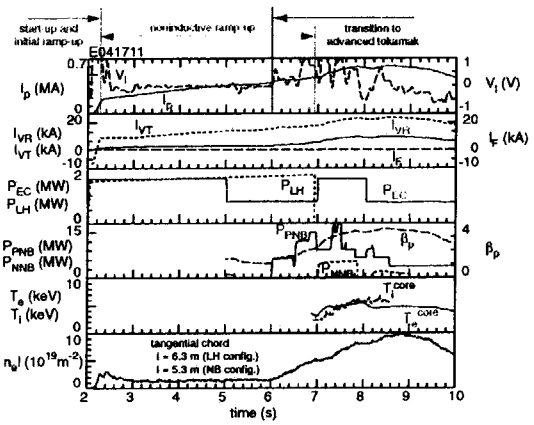

Fig. 1. Integrated scenario from plasma start-up to achievement of advanced tokamak plasma without the use of OH solenoid.

In these experiments, inboard turns of the VT coil supplied about 20% of the total poloidal flux input, but further improvement is possible. These results open up the possibility of OH-less operation, which is a requirement for ST reactors, and can also make a substantial improvement in the economic competitiveness of conventional aspect ratio tokamak reactors.

References

[1] Takase, Y., et al., Fusion Energy 2002 (Proc. 19th IAEA Conf., Lyon, 2002), paper PD/T-2.

3.7 Plasma Equilibrium and Confinement in a Tokamak with Nearly Zero Central Current Density in JT-60U [1]

T. Fujita, T. Oikawa, T. Suzuki, S. Ide, Y. Sakamoto, Y. Koide,
T. Hatae, O. Naito, A. Isayama, N. Hayashi, H. Shirai

In a toroidal system for confining a high temperature plasma, the poloidal magnetic field is necessary to suppress the drift of charged particles (ions and electrons) and to obtain good confinement. In a tokamak, which is one of the axisymmetric toroidal systems, the poloidal magnetic field is produced by a toroidal current in the plasma. A hollow current profile ("reversed shear configuration") has also been produced recently in the context of advanced tokamak concept, but a finite current at the center has been believed to be necessary for stable sustainment of the plasma.

Recently, it has been observed that a region with nearly zero toroidal current or a "current hole" is formed and sustained stably for several seconds in a central region of JT-60U reversed shear plasmas. In a typical discharge with $q_{95} \sim 5$, the radius of the current hole extended up to ~40% of plasma minor radius and the absolute value of safety factor at the axis, q(0) was estimated to be greater than 70. The central current density was estimated less than 7% of current density averaged over the plasma cross section. Though the temperature and density profiles were almost flat in the current hole, which indicated very large radial transport in the current hole, internal transport barriers (ITBs) were formed outside the current hole, and high temperature plasmas with $T_i(0) > 10$ keV were confined in the current hole by ITBs. Furthermore, the current hole with a radius of $\rho > 0.25$ was sustained for 4 to 5 seconds together with high confinement, HH_{98y2} ~1.16-1.45, without any global MHD instabilities. These results indicate the possibility of stable operation of tokamaks with no toroidal current at the axis and may lead to new concepts for tokamak reactors regarding current profiles and/or plasma current drivers.

The current hole was established by decrease in a toroidal electric field through the increase of off-axis bootstrap current in the ITB layer. One interesting point is that no substantial negative central current has been observed so far. This fact suggests that the decrease of central current stops when the central current density becomes zero. Furthermore, it seems that no current is generated in the current hole when electron cyclotron waves or neutral beams are injected tangentially for current drive. These observations of the stiffness of current hole suggest that the current hole is not a result of transient zero toroidal electric field in the plasma core, but of some kind of self-organized structure.

References

[1] Fujita, T., et al., Phys. Rev. Lett. **87**, 245001 (2001).

3.8 Response of Current Hole to Error Fields and Current Drive

T. Fujita, Y. Miura, T. Suzuki, S. Ide, T. Oikawa, A. V. Chankin,
Y. Sakamoto, Y. Koide, T. Hatae, O. Naito, A. Isayama, K. Hamamatsu

1. Introduction

Existence of a nearly zero current density region (a "current hole") was observed in JT-60U and JET tokamaks [1,2]. In JT-60U, a current hole with a normalized radius of $\rho > 0.25$ was maintained for 4-5 s without any global MHD instabilities [1]. Though the temperature and density profiles are almost flat in the current hole, internal transport barriers (ITBs) with a large pressure gradient and a large current density are formed outside the current hole. It is not well understood what determines the boundary between these two regions, namely the edge of the current hole. In 2002, response of current hole to non-axisymmetric error field and to inductive and non-inductive current drive were investigated to address this issue.

2. Response to Non-axisymmetric Error Fields

In reversed shear plasmas with strong ITBs, a box-type shape of temperature profiles is often observed, where a flat region exists around the axis or inside the ITB layer [3]. The point connecting the flat region and the steep gradient region (ITB layer) is called an ITB 'shoulder.' One may suppose that the appearance of the flat region, which implies very poor confinement there, is related to the existence of current hole. Since the poloidal field is very weak in and just outside the current hole, it is expected that the radial shift of particles from the magnetic surface is large. In some discharge, the banana width for thermal ions passing through the axis is almost equal to the radius of ITB shoulder [4]. However, as shown in Fig. 1, the radial drift of thermal electrons (solid lines) is a few cm for the case with q(0) = 100 and much smaller than that of thermal ions (dotted lines). Nested layers of electron orbits are maintained even in the current hole and the flat region in T_e profiles cannot be understood by the orbit width if q(0) = 100. This implies that anomalous transport exists or q(0) is much larger than 100. We also have the case that the shoulder in T_i is located at a larger radius than the width of largest banana of thermal ions.

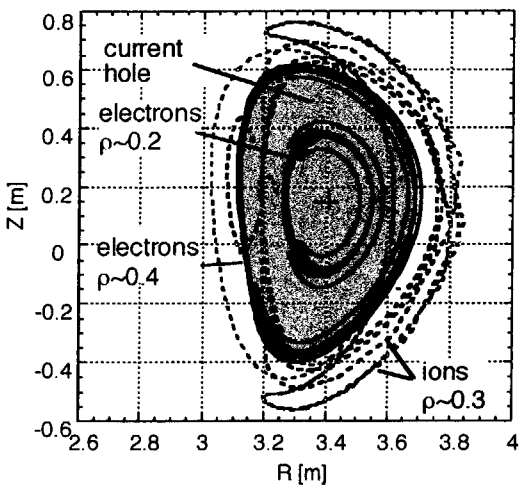

Fig.1. Orbits of thermal ions and electrons projected onto a poloidal crosssection for an equilibrium with q(0)=100. The shaded area indicates the current hole region where q>~50.

This suggests that the location of shoulder is not directly related to the weak poloidal field or existence of current hole.

The above discussion, however, assumes an ideal case without non-axisymmetric error fields. In actual experiments, we have error fields and they may break the nested magnetic surface in a very high q region. The location of ITB shoulder may be determined by the condition that the poloidal field becomes large enough to make closed or nested magnetic surface under the error fields. If so, the radius of ITB shoulder should depend on the magnitude of error fields. Some model also assumes that the radius of current hole is determined by the similar condition since the pressure gradient is required to generate the Pfirsh-Schlüter current and the bootstrap current just outside the current hole [5]. Then, the radius of current hole should depend on the magnitude of error fields.

To investigate the effect of error fields on profiles of temperatures and current density, a non-axisymmetric error field was applied to a current hole plasma. The error field was generated by 'DCW'-coils [6] and had a maximum value of ~40 Gauss in the plasma region, which was comparable to the poloidal field just outside the current hole. The dominant poloidal/toroidal mode numbers are m/n = 3/2. The experiments were performed with the high-elongation connection. The discharge scenario was similar to that employed in the high performance experiments in 2001 [7], in which the current hole and T_e-ITB were established with EC heating in a plasma with limiter configuration and T_i-ITB was formed with NB-heating after the divertor configuration was established. Figure 2 shows the case where the non-axisymmetric field was applied during a quasi steady phase with constant heating power and with T_i and T_e ITBs. The time evolution of T_e at several locations is shown in Fig. 2 (d).

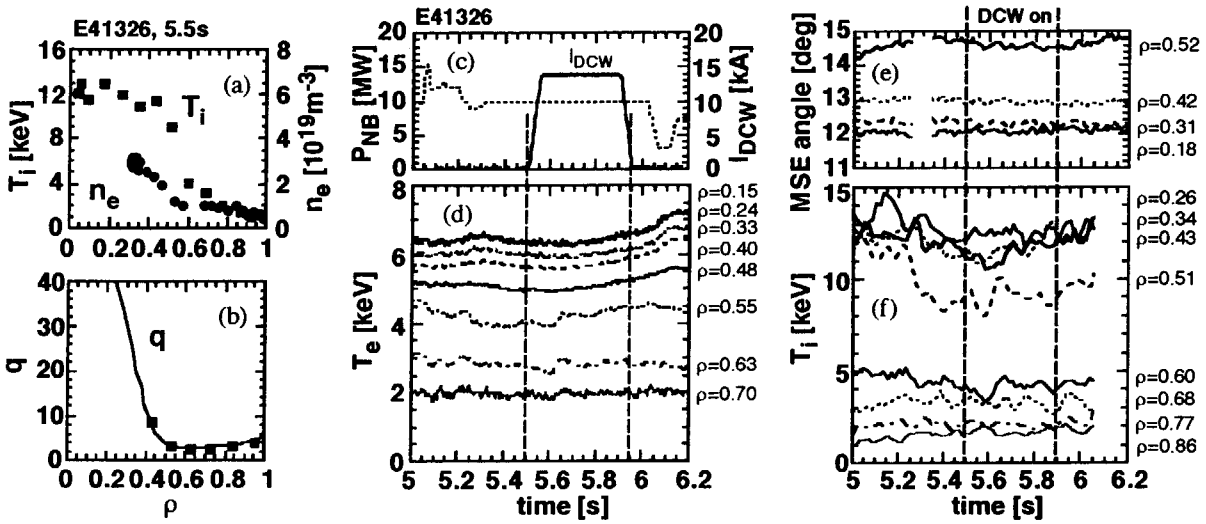

Fig. 2. Application of error field to a current hole. (a) Radial profiles of ion temperature and electron density. (b) Radial profile of q. (c) Time evolution of NB power and DCW coil current for error field generation. (d)-(f): Time evolution of (d) electron temperatures, (e) MSE polarization angles and (f) ion temperatures at several points. I_p = 1.4 MA, B_t = 3.7 T, q_{95} = 4.4, β_N ~0.8.

We find that the electron temperatures were hardly affected by the error field. No large responses were either observed in T_i and MSE polarization angles (poloidal fields) as shown in Figs. 2 (e) and (f) and in n_e and V_t (toroidal rotation of carbon ions). We also applied non-axisymmetric fields during the limiter phase before high power NB injection, where T_e ITB was maintained with EC heating and no clear responses were either observed.

It has been observed that the locations of ITB shoulder and the radius of current hole are not determined by error fields. This indicates that the cause to prevent generation of pressure gradient and the current density in and around the current hole is not the destruction of closed flux surface by error fields but other mechanisms.

3. Response to Current Drive

The cause of the formation of the current hole is considered the decrease in the inductive toroidal electric field E_ϕ^{ind}, which is caused by the increase of the off-axis non-inductive current. The current hole can be formed when the E_ϕ^{ind} becomes zero near the axis. Then, is E_ϕ^{ind} kept exactly zero for long sustainment of the current hole reaching several seconds? To address this issue, the response to the EC wave injected tangentially into the current hole was investigated. Though an off-axis peak due to the EC-driven current was observed in the current profile within 0.5 s after the start of EC injection in a plasma without the current hole, no current density was observed in a current hole when the EC wave was injected into a current hole [4]. This suggests that the picture that both of E_ϕ^{ind} and current density are zero in the current hole is improbable; if it is the case changes in the current profile should be caused by ECCD. Absence of this change suggests that the current density is clamped at zero in the current hole. However, in these experiments, negative E_ϕ^{ind} was generated in the current hole due to the electron heating (increase of off-axis bootstrap current) by the EC wave.

To obtain net positive current drive by the EC wave, EC wave injection under the constant plasma beta was attempted. The waveforms are shown in Fig. 3 (a). The EC wave was injected near the axis when the NB power was decreased so as to maintain the plasma beta nearly constant. The counter ECCD was also attempted by inverting the direction of plasma current. The plasma beta was similar for two discharges, but the electron density was larger and the electron temperature was lower for the counter ECCD case due to the change in wall recycling. The radial profiles of current density at t = 5.8 s are plotted in Fig. 3 (b). At this time, $E_\phi^{ind}(0)$ became small so that the inductive current was sufficiently smaller than EC-driven current, denoted by dotted lines, in the current hole. The measured current profiles, denoted by solid lines, indicate that the current density in the center was zero within the measurement error bars for both cases. Generation of positive and negative inductive electric field in the current hole was also attempted and no current was observed. These observations

imply that the current hole is not maintained since E_ϕ^{ind} is kept zero near the axis, but some mechanisms work to clamp the current density at zero level in the current hole. A resistive kink instability was proposed to explain the absence of negative j(0) [8], but this is unlikely to be the case in JT-60U where no MHD instabilities are observed. It is also noted that this model cannot explain the clamping of the current against the positive current drive.

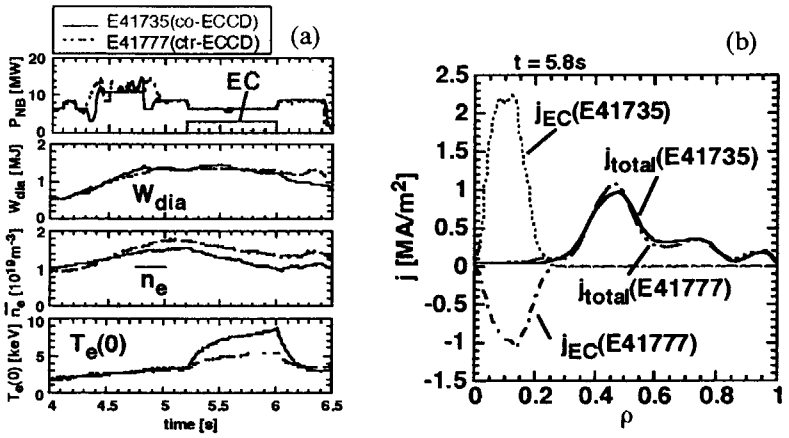

Fig. 3. Response to ECCD in plasmas with a current hole. E41735 for co-ECCD and E41777 for counter-ECCD. (a) Time evolution of NB power, EC power, plasma stored energy, line-averaged density and central electron temperature. (b) Radial profiles of current density at t = 5.8 s in two discharges.

4. Summary

The response of current hole plasma to error fields and to current drive was investigated. The error fields affected neither the position of ITB shoulder, where the pressure gradient started to develop, nor the radius of current hole, where the current density started to develop. The current drive generated neither positive nor negative currents in the current hole. These observations deny the picture that the weak poloidal field and the nearly zero toroidal electric field make the flat pressure profile and the nearly zero current density in the current hole, respectively. It is instead suggested that the profiles of the current density and the pressure in a current hole plasma are stiffly determined by some mechanisms.

References

[1] Fujita, T., et al., Phys. Rev. Lett. **87**, 245001 (2001).
[2] Hawkes, N. C., et al., Phys. Rev. Lett. **87**, 115001 (2001).
[3] Shirai, H., et al., Nucl. Fusion **39**, 1713 (1999).
[4] Fujita, T., et al., 29th EPS Conf. on Plasma Phys. Control. Fusion (Montreux, 2002) vol. 26B P-1.049.
[5] Chankin, A. V. et al., Plasma Phys. Control. Fusion **45**, 323 (2003).
[6] Ninomiya, H., et al., Plasma Devices and Operations **1**, 43 (1990).
[7] Fujita, T., et al., 3.3 in this review.
[8] Huysmans, G. T. A., et al., Phys. Rev. Lett. **87**, 245002 (2001).

3.9 Experimental Study on Physics of Electron Cyclotron Current Drive [1]

T. Suzuki, S. Ide, K. Hamamatsu, A. Isayama, T. Fujita, C. C. Petty [1)],
Y. Ikeda, K. Kajiwara, O. Naito, M. Seki, S. Moriyama
1) General Atomics, San Diego, California, US

Electron cyclotron current drive (ECCD) is expected to drive current in the center of ITER plasma, where the electron temperature T_e is higher than the volume averaged value $<T_e>$=12keV. ECCD in such a high T_e regime has not been demonstrated, and has not been investigated yet. Another important role of ECCD is the current profile control of a tokamak plasma to suppress instabilities, such as neoclassical tearing mode (NTM). For the NTM stabilization, ECCD is usually employed at off-axis, where particles trapped in the toroidicity induced magnetic well are considered to reduce non-inductively driven current. Since the trapped particle effect affects the required EC power for the current profile control, the effect on ECCD has been investigated. Recent progress of EC systems in JT-60U has made these experiments possible. Experimental measurement of EC driven current is based on the loop-voltage-profile analysis, which evaluates the transient inductive electric field in the plasma [2].

In order to study ECCD in a high T_e regime, a plasma with T_e =21keV at CD location has been produced by an optimized combination of ECCD (2.3MW) and ECH (0.6MW). When the minimum safety factor q_{min} approached to 2.5, a collapse localized around the q_{min} location occurred. ECH instead of ECCD for an EC system was employed to retard the collapse and to sustain the high T_e for 0.8s. The duration is enough to evaluate the transient loop-voltage-profile. Measured EC driven current j_{EC} profile was centrally peaked and was narrower than the calculated one, so that no significant radial diffusion of j_{EC} was observed. The calculation is based on the linear theory that includes neither a parallel electric field ($E_{//}$) effect nor a quasi-linear power density effect. The calculation includes the trapped particle effect, which will be described later. Measured EC driven current was 0.74±0.06MA, while the calculation shows 1.1MA. Corresponding CD efficiency $\eta_{CD}=I_{EC}n_eR_p/P_{abs}$ was 0.42×10^{19}A/W/m^2 and 0.63×10^{19}A/W/m^2, respectively. Here I_{EC}, n_e, R_p and P_{abs} represent the EC driven current, the electron density, the plasma major radius, and the absorbed EC power, respectively. The CD efficiencies for both the experiment and the calculation are much smaller than the predicted value in ITER (2.5×10^{19}A/W/m^2 at T_e=20keV and at $n_e=15\times10^{19}$m^{-3} [3]). It is considered that the difference is due to low n_e in the experiment (0.35×10^{19}m^{-3}), and due to lack of optimization of resonant conditions. Lack of electrons, to which EC waves couple in an optimized condition, reduces the CD efficiency. Actually, the calculation predicts the CD efficiency of 2.7×10^{19}A/W/m^2, under an optimized resonance condition in JT-60U. We assume that the T_e profile and the shape of the n_e profile in this optimization are the same as those in the above experiment. The effective charge number, which was 3 in the experiment, is assumed uniform

and unity. We made the following optimization according to the ITER design.

i) increase of parallel refractive index to the magnetic field $N_{//}$ (from 0.5 to 0.8 at the absorption location) by adjusting the angle between the EC ray and the toroidal field projected on the equatorial plane (from 67° to 43° at the antenna)

ii) increase of electron density n_e (from $0.35\times10^{19}m^{-3}$ to $15\times10^{19}m^{-3}$)

iii) increase of the wave frequency f_w and the toroidal field at the plasma center $B_t(0)$ (from 110GHz to 169GHz; from 3.9T to 6.0T)

iv) optimization of CD location by f_w (from 169GHz to 220GHz)

The optimization is based on the conventional theory that coupling of EC waves to faster $v_{//}$ electrons increases the CD efficiency. i) Electrons with faster $v_{//}$ can absorb the EC waves due to the increased Doppler shift. ii) Increase in n_e also moves the absorption of EC waves to faster $v_{//}$ side in the velocity space, since EC waves first couple to faster $v_{//}$ electrons, which exist much enough to absorb a large portion of EC power. Plasma frequency is f_p=120GHz at the plasma center. iii) To avoid the cyclotron cut-off ($f \leq f_p$) due to the increased n_e in the step ii), we increased both of $B_t(0)$ and f_w keeping the resonance condition. iv) Since the increase in $N_{//}$ in step i) shifts the absorption location to lower field side, wave frequency f_w should be increased for on-axis absorption. The above optimization drastically increases the ECCD efficiency. Quantitative comparison between the experiment and the calculation is in progress, considering both the parallel electric field effect and the quasi-linear effect.

The trapped particle effect has been investigated by comparing the normalized CD efficiency $\zeta=e^3\eta_{CD}/\varepsilon_0^2kT_e$ at various CD locations, where T_e is the electron temperature at the CD location. It is expected that the trapped particle effect reduces ζ more strongly in lower field side (LFS) deposition than in higher field side (HFS) deposition. We adjusted the electron density and the effective charge to the fixed values as much as possible in this experiment, although we assume primary dependencies on plasma parameters have been removed by the normalization. The normalized CD efficiency for the LFS deposition was about a half of that for the HFS deposition, when we compared them at the same $\varepsilon^{0.5}$, which is a measure of the trapped particle fraction at the outward mid-plane of a tokamak. The measured ζ agreed with the calculated one. The reduction of ζ can be an evidence of the trapped particle effect. An expected reduction of ζ with the $\varepsilon^{0.5}$ at LFS was not clearly observed, since the variation of $\varepsilon^{0.5}$ ($\varepsilon^{0.5}$~0.22-0.32 for ρ=0.17-0.35) was not enough to make the change in ζ larger than the experimental error. Further off-axis ECCD will show the trapped particle effect more clearly.

We have studied another dependence of ζ on the electron density at the same CD location under fixed T_e. In the experimental condition, T_e, B_t, and the trapped particle effect were fixed. We found that ζ strongly depends on n_e. The linear-theory can explain a part of the increase by (i) an increase of absorption of EC waves to electrons with faster parallel velocity and by (ii) moving the absorption location away from the trapping cone in a velocity space. We have already seen the

increase of CD efficiency due to the effect (i) in the on-axis ECCD optimization, as described above. Both of the $E_{//}$ effect and the quasi-linear effect can be neglected in a conventional theory under this experimental condition. There still exists an unresolved part of the increase in ζ, so that we need further study for the strong n_e dependence. The dependence is preferable in a reactor relevant high n_e plasma.

References

[1]Suzuki, T., et al., in Fusion Energy 2002 (Proc. 19th Int. conf. Lyon, 2002) IAEA-CN-94-EX/W2. submitted to Nuclear Fusion.
[2]Suzuki, T., et al., Plasma Physics and Controlled Fusion **44**, 1 (2002).
[3]Harvey, R. W., et al., Nuclear Fusion **37** (1997) 69.

3.10 Off-axis Current Drive with Neutral Beams

J. Hobirk[1], T. Oikawa, T. Fujita, T. Fukuda, A. Isayama, Y. Kamada, Y. Miura, A. Polevoi, T. Suzuki, K. Ushigusa

[1] Max-Planck-Institut für Plasmaphysik, EURATOM Association, Boltzmannstr. 2, 85748 Garching

1. Introduction

Neutral beam injection is a very robust tool for heating of high temperature plasmas and is used in most fusion experiments. In theory the neutral beam does not only heat the plasma but drives also current by the injection of fast particles either in the same or opposite direction to the plasma current. The fast particle current is in zeroth order compensated by electrons dragged with the ions. If $Z_{\rm eff} \neq Z_{\rm beam}$ then a net current can be created in the classical picture [1]. Despite this effect also the drag forces by the trapped electrons results in an unbalance between electrons and fast ions and create a net current. A more detailed description and a simplified calculation of the driven current profile can be found in [2]. The current drive by neutral beam injection is reported to be within the error bars by some experiments using zero dimensional analysis [3] for example by loop voltage analysis. Also radial resolved analysis has shown that on-axis current drive is within the the error bars using loop voltage profile analysis [4]. Significant changes of a measured current profile, for example by a Motional Stark Effect diagnostic [5] are expected by either on-axis counter current drive or by off-axis co current drive. The latter case is discussed in this paper.

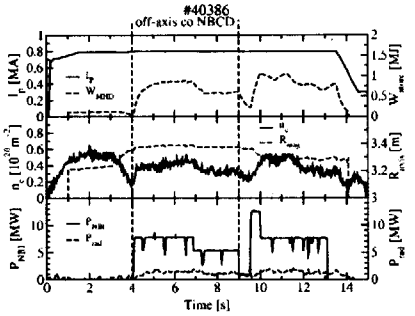

Figure 1: *Main time traces for a discharge with strong NB injection in co direction from $t = 4s$ to $t = 9s$. It the top graph the plasma current and the stored energy are plotted. In the middle the line integrated electron density (integration length 5.2m at $t = 4.9s$) and the R coordinate of the magnetic axis are represented. Last in the bottom graph the neutral beam injected power and the plasma radiation are drawn.*

2. Experiment description

JT-60U is according to modelling capable of driving an off-axis neutral beam current which can be a significant part of the total current. The plasmas discussed here have a small current of $I_P = 800$kA and the experiments are started well after the current ramp up. The current profile was clearly relaxed before neutral beam injection was used. Time traces of experiments with 5s off-axis co current drive (compared to 16s relaxation time of the current profile) are shown in figure 1. The notation here is as follows: in the upper graph the left y-axis describes the plasma current in MA. These discharges are heated with $P_{\rm NBI}$ between 5MW and 8MW and remained in L-mode due to the very low electron density of $\bar{n}_e = 5.8 \cdot 10^{18}\mathrm{m}^{-3}$ at $t = 4.9$s. The heating in is varied by neutral beams with perpendicular injection which have only a very small effect on the current profile. These discharges have an ion temperature which is in general higher than the electron temperature (fig-

ure 3) due to the dominant ion heating and the weak coupling of ions and electrons at these low densities and the density profile is peaked. The Z_{eff} profile is not calculated for these discharges but the line averaged Z_{eff} values are given by a visible bremsstrahlung diagnostic as $Z_{eff} = 2.4$ and the profile is assumed to be radial constant.

3. Experimental results

In figure 2 the time traces of the MSE diagnostic are presented. Some change in the measured angle is noticeable in the first second of the measurement and again at about $t = 7$s where the heating power is reduced by 2MW. This development in the polarisation angles is due to a change of the stored energy in the plasma which results in a different Shafranov shift. The MSE channels are fixed in space and not in flux so that this effects the angles immediately. Apart from changes in the stored energy content the MSE angles are stable and no significant slow changes on a current diffusive time scale are visible. A reconstruction of the q profiles based on the experimentally determined plasma equilibrium is shown in figure 3. A small change is visible between $\rho_{vol} \approx 0.5$ and $\rho_{vol} \approx 0.7$ but this change is still within the error bars as expected from the time development of the MSE angles. An expected effect of off-axis NBI current drive on the current profile is neither visible in the reconstructed q profile nor in the measured polarisation angles.

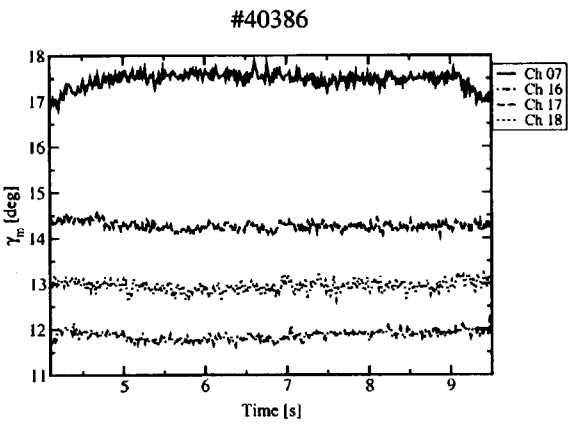

Figure 2: *Time traces of polarisation angles for off-axis co injection. Most inner channels at bottom and outward channels at the top.*

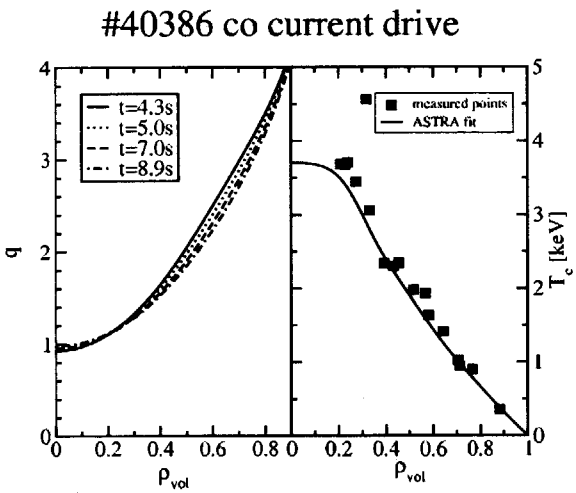

Figure 3: *q profiles from equilibrium reconstruction. The first profile is taken shortly after neutral beam injection and should represent the ohmic q profile. The last profile is taken shortly before the end of the experiment.On right hand side an example of an electron temperature profile at the end of the experiment.*

The MHD activity for co current drive experiment is a small 2/1 mode but no kind of reconnection is found. Sawteeth or fishbones are not excited which likely means the absence of a $q = 1$ surface due to the high edge $q_{eff} = 6.4$ ($q_{eff} = 8.7$ for #40286). This

is in agreement with the reconstructed q-profiles. Because of the existence of discharges without MHD activity in the detectable frequency range it seems unlikely that the small 2/1 mode has any effects of the current drive in these discharges.

The polarisation angles for off-axis counter injection into a very similar discharge are plotted in figure 4. After the initial phase, a slow decrease in the bottom channels and a slow increase in the top channels becomes evident. The slope is compatible with the current diffusion time scale but the absolute change is small. An equilibrium reconstruction of the q profile is shown in figure 5. Here a shaping of the q-profile is visible and it agrees with the expectations one has considering off-axis counter injection.

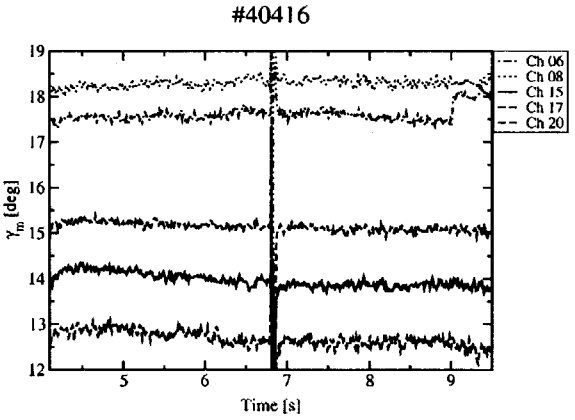

Figure 4: *MSE polarisation angles for off-axis counter injection case. The change in the first 500ms can be attributed to changes in plasma energy. From $t = 9s$ another beam source is injected which disturbs the signals.*

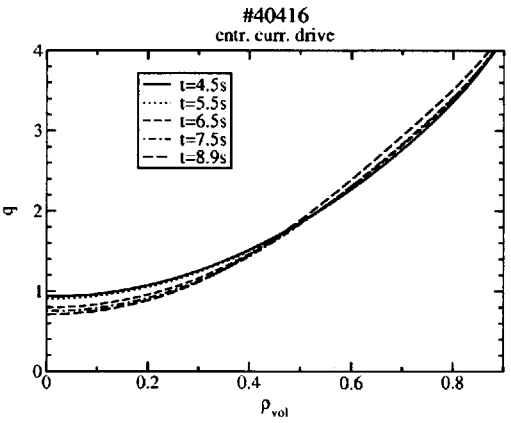

Figure 5: *Equilibrium reconstructed q profile development for off-axis NB counter injection.*

Even though for co current drive no influence on the current profile could be found experimentally, the drive of current by neutral beam injection can not be excluded. For a very similar discharge (at a higher magnetic field of $B_T = 3.2$T) the measured and calculated loop voltage is shown in figure 6. The measured loop voltage is not corrected for plasma excursions which becomes evident at $t \approx 3.5$s and also at the turn on of the additional heating. The time dependence during the neutral beam injection is reasonably modelled by ASTRA code [6] with linear Fokker-Plank solver [7]. The increase of the loop voltage due to the off-axis counter injection is the same in model and experiment and also the exponential decrease after switching to off-axis co injection can be seen in both curves. The development of the experimental loop voltage agrees with the calculated driven current.

4. Discussion

In this subsection some experiments have been discussed which are aimed to measure the off-axis current drive by neutral beam injection and its impact on the total current profile. For off-axis co current drive no obvious influence on the total current profile could be found but an influence on the loop voltage. For these discharges also modelling with ASTRA code has been performed. But in these very low density discharges the linear Fokker-Planck solver seems to be inappropriate because the plasma is locally dominated by the injected fast particles. For this reason the modelled time behaviour of the discussed discharges are not shown. The calculation with linear solver has resulted in a driven current of $I_{\mathrm{NBI}} = 641\mathrm{kA}$ for the co injection case and as $I_{\mathrm{NBCD}} = -497\mathrm{kA}$ for the counter injection case which are peaked at $\rho_{\mathrm{tor}} \approx 0.4$. The predicted influence is very strong and would lead to a reversed shear profile in the co injection case. For the counter injection case the influence is smaller but still somewhat larger than the measured influence in the same direction.

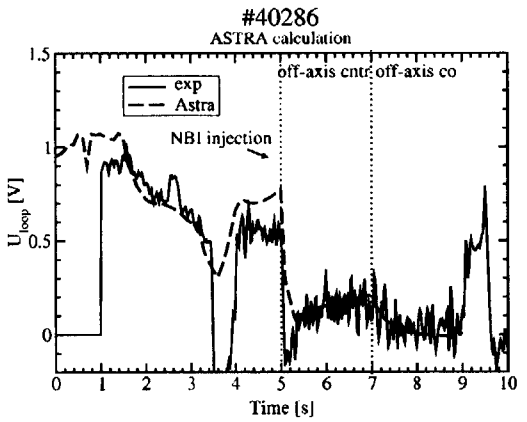

Figure 6: *The measured loop voltage (black) is not corrected for inductions in the coils due to radial position shifts. The time dependence of the loop voltage during NB injection is well reproduced by the model (broken line).*

The findings in the co injection case is very similar as in ASDEX Upgrade where not only the MSE system but also the MHD activity are consistent with the assumption that no current is driven by neutral beams off-axis. Also on ASDEX Upgrade the analysis of the ohmic transformer current shows that the neutral beam injection drives a current which should be off-axis.

Up to now two effects have been found to explain the absence of a change in the total current profile. One speculation could be a fast particle transport by micro turbulence, another the transport by Alfvén like MHD.

References

[1] Ohkawa, T., Nucl. Fusion **10**, 185 (1970).

[2] Mikkelsen, D. R., and Singer, C. E., Nucl. Technol./Fusion **4**, 237 (1983).

[3] Ide S., et al., Non-Inductive Current Drive Experiments for Profile Control in JT-60U, Proc 15th IAEA Fusion Energy Conference (Seville), IAEA-CN-60/A-5-I-4, 1994.

[4] Oikawa T., et al., Nucl. Fusion **41**, 1575 (2001).

[5] Fujita T., et al., Fusion Engineering and Design **34-35** , 28 (1997).

[6] Pereverzev G., et al., report IPP **5**/42, August 1991

[7] Polevoi A., Shirai H., Takizuka T., JAERI-Data/Code, 97-014, JAERI, March 1997

4. Transport in Core Plasmas

4.1 Dependence of Ion Thermal Diffusivity on Heat Flux at the Internal Transport Barrier in JT-60U

Y. Sakamoto, T. Suzuki, S. Ide, Y. Koide, H. Takenaga, Y. Kamada,
T. Fujita, T. Takizuka, H. Shirai, T. Fukuda

Internal transport barriers (ITBs) were observed in the weak positive magnetic shear (PS) plasmas and the reversed magnetic shear (RS) plasmas. These ITB structures are roughly classified into the weak ITB and the strong ITB. The weak ITB has a reduced thermal diffusivity (χ) in the core region compared with L-mode. The strong ITB has a large reduction of χ at the narrow ITB layer. An experiment to investigate the dependence of χ on heat flux at the weak ITB and the strong ITB is important for the physics understanding of the formation of ITBs. For this reason, the power of perpendicularly injected neutral beams was scanned in a detailed manner for PS and RS plasmas at fixed plasma parameters (toroidal magnetic field of 3.7T, plasma current of 1.3MA, line averaged density of 1.0-1.3x$10^{19}$$m^{-3}$, triangularity of 0.2 and balanced toroidal momentum input), and then the dependence of χ on the heat flux is investigated.

Transport properties of each heating power case are evaluated in the quasi-steady state condition. In the case of PS plasmas [1], the ion thermal diffusivity (χ_i) in the core region (r/a~0.46) generally increases with the heating power, similar to the L mode at low heating power. However, as a result of the intensive central heating, a weak ITB is formed without an apparent transition in the time evolution of ion temperatures, and then χ_i in the core region starts to decrease. Corresponding to a further increase of the heating power, a strong ITB is formed with an apparent transition, and then χ_i is reduced substantially. The level of χ_i at the strong ITB is three times as large as the neoclassical value. On the other hand, χ_i in the outside of ITB increases with increasing heating power, similar to the L-mode transport. In the case of RS plasmas [2], on the other hand, no power degradation of χ_i is observed in any of the heating regimes, suggesting absence of a threshold power for the weak ITB formation. The level of χ_i in the strong ITB is reduced to neoclassical value. The dependence of χ on the heat flux suggests there are multiple levels of reduced transport at the ITB for RS plasmas. This may reflect the discontinuous evolution of ion and electron temperature at the ITB in the case of the fine tuning of the heating power.

References

[1] Sakamoto, Y., et al., J. Plasma and Fusion Res. **78**, 941 (2002).

[2] Sakamoto, Y., et al., submitted to Nucl. Fusion.

4.2 Non-locality in Relation between E_r Shear and Diffusivity at the Internal Transport Barrier [1]

Y. Sakamoto, T. Suzuki, S. Ide, Y. Koide, H. Takenaga, Y. Kamada, T. Fujita,
T. Fukuda, T. Takizuka, H. Shirai, N. Oyama, Y. Miura

Several theoretical models for transport barrier formation suggest that the ExB flow shear plays an important role in suppressing the level of the turbulence and reducing the correlation length of the turbulence. The growth rate of micro-instability possesses a complex parameter dependence such as the magnetic shear, the scale length of density and temperature, and the ratio of ion and electron temperature, and so on. In order to address to the physics mechanism of the formation of weak and strong internal transport barriers (ITBs), the relation between ion thermal diffusivity (χ_i) and E_r shear is investigated by varying heating power with the plasma configuration and the magnetic shear as fixed as possible.

The strong E_r shear formed near the ITB layer, where a large reduction in χ_i was observed. It is seen that the ITB layer is located between the positions of the maximum and the minimum values of the E_r shear. The E_r shear becomes zero around the minimum of χ_i. Moreover, the experiments on the toroidal momentum input indicate that a reduction in either the maximum or the minimum values of E_r shear leads to degradation of the ITB [2]. These results indicate the non-locality in the relation between the E_r shear and the reduction of transport. Actually, abrupt variation of the diffusivity around the ITB (ITB event) was observed over a wide interval (30% of the minor radius) [3]. By considering the non-locality, we define the effective E_r shear near the ITB as $(dE_r/dr)_{eff} = (|(dE_r/dr)_{max}| + |(dE_r/dr)_{min}|)/2$. Experimental results of the relation between χ_i and $(dE_r/dr)_{eff}$ indicate that there exists a critical value of $(dE_r/dr)_{eff}$ to change the state from a weak to a strong ITB. The possible physical processes involved in the formation of weak and strong ITBs are considered as follows. The E_r shear increased with an increase in heating power due to the increase in the pressure gradient. The core confinement was improved, which corresponded to the formation of a weak ITB. When the plasma state changes from L-mode to the weak ITB, the E_r shear is enhanced by an increase in the heating power, and χ_i is gradually decreased. The growth of a weak ITB due to the gradual reduction in χ_i leads to an increase in the E_r shear. The transport properties change according to the transition from a weak to a strong ITB when the E_r shear exceeded the critical value.

References

[1] Sakamoto, Y., et al., submitted to Nucl. Fusion.

[2] Sakamoto, Y., et al., Nucl. Fusion **41** 865 (2001).

[3] Neudatchin, S.V., et al., 1999 Plasma Phys. Control. Fusion **41** L39.

4.3 Impact of Electron Heating on ITB Plasmas [1,2]

S. Ide, T. Suzuki, Y. Sakamoto, H. Takenaga, Y. Koide, T. Fujita, T. Fukuda,
Y. Kamada, H. Shirai, T. Takizuka, N. Oyama, A. Isayama and the JT-60 team

Toward realization of a steady state (SS) tokamak fusion reactor, it is important to assess characteristics of internal transport barriers (ITBs) under conditions which are relevant to those in a fusion reactor. Among those conditions, dominant electron heating is one of the most important ones, since in a fusion plasma electron heating by α particles will be predominant. However, in many experiments high performance plasmas are obtained by using positive-ion based neutral beam (P-NB) heating, and heating power is initially absorbed by ions predominantly. Thus the ion temperature (T_i) tends to be higher than T_e in these experiments. It is theoretically expected that $T_e/T_i > 1$ is a destabilizing factor to the ion temperature gradient (ITG) micro-instabilities, which is expected to be responsible to the confinement degradation. If the mode is dominant, it would affect formation and sustainment of ITBs under dominant electron heating. Therefore, it is important to investigate confinement improvement in such a condition. The experiments have been carried out by utilizing various heating systems equipped on JT-60U, especially electron cyclotron range of frequency (ECRF) and negative-ion based neutral beam (N-NB) injection systems.

In reversed magnetic shear (RS) plasmas, a ratio of T_e/T_i in the plasma core region was scanned by changing fractional power of electron heating by using ECRF or N-NB power. The ratio T_e/T_i was changed from ~0.8, which was typical maximum value in usual positive-ion based NB (P-NB) cases, to in excess of 1.2. In this regime it was found that the confinement enhancement relative to H-mode scaling ($HH_{98(y,2)}$) could be maintained higher than ~1.5, and could be higher than ~2 even at $T_e/T_i \sim 1.2$. The ITBs in both T_e, T_i and n_e were found to be maintained in such a dominant electron heating regime.

On the other hand in positive shear plasmas, it was found that the T_i ITB could be degraded or even lost with injection of ECRF. With the ECRF injection, the toroidal rotation (V_t) profile was fond to be flattened prior to the degradation of the T_i ITB, although the ration of Te and Ti was kept nearly constant. This suggests that the ECRF injection or direct electron heating affects the radial electric field structure, which is expected to influence the T_i ITB.

Reference

[1] Ide, S., et al., Plasma Phys. Controlled Fusion, **44**, A137 (2002).

[2] Ide, S., et al., Proc. of the 19th IAEA Fus. Energy Conf. Lyon, EX/C3-3 (2002).

4.4 Studies on Electron ITB Formation Condition in JT-60U

T. Fukuda, T. Fujita, Y. Sakamoto, K. Toi[1], K. Ida[1], T. Shimozuma[1] and K. Hill[2]
[1] National Institute for Fusion Science, Toki 509-5292, Japan
[2] Princeton Plasma Physics Laboratory, Princeton, New Jersey, 08543-0451, U.S.A.

1. Experimental and theoretical background

In regard to the formation of an ITB in the T_e profile under dominant electron heating mainly by the application RF waves, such as ECW, FW and LHW, it has only been known that the threshold heating power is substantially lower than the case of ion ITB formation [1] in weak or negative shear plasmas. The physics of electron ITB formation has not yet been resolved as much as that of ion ITB, where the sheared EXB flow is considered to carry a dominant role. In fact, well-defined experiments to address the electron ITB formation power threshold have not been performed, for example, in a way that the electron heating power is scanned under the absence of ion ITBs, in order to eliminate the possible synergism. In addition, compared to the case of ion ITB power threshold experiments, the analysis is more complicated in many cases, as the heating is often combined with current drive and the local magnetic shear is modified at the same time. The general findings obtained so far in various tokamaks are as follows. (1) The T_e profile is generally more resistant to forming barriers in NB heating experiments unless the weak or negative magnetic shear is produced, which implies that the physics involved in the formation of the ion and electron ITBs may be different. Therefore, it may not be possible to establish a comprehensive scaling of the threshold power for producing ITBs in T_i and T_e. Furthermore, it is clearly difficult to interpret the results of RF heating in terms of the global parameter dependence of the threshold power for the ion ITB formation, such as $n_e^{0.9} B_t^{0.23} a^{2.13}$ [2], as the location of the resonance or the coupling efficiency are modified simultaneously. (2) The production of negative or weak magnetic shear can significantly help the formation of ITBs in the T_e profile. (3) The location of an electron ITB is similar to that of ion ITB, and the T_e barriers are often weaker than T_i barriers in R/L_T, particularly in DIII-D and JT-60U when both ITBs are formed. Here, $L_T^{-1} = d(\ln T)/dr$. The influence of an ion ITB on the electron ITB formation is considered to be a challenging issue in ITB studies, as it may involve either simply an increase of α ($\alpha = -q^2 R d\beta/dr$) or interactions between zonal flows and electron turbulence in wave number space. In addition, the local maximum of $|R/L_{Te}|$ remains below 8-12 [3] in many of the normal or positive central shear plasmas. On the other hand, it is noticeably larger for negative shear discharges where a clear barrier structure is apparent in the T_e profiles.

It is considered also in theory that the presumed criteria for the ion ITB formation $\omega_{EXB}/\Gamma_L \geq 1$ [4] is too demanding for the high values of linear growth rate associated with short wavelength ETG, which is not sensitive to the sheared EXB flow. The result of simulation using the GS2 linear stability code performed for a standard ELMy H-mode discharge in JT-60U indeed indicates that the ETG spectrum has much larger $k_\theta \rho_s$ with negative real frequency, namely in the electron diamagnetic direction, and its magnitude is larger in comparison with ITG, as shown in Fig. 1. Here, k_θ and ρ_s respectively stand for the poloidal wave number and sound Larmor radius. In this case, the center of ITG turbulence spectrum and growth rate are observed respectively around 0.5 and 0.35×10^5 rad/s, whereas it is 40 and 1.2×10^5 rad/s for ETG. A heuristic approach to relate the suppression of ETG and sheared EXB flow was taken by Idomura et al. [5], where the anisotropic inverse cascade of the ETG turbulence by three-wave interactions are taken into consideration in a gyro kinetic particle simulation code. Beer et al. [6], has also proposed that the

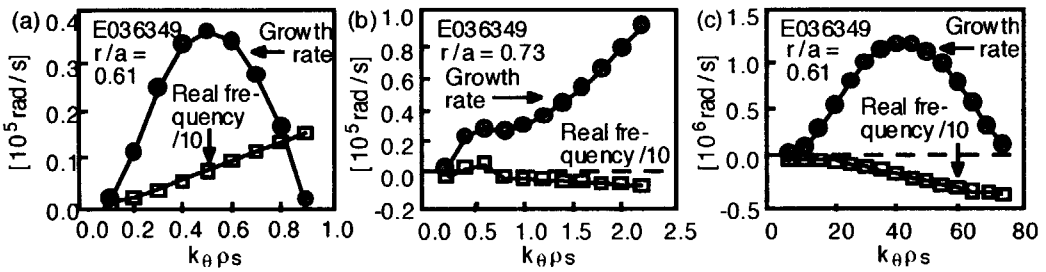

Fig. 1 Calculated $k_\theta \rho_s$ spectrum of the growth rate and real frequency for (a) ITG, (b) TEM/ETG and (C) ETG mode.

reversed precession drift of trapped electrons significantly reduce the growth rate of the trapped electron mode. The precession frequency, ω_{ps} is written in a form

$$\omega_{ps} = \frac{\Delta r}{\Delta \ell_\perp} \cdot \frac{(RB_\theta)^2}{B} \cdot \frac{\partial}{\partial \Psi} [\frac{cT_e G(\kappa,s,\alpha)}{eB_\theta R^2}], \qquad (1)$$

where $\Delta r/\Delta \ell_\perp$ and $(RB\theta)^2/B$ are respectively relevant to geometry of the turbulent eddies and the finite beta effect, and s is the magnetic shear defined as $rd(\ln q)/dr$. It is noteworthy that the function "G" in eq. (1) includes not only the magnetic shear but also the shaping factor κ i.e., elongation. Indeed, the formation of electron ITB is often observed high triangularity discharges with reduced κ. The practical criteria for the electron ITB formation in this model is $\omega_{ps} > \omega_t$, where ω_t is the decorrelation frequency of the electron turbulence. In a sense that the reversed magnetic shear and finite beta effect contribute to the reversal of precession drift, the significance of $s - \alpha$ pointed out in Ref. 7 may be another relevant key quantity.

2. Electron ITB formation experiment with high power ECH

In a dedicated experiment recently performed on JT-60U with high power ECH, where the NB heating power is suppressed and only the diagnostic beam is allowed, it has been found that the electron ITBs can be formed at farther inside the location of q_{min} radius, as shown in Fig. 2. The relevance of ion ITB location and q_{min} radius in negative shear plasmas is documented in JT-60U [8], JET [9] and other tokamaks, and the ion ITB physics is therein considered to be strongly related to sheared EXB flow. However, in case the NB heating power is increased, the location of electron ITB moves outward, and it coincides with that of ion ITB in high power NB heated discharges. Though it is not very clear, Fig. 3 (a) shows that a relatively weak electron ITB is produced near the q_{min} radius under P_{NB} of 7.6 MW, where the ion ITB is not present. On the other hand, in case P_{NB} is increased to 19.7 MW, the ITB location is expanded in radius, and both ion and electron ITB are formed near the $q = 2.5$ or 3 surface, which is often observed in high power heating of weak central shear plasmas in JT-60U, as documented in Fig. 3 (b) and (c). Similar to the double ITBs observed in JET, the second electron ITB can also be resolved farther inside near the q_{min} radius in central negative shear plasma in Fig. 3 (c). This result indicates the primary role of magnetic shear, and pressure gradient which is related to the E_r shear or the finite beta effect can also affect the electron ITB formation and its location.

Accordingly, more specific experiment was designed and performed, in order to resolve the electron ITB formation condition comprehensively. Here, the NB heating power was suppressed typically below 3.7 MW, where the ion ITB is not formed i.e., the effect of E_r shear is not present at least for ion ITB. For the quantitative treatment of the profile shape and clear definition of ITB formation, the normalized temperature gradient, $|R/L_{Te}|$ was referred to in this report. The significance of this quantity can be found elsewhere, such as

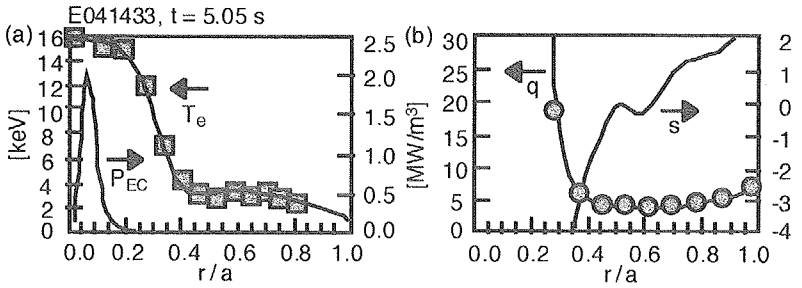

Fig. 2 (a) The location of electron ITB formation in negative central shear plasmas shown with the EC power deposition profile. Here, the NB heating power is suppressed, and only the diagnostic NB is applied. (b) The q and magnetic shear profile.

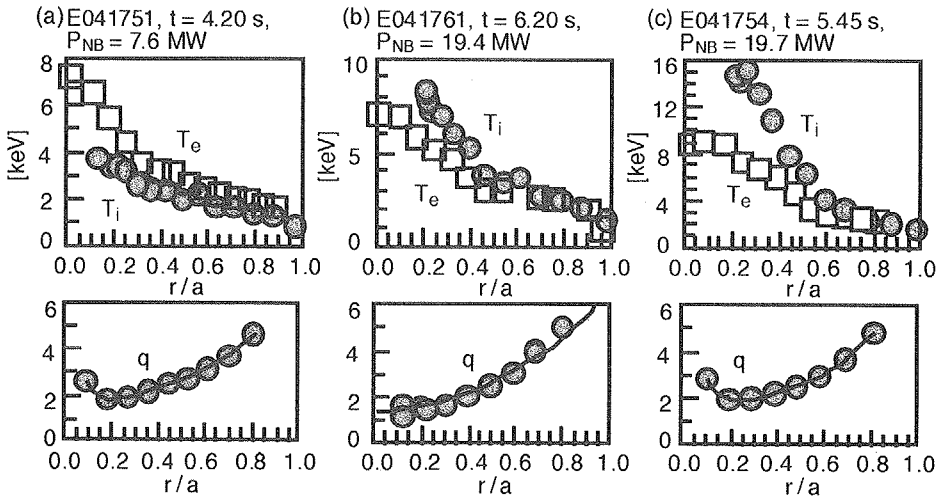

Fig. 3 The changes in the location of electron ITB formation with increased NB heating power under the inverted and monotonic q-profiles.

Refs. [3] and [10]. In particular, it has been found that the critical gradient in T_e profile in terms of $|R/L_{Te}|$ is limited in the range of 8-11 without apparent electron ITB [3]. The local maximum of $|R/L_{Te}|$, which is near the ITB foot position in most cases, is plotted against the EC heating power per particle in Fig. 4 (a) i.e., divided by the averaged density. In case the local magnetic shear at ITB is positive, the value of $|R/L_{Te}|$ never exceeds 10-12, even if the heating power is increased above 4 MW/10^{19} m^{-3}. This number is consistent with Ref. 3, which is based on the database from European tokamaks, such as JET and ASDEX-Upgrade. When the local shear is negative, however, the value of $|R/L_{Te}|$ continuously increases with the heating power without the sign of critical threshold, although the rate of increase is less than linear. Namely, the bifurcation phenomena is not observed in the case of electron ITB formation, similar to the case of weak ion ITB. This is in contrast with the formation of electron temperature transport barriers in heliotron or torsatron type helical devices with intrinsic negative central shear, where the formation of the "electron root" is directly related to the production of E_r shear, and the local maximum value of $|R/L_{Te}|$ has a critical value [11].

In Fig. 4 (b), the local maximum value of $|R/L_{Te}|$ is plotted against s -α. Here, the electron heating power is varied, although the total heating power is nearly fixed. The value of s was evaluated using the MSE diagnostic, however, the beam pressure contribution is hereby disregarded. The indications of this figure are that (1) negative or weak magnetic shear can help the formation of electron ITB, and (2) larger values of α at ITB contributes much either to the modification of the magnetic well structure or reduction of the local magnetic shear to enhance the value of $|R/L_{Te}|$ in negative shear plasmas. The slight in-

crease of $|R/L_{Te}|$ in the positive shear region shown in Fig. 4 (b) is ambiguous and no conclusive statements can be made. Although the normalization of $|R/L_{Te}|$ by $1+Z_{eff}(T_e/T_i)$ was undertaken, as suggested in Ref. 10, it was not possible to reduce the scatter of the plot. In addition, systematic dependence of $|R/L_{Te}|$ on s/q and $L_s=qR/s$ was also observed, as expected in the theoretical model [12].

3. Conclusion and discussions

The weak or negative shear seems to be indispensable for the electron ITB formation, and it can be produced without much heating power or E_r shear in JT-60U. Another evidence is that the critical value of $|R/L_{Te}|$ for the electron ITB formation does not exist under the negative magnetic shear. Should the competing processes of shearing rate and the growth rate of electron turbulence be the key element, the observation of either the sign of bifurcation or critical quantities related to the heating power threshold is plausible, which was not the case in the JT-60U experiment, although it is contrary to the case of the neoclassical ITB formation in LHD plasmas. Therefore, it may be conjectured that the role of sheared EXB flow is less significant for electron ITB than for ion ITB and modification of the magnetic well structure by the alpha-stabilization or finite beta effect together with the contribution of the local magnetic shear is more important.

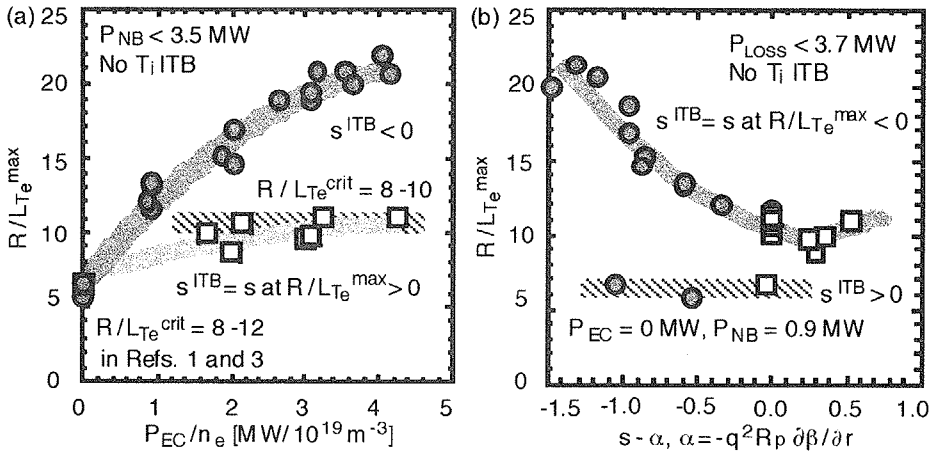

Fig. 4 Local maximum of R/LTe as a function of (a) the EC heating power per particle and (b) s-α.

References

[1] Connor, J.W. et al., "A Review of Internal Transport Barrier Physics for Steady State Operation of Tokamaks," submitted to Nucl. Fusion
[2] Sips, A.C.C. et al., Plasma Phys. Control. Fusion **44**, A391 (2002).
[3] Ryter, F. et al., Plasma Phys. Control. Fusion **43**, A323 (2001).
[4] Hahm, T.S. et al., Phys. Plasmas **2**, 1648 (1995).
[5] Idomura. Y. et al., Nucl. Fusion **41**, 437 (2001).
[6] Beer, M.A. et al., Phys. Plasmas **4**, 1792 (1997).
[7] Fukuyama, A. et al., Plasma Phys. Control. Fusion **37**, 611 (1995).
[8] Sakamoto, Y. et al., Nucl. Fusion **41**, 865 (2001).
[9] Joffrin, E. et al., Plasma Phys. Control. Fusion **44**, 1739 (2002).
[10] Jenko, F. et al., Phys. Plasmas **8**, 4096 (2001).
[11] Ida, K. et al., Phys. Rev. Lett. **86**, 5297 (2001).
[12] Hoang G.T. et al., Phys. Rev. Lett. **87**, 125001-1 (2001).

4.5 Studies of Ion Internal Transport Barrier Formation Condition in terms of Global Plasma Parameters [1]

T. Suzuki, Y. Sakamoto, S. Ide, Y. Koide, H. Takenaga,
Y. Kamada, T. Fujita, T. Takizuka, H. Shirai, T. Fukuda

1. Introduction

Improvement of confinement by internal transport barrier (ITB) is helpful for obtaining a compact reactor relevant core plasma. We have experimentally investigated dependencies of formation conditions of the ion thermal ITB on global plasma parameters, such as plasma current I_p, toroidal field B_t, and safety factor on plasma surface q_a. The formation condition is examined with heating power, which is an external control parameter. The heating power has been considered to play an important role to produce ITB through some mechanism, such as radial electric field shear [2]. Understanding of such dependencies is useful not only in scaling study, but also in physics study of the formation conditions of ITB. The former helps optimization of designing parameters of future devices, especially on the heating scheme and the heating power. The latter gives constraints on condition of ITB formation, with which theoretical models can be validated.

2. Experiments

Experiments have been done to investigate a threshold power of ITB formation. Figure 1 shows waveforms of plasma current (I_p) and of NB heating power (P_{NBI}) for discharges. The ITB was formed at the flat top phase of plasma current by increasing main NB heating power on shot by shot basis. Balanced momentum input was employed in this experimental series to eliminate an effect of plasma rotation. Nearly the same pre-heating during I_p ramp-up was employed to fix the magnetic shear profile just before the main heating (target). The target magnetic shear was reversed at normalized minor radius of ρ=0.4-0.5 as shown in Fig.2. The line averaged electron density $\bar{n}_e$ by an interferometer was feedback-controlled to $1.0\times10^{19}m^{-3}$ at the target. Since the fueling rate by the NB for strong heating exceeds particle loss rate by the transport, $\bar{n}_e$ continuously increased during the main heating. The increasing rate of $\bar{n}_e$ during

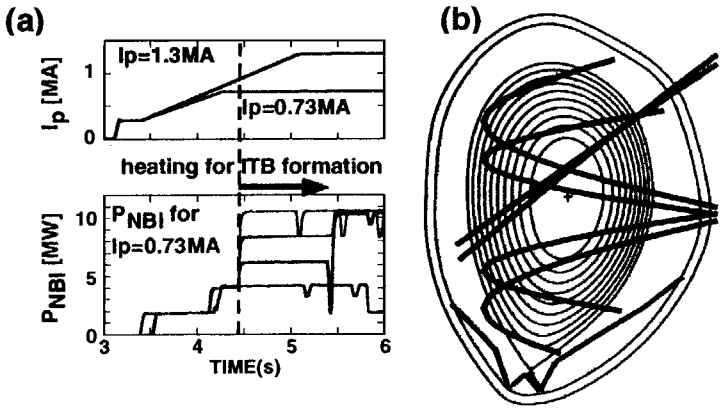

Fig. 1: (a) Waveforms of plasma current at I_p=0.73MA and 1.3MA (upper). Waveforms of NB heating power at I_p=0.73MA. To fix the q profile at the target, heating power during I_p ramp-up were almost same. (b) Configuration of the plasma, and NB lines used for scanning heating power.

the main heating depended on I_p, P_{NBI}, and the existence of the ITB. Configuration and shape of the plasma (shown in Fig. 1) are fixed to eliminate their effects. The I_p and B_t were scanned independently by a factor of about two, and hence, resulting safety factor at plasma surface q_a was varied by a factor of about two; (a): I_p=1.3MA, B_t=3.73T, q_a~7, (b): I_p=0.73MA, B_t=2.10T, q_a ~7, (c): I_p=0.73MA, B_t=3.73T, q_a ~13. Since the safety factor profiles in Fig.2 are similar to each other, resulting magnetic shear profile $\hat{s} \equiv (r/q)dq/dr$ are almost same.

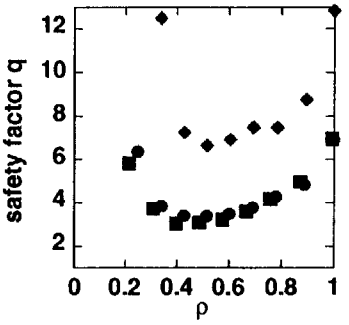

Fig. 2: Safety factor profiles measured by MSE. Larger q shows a typical discharge with I_p=0.73MA, Bt=3.73T. Others are for I_p=0.73MA, Bt=2.10T and for I_p=1.3MA, Bt=3.73T.

3. Analyses and Results

ITB formation was judged by reduction of an ion thermal conductivity χ_i normalized by a neo-classical ion thermal conductivity χ_{NC} ($\hat{\chi} \equiv \chi_i/\chi_{NC}$). Since I_p and B_t are different in each set of scans, the normalization has been introduced as an index of reduced conductivity. Transport analyses have been carried out in a quasi-steady state of stored energy and of the ion temperature profile (about 0.8s after the main heating). TOPICS code was used for the analysis with i) q profile and MHD equilibrium by MSE measurement, ii) T_i profile by CXRS, iii) T_e profile by Thomson scattering and/or ECE, iv) n_e profile by Thomson scattering and interferometers. Deposition profile of NB power has been evaluated by an orbit following Monte-Carlo (OFMC) calculation. We define formation of strong ITB usually seen in reversed shear (R/S) plasmas in JT-60U by a criterion $\hat{\chi} < 2$. When we assume conductivity by summation of neo-classical and anomalous components ($\chi_i=\chi_{NC}+\chi_{ano}$), the criterion corresponds to χ_{ano} is reduced down to χ_{NC}. Since $\hat{\chi}$ can be extremely large outside ITB, here we use "neo-classicality" $\hat{\chi}^{-1}$ to limit its domain. Thus, $\hat{\chi}^{-1} > 0.5$ is the corresponding criterion; neo-classicality of unity is the neo-classical transport. To avoid breakdown of the neo-classical theory, we avoid the analysis at high q region around the magnetic axis (ρ<0.4).

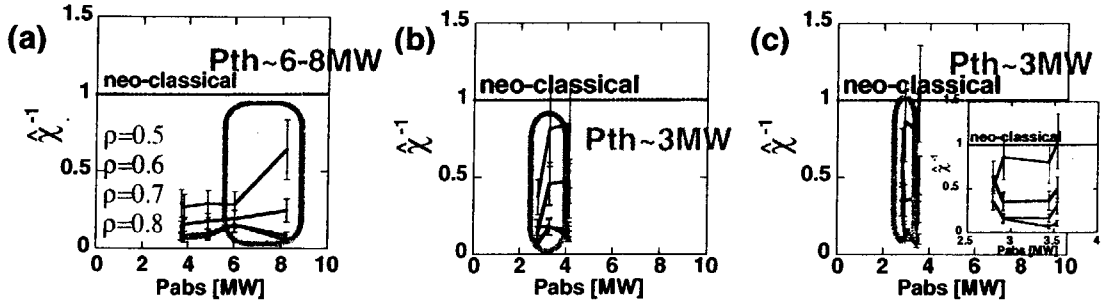

Fig. 3: The neo-classicality $\hat{\chi}^{-1}$ as a function of absorption power at various minor radii. (a): I_p=1.3MA, Bt=3.73T case. Improvement of confinement down to the criterion is seen for P_{abs}=6-8MW at ρ=0.5. (b): I_p=0.73MA, Bt=2.10T case. (c): I_p=0.73MA, Bt=3.73T case; the inset shows its detail. The threshold power is lower at lower I_p. The P_{th} differs at the same B_t or a_p when I_p differs.

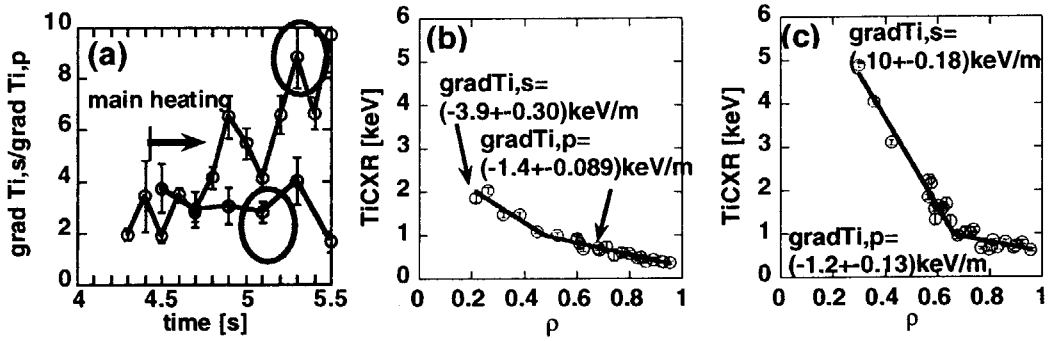

Fig. 4: (a) Temporal evolutions of (grad $T_{i,s}$)/(grad $T_{i,p}$) for below P_{th} and for above P_{th}. Ion temperature profiles for enclosed data by circles are shown in (b) and (c). (b) The ion temperature profile which does not show significant change. (c) T_i profile where the T_i gradient evolves to the ratio of about 10.

Figure 3 (a) shows the neo-classicality $\hat{\chi}^{-1}$ at several minor radii as a function of absorption power for a case (I_p=1.3MA, B_t=3.73T). When absorption power exceeds P_{th} of 6-8MW, increase of neo-classicality up to a half of neo-classical level occurs locally at a minor radius (ρ=0.5). No significant change has been observed outside the radius (ρ=0.6, 0.7, 0.8). The location where neo-classicality increased (ρ=0.5) corresponds to where the safety factor is minimum (Fig. 2). Errors in Fig. 3 are systematic ones assuming ±5% error of heat flux, ±5% error in ion density, ±20% error in T_i gradient. Whole results of scans are shown in Fig. 3. We can see dependence of P_{th} on I_p. The P_{th} was 3MW for I_p=0.73MA, and was 6-8MW for I_p=1.3MA. Dependencies of the P_{th} on B_t and q_a seem to be weaker in terms of the global parameter dependence than that on I_p. The weak dependence on the toroidal field is consistent with the previous result, although the magnetic shear profile was not fixed [3].

The above criterion of the ITB formation is consistent with other viewpoints, such as "spatial discontinuity of ion temperature gradient" and "departure from a stiff Bohm-type diffusion". That is to say, a ratio of ion temperature gradients at both sides of ITB reaches to a value (close to ten), when absorption power P_{abs} exceeds P_{th} (Fig. 4 (a)). The ratio (grad $T_{i,s}$)/(grad $T_{i,p}$) is defined by the most steep gradient (grad $T_{i,s}$) divided by that at the peripheral region (grad $T_{i,p}$). Since $T_{i,s}$ and $T_{i,p}$ are same at the boundary of the two regions, a ratio of corresponding inverse scale lengths L_{Ti}^{-1} is same as (grad $T_{i,s}$)/(grad $T_{i,p}$). The gradients of T_i have been determined by a "bi-linear" fitting; a simultaneous least square fitting to two connecting linear functions. The bi-linear function is

$$T_i(\rho) = (C_1\rho + C_2)H(\rho - C_3) + (C_4\rho + C_2)(1 - H(\rho - C_3)),$$

where $H(x)$ is the Heaviside's step function. The four free parameters C_1, ..., C_4 are determined by the least square fitting. We cannot see significant difference in the ratio below the P_{th}. Typical T_i profiles with/without ITB are also shown in Fig. 4

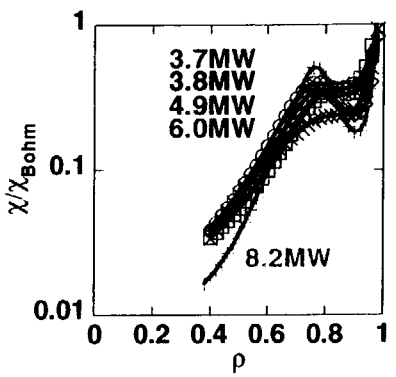

Fig. 5: Profiles of ion thermal conductivity normalized by the Bohm conductivity at various absorption powers. The shape of profile changes when absorption power exceeds the threshold power P_{th}.

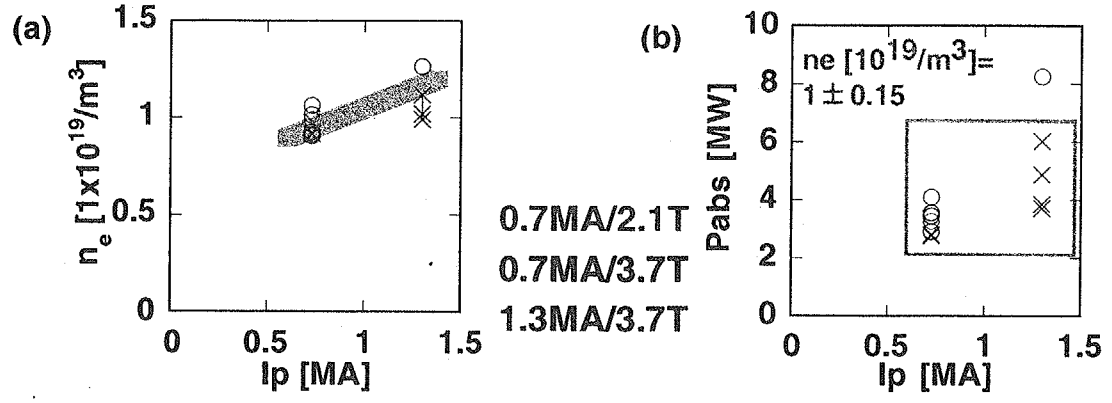

Fig. 6: (a) Data of this experiment on I_p-n_e plane. Slight positive correlation can be seen between them. Circles indicate ITB was formed, and crosses show no formation. (b) Positive dependence of P_{th} on I_p can be seen under nearly the same n_e (within 15%). The dependence seems to be stronger than that on n_e (a).

(b, c). We can see the threshold power from another aspect by comparing ion thermal conductivity normalized by the Bohm conductivity. The Bohm conductivity is a measure of the anomalous transport, and is defined by $\chi_{Bohm} = T_e/(eB_t)$, where e is an elemental charge. Fig. 5 shows profiles of χ_i/χ_{Bohm} at various absorption power for I_p=1.3MA, B_t=3.73T case. When P_{abs} exceeds P_{th}, χ_i/χ_{Bohm} decreases within ρ<0.5 so that shape of the profile changes, where ρ~0.5 is location of the ITB. On the contrary, the profiles of χ_i/χ_{Bohm} are stiff under the P_{th}, showing the conductivity is dominated by the Bohm-type diffusion

We see a slight correlation between I_p and n_e (Fig. 6(a)), where particle confinement may be affected by the change of plasma current. We used n_e at 50ms after the start of the main heating when differences in dn_e/dt appear. Such a correlation between I_p and n_e can be seen in an international ITB database [4]. As shown in Fig. 6(b), positive dependence of P_{th} on plasma current can be seen even under nearly the same n_e (within 15%; enclosed by rectangle). The dependence seems to be stronger than that on n_e.

4. Summary

We have defined a criterion of ITB formation $\hat{\chi}^{-1} > 0.5$, where anomalous transport reduces to neo-classical one. We found that the threshold power of the ITB formation depended on plasma current. Dependencies on B_t and on q_a seem to be weaker than that on I_p. The threshold was about 3MW for I_p=0.73MA and was 6-8MW for I_p=1.3MA. We confirmed the formation of ITB by continuous increase of a ratio of ion temperature gradient of ITB to the peripheral one. The ratio increased up to ten when ITB was formed, while it stayed almost constant without ITB. Another approach to the physics of ITB formation is a breakaway from the Bohm-type diffusion. When the absorption power exceeds P_{th}, ion thermal conductivity normalized by the Bohm conductivity changed its profile, suggesting a change in transport that could be characterized by the Bohm-type diffusion.

References

[1] To be submitted to Nuclear Fusion.
[2] Sakamoto, Y., et al., in Fusion Energy 2002 (Proc. 19th Int. conf. Lyon, 2002) IAEA-CN-94EX/P2-08. Submitted to Nuclear Fusion.
[3] Ide, S., et al., Phys. Plasmas **7** (2000) 1927.
[4] A. C. C. Sips, et al., Plasma Phys. Controlled Fusion **44** (2002) A391.

4.6 Dynamics and Interplay of L-H-L Transitions and ITB-events in Reversed Shear Plasmas with Internal Barriers in JT-60U [1]

S. V. Neudatchin[1)], T. Takizuka , H. Shirai, T. Fujita, A. Isayama,
Y. Kamada, Y. Koide, T. Suzuki, S. Takeji
1) present address: Nucl. Fusion Institute, RRC "Kurchatov Institute", Moscow, Russia

The "global" edge-core connection at "fast" L-H and H-L transitions was observed in some JT-60U and JET normal shear (NrS) regimes as instantaneous start of T_e rise (or decay) at the times of transitions, occurred simultaneously (within a few ms) in the region $\sim 0.3<r/a<1$. The T_e response was interpreted as abrupt non-local variations of electron heat diffusivity $\delta\chi_e$ at times of the transitions. The physical mechanism responsible for "global" nature of transport bifurcations at "fast" L-H-L transitions has not fully been clarified yet.

The response of internal transport barrier (ITB) to ELM-induced H-L transition and to L-H recovery is observed as T_e decay (or rise) in wide space region (up to ~0.3 of minor radius in the extreme case). The response is correlated within a few ms with L-H-L transitions and is interpreted as abrupt variations of electron heat diffusivity $\delta\chi_e$ which are obtained under various q profiles. The profile of $\delta\chi_e$ hardly penetrates into reverse shear (RS) region for the strong ITB. The spatial extent of $\delta\chi_e$ is related to the position of q_{min}, $r(q_{min})$, and penetrates into RS region deeper for the weak ITB than for the strong one, suggesting "global" edge-core connection penetrating through $r(q_{min})$ on a ms timescale. The value of $\delta\chi_e$ at $r(q_{min})$ is small for strong ITB (~0.05 m^2/s) and increases by an order of magnitude for the weak ITB. Absolute values of $\delta\chi_e$ in positive shear region (far enough from $r(q_{min})$) of RS plasmas with weak ITB are similar to those found earlier in JT-60U and JET NrS plasmas.

The formation of strong ITB via series of ITB-events is found during ELM-induced L-mode and recovering H-mode. During the L-mode, the first ITB-event improves transport around $r(q_{min})$ and the next ITB-event has the same effect in the positive shear region. Afterwards temporal ITB-event-degradation in positive shear zone causes L-H recovery. Later, strong ITB survives and improves further. Finally, the energy confinement time is nearly doubled in comparison with the H-mode before ITB-events. The first ITB-event could be caused by the gradual decay of T_e due to MHD activity for this case. Triggers of ITB-events are probably different in various plasmas of JT-60U. We will investigate them in near future [2].

Reference

[1] Neudatchin, S.V., Takizuka, T., Shirai, H., Fujita, T., Isayama, A., Kamada, Y., Koide, Y., Suzuki, T., Takeji, S., Plasma Phys. Control. Fusion **44**, A383 (2002).
[2] Neudatchin, S.V., Takizuka, T., Hayashi, N., et al., 19th IAEA Fusion Energy Conference, Lyon, 2002, EX/P2-06 (2002).

4.7 Energy Confinement Scaling for Reversed-shear Plasmas with Internal Transport Barrier in JT-60U [1]

T. Takizuka, Y. Sakamoto, T. Fukuda, T. Fujita, Y. Kamada, T. Suzuki, S. Ide, H. Shirai

An energy confinement scaling for reversed-shear plasmas with box-type internal transport barrier (ITB) and L-mode edge is developed based on the JT-60U data. The stored energy is divided into two parts, L-mode base part and core part surrounded by the ITB. The core stored energy W_{core} does not simply increase with the net heating power P_{net}. A scaling of core stored energy is given as $W_{scale} = C\,\varepsilon_f^{-1}\,B_{p,f}^{2}\,V_{core}$, where ε_f is the inverse aspect ratio at ITB foot, $B_{p,f}$ is the poloidal magnetic field at outer midplane ITB foot, and V_{core} is the core volume inside ITB foot (Fig. 1). This scaling is equivalent to the condition for the core poloidal beta $\varepsilon_f \beta_{p,core} = C_1$ with $C_1 \approx 1/4$. Though W_{core} is little dependent on P_{net}, the estimated heat diffusivity in the ITB region moderately correlates with a neo-classical diffusivity, and the neo-classical transport is not inconsistent with the data.

We can guess a candidate of the physics background of the present scaling being the combination of "MHD equilibrium limit" and "bootstrap current limit". It is known that an MHD equilibrium with high $\varepsilon\beta_p$ value is broken due to the appearance of magnetic separatrix inside a plasma. It is also known that the bootstrap current fraction is almost proportional to $\varepsilon^{0.5}\beta_p$ and the full non-inductive current sustainment is possible for high $\varepsilon^{0.5}\beta_p$ value. A core region in an RS plasma may be governed by these limits. With respect to the transport, the neo-classical nature is observed although W_{core} does not simply increase with P_{net}. By taking into account these considerations, we can guess that an RS plasma is dynamically self-organized under the fully consistent set of MHD equilibrium limit, bootstrap current limit, the energy transport and the current diffusion.

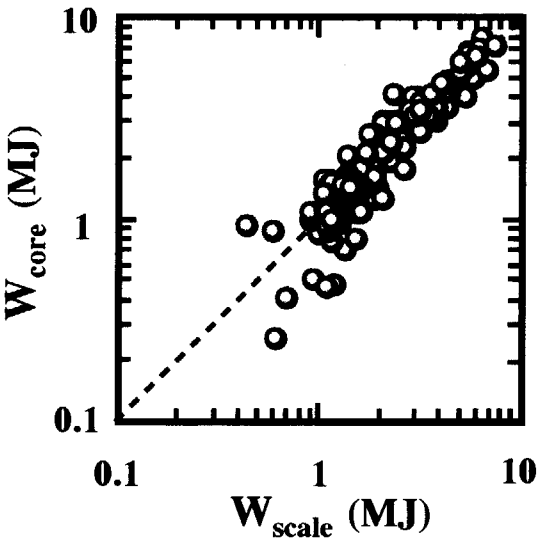

Fig. 1. Comparison of data W_{core} with present scaling W_{scale}.

Reference

[1] Takizuka, T., Sakamoto, Y., Fukuda, T., Fujita, T., Kamada, Y., Suzuki, T., Ide, S., Shirai, H., Plasma Phys. Control. Fusion **44**, A423 (2002).

4.8 Cold Pulse Propagation in the Vicinity of ITB on JT-60U

S. Inagaki[1)], A. Isayama, T. Fukuda, Y. Miura and H. Yamada[1)]
1) National Institute for Fusion Science, 322-6, Oroshi-cho, Toki-city, 509-5292 Japan

1. Introduction

The heat transport in thermonuclear plasmas has remained an unresolved issue. There exist a number of experimental observations defying the presently available understanding for not only the heat diffusivity but also the parameter dependence of confinement. Turbulence is considered to be important for heat transport in magnetically confined plasmas. Some turbulence models suggest that the heat transport can be non-local and/or that heat flux has a non-linear dependence on the temperature gradient. These complications violate the basic assumption of diffusive nature, which supports the validity of a static (power balance) analysis for heat transport. The transient transport analysis, in which the dynamic response of the plasma to a perturbation is investigated, is recognized to valuably complement static analysis. The static analysis uses the radial heat flux and the temperature gradient, while the transient analysis uses the change in the heat flux induced by a variation in the temperature gradient [1]. If the heat flux has a non-linear dependence on the temperature gradient, these do not give the same heat diffusivity.

A recent experimental progress on the formation of internal transport barriers (ITBs) has demonstrated a great improvement of the confinement of Tokamak plasmas. The clarification of the ITBs physics is now one of the most important issues in confinement studies. The use of modulated electron cyclotron heating in the RTP [2] and the use of shallow pellet injection in JET [3] are only a few of the experiments for transient transport analysis in plasma with ITBs. The heat pulse propagation resulting from a spontaneous ITB event has been analyzed in JT-60U [4]. The external perturbation experiment in JT-60U will extend our knowledge of ITB physics.

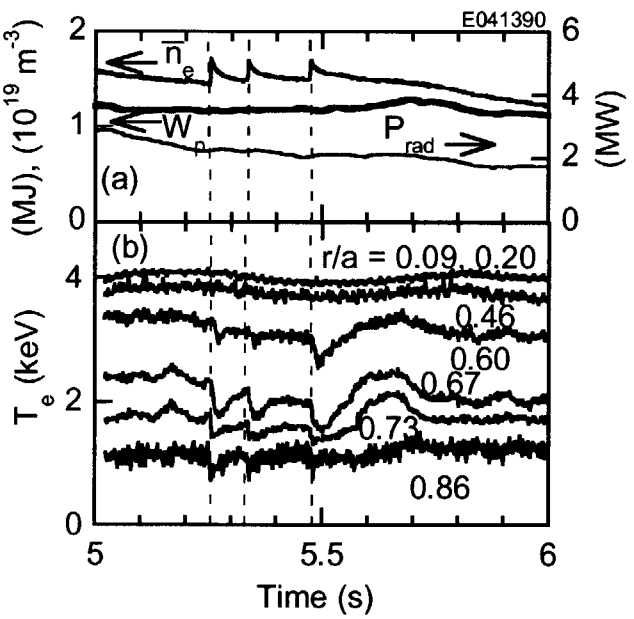

Fig. 1. Time evolutions of (a) stored energy, line averaged density and radiation loss (b) electron temperature at different radii.

2. Experimental Results

Cold pulse experiments are performed in reverse magnetic shear plasmas on JT-60U. The cold pulses are induced by pellets injected into the edge. The typical time evolutions of stored energy W_p, radiation power P_{rad}, line averaged density $\overline{n}_e$ and electron temperature T_e at different radii are shown in Fig. 1. The plasma current I_p and the injected neutral beam power P_{NB} are constant (I_p =1 MW, P_{NB} = 7.6 MW) for t = 5-6s. The formation of the strong ITBs is observed in n_e, T_e and T_i profiles as shown in Fig. 2. The ITBs are sustained for this period. The pellets typically ablate within 1 ms in the region of r/a>0.8 and provide cold electrons. The cold pulse generated in the edge region propagates towards the ITB region. Because the changes of W_p and P_{rad} after the pellet injection are negligible, the global confinement is not changed and the cold pulse is considered as a perturbation. We assume that the particle diffusivity is much smaller than the electron heat diffusivity, and thus the electron heat transport dominates in the cold pulse propagation. When the cold pulse approaches the electron ITB foot, a unique feature which can not be explained by diffusive nature is observed. The time evolution of the radial profile of the cold pulse amplitude is shown in Fig. 3. The electron heat diffusivity estimated from static (power balance) analysis (using the TOPICS code) is also shown in Fig. 3. The negative peak of the cold pulse amplitude (indicated by open circles in the figure) is enhanced in the outer region of ITB and the cold pulse amplitude is strongly damped inside the ITB. Simple heat diffusivity (constant in time

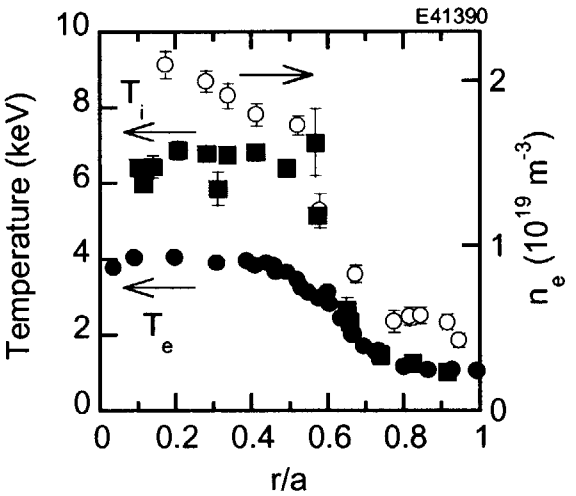

Fig. 2. Radial profiles of ion and electron temperature and electron density just before the second pellet injection (at 5.3 s)

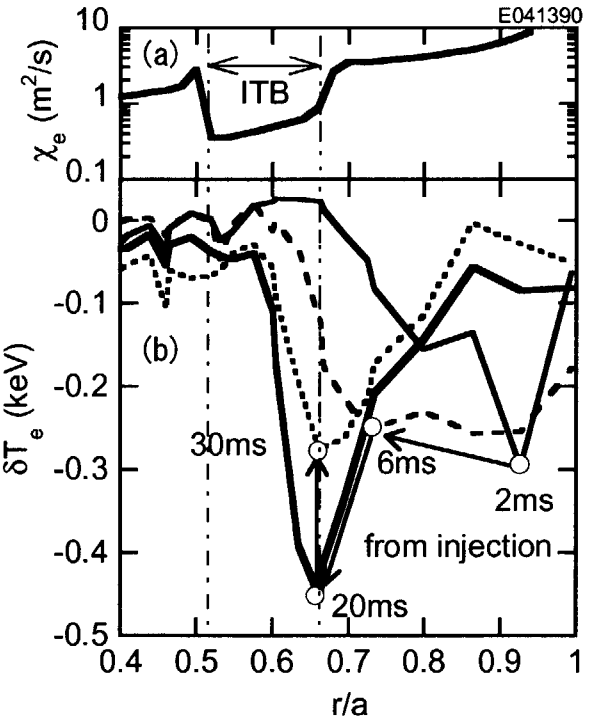

Fig. 3. Radial profiles of (a) electron heat diffusivity estimated from the static analysis and (b) amplitude of the cold pulse. The open circles indicate the negative peak of the amplitude of the cold pulse.

and continuous in space) can only explain the damping of the cold pulse amplitude. The cold pulse reaches its minimum at r/a = 0.65 with a time delay of 20 ms from the pellet injection. Since the negative peak of the cold pulse is separated from the cooling source spatially and temporally, the enhancement of the cold pulse peak is not related to the cooling source directly. A similar phenomenon is observed in the strong ITB plasma sustained by a high level of heating power in JET [3]. However, the enhancement of the negative peak of the cold pulse appears inside the ITB in the JET plasma. On the contrary, the negative peak of the cold pulse can't penetrate inside the ITB in the JT-60U plasmas as shown in Fig. 3(b).

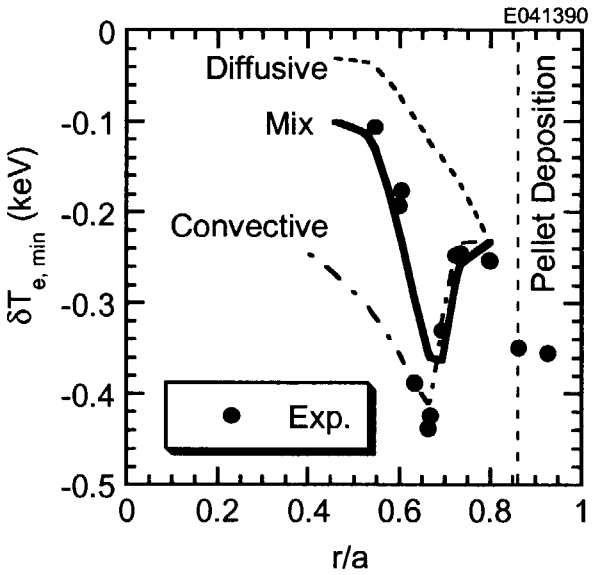

Fig. 4. Minimum amplitudes of the cold pulse at different radii. Three different transport models are compared with experimental results.

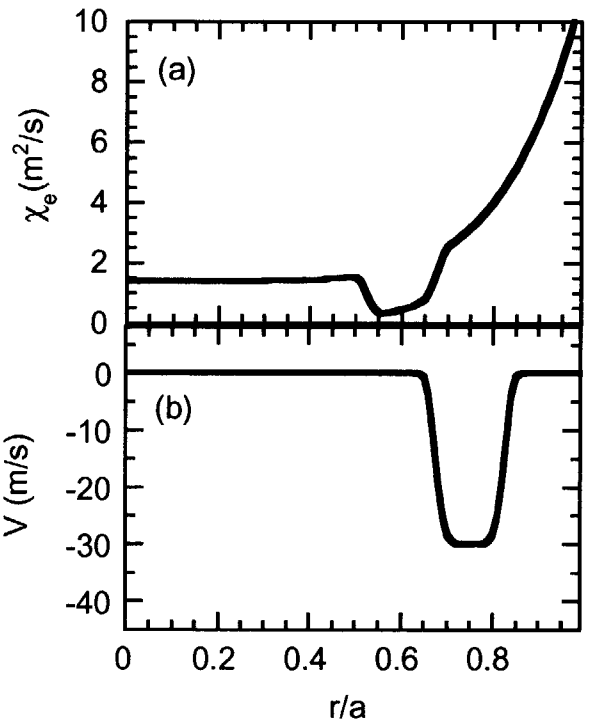

Fig. 5. Radial profiles of (a) electron heat diffusivity and (b) convection velocity used in a model, which give the best reproduction of the experimental observation in Fig. 4.

3. Comparison with empirical models

The growth of the cold pulse (variance with simple heat diffusion propagation) suggests the role of inward heat convection. Simulations with different empirical heat transport models have been examined. The empirical models used here consider 1) diffusive : $\delta q_e = -n\chi_e \nabla \delta T_e$, 2) convective : $\delta q_e = 3nV\delta T_e/2$ and 3) mixed heat transport : $\delta q_e = -n\chi_e \nabla \delta T_e + 3nV\delta T_e/2$. In these simulations, the perturbed heat transport equation (density perturbation and off-diagonal terms are neglected) is solved numerically by using the time dependent boundary condition. Figure 4 shows the comparison of the minimum amplitudes of the cold pulse at different radii between simulations and experimental results. In the diffusive model, the electron heat diffusivity obtained from static analysis is employed. The simulated

amplitude with the diffusive model is much smaller than the observed one. In the convective model, inward pinch is introduced so that the negative peak of the cold pulse can be reproduced. In this case, it is difficult to reproduce the strong damping of the cold pulse amplitude inside the ITB. The best reproduction of the experimental observation is obtained with the model which has both diffusive and convective features. The radial profiles of the heat diffusivity and the heat convection velocity used in this model are shown in Fig. 5. Here the heat diffusivity is approximately the same as one obtained from the static analysis. The characteristics of this model are the following: the ITB plasma has a diffusive nature in the localized region and its reduced heat diffusivity can explain the strong damping of the cold pulse amplitude, while the convection is dominant in the region just outside the ITB, which leads to the enhancement of the cold pulse. A number of Tokamak researches have reported that the heat diffusivity obtained from the transient analysis is larger than one obtained from the static analysis. This enhancement of the heat diffusivity is considered to be due to the temperature gradient dependence of the heat diffusivity. Such dependence leads to a "stiff" temperature profile. The transient response observed inside the ITB in JT-60U is, however, in good agreement with the prediction from the static plasma behavior. This suggests that the ITB is not a "stiff" region. On the contrary, the transient response outside the ITB is quite different from the static one. If the heat diffusivity has the dependence on temperature and/or temperature gradient, the convective term will appear in the perturbed heat transport equation. Thus the strong dependence of heat diffusivity on the temperature and/or the temperature gradient is one of the candidates for the large inward convection observed in this experiment. This dependence is very useful to test some first-principle transport models such as the "critical-gradient model" including the ITG, ETG mode and $\boldsymbol{E}\times\boldsymbol{B}$ shear stabilization [5]. In the future, the effects of off-diagonal terms should be treated experimentally and theoretically.

4. Summary

The heat transport of ITB plasma in JT-60U is investigated by using cold pulse propagation induced by the pellet injection. The experimental results show 1) the ITB is a localized and reduced heat diffusivity region where the cold pulse amplitude is damped strongly, 2) the inward heat convection is dominant outside the ITB region where the cold pulse amplitude grows.

References

[1] Lopes Cardozo N. J., Plasma Phys. Control. Fusion **37**, 799 (1995).
[2] Mantica P., et al., Phys. Rev. Lett. **85**, 4534 (2000).
[3] Mantica P., et al., Plasma Phys. Control. Fusion **44**, 2185 (2002).
[4] Neudatchin S. V., et al., Plasma Phys. Control. Fusion **43**, 661 (2001).
[5] Waltz R., et al., Phys. Plasma **4**, 2482 (1997).

4.9 Relationship between Particle and Heat Transport in ITB Plasmas [1]

H. Takenaga, S. Higashijima, N. Oyama, L. G. Bruskin, Y. Koide, S. Ide, H. Shirai, Y. Sakamoto, T. Suzuki, K. W. Hill [1)], G. Rewoldt [1)], G. J. Kramer [1)], R. Nazikian [1)], T. Takizuka, T. Fujita, A. Sakasai, Y. Kamada, H. Kubo and the JT-60 Team

1) Princeton Plasma Physics Laboratory, Princeton, New Jersey, 08543-0451, U.S.A.

Optimization of the discharge scenario for attaining high density, high radiation loss fraction and high fuel purity is necessary in reversed shear (RS) and high β_p mode plasmas, in order to achieve the highly integrated plasma performance towards the ITER steady-state operation. Since these issues are closely related to the particle (bulk plasma and impurities) transport, the relationship between particle and heat transport has been systematically investigated in RS and high β_p mode plasmas.

The electron effective diffusivity defined considering only diffusion term is well correlated with the ion thermal diffusivity in the ITB region of both RS and high β_p mode plasmas. In order to understand the relationship between particle and heat transport, the particle and heat fluxes estimated based on the linear stability analysis using the FULL code are compared with the experimental value in the box-type RS plasma. The analysis result shows a positive linear growth rate at the ITB region even with sheared ExB rotation effects, indicating that the anomalous flux still remains in the ITB region. The ratio of particle flux to the electron heat flux ($\Gamma_e T_e/q_e$) is estimated to be around unity in the ITB, and the ratio drops to a value just slightly negative outside the ITB. Although the experimental profile of this ratio decreases much smoothly from around unity in the ITB to about 0.1 outside the ITB, it shows a similar tendency. The ratio of the ion anomalous conductive heat flux to the electron heat flux (q_i^a/q_e) has a similar value of 5-7 for both experiment and calculation outside the ITB. However, in the ITB region, this ratio for the calculation is much smaller than that for the experiment. A possible reason for the disagreement is that the FULL code analysis represents the linear limit based on a local theory. This effect should be investigated in a future work.

No helium and carbon accumulation inside the ITB is observed even with ion thermal diffusivity (χ_i) reduced to a neoclassical level. On the other hand, the heavy impurity argon is accumulated inside the ITB. The argon density profile estimated from the soft x-ray profile is more peaked, by a factor of 2-4 in the RS plasma and of 1.6 in the high β_p mode plasma, than the electron density profile. The helium diffusivity (D_{He}) and χ_i are at an anomalous level in the high β_p mode plasma, where D_{He} and χ_i are higher by a factor of 5-10 than the neoclassical value. In the RS plasma, D_{He} is reduced from the anomalous to the neoclassical level, together with χ_i. The carbon and argon diffusivities are estimated to be higher by a factor of 4-9 than the neoclassical value in the ITB region by assuming the neoclassical inward velocity, even when χ_i is reduced to the neoclassical level. It is noted that the inward velocity of carbon and neon has been estimated to be the same level as the neoclassical value [2]. The control method of the heavy impurity accumulation inside the ITB is discussed in 8.1.

[1] Takenaga, H., et al., in Fusion Energy 2002 (Proc. 19th Int. conf. Lyon, 2002) IAEA-CN-94-EX/C3-5Rb. submitted to Nucl. Fusion.

[2] Takenaga, H., et al., Fusion Science and Technology **42**, 327 (2002).

4.10 Responses of Internal Transport Barrier to External Perturbations

H. Takenaga, N. Oyama, L. G. Bruskin, Y. Koide, S. Ide, T. Fujita,
K. W. Hill [1], G. Rewoldt [1], G. J. Kramer [1], R. Nazikian [1]

1) Princeton Plasma Physics Laboratory, Princeton, New Jersey, 08543-0451, U.S.A.

1. Introduction

A reversed shear (RS) plasma with an internal transport barrier (ITB) is one of the most attractive operation modes for a steady-state tokamak reactor due to its high confinement and high bootstrap current fraction. In the RS plasma, ITB transport is strongly linked with density and temperature profiles, current profile, rotation/electric field profile, etc.. These linkages introduce various responses to external perturbations in the RS plasma. In order to understand these linkages, the responses to external perturbations induced by pellet and ECRF injections are investigated in this report.

2. Response to Pellet Injection

In order to investigate the ITB response to the pellet injection, pellet was injected from the high-field-side at the top into the high elongated RS plasma with a strong ITB [1]. Figure 1 shows wave-forms with the plasma current of I_p=2.2 MA and the toroidal magnetic field of B_T=4 T. The first pellet is injected at t=6.32 s (as the edge density jump is observed) during the I_p flat-top in the relatively constant density and stored energy phase. The position of the pellet penetration is estimated to be r/a=0.7-0.8, which is in the region outside the ITB. In this discharge, high frequency component of the O-mode reflectometer signal is drastically reduced by one order of magnitude, as well as the low frequency component, 6 ms after the pellet injection. The cut-off layer is located in the ITB region in this case. The central density and the stored energy start to increase from the timing of the reduction of the high frequency component. The confinement is improved from HH_{y2}=0.82 (H_{89P}=1.6) at t=6.3 s to 1.3 (2.6) at t=7 s. Figure 2 shows density and temperature profiles before (t=6.3 s) and after (t=7.0 s) the pellet injection. The density profile inside the ITB is evaluated based on the interferometer, because Thomson scattering system is not available in this region due to an inward shifted configuration with the high elongation. The density profile substantially increases inside the ITB, while the ion and electron temperature profiles are not largely changed. Particle and power balance analysis indicates reduction of effective particle diffusivity and ion thermal diffusivity (χ_i), but no reduction of electron

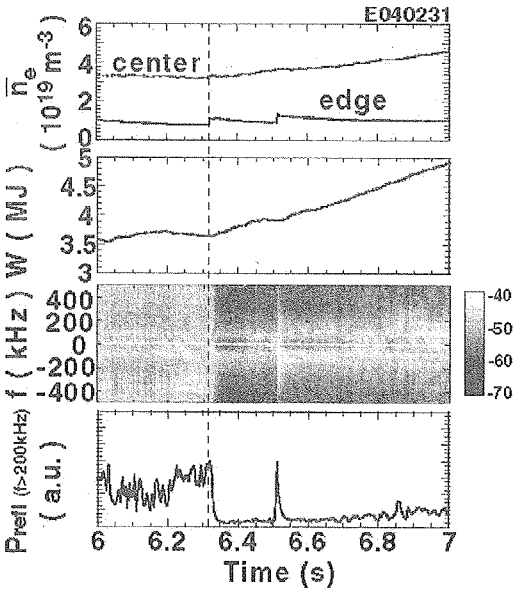

Fig. 1 Wave-forms of the RS plasma with pellet injections (I_p=2.2 MA, B_T=4 T, P_{NB}=10 MW) : density, stored energy, spectrogram of the reflectometer signal and its integral over f > 200 kHz.

thermal diffusivity (χ_e) by the pellet injection. Although the ion temperature profile does not change, χ_i is reduced to a neoclassical level after the pellet injection, because ion heat flux is reduced due to the increase of equi-partition term (ion to electron). The value of χ_e is not reduced, because the increase of dWe/dt term, which mainly comes from the density increase, is cancelled by the increase of equi-partition term. It is noted that χ_i and χ_e might not represent the transport properties in this discharge, because the temperature profiles seem to be stiffened.

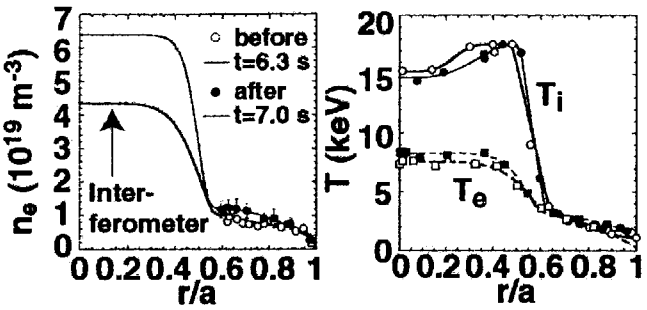

Fig. 2 Profiles of density and temperatures before (open symbols and black lines) and after (closed symbols and gray lines) the pellet injection.

The reduction of the high and low frequency components of the O-mode reflectometer signal indicates the change of density fluctuation level and/or wave number of the fluctuation. So far, the reduction of the density fluctuarion was not observed in the ITB formation phase of JT-60U RS plasma, although the reduction of the correlation length was observed [2]. In order to understand whether the confinement improvement is caused by the reduction of the density fluctuation or not, the density fluctuation level is estimated from the analytical solution of time-dependent 2D full-wave equation [3] for various poloidal and radial wave numbers (k_θ and k_r). In this analysis, the F-index defined as $F=\sigma(P)/\langle P\rangle$ is compared with the measurement, where $\sigma(P)$ and $\langle P\rangle$ are the standard deviation and the average of the total power received by the reflectometer detector. The density fluctuation is given by assuming Gaussian k spectrum. The density fluctuation is estimated to be ~1.5% before the pellet injection and ~0.5% after the pellet injection with $k_\theta=k_r=3$ cm^{-1}. Here, the wave number is determined based on the linear stability analysis using the FULL code in RS plasma. The estimated density fluctuation is consistent with the 2D full wave code calculation [4], which shows the fluctuation level of 1.3% before and 0.8% after the pellet injection. The fluctuation level changes in the range of 0.8-1.8% before and 0.3-0.6% after the pellet injection by changing k_θ=1-5 cm^{-1} and k_r =1-5 cm^{-1}. Since the detailed density profile inside the ITB is not measured in this discharge, the uncertainty of the density profile induces relatively large error range of 1.0-1.7% before and 0.4-0.7% after the pellet injection with $k_\theta=k_r=3$ cm^{-1}. These analyses indicate that the density fluctuation is reduced by the pellet injection even though the wave number changes in the range of k_θ=1-5 cm^{-1} and k_r =1-5 cm^{-1}. In these analyses, F-index is used for the fluctuation index. However, the frequency spectrum of the O-mode reflectometer signal is not correctly reproduced. Improvement of the analysis model is necessary to estimate the fluctuation level consistent with the measured frequency spectrum

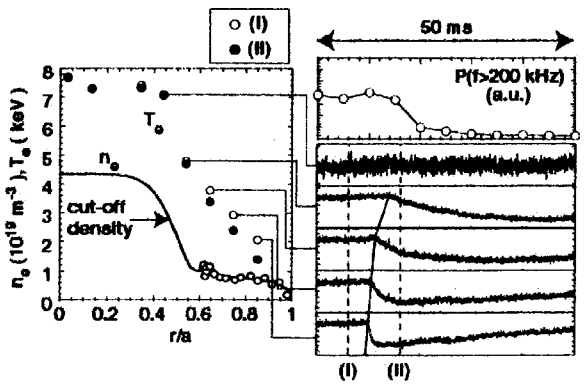

Fig. 3 Density and electron temperature profiles and time evolution of electron temperature for pellet injection.

by assuming non-Gaussian k spectrum.

Next, we discuss how the pellet injection affects the density fluctuation in the ITB. The cold pulse induced by the pellet injection propagates from the outside of the ITB into the ITB region as shown in Fig. 3. A large time delay of the cold pulse propagation is observed in the ITB region (r/a=0.5-0.6). Thus, the electron temperature gradient becomes large in the ITB, when the high frequency component is reduced. In the discharge where frequency spectrum of the O-mode reflectometer is not changed by the pellet injection, the electron temperature gradient in the ITB is not increased. The electron temperature gradient might be related to the reduction of the high frequency component. Further study is necessary to understand the mechanism responsible for the reduction of the density fluctuation based on the micro-instability theory.

3. Response to ECRF Injection

In order to investigate the ITB response to the ECRF injection, short pulse injection (~0.3 s) of ECRF was applied inside the ITB of the RS plasma with I_p=1.3 MA and B_T=3.7 T as shown in Fig. 4. The stored energy increases during the ECRF injection. The increasing rate of the stored energy (dW/dt~2.5 MW) is about 1.8 times larger than the ECRF power (P_{EC}~1.4 MW) during the ECRF injection. The stored energy increases until 0.1 s after the end of the ECRF injection, although the increasing rate decreases to 0.8 MW. This value is almost the same as ($dW/dt_{during\ EC}$-P_{EC}), indicating that higher confinement during the ECRF injection is kept until 0.1 s after the end of the ECRF injection. Then, the stored energy is kept at a constant value. The density starts to increase by the ECRF injection, and it increases even after the ECRF injection. The confinement is improved from H_{89P}=1.9 before (t=5.8 s) to 2.6 after (t=6.5 s) the ECRF injection even with the same NB heating power. The value of χ_e at the ITB after the ECRF injection is reduced by a factor of 2-3 compared with that before the ECRF injection as shown in Fig. 5. On the other hand, χ_i at the ITB is not reduced. In this discharge, the O-mode reflectometer signal from the ITB region (r/a~0.5-0.6) is not changed, indicating no reduction of the density fluctuation.

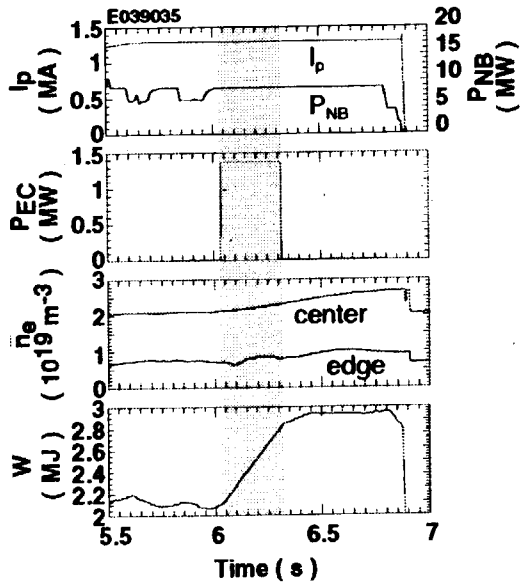

Fig. 4 Wave-forms of RS plasma with short pulse ECRF injection : plasma current and NB heating power, EC power, densities and stored energy.

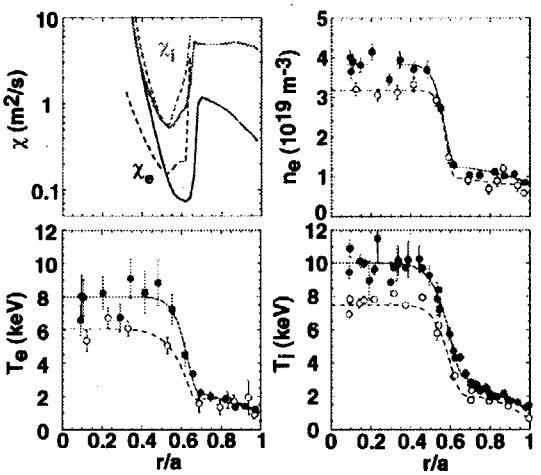

Fig. 5 Profiles of χ_i (gray) and χ_e (black), density, electron and ion temperatures. Open symbols and dashed lines show the data before the ECRF injection. Closed symbols and solid lines show the data after the ECRF injection.

In order to investigate heating power dependence of the confinement improvement, the background NB power and the ECRF injection power are scanned in the hydrogen RS plasma. ECRF (P_{EC}=2.5 MW) is first injected with the background NB power of P_{NB}=7.5 and 6.0 MW. The stored energy stays constant until collapse with P_{NB}=7.5 MW and decreases with P_{NB}=6.0 MW after the ECRF injection. In order to keep the constant stored energy after the ECRF injection, sufficient background heating is necessary.

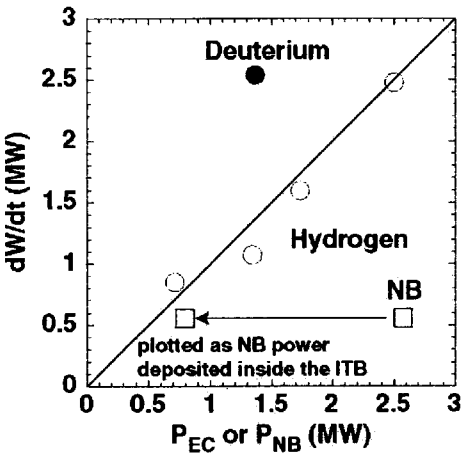

Fig. 6 Relationship between stored energy increasing rate and injection power of ECRF or NB.

Next, P_{EC} is scanned from P_{EC}=0.7 to 2.5 MW with P_{NB}=7.5 MW. The value of dW/dt is almost proportional to P_{EC} in the hydrogen plasma as shown in Fig. 6. In these discharges, the stored energy is kept at constant value after the ECRF injection. Therefore, there is no threshold value of P_{EC} for the confinement improvement. In the discharge with a short NB pulse (=0.3 s), dW/dt is smaller than that in the ECRF injected discharge. However, dependence of dW/dt on the heating power deposited inside the ITB is similar.

The reduction of the high frequency component of the O-mode reflectometer signal is observed, when ECRF is injected in the hydrogen RS plasma. In the cases with P_{EC}=1.7 and 1.3 MW, the high frequency component is quickly reduced during the ECRF injection. On the other hand, the high frequency component is gradually reduced with P_{EC}=0.7 and 2.5 MW. Different behavior of the O-mode reflectometer signal seems to be related to the confinement improvement of the background plasma. However, systematic understanding has not been obtained yet.

4. Summary

Responses to the external perturbations induced by pellet and ECRF injections are studied in the RS plasma. The high frequency component of the O-mode reflectometer signal is reduced by a pellet injection, and the density substantially increases inside the ITB without a large change of temperature. The stored energy increases during the ECRF injection and stays constant after the ECRF injection. The value of dW/dt is larger than the ECRF power in the deuterium plasma and is almost the same as the ECRF power in the hydrogen plasma. In order to understand the physical mechanisms of the responses through the linkages between ITB transport and plasma parameters, further study is necessary based on the micro-instability theory.

References

[1] Takenaga, H., et al., in Fusion Energy 2002 (Proc. 19th Int. conf. Lyon, 2002) IAEA-CN-94-EX/C3-5Rb. submitted to Nucl. Fusion.

[2] Nazikian, R., et al., in Fusion Energy (Proc. 17th Int. Conf. Yokohama) **Vol4**, 1689 (1998).

[3] Bruskin, L. G., et al., Plasma Phys. Control. Fusion **44**, 2305 (2002).

[4] VALEO, E. J., et al., Plasma Phys. Control. Fusion **44**, L1 (2002).

4.11 Particle Transport during Electron Cyclotron Heating

H. Takenaga, N. Oyama, S. Ide

1. Introduction

Density clamp by electron cyclotron heating (ECH) is a common phenomenon in torus plasmas for both tokamak and helical devices [1, 2]. During the density clamp caused by the center deposited ECH, the electron density profile changes from peaked one to flat or hollow one. In JFT-2M, the density clamp has been explained by the extra outward particle flux induced by ECH at the deposition layer [3]. This extra outward particle flux is not ascribed to the off-diagonal flux term depending on the electron temperature and its gradient. Several theoretical models have been proposed as candidates for physical mechanism of the density clamp [4]. However, the mechanism providing the extra outward particle flux has not been understood well. The density clamp has been observed clearly in small and medium size machines. Recently, clear density clamp was observed in the plasmas with internal transport barriers (ITBs) [5] accompanied with relaxation of heavy impurity accumulation even in the large machines. On the other hand, the density clamp is not clear in the ECH plasmas without ITB on the large machines. It is important for understanding of the physical mechanism of the density clamp to investigate whether clear density clamp occurs in the ECH plasmas without ITB on the large tokamak of JT-60U or not.

In this report, the particle transport during ECH is discussed. The experimental results are described in Section 2, where time behavior of the line averaged electron density and the density profile during ECH are discussed. The particle transport simulation is performed in Section 3 in order to understand the observed time behavior of the electron density. Section 4 is a summary.

2. Experimental Results

In order to identify the density range, where the density decreases by applying ECH, the density scan was performed in the ECH plasmas at I_p=1.2 MA and B_T=3.7 T. Hydrogen gas-puffing was used for plasma break down, and He gas-puffing was used to increase the density because the density is easily kept at constant value after short pulse He gas-puffing. ECH was applied in the plasma center (r/a~0.1) in a current drive mode at the toroidal injection angle of 20 degree.

Figure 1 shows the wave-forms for (a) high density ($\bar{n}_e/n_{GW}$=0.46, where $\bar{n}_e$ is the line averaged electron density and n_{GW} is Greenwald density) and (b) low density ($\bar{n}_e/n_{GW}$=0.36) cases. In the high density case, $\bar{n}_e$ increases first by applying ECH, and then $\bar{n}_e$ starts to decrease at 0.2 s after the start of ECH. The density decreases by about 4% during ECH compared with that before ECH. After ECH is switched off, $\bar{n}_e$ recovers to the same level as that before ECH. In this discharge, the plasma position moves inward by 1-2 cm during ECH, however, the effect of the plasma movement on $\bar{n}_e$ is smaller than 1%. Therefore, the decrease of $\bar{n}_e$ could be ascribed to the change of particle transport during ECH. In the low density case, $\bar{n}_e$ increases during the ECH, and continues to increase until 0.2 s after ECH. The Hα emission increases during ECH, indicating enhancement of recycling probably due to the increase of

heat load onto the divertor plates and/or first wall. Therefore, even if the density decreases during ECH, the decrease of the density might be masked by the increase of the density due to the enhancement of the recycling. In the high density case, the Hα emission also enhanced. However, the effects of enhanced recycling could be small in the high density case compared with the low density case, because the contribution of the electron source from He is larger in the high density case.

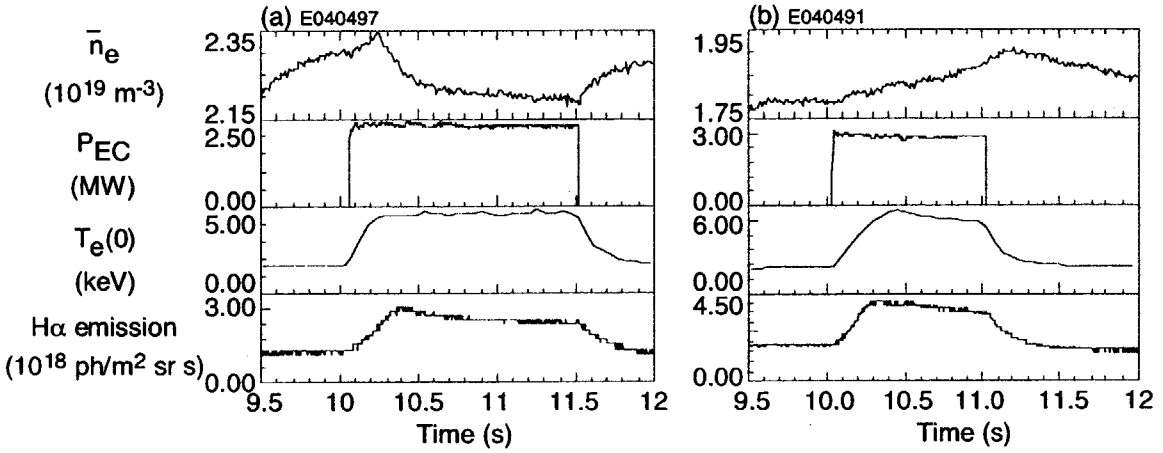

Fig. 1 Wave-forms of the ECH plasmas for (a) high and (b) low density cases : line averaged electron density ($\bar{n}_e$), EC power (P_{EC}), central electron temperature ($T_e(0)$) and Hα emission.

Figure 2 shows the dependence of the difference ($\Delta\bar{n}_e$) in $\bar{n}_e$ before and during ECH on the target $\bar{n}_e$ before ECH. The positive value means the increase of $\bar{n}_e$ during ECH. The value of $\Delta\bar{n}_e$ decreases with increasing the target $\bar{n}_e$. The negative value of $\Delta\bar{n}_e$ (decrease in $\bar{n}_e$) is observed only in the relatively high density range of $\bar{n}_e > 2\times10^{19}$ m^{-3}. In this data-set, data with the EC power (P_{EC}) of 1.1-2.6 MW are included. However, EC power dependence of $\Delta\bar{n}_e$ is weak.

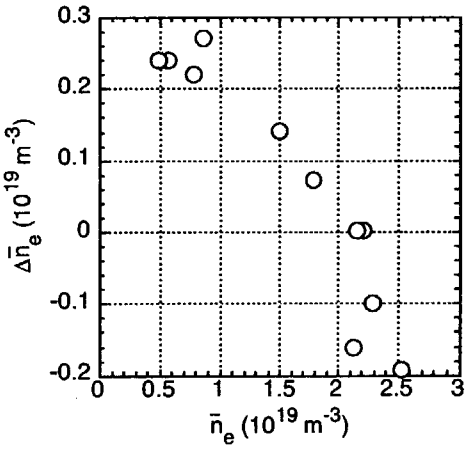

Fig. 2 Dependence of difference in the density before and during ECH on the target density before ECH.

The density profiles of the discharge with a largest decrease in $\bar{n}_e$ are shown in Fig. 3 together with the calculated EC deposition profile. The density increases in the central region during ECH compared with that before ECH, while the density decreases in the region of r/a=0.5-0.9. After ECH, the density profile recovers to the same shape as that before ECH. The position of ECH is in the range of r/a<0.2 as shown in Fig. 3. The particle transport outside the ECH deposition layer is changed, indicating that the profile change can not be explained by the extra outward particle flux induced at the ECH deposition layer. This result suggests that the mechanism of the decrease of the density observed here is different from that of the density clamp observed in the small or medium size machines.

Figure 4 shows the time evolution of the electron density in the same discharge in Fig. 3. In the central region of r/a<0.4, the electron density increases first, and then gradually

decreases. In the region of r/a=0.6-0.9, the electron density decreases during ECH, and it recovers after ECH is switched off. The time scale of the electron density recovery seems to be longer compared with the time scale of the central density increase during the on-set phase of ECH. In fact, $\bar{n}_e$ also recovers slowly after ECH in this discharge, although $\bar{n}_e$ quickly recovers in the discharge shown in Fig 1 (a). In small or medium size machines, the central density decreases by applying the ECH and the density profile becomes flat or hollow. The time evolution of the electron density profile exhibits different features from the density clamp observed in small or medium size machines.

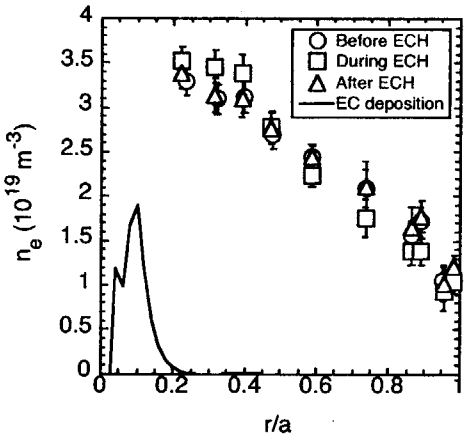

Fig. 3 Density profile before, during and after ECH. The deposition profile of ECH is also plotted.

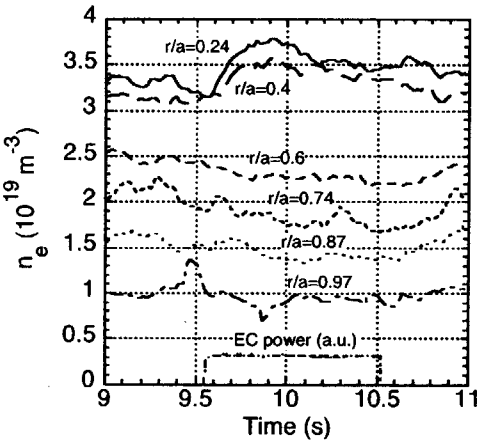

Fig. 4 Time evolution of the electron density. The ECH power is also shown in this figure.

3. Simulation of Particle Transport

In order to understand the time behavior of the electron density profile, particle transport is simulated using the simple model, where spatially constant diffusion coefficient (D) is assumed. The convection velocity (v) is determined to satisfy the measured electron density profile with the spatially constant diffusion coefficient in the steady-state phases before and during ECH. The diffusion coefficient is assumed to be the same value for both before and during ECH. The edge localized particle source is only considered in this simulation. The source rate is adjusted to fit the calculation to measurement in the steady-state phase. The profiles of v before and during ECH estimated by assuming D=0.5 m^2/s are shown in Fig. 5. The positive side means the inward convection velocity. The inward convection velocity during ECH is smaller in the range of r/a=0.15-0.35 and 0.65-0.8, and larger in the range of r/a=0.35-0.65 than that before ECH. The convection velocity in the regions outside the deposition layer of ECH is changed.

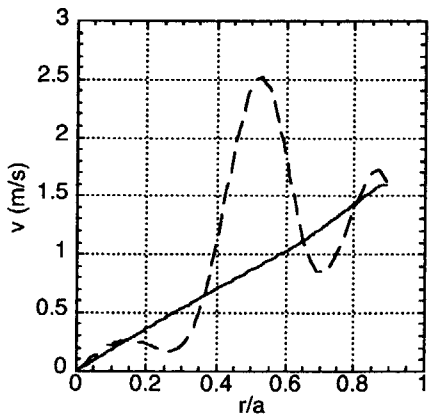

Fig. 5 Profile of the inward convection velocity before (solid line) and during (dashed line) ECH with D=0.5 m^2/s.

In order to check the consistency of the estimated particle transport coefficients with the experimental results, the time evolution of the

density is calculated with (a) D=1 m^2/s, (b) D=0.5 m^2/s and (c) D=0.1 m^2/s as shown in Fig. 6. In these figures, v during ECH is used in the range of 1-2 s, and v before ECH is used in other range. In the case of D=1 m^2/s, the central density increases first, and then decreases, while the electron density decreases in the range of r/a=0.6-1.0. This result is similar to the experiment, however, the time scale of the density change seems to be small compared with the experiments. In the case of D=0.5 m^2/s, the central density also increases first, and then decreases, and the electron density decreases in the range of r/a=0.6-1.0 as well as the case of D=1.0 m^2/s. The time scale for the electron density change seems to be similar to the experimental results. In the case of D=0.1 m^2/s, the central density continues to increase during ECH. The time scale of the electron density is larger than the experiments. The particle transport simulation with D=0.5 m^2/s seem to be consistent with the time behavior of electron density. However, in this report, the comparison between the simulation and the experiment is limited to qualitative discussion. Further study is necessary for quantitative comparison between the simulation and the experiment.

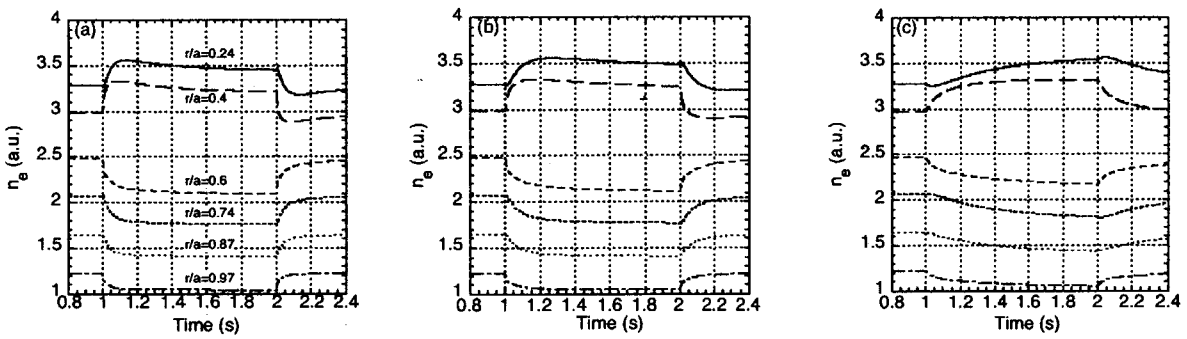

Fig. 6 Time evolution of simulated electron density with (a) D=1 m^2/s, (b) 0.5 m^2/s and (c) 0.1 m^2/s.

4. Summary

The decrease of the line averaged density is observed during ECH in the relatively high density region. The central density increases, while the density in the region of r/a=0.5-0.9 decreases. This change of the density profile is different from the density clamp observed in the small or medium size machines, where the density profile becomes flat or hollow. The time evolution of the density is consistent with the particle transport simulation, where the inward convection velocity during ECH being smaller in the range of r/a=0.15-0.35 and r/a=0.65-0.8 and larger in the rage of r/a=0.35-0.65 than that before ECH is used with the spatially constant diffusion coefficient of about 0.5 m^2/s.

References

[1] La Haye, R.J., et al., Nucl. Fusion **21**, 1425 (1981).
[2] Zushi, H., et al., Nucl. Fusion **28**, 1801 (1988).
[3] Nagashima, K., et al., Nucl. Fusion **35**, 994 (1995).
[4] Hsu, J.K., et al., Phys. Rev. Lett. **53**, 564 (1984).
[5] Takenaga, H., et al., in Fusion Energy 2002 (Proc. 19th Int. conf. Lyon, 2002) IAEA-CN-94-EX/C3-5Rb. submitted to Nucl. Fusion.

4.12 Influence of the Maxwell Stress on the Zonal Flow Formation in JT-60U Reversed Shear Plasmas [1]

T. Fukuda, M. Wakatani [1] and T. Fujita
1) Graduate School of Engineering, Kyoto Univ., Uji 611-0011, Japan

An exploratory control of transport barriers using the perturbative schemes has been undertaken in JT-60U, where the possible enhancement of Maxwell stress component was envisaged by the externally induced non-resonant magnetic fluctuations. The suggested approach might be applied in steady-state burning plasmas with internal transport barriers (ITBs), where the external heating fraction is small and electron heating is predominant.

Although the direct control of ITB quality by the modification of the toroidal torque input and heating power has been demonstrated in JT-60U[2], it is necessary to develop an advanced scheme in burning plasmas, where the profiles are self-organized in steady-state with a considerably high bootstrap current fraction (f_{BS}) with ITB, and the contribution of external heating is much less dominant. An perturbative control techniques have been explored in JT-60U, one of which considers the enhancement of Maxwell stress. Ref. 3 indicates that the Maxwell stress term and viscous diffusion makes converse contributions to the Reynolds stress in the poloidal flow evolution equation, as described below.

$$\frac{\partial}{\partial t}\langle V_\theta \rangle = -\frac{1}{r^2}\frac{\partial}{\partial r}(r^2\langle \tilde{V}_r \tilde{V}_\theta \rangle) + \frac{1}{r^2}\frac{\partial}{\partial r}\left(\frac{r^2}{\hat{\beta}}\langle \tilde{B}_r \tilde{B}_\theta \rangle\right) + \mu\frac{\partial}{\partial r}\left(\frac{1}{r}\frac{\partial}{\partial r}\langle rV_\theta \rangle\right). \quad (1)$$

The first term in the right hand side of eq. (1) is the Reynolds stress, whereas the second term is the Maxwell stress. The last term is the contribution from the viscous diffusion. It should be noted here that the first two terms have opposite signs to each other. Here, $\hat{\beta} = \{nT_e/(B_t^2/\mu_o)\}(R^2/a^2)$.

A dedicated experiment has been performed in JT-60U, where a train of pulsed non-resonant asymmetrical 2/1 magnetic perturbation was externally applied to the reversed shear (RS) plasmas at the time when ITBs were reproducibly formed. The applied magnetic field was around 40 gauss near the location of ITB, which is approximately a factor of 2-3 smaller than the poloidal component of the equilibrium magnetic field. Although it was not possible to completely suppress the ITB formation, reduction in T_{io} and local maximum of L_{Ti}^{-1} was observed, seemingly due to slower inward penetration of the magnetic field, which might result in the reduction of perturbation intensity. Here, L_{Ti} stands for the characteristic length of the T_i gradient. On the other hand, the application of static field did not provide as much effect. In addition, the influence of resonant magnetic fluctuations on the ITB formation still remains to be resolved in the future experimental campaign.

References

[1] Fukuda, T. et al., Plasma Phys. Control. Fusion **44**, 39 (2002).
[2] Sakamoto, Y. et al., Nucl. Fusion **41**, 865 (2001).
[3] Carreras, B. A. et al., Phys. Fluids B **5**, 1491 (1993).

4.13 Validation of the Asymmetric Pressure Perturbation Model for the Active Control of Sheared E×B Flow in Steady-state Burning Plasmas with ITB [1]

T. Fukuda, M. Wakatani [1)], H. Takenaga and N. Oyama
1) Graduate School of Engineering, Kyoto Univ., Uji 611-0011, Japan

An extensive investigation on the active control of transport barriers in steady-state burning plasmas using the perturbative schemes has been suggested for validation in JT-60U, besides the enhancement of Maxwell stress described in the previous subsection. The alternative scheme herein introduced is to apply the pressure perturbation, based on the assumption that the zonal flow might couple with the Pfirsch-Schlüter flow via the toroidal curvature. The interaction of the zonal flow with the geodesic acoustic mode can also be considered at the time of ITB formation. The assumed model is based on the equation below [2].

$$\frac{\partial}{\partial t}\left\{\frac{1}{2}\langle V_\theta\rangle^2\right\} = \left\{\langle\Omega\rangle\langle V_r V_\theta\rangle\right\} - \omega_B\left\{\langle P\sin\xi\rangle\langle V_r V_\theta\rangle\right\}. \quad (1)$$

The left hand side of the equation is the time derivative of the kinetic energy of zonal flow, and the first term in the right hand side is the Reynolds stress term. Here, $<\Omega>=<\partial V_\theta/\partial r>$, ξ is the poloidal angle and ω_B is the toroidal drift frequency. It should be noted here in eq. (1) that $P\sin\xi$ term changes its sign above and below the equatorial plane. Therefore, up and down asymmetry in the pressure perturbation can either enhance or suppress the formation and sustainment of sheared E×B flow depending the sign of $<P\sin\xi>$. It is noteworthy that enhancement of the Maxwell stress only suppresses or degrades the ITB on the contrary. An exploratory experiment to validate the above model has also been recently performed in JT-60U. During an increase of NB heating power at the current ramp, the value of ρ_s/L_{Ti} increases slowly, and it suddenly start to increase rapidly at the time of ITB formation when it reaches the critical value of 1.6×10^{-2}, close to the number evaluated in JET. Here, ρ_s represents the sound Larmor radius. Right after the injection of the first pellet from the HFS top, the stored energy continuously increased significantly and ρ_s/L_{Ti} further increases, whilst the NB heating power was kept constant. The broadband density fluctuations at ITB is often reduced in a few 100 μs, which is much faster than the characteristic time of the profile evolution in JT-60U, though the influence of local changes in n_e and T_e gradient is possible. On the other hand, the pulsed heavy gas puff from the top degraded the ITB quality, accompanied by the momentary increase of the collisionality. The ITB quality is soon recovered in terms of L_{Ti}^{-1}, however, the ITB radius is shrank and the global stability is degraded, which may be related to the collisional damping of the **E×B** flow. However, the different effect of the HFS top and equatorial plane pellet injection was not observed, possibly related to the practical difficulties involved in inducing the asymmetric perturbations on the flux surface.

References

[1] Fukuda, T. et al., Plasma Phys. Control. Fusion **44**, 39 (2002).
[2] Lin, Z. et al., Phys. Plasmas 7, 1857 (2000).

4.14 Burning Plasma Simulation and Burn Control Trial in Reversed Shear Plasma

H. Takenaga, N. Oyama, S. Ide, I. Yonekawa, Y. Kawamata, M. Sueoka,
Y. Koide, T. Fukuda, T. Fujita

1. Introduction

Reversed shear (RS) plasma with internal transport barriers (ITBs) is one of the most attractive operation modes for an advanced steady-state tokamak operation. In the RS plasma, confinement improvement is closely linked with heating power, where the confinement is improved by increasing the heating power. Higher heating power often leads to disruption or high β collapse due to large pressure gradient at the ITB. Therefore, the ITB control is necessary to sustain the ITB. In the present non-burning plasma, the ITB is mainly controlled by the external heating power, where the heating power is increased to make the ITB stronger or is decreased to make the ITB weaker. On the other hand, in a burning plasma with a high fusion gain, it is difficult to control the ITB by the external heating power, because α particle heating is dominant. In addition, since the confinement improvement leads to the increase of α particle heating power in the burning plasma, the loop between the confinement improvement and the increase of α particle heating is expected to cause disruption or high β collapse in the burning RS plasma. Therefore, it is important to develop the ITB control method for breaking this loop in the burning RS plasma.

In order to investigate the ITB controllability in the burning plasma, the burning plasma simulation scheme is developed. In this scheme, the heating power being proportional to the DD neutron yield rate is applied using the real-time feedback control system for the simulation of α particle heating. This burning plasma simulation is applied to the RS plasma, and the ITB control with a small fraction of the external heating power is tried. The ITB control by momentum input using the tangential NB has been demonstrated in JT-60U [1]. However, it is difficult to use the momentum input for the ITB control in a fusion reactor, because high power input is necessary to control the ITB by the momentum input. The burn control due to the increase of radiation loss inside the ITB and/or dilution by impurity injection can be considered as one of the ITB control methods. Ar accumulation inside the ITB and enhancement of the radiation loss in the main plasma by Ar gas-puffing have been observed in JT-60U [2, 3]. In fact, the decrease of the neutron yield rate has been observed by Ar gas-puffing. On the other hand, Ne is not accumulated inside the ITB and the divertor radiation loss is enhanced by Ne gas-puffing. Therefore, the Ar gas-puffing is expected to be effective for the burn control.

In this report, first results of burning plasma simulation and burn control trial in the RS plasma are discussed. In Section 2, the burning plasma simulation scheme is described together with typical examples in the RS plasma. Ar gas-puffing is applied into the RS plasma

with the burning plasma simulation in Section 3. Section 4 is a summary.

2. Burning Plasma Simulation

In order to simulate a burning plasma, two groups of NB (A and B) are used. Figure 1 shows burning plasma simulation scheme. The NB input power for group A (P_{NB}^{A}) is controlled proportionally to the DD neutron yield rate (S_n) using the real-time control system for the simulation of α particle heating. The value of P_{NB}^{A} is determined as $P_{NB}^{A}=\alpha\times S_n$, where α is the proportional gain. The NB input power of group B (P_{NB}^{B}) is determined by the preprogramming value for the simulation of the external heating. The fusion gain (Q) is defined as $Q=5\times P_{NB}^{A}/P_{NB}^{B}$ in the burning plasma simulation. In this scheme, the dependence of DT fusion reaction rate on the ion temperature and DT density ratio is not considered. Only the loop of the confinement improvement and the increase of heating power is simulated. Since beam-thermal neutron yield gives a large contribution to the total DD neutron yield, the linkage of the loop becomes stronger than that in the real DD burning plasma, where thermal-thermal neutron yield is dominant.

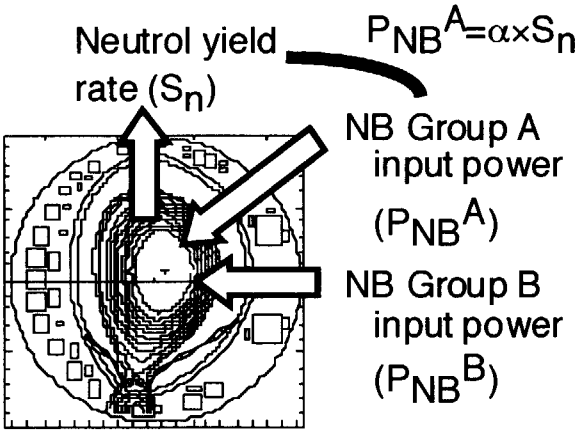

Fig. 1 Illustration of burning plasma simulation scheme.

This scheme is applied to the RS plasma with I_p=1.0 MA and B_T=3.73 T. Figure 2 shows typical wave-forms of the burn simulated plasmas. The S_n proportional control of group A NB heating power was applied from t=5 s with P_{NB}^{B}=3.8 MW after the formation of the ITB. In the case (a) with a small proportional gain ($\alpha=1.6\times10^{15}$), the constant NB power (P_{NB}^{A}=5.1 MW and P_{NB}^{B}=3.8 MW : Q=6.67) is injected even during the S_n proportional control phase. The stored energy and the line averaged electron density are kept at a constant value. In this case, the linkage of the loop for the confinement improvement and the increase of the heating power is weak due to the small proportional gain. Therefore, the heating power is kept at constant value.

On the other hand, in the case (b) with a large proportional gain ($\alpha=2.7\times10^{15}$), P_{NB}^{A} is increased from 5.1 MW at Q=6.67 to 10.7 MW, which is limited by number of applied NB units, at Q=14 with increasing the neutron yield rate. The stored energy and the line averaged electron density increase until the disruption. In this case, the linkage of the loop for the confinement improvement and the increase of heating power is strong. Therefore, once heating power is increased, the confinement is improved and the neutron yield rate is increased. Then, P_{NB}^{A} is increased until the limitation. The strong ITB is produced by this loop, and plasma is disrupted. The linkage of the confinement improvement and the increase of the

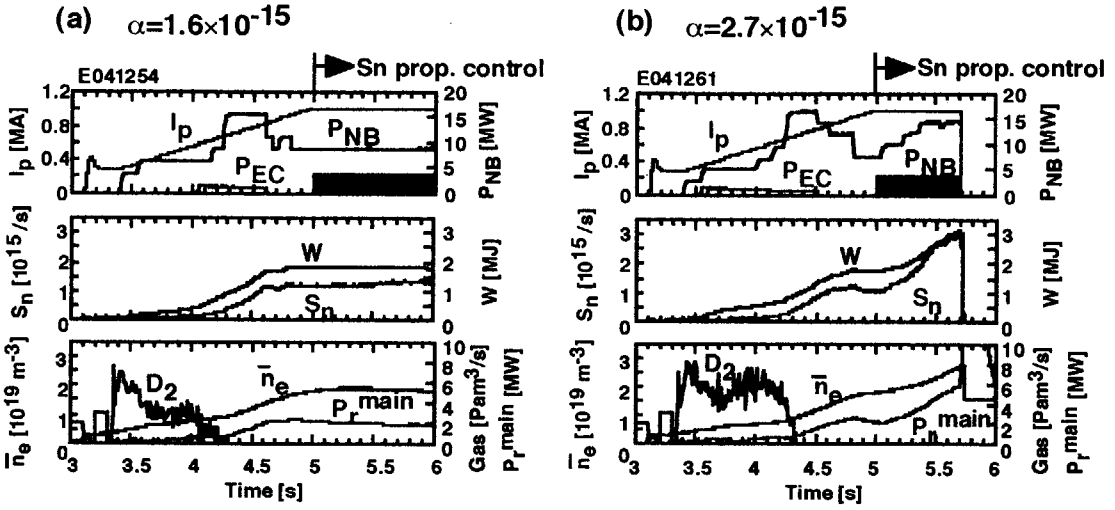

Fig. 2 Typical wave-forms of the burn simulated plasmas with (a) a small proportional gain and (b) a large proportional gain. Upper figures : plasma current (I_p), ECH power (P_{EC}), NB heating power (P_{NB}), filled area shows preprogramming NB power. Middle figures : neutron yield rate (S_n), stored energy (W). Bottom figures : line averaged density ($\bar{n}_e$), gas-puffing rate for D_2 gas and radiation loss power in the main plasma (P_r^{main}).

heating power can be simulated with the large proportional gain.

3. Trial of Burn Control by Using Ar Gas-Puffing

Ar gas-puffing is applied in the case with $\alpha=2.7\times10^{-15}$ to suppress the increase of NB power and disruption as shown in Fig. 3. The Ar gas-puffing was applied simultaneously with the S_n proportional control at t=5 s. However, the radiation loss in the main plasma starts to increase 250-300 ms after the Ar gas-puffing due to a time delay of the Ar gas-puffing from the gas valve to the vacuum vessel. In these discharges, $P_{NB}{}^B$ is also set to be 3.8 MW. With Ar gas-puffing of 5 Pam^3/s×0.15 s, the increase of NB power is not suppressed. The value of $P_{NB}{}^A$ is quickly increased from 5.1 MW to 14.1 MW (Q=19) and disruption occurred at t=5.5 s. The radiation loss in the main plasma is increased from 3 to 7 MW by Ar gas-puffing. However, the increase of $P_{NB}{}^A$ is faster than the increase of the radiation loss in the main plasma. The increase of $P_{NB}{}^A$ is faster than that in the discharge shown in Fig. 2 (b) without Ar gas-puffing even with the same proportional gain. The linkage of the confinement improvement and the increase of the heating power could be stronger in this discharge. The burn control by Ar gas-puffing is insufficient for the ITB control in this discharge.

With Ar puffing of 5.8 Pam^3/s×0.15 s, disruption is occurred before the increase of the heating power. In this discharge, the radiation loss in the main plasma quickly increases. Thus, the disruption seems to be caused by Ar gas-puffing in this case. Sufficient burn control by Ar gas-puffing has not been achieved yet. Further optimization of Ar gas-puffing scenario

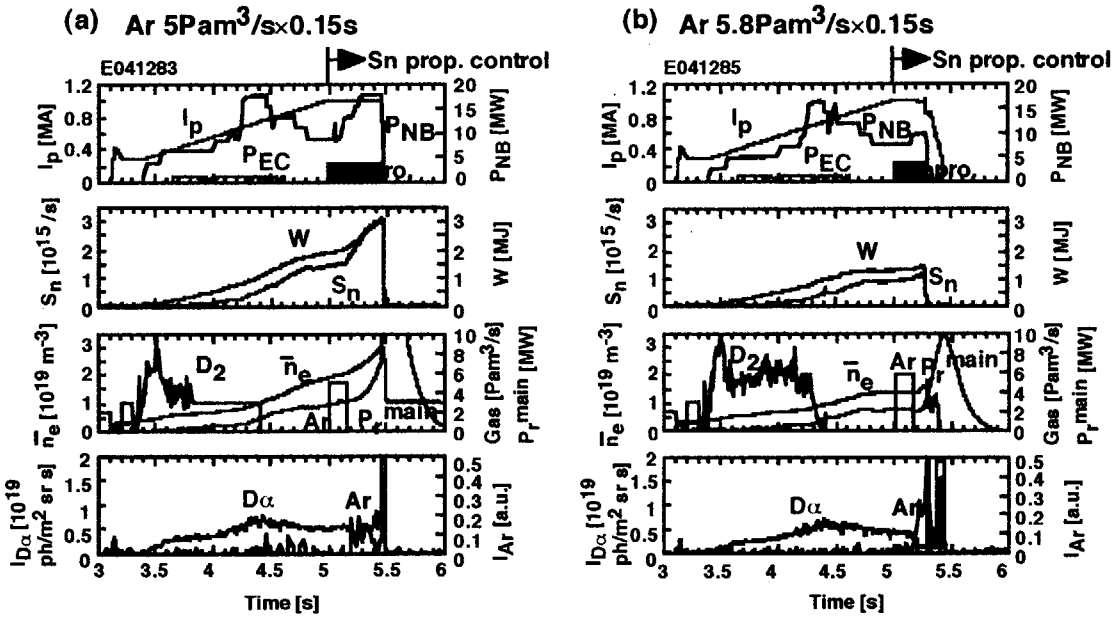

Fig. 3 Typical wave-forms of burn control trial with Ar puffing of (a) 5 Pam³/s×0.15 s and (b) 5.8 Pam³/s×0.15 s. First column : plasma current (I_p), ECH power (P_{EC}), NB heating power (P_{NB}), filled area shows preprogramming NB power. Second column : neutron yield rate (S_n), stored energy (W). Third column : line averaged density ($\bar{n}_e$), gas-puffing rate for D_2 and Ar gases and radiation loss power in the main plasma (P_r^{main}). Bottom column : Dα and Ar emissions.

(puffing rate and timing) is necessary considering the time delay of Ar gas-puffing to develop the burn control by using Ar gas-puffing.

4. Summary

Burning plasma simulation is applied to the RS plasma, where the heating power of the group A is proportional to the DD neutron yield rate and the heating power of the group B is preprogrammed. With the proportional gain of $\alpha=2.7\times10^{-15}$, the plasma is disrupted by the loop of the confinement improvement and the increase of the heating power. In order to suppress the increase of the heating power and disruption, burn control by Ar gas-puffing is applied for enhancement of the radiation loss in the main plasma and dilution. However, sufficient burn control has not been achieved. Further optimization of Ar gas-puffing scenario is necessary to develop the burn control method.

References

[1] Sakamoto, Y., et al., Nucl. Fusion **41**, 865 (2001).

[2] Takenaga, H., et al., in Fusion Energy 2002 (Proc. 19th Int. conf. Lyon, 2002) IAEA-CN-94-EX/C3-5Rb. submitted to Nucl. Fusion.

[3] Kubo, H., et al., accepted in J. Nucl. Mater.

4.15 Perturbative Transport using Modulated ECH

A. Isayama and S. Inagaki [1)]
1) National Institute for Fusion Science

1. Introduction

Perturbative transport experiments provide useful information on the properties of the confined plasma. For evaluation of the heat diffusivity, various transient phenomena have been utilized such as heat propagation by a sawtooth crash and cold pulse propagation by pellet injection [1, 2]. Among them, heat wave propagation by modulated electron cyclotron heating (MECH) has advantages that electrons are predominantly heated and that the heating location can be limited in a narrow region. So far, systematic experiment, in particular MECH in NB-heated plasmas, was not previously performed in JT-60U. In this section first result on MECH experiment in NB-heated plasmas performed in 2002 is described.

2. Experiment

Typical waveforms and plasma shape of an MECH experiment are shown in Fig. 1, where plasma parameters are as follows: I_p=1 MA, B_t=3.7 T, R=3.32 m, a=0.88 m, q_{95}=7.4. Line-averaged electron density before MECH is about 1×10^{19} m^{-3}. The central safety factor is kept above unity to avoid sawtooth oscillations. As shown in Fig. 1, MECH of ~0.7 MW was injected at t=3.5 s, when electron density and stored energy became almost stationary after the NB injection of 13 MW. According to a ray tracing code, EC is deposited at ρ=0.1 with the full-width half-maximum of $\Delta\rho$~0.05. In order to observe the heat wave propagation in wider region, modulation frequency f_0 is set at 12.2 Hz, which corresponds to about twice as large as energy confinement time.

Time evolution of electron temperature measured with the 20-channel ECE grating polychromator [3] is shown in Fig. 2. Temperature oscillations due to MECH are clearly observed. Typically, perturbations were observed at $\rho \lesssim 0.4$ in this series of discharges. Heat wave propagation was investigated by Fourier-transforming the ECE signals. Spectrum at ρ~0.25 in shot E41745 is shown in Fig. 3. It can be seen that there is a sharp peak at 12.2 Hz corresponding to the perturbation by MECH. Note that in obtaining the spectrum ECE data at 3.70-4.03s, which corresponds to 16384 data points, are used for the FFT. Profiles of amplitude and phase at the MECH frequency are shown in Fig. 4. In this figure, profiles for low NB power (P_{NB}=4.6 MW; E41742) are also shown. It can be seen that in both cases amplitude decreases and phase delay increases with increasing the distance from the deposition location, which shows the diffusive property. Amplitude of the perturbation in E41742 is about twice as large as that in shot E41745. On the other hand, phase profile is almost identical in all cases.

3. Analysis

Heat diffusivity in the cylindrical geometry evaluated from heat wave propagation, χ_e^{HP}, is described as [4]:

$$\chi_e^{HP}=\frac{(3/4)\omega}{\varphi'(A'/A+1/2r-1/2r_n)}$$

Here, A and φ are the amplitude and phase of T_e at f_0, respectively. X' denotes differentiation of variable X with respect to r, and $\omega=2\pi f_0$, $r_n=-n_e/\nabla n_e$. Note that contribution of convective term is assumed to be small and ignored in the above expression. Profiles of χ_e^{HP} in shots E41742 and E41745 are shown in Fig. 5. It can be seen that the value of χ_e^{HP} is in the range of 1 to 5, and that no significant dependence on NB injection power is observed. Heat diffusivity derived by using the TOPICS code, χ_e^{PB}, which corresponds to the diffusivity at steady state is also shown in Fig. 5. The value of χ_e^{PB} is in the range of 0.6 to 2, and also no significant dependence on NB power is observed. The ratio χ_e^{HP}/χ_e^{PB} is in the range of 1-6($\geq$1). In some devices, it has been reported that heat diffusivity significantly increases above a critical value of the inverse scale length of electron temperature $L_{T_e}^{-1}=\nabla T_e/T_e$ [5]. In the above dataset, however, no significant dependence of χ_e^{HP} and χ_e^{PB} on $L_{T_e}^{-1}$ was observed.

4. Summary

Perturbative transport experiment in NB-heated plasmas using MECH was performed. Heat wave propagation at different NB power was investigated. It was found that heat diffusivity was in an order of 10^{-1} to 1 in all cases. Comparing χ_e^{HP} with χ_e^{PB}, χ_e^{HP} was larger than χ_e^{PB} by a factor of 1 to 6.

References

[1] Lopes Cardozo N J, Plasma Phys. Control. Fusion **37**, 799 (1995).

[2] Inagaki S, *et al.*, this review, section 4.8.

[3] Isayama A, *et al.*, Rev. Sci. Instrum. **73**, 1165 (2002).

[4] Jacchia A, *et al.*, Phys. Fluids B **3**, 3033 (1991).

[5] Ryter F, *et al.*, Nucl. Fusion **41**, 537 (2001).

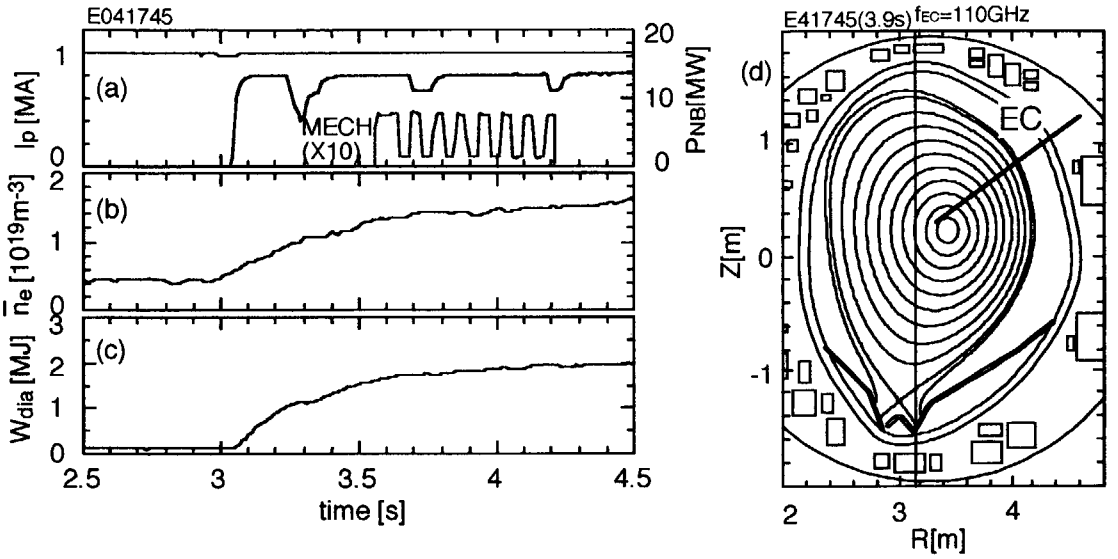

Fig. 1: Typical waveform of a modulated ECH experiment: (a) plasma current, NB power and MECH power; (b) line-averaged electron density; (c) stored energy; (d) plasma shape and ray of EC wave.

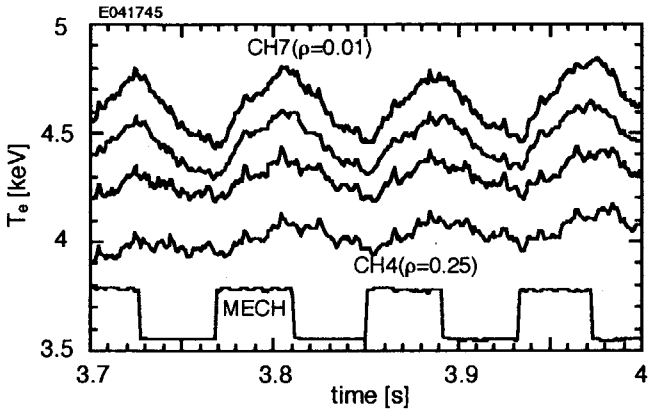

Fig. 2: Time evolution of electron temperature

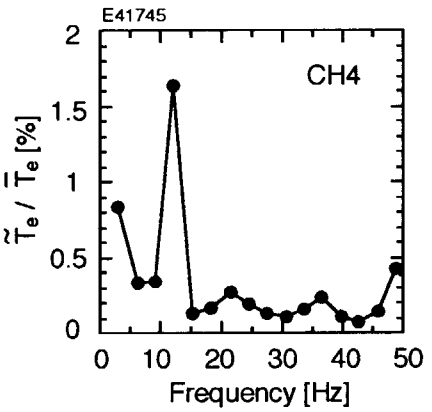

Fig. 3: Power spectrum of electron temperature perturbation at channel 4.

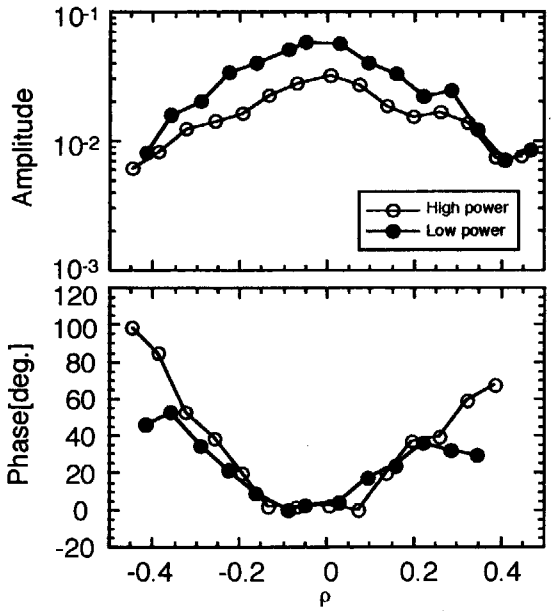

Fig. 4: Profiles of (a) amplitude and (b) phase at 12.2 Hz.

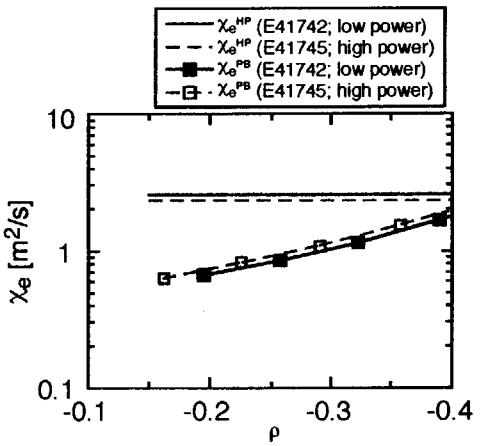

Fig. 5: Profiles of heat diffusivity.

5. Improved Confinement at High Density and H-mode Pedestal

5.1 Influence of Ar Puff on High Density ELMy H-mode Plasmas

N. Asakura, S. Higashijima, K. W. Hill[1)], H. Kubo, Y. Miura, T. Nakano, S. Konoshima, K. Itami, S. Sakurai, H. Takenaga, H. Tamai, H. Shirai, T. Takizuka, Y. Kamada , T. Fujita, W. Dorland[2)], D. R. Ernst[3)], D. Mikkelsen[1)] , G. Rewoldt[1)]

1) Princeton Plasma Physics Lab., Princeton University, PO Box 451, Princeton, NJ 08543,

2) Institute for Plasma Research, Univ. of Maryland, College Park, MD 20742,

3) Plasma Science and Fusion Center, Massachusetts Institute of Technology,Cambridge, MA,

1 Introduction

Energy confinement and divertor power handling of high-density ELMy H-mode plasmas have been improved with Ar seeding in JT-60U. Characteristics of the core and edge plasmas and behavior of impurity ions are summarized in Sec. 2, [1,2]. Mechanism of the improved energy confinement was investigated, using ITG/TEM, ETG suppression model in Sec. 3[3]. Recent results of the ELMy H-mode operation near Greenwald density limit (n^{GW}) are summarized in Sec. 4.

2 Improvement of Plasma Confinement and Reduction of Divertor Head Load [1, 2]

Good confinement ELMy H-mode plasma with $HH_{98(y,2)} = 1$ is required for ITER operation at electron density of ~0.85 n^{GW} with plasma purity (n_i/n_e) of ~80%. ($HH_{98(y,2)}$ is the improvement of thermal energy confinement time compared with IPB98(y,2) scaling [4], n_i is fuel ion density, n_e is electron density, and n^{GW} is the Greenwald density.) At the same time, large radiation-power fraction (P_{rad}/P_{heat}) of ~0.7 is crucial for acceptable divertor heat load during the steady-state period. (P_{rad} is radiation power, and P_{heat} is net heating power.) Furthermore, large heat flux exhausted by Type-I ELMs may reduce the lifetime of divertor tiles. Therefore, it is necessary to reduce ELM heat load as well as to increase the radiation fraction for steady-state heat load between ELMs.

Impurity injection is one of candidates to reduce divertor heat load by radiation enhancement with high energy confinement at high density. In JT-60U, radiation fraction in the steady-state ELMy H-mode plasma with the triangularity (δ) ~0.35 was extended to P_{rad}/P_{heat}~0.8 in the improved confinement of $HH_{98(y,2)}$~1[5]. However, upper limit of the electron density of n_e ~0.66 n^{GW} was lower than ITER requirement, and large ELM energy was not reduced. High triangularity plasma of δ ~0.5 with Ar injection was attempted in order to increase plasma temperature and pressure at the pedestal, which would enhance the core confinement. $HH_{98(y,2)}$ ~1 and P_{rad}/P_{heat} ~0.8 were obtained at $n_e = 0.66\ n^{GW}$ [2], and they were comparable to the reference shots [5]. However, the ELMs became grassy, i.e. maybe Type-II: the frequency increased and amplitude was reduced.

In order to extend the density regime with the improved confinement and radiation-power fraction, we attempted to shift the outer divertor strike-point from the divertor tile to dome-side/top tiles, where the plasma shape such as δ ~0.35 was maintained [6] in the Ar seeded ELMy H-mode. In particular, the good confinement plasma was maintained in high density regime for the "dome-top" configuration that

the outer strike point was located on the dome-top. Confinement improvement, electron density, and radiation-power fraction reached the ITER relevant regime. Confinement improvement, electron density, and radiation-loss-power fraction reached the ITER relevant regime; $HH_{98(y,2)} \sim 1$, $n_e \sim 0.8\ n^{GW}$, and $P_{rad}/P_{heat} \sim 0.8$. Electron density profile was slightly peaked with Ar injection, and TRANSP analysis showed that the improvement was mainly attributed to an improvement of ion energy confinement. At the same time, the maximum divertor heat load due to ELMs has been reduced by a factor of 3 - 5 with keeping the good energy confinement. Such large reduction was observed only for the case of the "dome-top" configuration with Ar seeding. These experiments suggest that the plasma confinement was influenced by the divertor plasma configuration. Detail analysis of the divertor and edge plasmas is in progress to understand the mechanism.

3 Analysis of Transport Properties and ITG/TEM, ETG Stability [3]

Since confinement degrades dramatically at high density with D_2 puffing only, [7] addition of argon puffing in the dome-top configuration has been used to regain H-mode confinement [$HH_{98(y,2)}$] at high density [$n_e \sim 0.8\ n^{GW}$], as well as to reduce the divertor heat load [$P_{rad} \sim 0.8\ P_{heat}$]. [1,2] To try to better understand the confinement improvement with Ar seeding, transport calculations using the TRANSP code, and ITG/ETG microstability calculations using the GS2 and FULL codes have been done.

GS2 code calculations were compared for an Ar seeded and a reference plasma without argon with I_p = 1.2 MA, B_T = 2.5 – 2.6 T, P_{NBI} = 18 MW, elongation κ = 1.4, and triangularity δ = 0.3. For the reference discharge, the maximum growth rates for both the ITG/TEM ($3 - 6 \times 10^4\ s^{-1}$ at $k_\theta \rho_s \sim 0.5$) and ETG ($1 - 4 \times 10^6\ s^{-1}$ at $k_\theta \rho_s \sim 40$) modes were significant throughout the range ρ = 0.25 – 0.85. However, for the Ar-seeded discharge the ITG/TEM maximum growth rate, γ_{ITG}, was greatly reduced in the region ρ = 0.6 – 0.7. The ETG growth rate was significantly reduced everywhere and vanished in the range ρ = 0.53 – 0.7. The ExB shearing rates were much smaller than the ITG growth rates over the profile. The effect of rotation on γ_{ITG} was calculated by the FULL code to be small.

The effect of adding or removing Ar to the discharges was simulated by GS2. Adding the same Ar fraction to the reference discharge as was measured in the Ar discharge resulted in a reduction of γ_{ITG} by only about 10% at ρ = 0.3 and 30% at ρ = 0.7; although reduced, these rates did not drop to the low levels observed in the Ar-seeded discharge. Simulated removal of the Ar from the Ar seeded discharge increased γ_{ITG} by 10 – 20% over ρ = 0.2 – 0.5, but did not increase the growth rate from the low levels near ρ = 0.65. Thus, the small T_i gradient in this region, rather than the effects of the Ar seeding, was the dominant factor in reducing γ_{ITG} to the low levels observed in the Ar seeded discharge.

The effect on the growth rates of adding Ar was not sufficient to quantitatively explain the level of confinement improvement. To better understand the bifurcation toward better confinement afforded by Ar seeding, the time evolutions of the ExB shearing rates and the drift mode growth rates following the start of Ar injection should be compared with the evolutions in a reference discharge. The effect of the increasing relative importance of the TEM mode toward peaking the density profile via its particle pinch should also be investigated. [8]

4 Extending Improved Plasma Confinement Operation near Greenwald Density Limit.

In order to extend the operation regime (higher density and long period) of the high-density ELMy H-mode plasma ($HH_{98(y,2)}$~1, n_e ~0.8 n^{GW}, and P_{rad}/P_{heat} ~0.8, which was only obtained in the dome-top configuration), one of the important steps was improving reproducibility of the good performance. In 2001, a FB control to fix the strike-point locations has been established by CCS (Cauchy-Condition Surface) method [9], which could maintain the outer strike-point on the dome top while the plasma confinement and pressure changed as shown by thin lines in Fig.1 (shot# 39530). Separation between the outer-leg separatrix and the outer roof of the dome (Dome-top gap) was less than 0 as shown in Fig.1 (c), with deuterium and argon (Ar) puffing (I_p=1.2MA, B_t=2.4T, q_{95}=3.6, δ=0.36, κ=1.38, P_{NB}= 17 MW). FB control of Ar gas puff with radiation power as an actuator was prepared for these experiments. However, the response of the radiation power after Ar injection was slow. Thus, a constant rate of Ar gas puff was used, and deuterium gas puff was used to maintain the high n_e by FB-control.

The "dome-top" configuration was kept in 6.2-9.6s, and the good energy confinement were sustained with n_e increasing up to ~0.8 n^{GW}: at 7.7s, H_{89L}~1.64 ($HH_{98(y,2)}$~0.97) and P_{rad}/P_{heat} ~0.8, where toroidal ripple loss fraction of fast ions was 15-18%. Energy confinement was enhanced (H_{89L}~1.72, correcting the ripple loss fraction of 14%) during an injection of negative NB (N-NBI), t = 8.4-9.0s, while the thermal energy confinement was slightly reduced ($HH_{98(y,2)}$~0.90 due to an increase in fast ion component in the total stored energy). T_e at center increased from $T_e(\rho=0.1)$ ~5 to 6 keV, while T_i profiles were quite similar:

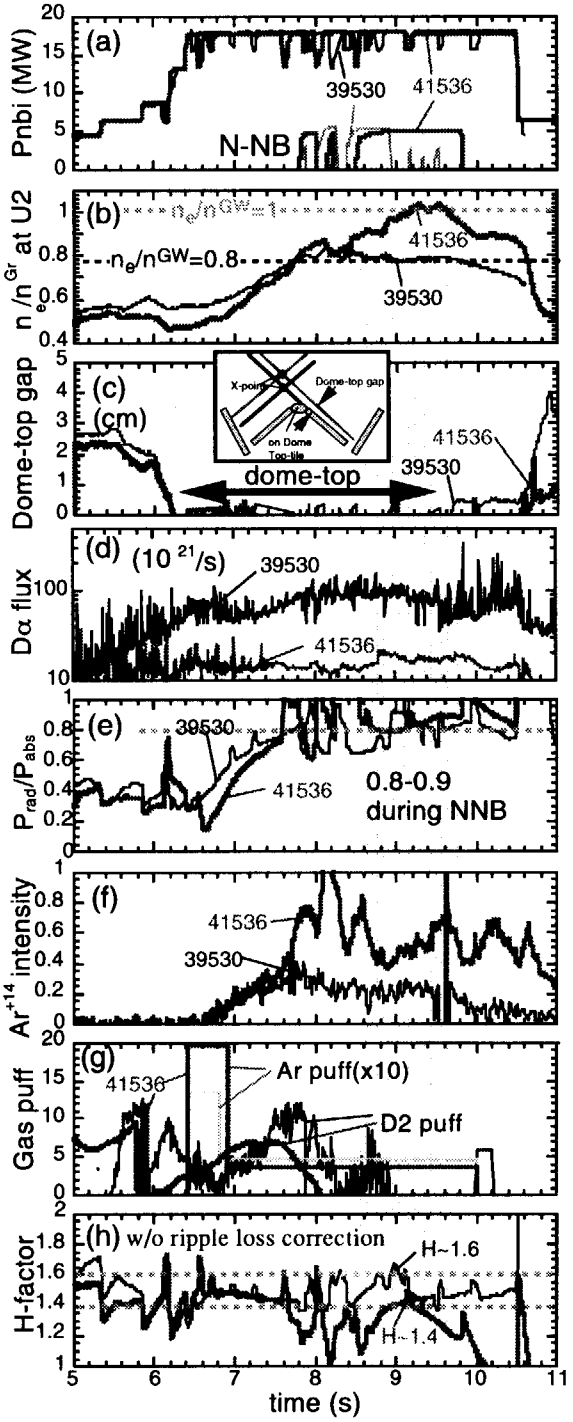

Fig. 1. Comparison of shot#39530 (thin lines) and 41536 (thick lines): (a) P-NB and N-NB powers, (b) line-averaged n_e at U2 (r/a~0.35), (c) Dome-top gaps (δ<0 for dome-top configration), (d) Dα signals in the divertor, (e) total radiation fractions, (f) Ar+14 intensities, (g) D2 and Ar gas puffing rates, (h) H89L without correction of ripple loss of fast ions.

$T_i(\rho=0.2)$ ~7.5 keV. Heating of the core plasma by N-NBI of 4.3MW was observed as electron heating. It should be noted that ELM activity was reduced only during the "dome-top" configuration.

In 2002, N-NB system was improved and long pulse length was available. A few trials were done to extend the high-density operation of the ELMy H-mode plasma near "Greenwald density limit". A typical discharge (shot# 41536) is shown by thick lines in Fig.1, and the outer strike point was kept on the dome-top up to 9.7 s. During the long injection of N-NB (8.5 – 9.8s), n_e was increased up to n_e/n^{GW}~1, and a density profile became more peaked. Ar ions were penetrating into core region after 7.7 s, which might be caused by a detachment of the divertor plasma since ion saturation currents (I_s) of inner divertor probes were reduced. At the same time, H-factor decreased. However, the good energy confinement was recovered during the long N-NBI: at 9.0 s, H_{89L}~1.58 (toroidal ripple loss fraction of fast ions is12%) and $HH_{98(y,2)}$~0.89 were achieved with large radiation fraction of P_{rad}/P_{heat} ~0.8. Here, $n_e(\rho=0.1)$~ $8\times10^{19}m^{-3}$, $T_e(\rho=0.1)$~ 4 keV, and $T_i(\rho=0.2)$~6 keV. At the same time, Ar ions and radiation fraction were reduced, and Z_{eff} became relatively small ~ 3.3. This condition of $n_D(\rho=0.1)/n_e(\rho=0.1)$~0.76 corresponds to slightly less than 0.8 (for ITER design). Good correlation of the energy confinement degradation over a radiation power fraction of 80% (and large Ar ion penetration) suggests that control of the divertor detachment would be one of key issues to maintain the good performance of ELMy H-mode plasma near "Greenwald density limit".

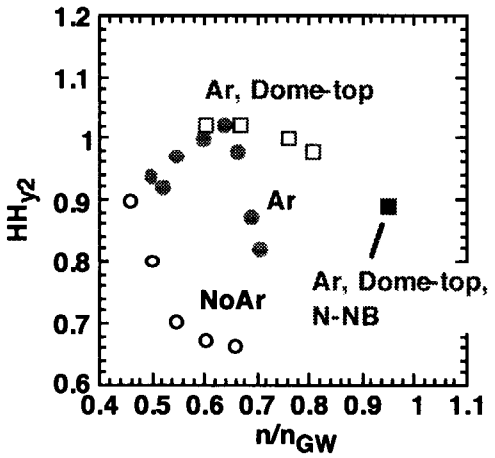

Fig. 2. HH factor as a function of normalized density in ELMy H-mode. Shot39530(open squares) with P-NB, and Shot41536 with N-NB(closrd square) [10]

5 Summary

In 2001-2002, high-density ELMy H-mode plasmas with Ar gas seeded were sustained with the dome-top configuration, and the operation was extended near "Greenwald density limit", during long N-NB injection. Mechanism of the improved confinement of the Ar seeding was investigated using a model of ITG stabilization by shear plasma flow. Tentative calculation results showed that reduction of the growth rate due to Ar ion distribution was insufficient to explain the observed confinement improvement. Development of FB methods (such as Ar, deuterium gases, and strike-point position) was also an important issue to sustain the good energy confinement plasma near "Greenwald density limit".

Reference

[1] Higashijima, S. et al., J. Nucl. Mater. 313-316 (2003) 1124.
[2] Kubo, H. et al., Phys. Plasmas 9 (2002) 2127.
[3] Hill, K. W. et al., Proc. 19th IAEA Fusion Energy Conference, IAEA-CN-94/EX/P2-03, Lyon, France (2002).
[4] ITER EDA documentation series No. 18, "ITER-FEAT outline design report" (International Atomic Energy Agency, Vienna, 2001).
[5] Kubo, H. et al., Nucl. Fusion **41**, (2001) 227.
[6] N. Asakura et al., JAERI-Review 2002-022 (2002) 91.
[7] N. Asakura et al., Plasma Phys. Control. Fusion **39** (1997) 1295.
[8] M. Z. Tokar et al., Phys. Rev. Lett. **84** (2000) 895.
[9] Y.M.Miura, et al., "Review of JT-60U experimental results in 200)", JAERI-Review 2002-022 (2002) 81.
[10] T. Fujita, et al., Proc. 19th IAEA Fusion Energy conf., Lyon (2002), OV/I-3.

5.2 High Density and High Confinement ELMy H-mode Plasmas with Gas-puffing

H. Takenaga, N. Oyama, N. Asakura, S. Konoshima, H. Kubo, Y. Kamada, Y. Miura

1. Introduction

High density and high confinement operation is essential in a fusion reactor. In ITER, the standard scenario will be operated at 85% Greenwald density (n_{GW}) with HH_{y2}=1, where HH_{y2} is a confinement enhancement factor over the IPB98(y,2) ELMy H-mode scaling. In DEMO reactor, over Greenwald density operation is required. However, the confinement degrades near the Greenwald density especially in the large tokamak. In JET, high confinement (HH_{y2}=1) has been achieved at high density ($\bar{n}_e/n_{GW}$>1) by optimizing the operation scenario with a high triangurality (δ~0.45) and medium gas-puffing [1]. In JT-60U ELMy H-mode plasmas, high confinement was not obtained at high density ($\bar{n}_e/n_{GW}$>0.5) even with a high δ (~0.5), where the pedestal temperature decreases with increasing pedestal density, and the central temperature decreases due to a profile stiffness [2]. It is important for avoidance of the confinement degradation to keep the high pedestal temperature and/or to break the profile stiffness. In this report, the effects of (1) plasma configuration, (2) density ramp-up scenario, (3) wall temperature, (4) toroidal rotation and (5) NB heating power on the confinement degradation are investigated, in order to achieve the high density and high confinement in JT-60U. The confinement enhancement factor (H_{89P}) over the ITER89 L-mode scaling is used for an index of the confinement degradation in this study, because it is easily estimated. Although the density dependence of ITER89 L-mode scaling is different from that of IPB98(y,2) ELMy H-mode scaling, H_{89P} well expresses the confinement degradation at the high density.

2. Effects of Plasma Configuration

The effects of configuration on the confinement degradation are investigated in the inward-shifted, outward-shifted, high-δ with a small outer plasma-wall gap (Δ_0), large-volume and small-volume configurations shown in Fig. 1. The plasma parameters : plasma current (I_p), toroidal field (B_T), plasma minor radius (a), safety factor at 95% flux surface (q_{95}), triangurality (δ) and elongation (κ), are listed in Table 1. In the inward-shifted configuration, NB passes a central region compared with other configurations. In the outward-shifted configuration, plasma surface interaction is expected to be enhanced around the main plasma at the low field side. Based on the JT-60U database, the outward-shifted configuration seems to be effective to increase the density with a small gas-puffing rate. The high-δ and small-Δ_0 configuration might affect the confinement at high density, because Δ_0 is small in the JET high-δ

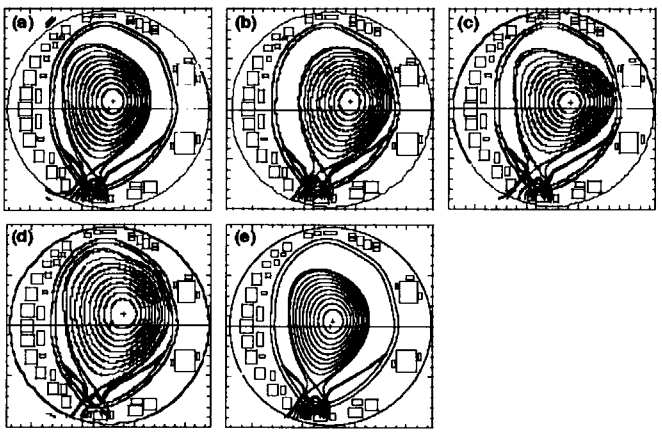

Fig. 1 Plasma configurations used for the study of plasma configuration effects. (a) inward-shifted, (b) outward-shifted, (c) high-δ with a small Δ_0, (d) large-volume and (e) small-volume configurations.

plasma and JET gains 10% in density (from $\bar{n}_e/n_{GW}$=0.9 to 1.0) with keeping high confinement by reducing Δ_0 from 5 cm to 2.5 cm in Ar seeded experiment [3]. In JT-60U reversed shear plasmas with a large-volume, high $\bar{n}_e/n_{GW}$ (>1) has been obtained with good confinement (HH_{y2}~1.2) even at low edge density due to an internal transport barrier and low n_{GW} (because of large a). In the large-volume configuration, $\bar{n}_e/n_{GW}$ is expected to be high due to the low n_{GW}. Conversely, n_{GW} is higher in the small-volume configuration compared with other configurations.

Table 1 Plasma parameters in various configurations.

	Config.	Ip (MA)	B_T (T)	a (m)	q_{95}	δ	κ
(a)	Inward	1.0	2.1	0.82	3.7	0.25	1.5
(b)	Outward	0.9	1.9	0.89	3.4	0.26	1.4
(c)	High-δ	0.7-1.0	2.0	0.94-0.98	3.8-5.2	0.47-0.5	1.2
(d)	Large-Vol.	1.2	2.0	1.0	3.7	0.3	1.4
(e)	Small-Vol.	1.0	2.1	0.77	3.1	0.23	1.5

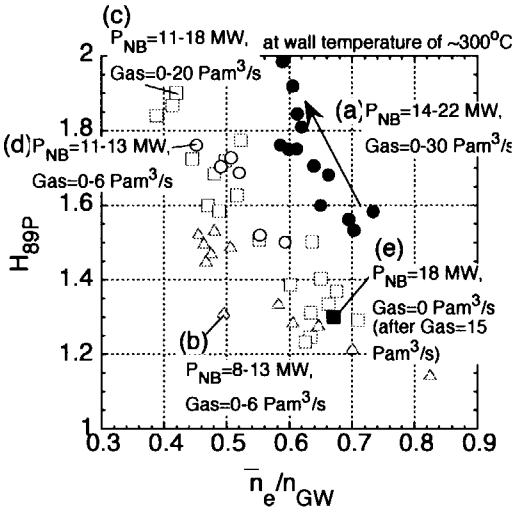

Fig. 2 H_{89P} as a function of $\bar{n}_e/n_{GW}$ for various configurations. Closed circles, open triangles, open squares, open circles and closed squares show the data in the (a) inward-shifted, (b) outward-shifted, (c) high-δ, (d) large-volume and (e) small-volume configurations, respectively. The NB heating power and the gas-puffing rate are written in the figure.

The dependence of H_{89P} on $\bar{n}_e/n_{GW}$ is shown in Fig. 2 for the various configurations. In these plasmas, a preprogrammed time constant gas-puffing was applied simultaneously with the NB heating, and the wall temperature was set to be ~300°C. Since the fractions of perpendicular NB injection and ripple loss are large in JT-60U, the counter toroidal rotation is observed at the plasma edge in these plasmas. In the inward-shifted configuration, higher H_{89P} than in other configurations is obtained. In the discharge with the heating power of P_{NB}=11-18 MW and gas-puffing of 20 Pam³/s, H_{89P}=1.85 (HH_{y2}=0.96) is achieved at $\bar{n}_e/n_{GW}$=0.61 with β_N=2.3, Z_{eff}=2.8 and radiation fraction of 74% at 0.5 s after switched-off of the gas-puffing. In this configuration, H_{89P} decreases to about 1.6 at $\bar{n}_e/n_{GW}$ =0.7 with P_{NB}=18 MW during gas-puffing of 20 Pam³/s. After the gas-puffing, H_{89P} increases with decreasing $\bar{n}_e/n_{GW}$ as shown by the arrow in Fig. 2. In the inward-shifted configuration, the density is quickly increased by applying the gas-puffing and the NB heating simultaneously (fast density ramp-up), and then, the density is saturated during the gas-puffing. The effect of the density ramp-up scenario is discussed in the next section. In the high-δ and small Δ_0 configuration with I_p=1.0 MA, the density continues to increase after the fast density ramp-up, and reaches up to 63% of n_{GW} with smaller gas-puffing rate of 15 Pam³/s as expected. However, H_{89P} is smaller than that in the inward-shifted configuration. In the discharge, where the configuration is changed from the high-δ to the inward-shifted configuration, n_{GW} increases due to a smaller minor radius in the inward-shifted configuration, and $\bar{n}_e$ also increases together with n_{GW}. The edge density seems to increase before an increase of the central density. The Greenwald density could be related to the edge density. In the outward-shifted configuration, the density also continues to increase after the fast density ramp-up, and the density can be increased up to $0.8n_{GW}$ by a long gas-puffing for 9 s with a small gas-puffing rate of 6 Pam³/s as expected from the database. However, H_{89P} is smaller than others. In the small-volume configuration, dependence of H_{89P} on $\bar{n}_e/n_{GW}$ shows similar

tendency as that in the large-volume configuration. In the large-volume configuration, $\bar{n}_e/n_{GW}$ is not increased without the internal transport barrier even at lower n_{GW}. In the large- and small-volume configurations, H_{89P} is smaller than that in the inward-shifted configuration and almost the same as that in the high-δ configuration. The pedestal ion temperature is higher in the inward-shifted configuration than in other configurations. The higher confinement could be achieved by keeping the higher pedestal temperature in the inward-shifted configuration.

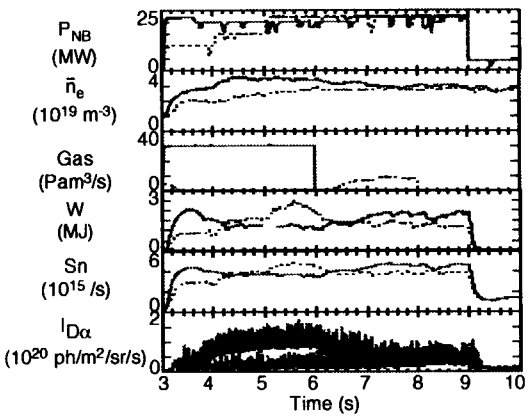

Fig. 3 Wave-forms of discharges for fast (solid lines) and slow (dotted lines) density ramp-up.

3. Effects of Density Ramp-up Scenario

The fast $\bar{n}_e$ ramp-up discharges in the inward-shifted configuration with the higher H_{89P} is compared with the slow $\bar{n}_e$ ramp-up discharge at the wall temperature of ~300°C as shown in Fig. 3. In the slow $\bar{n}_e$ ramp-up discharge, the density was increased using the feedback control system. The counter toroidal rotation is observed at the plasma edge for both discharges. In the fast $\bar{n}_e$ ramp-up discharge, the density gradually decreases and the stored energy increases after the gas-puffing. In the slow $\bar{n}_e$ ramp-up discharge, the same density is obtained with the smaller gas-puffing rate. The value of H_{89P} is higher in the fast $\bar{n}_e$ ramp-up discharge than that in the slow $\bar{n}_e$ ramp-up discharge as shown in Fig. 4. In the slow $\bar{n}_e$ ramp-up discharge, H_{89P} is almost the same as that in the high-δ and large-volume configurations. The density profile is not peaked in the fast $\bar{n}_e$ ramp-up discharge compared with that in the slow $\bar{n}_e$ ramp-up discharge. In the fast $\bar{n}_e$ ramp-up discharge, a higher pedestal ion temperature is observed (~1.5 keV) compared with that in the slow $\bar{n}_e$ ramp-up discharge (~1.2 keV) in a same $\bar{n}_e/n_{GW}$ (~0.6) range.

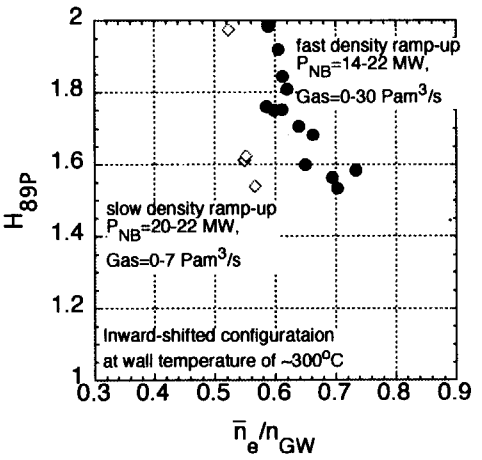

Fig. 4 Comparison of H_{89P} for fast (closed circles) and slow (open diamond) density ramp-up discharges, respectively.

4. Effects of Wall Temperature

In JT-60U, increase of the edge density has been observed just after the type-I ELMs due to enhancement of recycling [4]. This could affect the confinement and/or edge conditions. The recycling properties could be different for different wall temperature. The effects of the wall temperature is investigated in the inward-shifted configuration with the fast $\bar{n}_e$ ramp-up scenario by changing the wall temperature from ~300°C to ~150°C. The counter

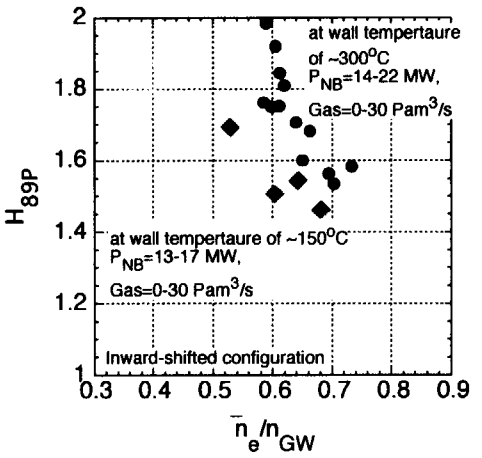

Fig. 5 Comparison of H_{89P} with the wall temperature of ~300°C (closed circles) and ~150°C (closed diamond), respectively.

toroidal rotation is also observed in the plasma edge for these plasmas. The value of H_{89P} is smaller at ~150°C than at ~300 °C as shown in Fig. 5. At the wall temperature of ~150°C, recycling is enhanced and ELM frequency is high, although Z_{eff} is lower. The enhanced recycling and higher ELM frequency could affect the confinement.

5. Effects of Toroidal Rotation and Heating Power

The counter toroidal rotation is observed in the plasma edge for the discharges discussed above. The effects of the toroidal rotation are investigated using combinations of counter (4.2 MW) and perpendicular (11 MW) injections and co (4.2 MW for P-NB and 5 MW for N-NB) and perpendicular (2.2 MW) injections in the inward-shifted configuration with the fast $\bar{n}_e$ ramp-up at the wall temperature of ~150°C. The net heating power is ~10 MW in both cases, because the ripple loss power is larger for perpendicular injection than for the co- and counter-injections. The toroidal rotation in the co-direction is observed including the edge region for the co+perpendicular injection as shown in Fig. 6, while the counter toroidal rotation is observed for the counter+perpendicular injection. However, the confinement is not changed drastically with the toroidal rotation in the co-direction as shown in Fig. 7 considering the density dependence. Power dependence in the inward-shifted configuration at the wall temperature of ~150°C is also plotted in Fig. 7. Higher NB heating power gives higher H_{89P} at high $\bar{n}_e/n_{GW}$ region. Even at the wall temperature of ~150°C, H_{89P} recovers to the same region as data at the wall temperature of ~300°C with the high power heating including the central heating by N-NB. It is noted that the toroidal rotation seems to be in the co-direction in this discharge, although the fraction of perpendicular NB injection is large.

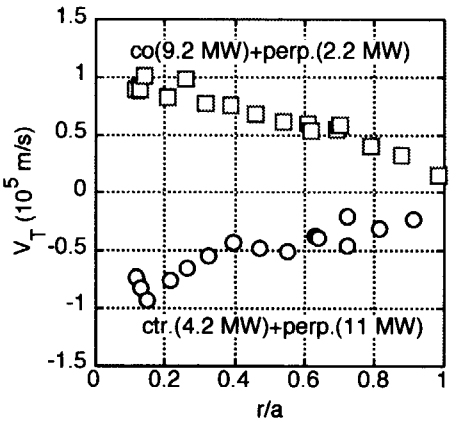

Fig. 6 Toroidal rotation for co+perp. (squares) and ctr.+perp.(circles) injections.

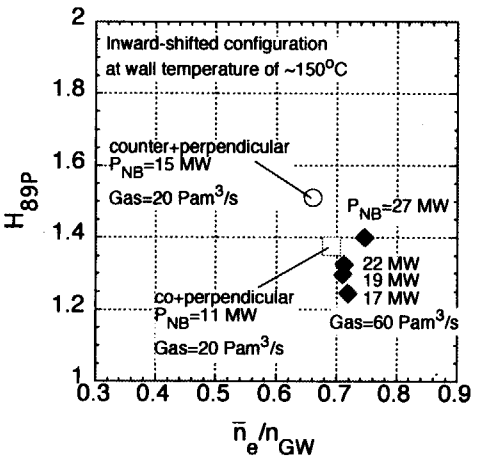

Fig. 7 Dependence of H_{89P} on toroidal rotation (circles and squares) and heating power (closed diamonds).

6. Summary

Dependence of H_{89P} on the plasma configuration, the density ramp-up scenario, the wall temperature, the toroidal rotation and the heating power is investigated. The inward-shifted configuration, the fast density ramp-up, high wall temperature and higher heating power give higher H_{89P}. These conditions could be effective to keep the high pedestal temperature.

References

[1] Ongena, J., et al., in Fusion Energy 2002 (Proc. 19th Int. Conf. Lyon, 2002).
[2] Urano, H., et al., Plasma Phys. Control. Fusion **44**, A437 (2002).
[3] Ongena, J., private communication.
[4] Chankin, A.V., et al., Nucl. Fusion **42**, 733 (2002).

5.3 Study of Pellet Injection Characteristics and Extension of Operation Region to High Density Using High-Field-Side Midplane Pellet Injection

H. Takenaga, Y. Kamada, A. Polevoi[1)], H. Kubo, K. Kizu,
T. Sasajima, H. Ichige, H. Hiratsuka

1) ITER International Team ITER Naka Joint Work Site, Naka-machi, Naka-gun, Ibaraki-ken 311-0193, Japan

1. Introduction

In order to extend the operation region to high density without confinement degradation, a multiple pellet injector was installed with injections from the low-field-side midplane [LFS(mid)] and from the high-field-side at the top [HFS(top)] in 2000 [1]. The HFS(top) pellet injection is more effective for density increase in the NB heated plasma compared with the LHS(mid) pellet injection [2]. This result is consistent with radial displacement theoretically predicted based on the ExB drift model [3], where deeper deposition is suggested for the high-field-side pellet injection. Using the HFS(top) pellet injections, accessible density region in the high β_p mode plasma has been extended to 70% of the Greenwald density with a confinement enhancement factor over the ITER89P scaling of about 2 and a normalized beta of 2.2 [2]. In 2001, the LFS(mid) pellet injection was modified for a high-field-side midplane [HFS(mid)] injection to optimize the direction of the ExB drift. For the HFS(mid) pellet injection, deeper penetration is expected, because the ExB drift is towards the plasma center.

In this report, the pellet injector system is described in Section 2. The characteristics of the HFS(mid) pellet injection are discussed for OH and NB plasmas in Section 3 and Section 4, respectively. Furthermore, the results for the extension of the operation region to high density in high β_p mode plasma using the HFS(mid) pellet injections are discussed in Section 5, followed by a summary in Section 6.

2. Pellet Injector System

The pellet injector can inject (30-40) 2.1 mm cubic pellets in each discharge. The injection frequency (f) of 10 Hz (designed maximum value is 20 Hz) and the injection speed (v) in the designed range of 100-1000 m/s have been achieved. Figure 1 illustrates the layout of the pellet injections. The injection lines were arranged for injections from the low-field-side midplane [LFS(mid)] and the high-field-side at the top [HFS(top)] in 2000 campaign. In 2001 and 2002 campaigns, the LFS(mid) pellet injection was modified to the high-field-side midplane [HFS(mid)] pellet injection by

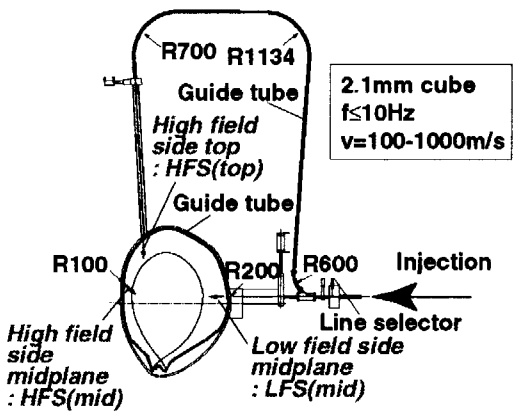

Fig. 1 Layout of the pellet injections.

installing the guide tube behind the carbon tiles in the vacuum vessel. The HFS(mid) injection is arranged at about 450 mm height from the midplane with an angle of 45 degree as shown in Fig. 1. The curvature radius of the guide tube for the HFS(mid) injection is 200 mm at the port edge and 100 mm near the end of the guide tube as shown in Fig. 1. These curvature radii are smaller than those of guide tube for the HFS(top) injection. Therefore, one concern for the HFS(mid) injection is a break of the pellet inside the guide tube due to small curvature radius.

3. Characteristics of HFS(mid) Pellet Injection in OH Plasmas

Figure 2 shows time evolution of line averaged electron density ($\bar{n}_e$) in an OH plasma at the plasma current of I_p=1.2 MA and the magnetic field of B_T=3 T with the HFS(mid) pellet injections (v=100 m/s and f=5 Hz). The actual injection frequency is 2 Hz, which is lower than the ejection frequency. The reduction of the frequency indicates that the ejected pellets are broken in the guide tube. The effective particle confinement time defined as τ_p^*=Ne/(S_{pellet} – dNe/dt), where Ne is the total number of electrons and S_{pellet} is the time averaged particle source due to the pellet injections, is estimated to be 1.7 s. This value is similar as or larger than that for both LFS(mid) and HFS(top) pellet injections (~1.2 s) and larger than that for gas-puffing (~ 0.6 s).

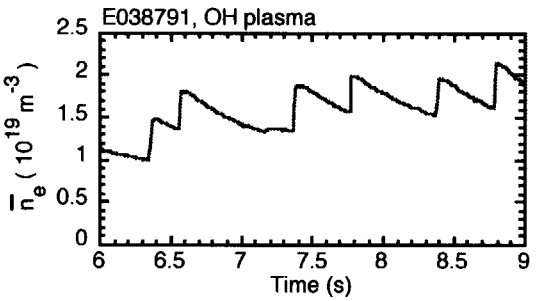

Fig. 2 Typical wave-form of line averaged electron density with the HFS(mid) pellet injections.

The increment of the number of electrons (ΔNe) for each pellet injection estimated using 2 or 3 interferometers with a sampling time of 1 ms is shown in Fig. 3 as a function of v. For the HFS(mid) pellet injection, the maximum value of ΔNe reaches up to 90% of the particles for a 2.1 mm cubic pellet. The value of ΔNe for the HFS(mid) pellet injection is larger than that for the HFS(top) pellet injection, although the minimum curvature radius of the guide tube is smaller for the HFS(mid) pellet injection than that for the HFS(top) pellet injection. However, the number of absorbed particles for both HFS(top) and HFS(mid) injections seems to be similar due to higher reduction rate of injection frequency in the HFS(mid) pellet injection.

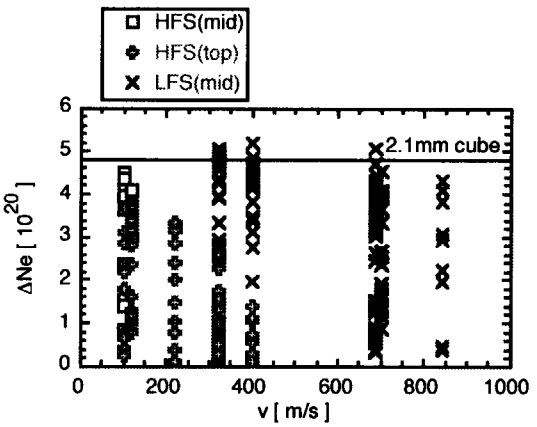

Fig. 3 ΔNe as a function of v. Squares, plus symbols and cross symbols show the data for HFS(mid), HFS(top) and LFS(mid) injections, respectively.

4. Characteristics of HFS(mid) Pellet Injection in NB Heated Plasmas

Figure 4 shows the wave-forms of $\bar{n}_e$ and the NB heating power (P_{NB}) in the discharges (I_p=1.5 MA and B_T=3.5 T) with the HFS(mid) pellet injection (v=100 m/s and f=10 Hz) and

without the pellet injection. The value of $\bar{n}_e$ increases by about 50% in the discharge with the HFS(mid) pellet injection. The value of τ_p^* is estimated to be 1.8 s for the discharge with the HFS(mid) pellet injection, which is larger than that for the discharge with the HFS(top) pellet injection (~0.5 s). The longer τ_p^* might be due to the deeper penetration, although the wall condition could also affect the value of τ_p^*. In Fig. 5, ΔNe is plotted as a function of P_{NB}. For the HFS(mid) pellet injection (I_p=1.5 MA, B_T=3.5 T and v=120 m/s), the maximum value of ΔNe is almost constant in the range of P_{NB}<15 MW. However, it decreases with increasing P_{NB} in the range of P_{NB}>15 MW. One of the explanations for the reduction of ΔNe for the HFS(mid) pellet injection is ablation in the SOL as well as for the HFS(top) pellet injection. The maximum value of ΔNe for the HFS(mid) pellet injection is almost double compared with that for the HFS(top) pellet injection in the range of P_{NB}=5-15 MW. The total amount of particles absorbed during the discharge is almost the same for both HFS(top) and HFS(mid) injections because of the higher reduction rate of the number of absorbed pellets for the HFS(mid) injection.

The pellet penetration deeper than that predicted by the neutral gas shielding (NGS) model is observed for the HFS(mid) pellet injection as shown in Fig. 6. The deeper penetration depth is consistent with the SMART (simplified mass ablation and relocation treatment) model prediction [4], where the ablation model by Kuteev [5], the initial cloud size model by Parks [3] and the mass relocation model by Strauss [6] are included.

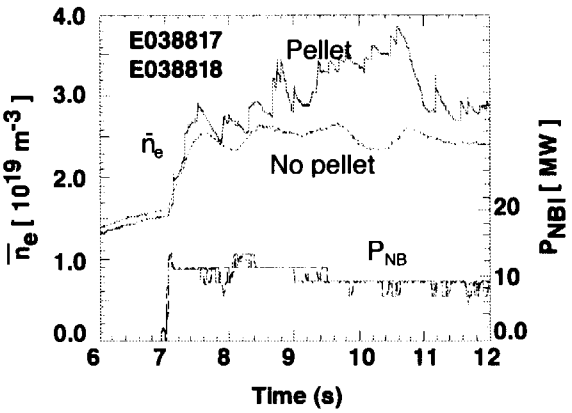

Fig. 4 Wave-forms of line averaged electron density and NB heating power with the HFS(mid) pellet injection and without pellet injection.

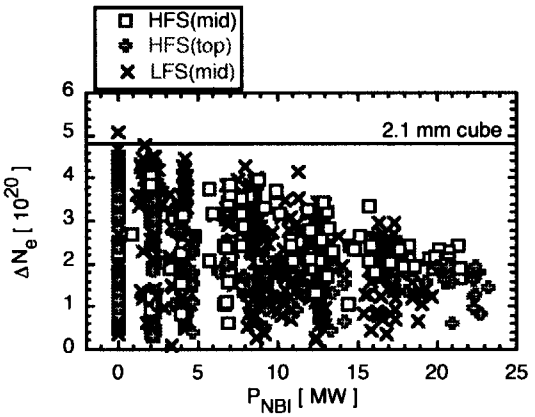

Fig. 5 ΔNe as a function of P_{NB}. The meanings of the symbols are the same as those in Fig. 3

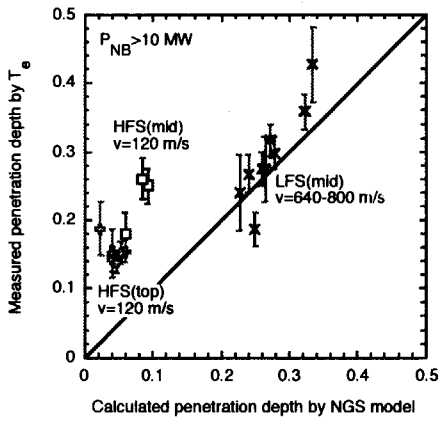

Fig. 6 Comparison of penetration depth between calculation and measurement. The meanings of the symbols are the same as those in Fig. 3.

5. Extension of Operation Region to High Density in High β_p Mode Plasma

The HFS(mid) pellet injection is applied to high β_p mode plasmas with a high

triangularity (δ>0.5) configuration (I_p=1 MA), in order to extend the operation range with the good confinement to high density. Figure 7 shows dependence of the confinement improvement factor over the ITER89P scaling (H_{89PL}) on the density normalized to the Greenwald density (n_{GW}). The accessible density range with H_{89PL}~2 is extended by the HFS(mid) and HFS(top) pellet injections. The density does not increase with the LFS(mid) pellet injection due to fast density decay [2]. The confinement degrades with gas-puffing. The value of ΔNe is larger for the HFS(mid) pellet injection than that for the HFS(top) pellet injection. However, the number of absorbed pellet is smaller for the HFS(mid) pellet injection than that for the HFS(top) pellet injection. When 4 pellets are injected actually with f=10 Hz, the density increases more for the HFS(mid) pellet injection compared with for the HFS(top) pellet injection. The HFS(mid) pellet injection could be more effective to extend the operation range compared with the HFS(top) pellet injection, if the same injection frequency is achieved. The achieved density is so far limited below $\bar{n}_e/n_{GW}$=0.7 for both HFS(mid) and HFS(top) pellet injections[7, 8].

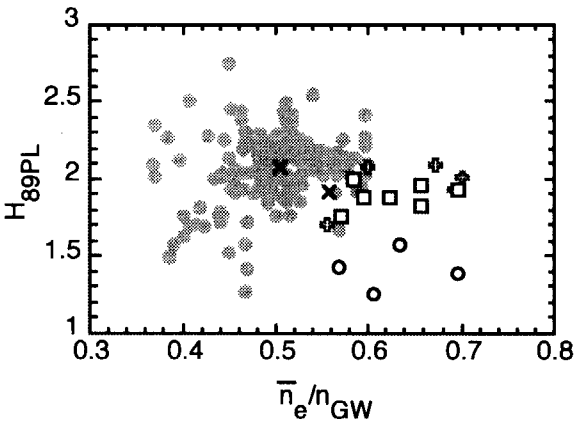

Fig. 7 H_{89PL} as a function of $\bar{n}_e/n_{GW}$. Gray symbols show the data without pellet injection and gas-puffing. Open circles show the data with gas-puffing. Squares, plus symbols and cross symbols show the data for HFS(mid), HFS(top) and LFS(mid) pellet injections, respectively.

6. Summary

The density jump for the HFS(mid) pellet injection is larger than that for the HFS(top) pellet injection in both OH and NB plasmas, although the minimum curvature radius of the guide tube is smaller. However, the number of absorbed pellets is smaller for the HFS(mid) pellet injection than that for the HFS(top) pellet injection. The achieved density with the H_{89P}~2 is so far limited below $\bar{n}_e/n_{GW}$=0.7 for the HFS(mid) pellet injection as well as for the HFS(top) pellet injections, although each HFS(mid) pellet injection is more effective due to deeper deposition for extension of the operation range to high density.

References

[1] Kizu, K., et al., Fusion Eng. Des. **58-59**, 331 (2001).
[2] Takenaga, H., and the JT-60 team, Phys. Plasmas **8**, 2217 (2001).
[3] Parks, P.B., et al., Phys. Plasmas **7**, 1968 (2000).
[4] Polevoi, A., Shimada, M., Plasma Phys. Control. Fusion **43**, 1525 (2001).
[5] Kuteev, B., Nucl. Fusion **35**, 431 (1995).
[6] Strauss, H.R., and Park, W., Phys. of plasmas **5**, 2676 (1998).
[7] Kamada, Y., et al., Plasma Phys. Control. Fusion **44**, A279 (2002).
[8] Kubo, H., and The JT-60 Team, Phys. Plasmas **9**, (2002).

5.4 Edge Pedestal Structure in Type I and Type II ELMy H-mode [1]

Y. Kamada, H. Takenaga, H. Urano, T. Takizuka, T. Hatae, Y. Miura

With multiple pellet injection into high triangularity (δ) H-mode discharges, JT-60U has enhanced the pedestal pressure of the ELMy H-mode by factors of 2-2.5 at the same plasma current and plasma shape, and extended the high confinement regime to a high density. Based on the expanded H-mode regimes, we have clarified the pedestal parameter-linkages determining the pedestal structure as shown in Fig.1: The pedestal width Δ_{ped} increases with ρ_{pi} and does not depend on $\beta_{p\text{-}ped}$. The normalized pressure gradient α is almost constant at low δ, while $\alpha \propto \beta_p$ at high δ. We have found that the pedestal stored energy W_{ped} increases with the core energy (or β_p-core) at high δ (>0.3-0.4), while W_{ped} is low and almost constant at low δ (<0.2). In addition, we have expanded the type II (grassy) ELMy high confinement regime with a small heat load on to divertor plates to the low-q (q_{95}=3.8) regime at δ=0.55, and demonstrated successful compatibility of the type II ELMs with the pellet injection. Based on a variety of JT-60U H-mode experiments, possible linkages among the pedestal and the core parameters has been proposed (Fig.2).

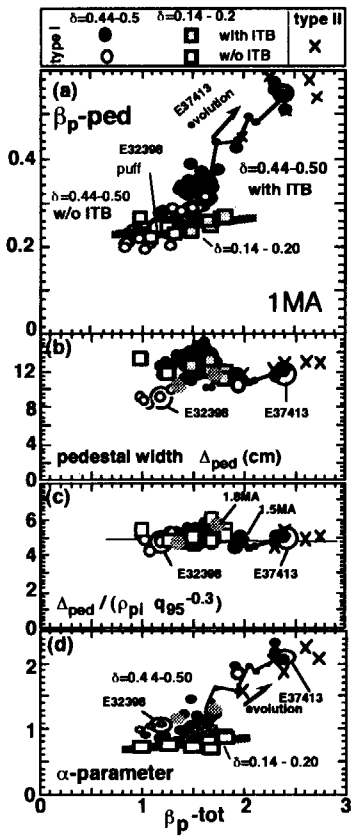

Fig.1: Total-β_p-dependence of (a) the pedestal β_p (β_p-ped) for I_p=1MA, (b) pedestal width (Δ_{ped}), (c) Δ_{ped} normalized to the scaling, and (d) the edge α-parameter.

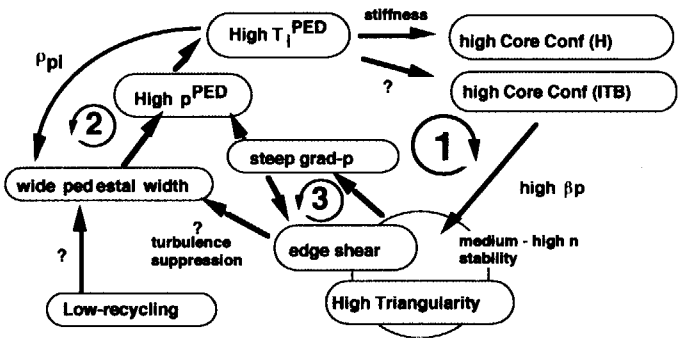

Fig.2: Possible correlations (feedback loops) among pedestal and core parameters: Loop (1) ; Improved pedestal stability (high δ, high βp, magnetic shear) steepens pedestal pressure gradient and enhances pedestal pressure (p^{PED}). High p^{PED} allows high pedestal temperature (T^{PED}). High T^{PED} improves core confinement when core kinetic profile shapes are stiff. High core confinement increases β_p. Loop (2); High T^{PED} widens pedestal width and then enhances p^{PED}. Loop (3); Pedestal pressure gradient drives bootstrap current and affects edge magnetic shear.

[1] Y. Kamada et al., Proc. 19th IAEA Fusion Energy Conference, Lyon, 2002, IAEA-CN-94 / EX / P2-04. submitted to Nucl. Fusion.

5.5 Asymmetry of Collapse of Density Pedestal by Type I ELM on JT-60U [1, 2]

N. Oyama, Y. Miura, A. V. Chankin, N. Asakura, K. Itami, T. Oikawa, H. Takenaga, M. Sugihara, Y. Kamada, K. Shinohara and the JT-60 Team

The study of the collapse of the pedestal structure due to type I ELMs is important to clarify its mechanism and to reduce its severe heat loads on the divertor target, which can erode the divertor target plate in the next step devices such as ITER. Since the ELM heat load strikes the divertor target not as a time-averaged load but as an instantaneous heat pulse, not only the evaluation of ELM energy but also the time scale of the collapse and transport from the viewpoint of individual ELM pulse is very important. In JT-60U, the study of detailed dynamics of the collapse of the density pedestal has been started using O-mode reflectometer. Expelled particles from the plasma have been measured using scrape-off layer (SOL) Mach probe and fast infrared TV camera (IRTV). These kinds of detailed ELM measurement can provide important information to develop theoretical models of ELMs.

Simultaneous fast ELM measurements using reflectometer, interferometers, D_α intensity and magnetic probe reveal the detailed characteristics of type I ELMs. From the phase signal of the reflectometer indicating the radial movement of the cut-off layer, four different phases in an ELM event and radial extent of the collapse of density pedestal up to twice the pedestal width were observed. The following three kinds of edge density measurements consistently indicate that the collapse of the density pedestal during type I ELMs in JT-60U is localized at the low-field side midplane: 1. The collapse of the pedestal density was manifested as fast inward movement of the cut-off layer at the low-field side and the increase in D_α intensity. At this time, however, no considerable reduction was observed on high-field side interferometer. 2. No density increase corresponding to the direct particle loss from the high-field side midplane to the scrape-off layer was observed in SOL/separatrix density measurements. 3. Horizontal interferometer clearly exhibited fast density loss simultaneously with the increase in D_α intensity. However, no immediate response was observed on both high- and low-field side vertical interferometers.

Expelled particles from LFS midplane were measured by using LFS midplane and X-point Mach probes together with IRTV. Time delay of the enhanced ion saturation current between the two probes, and time constant of the peak heat load and the enhancement of the plasma flow toward divertor target suggest that the convective plasma flow provides large contribution to the ELM heat load.

References

[1] Oyama, N., et al., submitted to Nucl. Fusion.
[2] Oyama, N., et al., in Fusion Energy 2002 (Proc. 19th Int. conf. Lyon, 2002) IAEA-CN-94-EX/S1-1. submitted to Nucl. Fusion.

5.6 Mechanism for Energy Loss by ELMs

A.V.Chankin, N.Oyama, M.Sugihara, Y.Kamada, Y.Miura

1. Introduction

The purpose of these experiments was to clarify the mechanism for energy loss during type I ELMs and to investigate the cause of the reduction of ELM energy loss in type II ELMs. On the type I ELM physics, a number of discharges with variable type I ELM size and frequency, covered by fast edge measurements, were proposed. The ELM mechanism was to be established based on statistical analysis of the correlation between energy drop ΔW_{ELM}, pedestal temperature drop $\Delta T_{e,ped}$, pedestal collisionality $\nu^*_{e,ped}$, level of Mirnov probe fluctuations $\tilde{B}_\theta$, edge density evolution and duration of the MHD phase of the ELM τ_{ELM}.

Data from several machines indicate the reduction of type I ELM energy loss in plasmas with high pedestal collisionality ν^*_e [1]. However, other possible scalings for $\Delta W_{ELM}/W_{ped}$, e.g. relating to the parallel transport ($\tau_\parallel$) [1] or the Greenwald fraction (n_{ped}/n_{GW}), can also be considered. Previous experiments, based on the analysis of fast signals of the pedestal parameters in JT-60U [2], have revealed good correlation between the ELM energy and ν^*_e. The data available in the database, however, were insufficient to address the above issues. The main drawbacks of the existing data were lack of synchronization between different signals, since they were digitized by different ADCs, and absence of quality ELM W_{dia} measurements. These obstacles have been removed in the last campaign in 2002.

The cause of a significant reduction in $\Delta W_{ELM}/W_{ped}$ in type II ELMs compared to type I ELMs is presently not known. One possible explanation relates it to high q values necessary for obtaining this regime. Based on the calculations described in [3], it is expected that in high q plasmas unstable MHD modes have larger toroidal number n and are more spatially localized due to their shorter wavelength. They should therefore perturb a smaller region. To check this hypothesis, fast $T_{e,ped}$ measurements have been performed in a type II ELMy regime in JT-60U.

2. Type I ELM experiments

The data presented below were obtained in plasmas with the following parameters: I_p=1.0-2.3 MA, B_T= 2.0-4.1 T, input power P_{IN}=4-25 MW, triangularity δ=0.28-0.34, elongation κ=1.36-1.60, safety factor q_{95}=3-5, ELM frequency f_{ELM}=12.5-90 Hz and diamagnetic stored energy W_{dia}=1.0-5.3 MJ. Figure 1 shows that the ratio $\Delta W_{ELM}^{dia} / W_{ped}$ is below 10% in JT-60U, lower

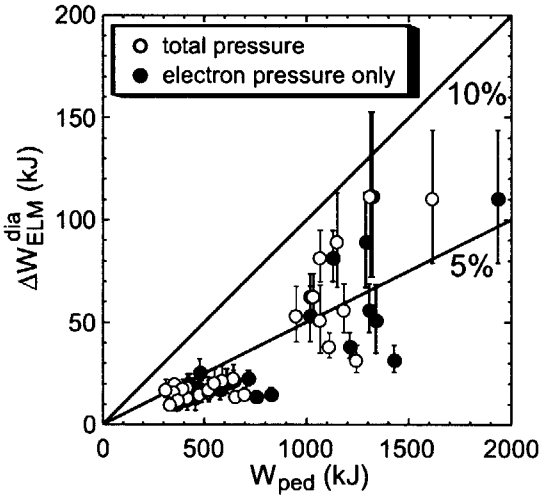

Fig. 1. ELM energy loss versus total pedestal pressure and electron pressure×2 integrated over the plasma volume.

Fig. 2. Fractional ELM energy loss versus electron collisionality of the pedestal plasma, characteristic time for ion transport from the pedestal to the divertor and pedestal density fraction to the Greenwald density limit. The data from other devices are quoted from [4].

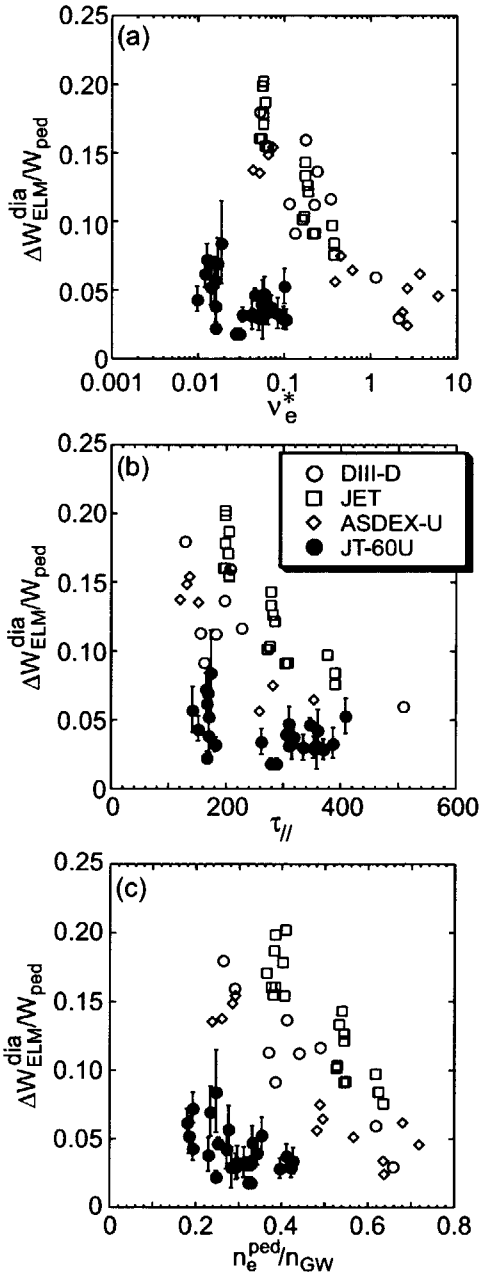

than in other major machines [4]. In Fig. 2, this ratio is plotted against the tree main figures of merit discussed above. In a typical ELMy H-mode plasma, the pedestal density is lower and temperature higher in JT-60U than in other machines. Consequently, most of the data in the collisionality dependence were clustered in lower ν_e^*

region (expected ITER value for ν_e^* is 0.035), and dynamic ranges of $\tau_{||}$ and n_{ped}/n_{GW} dependencies were also limited in JT-60U. Due to a significant scatter and limited dynamic range, it is difficult to establish any clear dependence of $\Delta W_{ELM}^{dia}/W_{ped}$ on the parameters. Figure 2 also shows that $\Delta W_{ELM}/W_{ped}$ in JT-60U is smaller than in other machines. Even if one allows for a possible factor of 1.55 correction (ΔW_{ELM} measured by the IR camera is larger by this factor than ΔW_{ELM}^{dia} in JT-60U, with ΔW_{ELM} invoked from MHD equilibrium reconstruction being in between these two values), most of the points would still lie below those from other machines. Due to small ΔW_{ELM}, despite even higher f_{ELM} in JT-60U, the calculated fraction of $f_{ELM}\times\Delta W_{ELM}$ to the heating power is 5-20%, smaller than in other machines.

3. Type II ELM experiment

Plasma configuration used for this experiment, shown in Fig. 3, was similar to the one used earlier for high β_p experiments. However, the toroidal field was raised to B_T=4T (with I_p=1MA) to allow for fast edge T_e measurements by HRS. Other parameters were: P_{NBI}≈14MW, q_{95}=6.6-7.0, δ=0.55-0.59 and β_p =1.3-1.6. Temperature profiles and waveforms of some other parameters are shown in Figs. 4,5. Out of HRS channels covering the pedestal region, only channels 5 and 6 (see Fig. 5) showed significant response to ELMs. Ch. 6, just outside the pedestal edge, showed T_e drops after each ELM, while Ch. 5 showed T_e spikes. These data allow one to eliminate a hypothesis according to which small size of type II ELMs is caused by the existence of a narrow unstable region just inside of the separatrix, whose width is

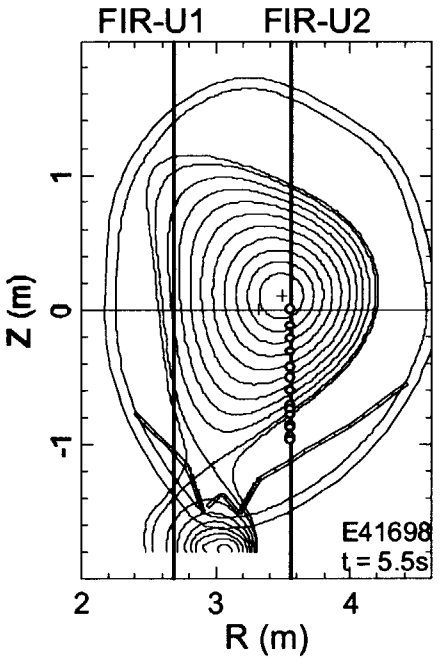

Fig. 3. Plasma configuration used for the type I ELM experiment. Open circles indicate the measured position of YAG Thomson scattering.

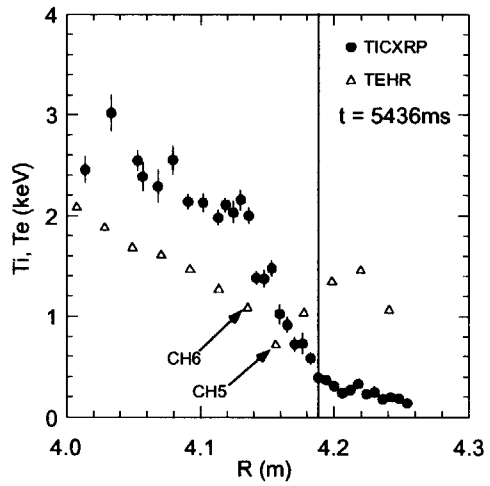

Fig. 4. Ion (full circles) and electron (open triangulars) temperature profiles in the type II ELM experiment.

much smaller than the pedestal width. T_e spikes seen on the Ch. 5 are likely to be the result of a temperature wave propagating outward following each ELM.

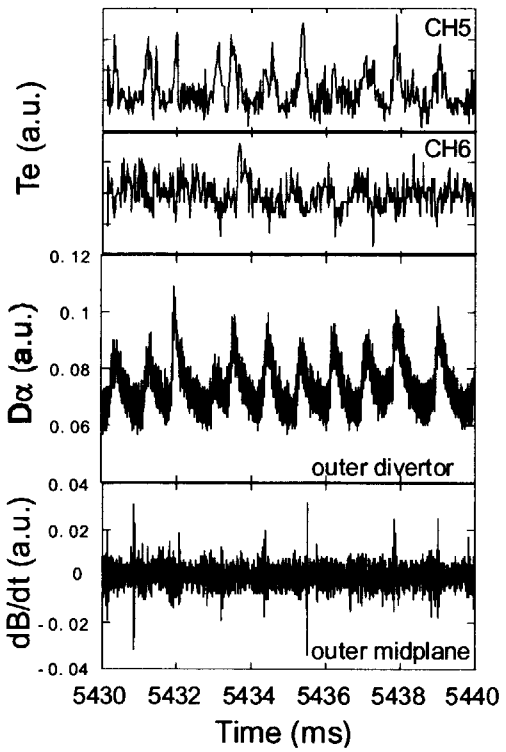

Fig. 5. Waveforms of edge Te, divertor D_α and the Mirnov probe signal in the type II ELM experiment.

4. Summary

The energy loss due to type I ELMs in JT-60U was found to be less than 10% of the pedestal stored energy. It shows weak dependence on parameters $\nu^*_{e,ped}$, $\tau_{||}$ and n_{ped}/n_{GW}. In the type II ELM experiment, fast dynamics of the edge T_e observed in the pedestal region was found to be similar to the one observed in type I ELMs. This implies that small energy drop in type II ELMs compared with type I ELMs is probably due to small amplitude of unstable modes responsible for the ELM, rather than the result of the narrowness of the unstable region.

References

[1] Loarte A, Saibene G, Sartori R et al., "ELM Energy and Particle Losses and their Extrapolation to Burning Plasma Experiments", paper P2-46 presented at 15th International Conference on Plasma Surface Interactions in Contr. Fusion Devices, May 27-31, 2002, Nagaragawa Convention Center, Gifu, Japan, to be publ. in J. Nucl. Mater.
[2] Chankin A V, Asakura N, Fukuda T et al., Nucl. Fusion **42** (2002) 733.
[3] Lao L L, Kamada Y, Oikawa T et al., Nucl. Fusion **41** (2001) 295.
[4] Loarte A, et al., 2001 Fusion Energy 2000 (Proc. 18th Int. Conf. Sorrento, 2000) (Vienna: IAEA) CD-ROM file http://www.iaea.org/programmes/ripc/physics/fec2000/html/node1.htm

5.7 Studies on H-mode Transition using 2nd Harmonic X-mode ECH

N. Oyama, T. Suzuki, H. Takenaga

1. Introduction

H-mode transition with the predominant electron heating is one of the important studies toward the realization of the H-mode plasma in ITER, since main heating devices in ITER are electron heating dominant method such as N-NBI and ECH. The H-mode transition and its properties under electron heating dominant condition using N-NBI were studied, and H-factor (H_{89}) in this plasma was similar level of that obtained by P-NBI at T_e~T_i in JT-60U [1]. In this case, the threshold power was also similar to the predicted value using P-NBI in JT-60U [2]. Thanks to the recent progress of the development of ECH system, higher ECH power up to 3.0MW with long pulse duration up to 3s has been available. To confirm the threshold power using only ECH in JT-60U will contribute to the LH power scaling study for ITER, since the effect of heating method on the LH threshold power has not been fully understood yet.

2. Experimental Result

2.1 Experimental Conditions

Because of the limited EC power, the experiments were carried out under lower toroidal magnetic field (B_T), where we expected lower threshold power. Since the higher absorption rate was also expected using 2nd harmonic X-mode ECH, the following plasma parameters were selected: I_p = 1.1MA, B_T= 2.0T, q_{95} ~ 3.2, κ ~ 1.4, δ ~ 0.27, S ~ 142m^2. As shown in Fig. 1, resonant layer of 2nd harmonic X-mode ECW was located at the plasma center, and almost all EC power was absorbed near the plasma center in this configuration. According to the H-mode threshold power scaling from closed-divertor devices [3],

$$P_{th} = 0.076[B_T]^{0.66}[\bar{n}_{20}]^{0.465}S^{0.79}(\mathrm{MW}) \quad (1),$$

the expected threshold power was about 2.3 MW for the plasma density of $\bar{n}$ =1.3×10^{19} m^{-3}, which is similar value of LH threshold power under the W-shaped pumped divertor geometry in JT-60U [2].

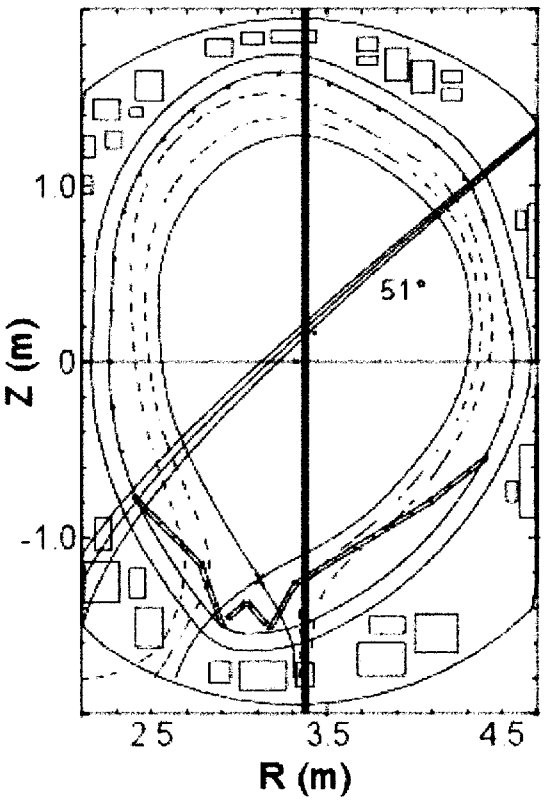

Fig. 1. Plasma configuration together with central ray of ECW and resonant position of 2nd harmonic ECW (vertical line).

2.2 H-mode Characteristics using 2nd Harmonic X-mode ECH

Figure 2 shows the typical waveforms of LH transition using 2nd harmonic X-mode ECH in JT-60U. During first 600 ms with one ECH injection (P_{EC} = 0.83 MW), the plasma remained L-mode state due to smaller heating power than LH threshold power. Then, LH transition occurred 50 ms after the increase of EC power at 9.65s. The plasma density increases following the L-H transition up to 59 % of Greenwald density limit without gas puffing as shown in Fig. 2(b) and (c).

In this plasma, type I like ELM was appeared at 10s and continued about 200 ms. The H factor (H_{89}) in this ELMy phase was 1.4. When ELM frequency increased more than 500 Hz at 10.18s, plasma confinement was started to decrease even in the same EC power. (just

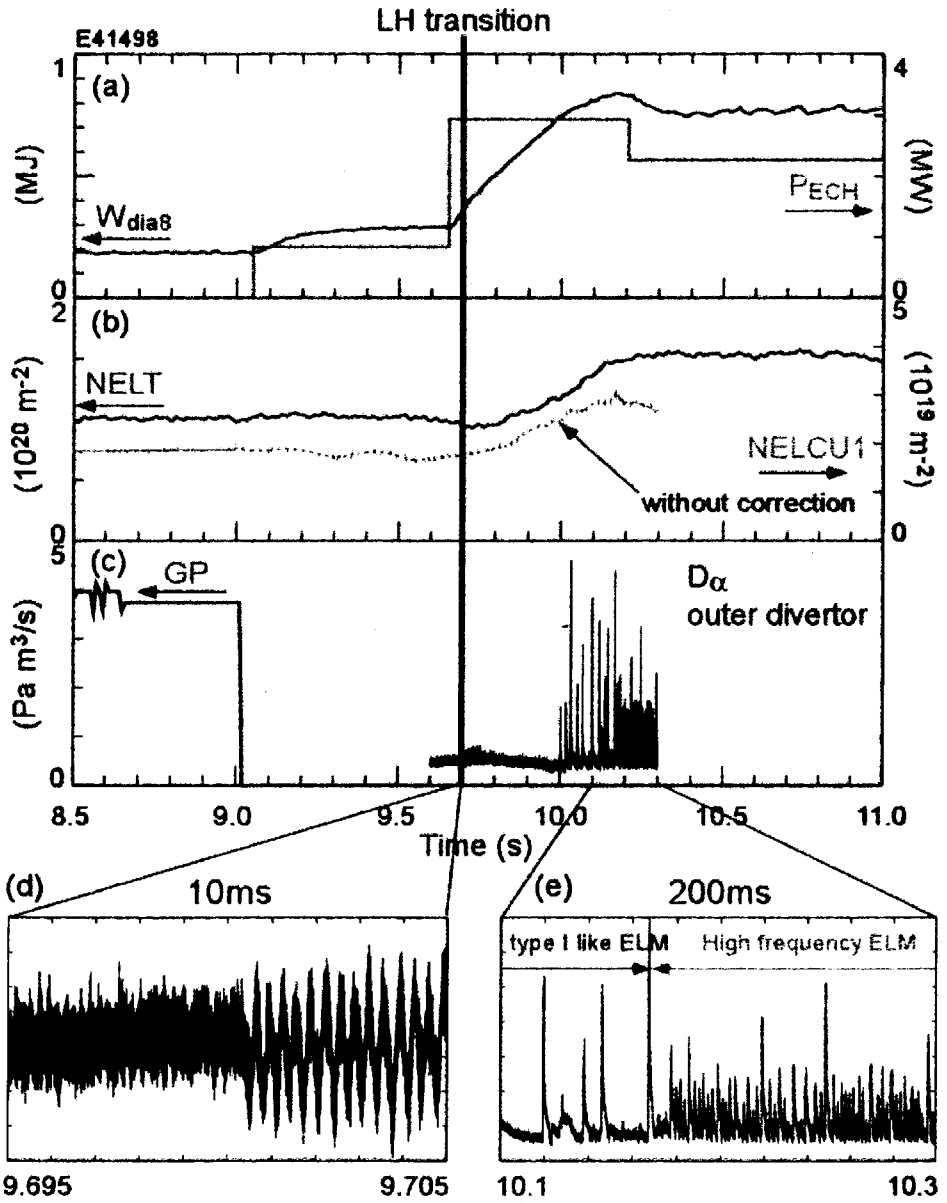

Fig. 2. Typical waveforms of the LH transition using 2nd harmonic X-mode ECH. (d) and (e) show the expanded view of the divertor D_α signal. Dotted line in (b) after 9s shows line-integrated density of FIR-U1 without fringe correction.

before EC power reduction). Since heating power, edge density and temperature were almost constant just before this frequency change, the cause of the phenomenon was unclear. Looking at the time evolution of the D_α intensity, last type I ELM may trigger the change of ELM frequency or ELM type. Figure 3 shows the electron density and temperature profile in L- and H-mode phase. Although the pedestal structure was not clear, the increase of the plasma density in the whole region was observed without gas puffing. On the other hand, edge temperature remained in the low level comparing to the core region.

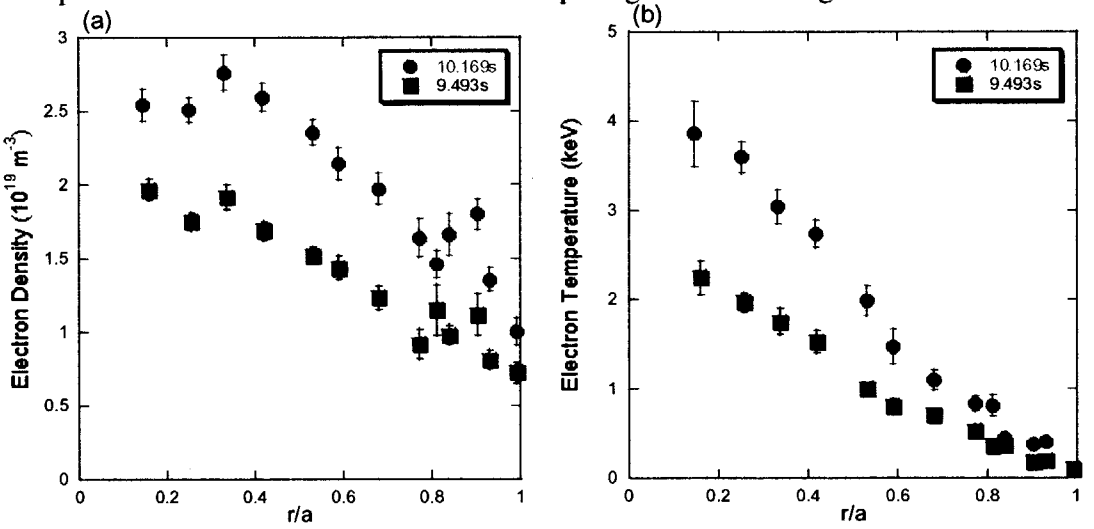

Fig. 3. Electron density and temperature profiles in L- (square) and H-mode (circle).

2.3 Comparison of LH Threshold Power Between P-NBI and ECH

The threshold power of L-H transition is defined by $P_{LOSS} = P_{ECH} + P_{OH} - \frac{dW}{dt}$, which is same definition as Ref. 1 and 2. Figure 4 shows the threshold power as a function of the line-averaged density. The dynamic range of the density was limited by the lower plasma current than the P-NB case, because of lower magnetic field in order to obtain lower threshold power in this experiment. It is noted that the line-averaged density for ECH H-mode case was evaluated using CO_2 laser interferometer. Comparing to the P-NB heating case in JT-60U, the threshold power for ECH case seems to be smaller than that for P-NB case, when the difference of triangularity of target plasma, 0.16 for PNB case and 0.27 for ECH case, was not considered. The threshold power of the ECH H-mode was also smaller than that from the scaling as shown in Eq. (1).

Looking at the no transition case in Fig. 4, although the P_{LOSS} for no transition case was about 20% higher than the P_{LOSS} for smallest case, the plasma remained L-mode phase. One possibility of the reason is density dependence of the threshold power. However, lower boundary of the P_{LOSS} for higher density region ($\bar{n}$ >2.0×10^{19}) was not clear in the current database, because of the large one step of the EC power and difficulty of the target density control. To confirm the threshold power in whole density range, further systematic experiments with careful operation scenario are required.

2.4 Effect of Pellet Injection on LH Threshold Power and ELM Characteristics

In DIII-D, the reduction of threshold power by 33% was observed with pellet injection [4]. However, the physical mechanism of the reduction has not been understood yet. The local fueling by pellet injection would provide transient steep density gradient near the pedestal, which might change the ELM characteristics through the change of the edge stability. Therefore, the effects of pellet injection on the threshold power and ELM characteristics were studied. The EC power was increased stepwise by 0.8, 1.43 and 2.11 MW during pellet injection. However, the threshold power was almost the same as the only ECH case as shown in Fig. 4. Since the LH transition occurred between pellets, the direct effect of the pellet injection was not observed so far. On the other hand, when the pellet injected during ELM free phase with 2.31 MW EC power, the type III like ELM was appeared again together with the small increase of the stored energy as a result of the increase of the plasma density.

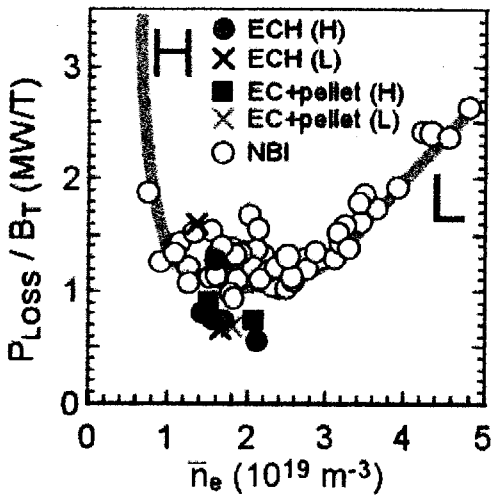

Fig. 4. Threshold power of the H-mode transition as a function of line averaged density. Open circles show H-mode plasma with P-NBI [2]. Closed symbol and crosses show the H- and L-mode, respectively. Line-averaged density for ECH H-mode was using CO_2 laser interferometer.

3. Summary

Using 2nd harmonic X-mode ECH, the H-mode plasma with ELMs was obtained. The H-factor of 1.4 for ECH H-mode plasma was obtained during type I like ELMy phase. The effect of pellet injection on the threshold power was not observed clearly. Because of the limitation of the EC heating power and difficulty of the target density control, the experiments were only covered narrow dynamic range of the line-averaged density. Therefore, further systematic experiments are required in order to confirm the threshold power using ECH in JT-60U. More data in higher density region, $\bar{n} \geq 2.2\times10^{19}$m^{-3}, will contribute to H-mode power threshold database for ITER.

References

[1] Oikawa, T., et al., Nucl. Fusion. **40**, 435 (2000).
[2] Fukuda, T., et al., Plasma Phys. Control. Fusion **42**, A289 (2000).
[3] Snipes, J. A., et al., Plasma Phys. Control. Fusion **42**, A299 (2000).
[4] Gohil, P., et al., Bull. Am. Phys. Soc. **44**, 73 (1999), Baylor, L. R., Phys. Plasmas, **7**, 1878 (2000)

6. MHD Instability and High-energy Ions

6.1 Real-time Stabilization of Neoclassical Tearing Mode [1]

A. Isayama, K. Nagasaki[1)], T. Fukuda and S. Ide
1) Institute of Advanced Energy, Kyoto University

Stabilization of NTMs by EC is important to sustain high beta plasmas. In JT-60U, it was demonstrated that the 3/2 NTM can be completely stabilized by injecting the fundamental O-mode EC wave to the center of the magnetic island. At the same time, it has been found that the precise adjustment of EC injection angle is indispensable in order to achieve the complete stabilization. In case the deposition location is misaligned by only about half of the island width (~several centimeters), the stabilization effect by EC was significantly decreased.

In 2002, extensive development has been made in the real-time control system, where the plasma shape is first reconstructed in real-time (every 10 ms) with the Cauchy condition surface method [2], and the mode location is coarsely estimated. Subsequently, fine tuning is performed by evaluating the electron temperature perturbation profile, utilizing the fact that an M-shaped perturbation profile is obtained at the magnetic island and that the center of the island corresponds to the local minimum point of the profile. In obtaining the perturbation profile, standard deviation of the ECE heterodyne radiometer signal is evaluated. This evaluation method has the advantage that the mode amplitude can be obtained without evaluating the mode frequency.

By the application of this system, a 3/2 NTM has been completely stabilized in high beta region (β_p~1.2, β_N~1.5), as shown in Fig. 1. By the stabilization beta value increased by about 10%. The 3/2 mode did not appear even after the turn-off of the EC wave until bN reaches 1.67. This shows confinement improvement: H-factor increased from 1.8 to 1.9. The ratio of the EC-driven current to the bootstrap current at the mode rational surface is an important parameter as a measure of the efficiency of the stabilization. According to the Fokker-Planck code and the ACCOME code, the maximum EC-driven current density at the mode rational surface is comparable to the bootstrap current density (~0.25 MA/m^2), which shows that the stabilization was effectively accomplished.

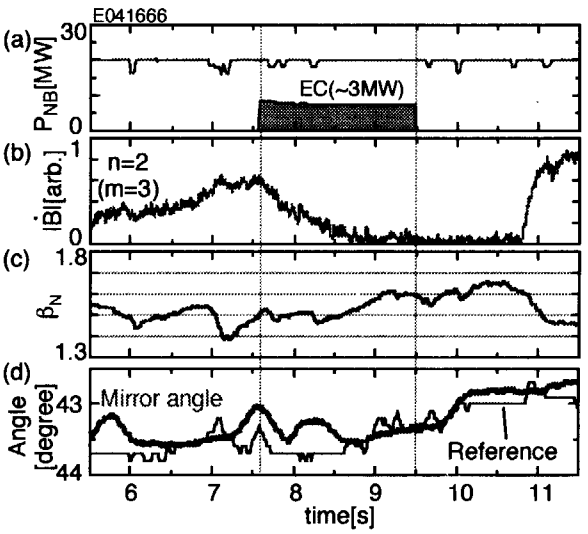

Fig. 1: Typical waveforms of a real-time NTM stabilization experiment: (a) injection power of NBs and EC, (b) amplitude of magnetic perturbations with n=2, (c) normalized beta, (d) Angle of the EC steering mirror and the target angle for feedback.

References

[1] Extended version of this paper is presented at the 19th IAEA Fusion Energy Conference, IAEA-CN-94/EX/C2-2; submitted to Nuclear Fusion.
[2] Kurihara K. *et al.*, Fusion Eng. Design **51-52**, 1049 (2000).

6.2 Stabilization Effect of Early ECCD on Neoclassical Tearing Mode [1]

K. Nagasaki[1)], A. Isayama, S. Ide and JT-60 Team
1) Institute of Advanced Energy, Kyoto University, Gokasho, Uji, Kyoto 611-0011, Japan

Suppression of neoclassical tearing mode (NTM) is an important task for sustaining high β plasma stably in tokamak devices. The electron cyclotron current drive (ECCD) is an attractive method to stabilize the NTM, since the current is driven locally at the Doppler shifted cyclotron resonance. It is theoretically predicted that the EC injection at the growth phase is more effective than at the saturation phase because of the nonlinearity of the mode growth. However, no experimental results have ever been presented how the mode responds to the EC injection timing. In JT-60U tokamak, the stabilization of an m=3/n=2 NTM has been studied experimentally by applying a local ECCD. The EC power is injected before the mode onset, and its effect is compared with the ECCD applied at the saturation phase.

When the EC power of 2.3 MW (three units) is applied before the mode onset corresponding that the calculated maximum EC driven current density is 0.23 MA/m^2 at r/a=0.49, the 3/2 mode is completely stabilized, and the normalized β, β_N of 1.5 is maintained during the EC pulse of 3 sec. On the other hand, when the same EC power is applied after the 3/2 mode evolves and saturates, the mode amplitude is decreased but not completely suppressed. In this case, the position of EC driven current is real-time controlled by detecting the mode location, because the magnetic island meanders during the discharge. The higher power of 2.9 MW (four EC units) is needed to suppress the mode completely at the saturation phase [2]. These results indicate that the ECCD at the mode growth phase is more effective to stabilize the NTM than that at the saturation phase.

The magnetic fluctuation level is much reduced when the EC power is applied before the mode onset. According to the modified Rutherford equation, the delay time of the mode onset from the NB injection can be longer as the EC power increases. The EC current reduces the growth rate of the magnetic island, and the critical width of the seed island for exciting the NTM is larger, leading that the delay time is longer. The stabilization effect is sensitive to the position of the EC driven current. The precise adjustment of the power deposition is required to achieve the effective stabilization. The mode is not suppressed well as the position of the EC driven current is deviated from the q=3/2 rational surface by the half of the island width, where the ECCD is well localized within the radius of Δr/a= 0.05. When the power absorption position is shifted outwardly from the optimum, the mode amplitude is reduced but gradually increases during the EC pulse duration.

Authors thank JAERI staff for the JT-60U operation and useful discussions. One of the authors (K. N.) is grateful to Heliotron J staff for continuous discussions. This work was supported by JT-60 collaboration research.

[1] Nagasaki K., et al., submitted to Nucl. Fusion
[2] Isayama A., et al., 19th IAEA Fusion Energy Conference, IAEA-CN-94/EX/C2-2 (2002)

6.3 Effect of ECH/ECCD on Sawtooth Oscillations in NB-heated Plasmas in JT-60U [1]

A. Isayama, S. Ide, Y. Ikeda, T. Suzuki and K. Kajiwara

Sawtooth oscillation, which is a kind of magnetohydrodynamic instabilities in the central region of a plasma, has been observed in many devices since 1970s. Although a number of experimental and theoretical research have been done, underlying physics of the sawtooth oscillations has not been fully understood yet. Effects of additional heating and/or current drive tools on sawtooth oscillations have been investigated in many devices: For example, in JT-60/JT-60U, behavior of sawtooth oscillations during neutral beam (NB) injection, lower hybrid heating/current drive, ion cyclotron heating, and electron cyclotron heating (ECH)/ electron cyclotron current drive (ECCD) have been investigated [2-5]. In most cases, however, these experiment have been done from the viewpoint of stabilization.

In this paper, effects of ECH/ECCD on sawtooth oscillations in NB-heated plasmas have been investigated. In particular, we have investigated the destabilization effect by EC injection inside the inversion radius. It has been found that sawtooth period can be significantly decreased by injecting EC wave in co-direction. In this case, the normalized sawtooth period $\tau_{ST}/T_e(0)^{1.5}$ reaches 1/10 of that in the OH phase. Unlike the sawtooth behavior, no significant difference in stored energy has been observed between the co- and counter-ECCD cases. One of the reasons is that energy released by a sawtooth crash is small since inversion radius is small in this series of discharges. While the reachable central electron temperature for the co-ECCD case is similar to that for the counter-ECCD case, the central electron temperature averaged over one sawtooth period for the co-ECCD case is lower than that for the counter-ECCD by several percents. This suggests that heat and particles in the core region can be effectively expelled by co-EC injection without serious confinement degradation.

References

[1] Isayama A *et al.*, Journal of Plasma and Fusion Research SERIES **5**, 324 (2002).

[2] Ishida S *et al.*, Nucl. Fusion **30**, 552 (1990).

[3] Kamada Y *et al.*, Nucl. Fusion **33**, 225 (1993).

[4] Kimura H *et al.*, *Radio Frequency Power in Plasmas* (AIP Conference Proceedings 289), American Institute of Physics, New York, 1994, ISBN 1-56396-264-0, pp.52-55.

[5] Isayama A *et al.*, Fusion Eng. Design **53**, 129 (2001).

6.4 Property of Alfven Eigenmode in JT-60U Reversed Shear and Weak Shear Plasmas

M. Takechi, A. Fukuyama[1], K. Shinohara, M. Ishikawa[2], Y. Kusama, S. Takeji, T. Fujita, T. Oikawa, T. Suzuki, N. Oyama, T. Ozeki, A. Morioka, C. Z. Cheng[2], N. N. Gorelenkov[2], G. J. Kramer[2], R. Nazikian[2]

1) Department of Nuclear Engineering, Kyoto University, Kyoto 606-8501, Japan.
2) Plasma Research Center, University of Tsukuba, Tsukuba-shi 305-8877, Japan.
3) Princeton Plasma Physics Laboratory, Princeton, NJ 08543, USA

A reversed shear (RS) plasma is potentially an efficient operation mode for steady state tokamak reactors with good confinement and a large bootstrap current fraction. MHD instabilities driven by energetic particles such as the Toroidal Alfven Eigenmode (TAE) and the fishbone have been extensively studied especially in positive shear plasmas. However, characteristics of Alfven Eigenmode (AE) in RS plasmas is not well-known, e.g., puzzling AEs have been observed with large and rapid upward chirping in frequency, which cannot be explained by TAE type modes. We performed NNB-AE experiment in JT-60U RS plasmas with accurate q-profile measurement to investigate the property of AEs in RS plasmas [1]. We provide a theory of the reversed-shear-induced Alfven Eigenmode (RSAE) model to interpret the observed fast frequency chirping AEs [2]. The accurate reconstruction of q-profile is required for AE study. The experiments were carried out with a relatively high toroidal field of 3.73 T and plasma current of 1.3 MA, because the q-profile measurement is more accurate with a higher magnetic field. Furthermore, to compare the experimental results with the RSAE model, the position of q_{min} was formed at the more outer region of plasma as possible and the value of q_{min} was reduced to below 3. The n = 1 NNB-AEs with a rapid frequency sweeping and then saturation of frequency as q_{min} decreases were observed in these plasmas and can be explained by RSAEs and the transition from RSAE to TAE, respectively. The previously observed rapid frequency sweeping of ICRF-AE with n > 1 in JT-60U RS plasmas can also be well explained by the RSAE model. The AE amplitude is maximum during transition from RSAE to TAE, e.g., $\sim 2.4 < q_{min} < \sim 2.7$ for the n=1 mode. The n=1 AE seems to be the largest mode in RS plasmas, because when β_h is relatively low ($\beta_h < \sim 0.2$ %), only n = 1 AE is observed. From the RSAE model, RSAEs with n transit to TAE n times when q_{min} decrease by unity. Therefore, n = 1 RSAE transits to TAE only once. It is preferable to operate RS plasmas outside of the q_{min} transition range for n = 1 AE to avoid the largest amplitude AE.

We newly installed a six channel neutron profile monitor to measure 2.45 MeV DD fusion neutron profiles for investigation of fast ion behavior [3]. By using this neutron profile monitor, we observed the redistribution of fast ions in weak shear (WS) deuterium discharges with $B_t \sim 1.2$ T and $\beta_h \sim 0.6$ %, when large bursting AEs were destabilized. As opposed to this, substantial fast ion loss was observed in RS deuterium discharges with $B_t \sim 2.1$ T and $\beta_h \sim 0.4$ %, when the n = 1 mode amplitude became large at transition from RSAE to TAE. Difference in transport of fast ions seems to be explained by the difference of the structure of eigenfunctions of these AEs in WS and RS plasmas.

References

[1] M. Takechi et al., the 19th IAEA Fusion Energy Conf., Lyon 2002, EX/W-6.
[2] A. Fukuyama et al., the 19th IAEA Fusion Energy Conf., Lyon 2002, TH/P3-14.
[3] M. Ishikawa et al., submitted to Review of Scientific Instrument (2002)

6.5 Enhanced Beam Stopping Cross-section by Fast Ions Generated by N-NB

K. Okano[1)], N. Umeda, Y. Kamada, K. Tobita
1) Central Research Institute of Electric Power Industry (CRIEPI), Tokyo, Japan

In toroidal systems such as tokamak, circulating fast ions generated by neutral beam injection can affect the beam stopping cross-section of the neutral beam itself, because of the interaction between the neutrals and the fast ions[1]. The contribution to the beam-stopping cross-section by this "beam-particle self-interaction (BPSI) " can be notable especially in the case of comparatively low density plasma and high beam energy (>>100 keV). The point-model formula of BPSI has suggested that, in some low density cases, the increment rate of cross-section could be larger than the increment due to the multi-step ionization process[2]. An improved formula has been programmed into a tokamak simulation code, where beam power deposition profiles are calculated in 3-D real space. The overall enhancement of beam stopping cross-section has been evaluated by comparing the beam shine-through power with and without BPSI. Since the BPSI effect depends on the absorbed beam power, the calculation has been done iteratively in order to obtain the self-consistent solution. It is shown that the BPSI effect will be marginally detectable in JT-60U with both of H_0- and D_0- beam by injecting the power of 2-3 MW at 350keV [3].

In a campaign of JT-60U experiments in 2001, several shots were devoted to the detection of BPSI effect. There are two N-NB lines in JT-60U system. The each beam power was 2-3 MW in the typical cases. In the BPSI experiment, one of N-NB lines is injected first in the target plasma sustained at $2\text{-}3\times10^{19}m^3$. The fast ion flow in the plasma due to this first N-NB line will build up within about 1 seconds, which depends on the beam slowing down time. Then, a second N-NB line is triggered after 0.5 seconds. Note that a lower density results in a larger BPSI effect but requires a longer beam pulse. The change due to the BPSI can be known from the data of a single shot, by comparing the shine-through of 1st and 2nd beams just after each injection trigger. Weakness of this method is that the beam power to build the fast ion flow becomes half and the magnitude of BPSI effect might be half. The data from those initial experiments shows that the magnitude of BPSI is still marginal to detect. The further analysis is mainly obstructed by the noise of IR camera to detect the shine-through power on the wall. The S/N ratio will be improved if a longer duration of N-NB can be injected in a lower density plasma. Since the N-NB pulse has been extended during in 2002, the BPSI experiment with a longer N-NB pulse will be planed in the next campaign of JT-60U.

References

[1]Okano, K., Nuclear Fusion **31**(1991)1349.
[2]Janev, R.K. Boley, C.D., Post, D.E., Nucl.Fusion **29**(1989)2125.
[3]Okano, K., et al., P2.88 in Proc. 28th EPS Conf. on Contr. Fusion and Plasma Phys. (2001)

7. Disruption and Plasma Equilibrium

7.1 Characterization of Axisymmetric Disruption Dynamics toward VDE Avoidance

Y. Nakamura, R. Yoshino,
R. Granetz[1],G. Pautasso[2], O. Gruber[2] and S.C. Jardin[3]
1) Plasma Science and Fusion Center, MIT, Cambridge, Massachusetts 02139, USA
2) MPI für Plasmaphysik, EURATOM Association, D-85748 Garching, Germany
3) Princeton Plasma Physics Laboratory, PO Box 451, Princeton University, NJ 08543, USA

Forced disruption experiments under collaboration with Alcator C-Mod and ASDEX-Upgrade, and MHD simulations by using of Tokamak Simulation Code (TSC) [1] have explicated the underlying mechanisms of Vertical Displacement Events (VDEs) and a diversity of axisymmetric disruption dynamics. First, any tokamak has been verified to possess its own neutral point, which is known as an advantageous vertical plasma position to avoiding VDEs during the plasma current quench [2-4]. The vertical location of the neutral point is also revealed to be fairly insensitive to plasma shape and current profile parameters. Secondly, a rapid flattening of the plasma current profile frequently seen at thermal quench is newly clarified to play a substantial role in dragging a single null-diverted plasma vertically towards the divertor. As a consequence, the occurrence of downward-going VDEs predominates over the upward-going ones in bottom-diverted discharges, more specific to the ASDEX-Upgrade than the JT-60U.

Figure 1 shows vertical excursions of the plasma current centroid due to the disruption induced VDE in the ASDEX-Upgrade [5]. The neutral point, which is supposed to be linked up closely with a geometry of shell structures and plasma shaping coils being much different from tokamak to tokamak, was numerically determined at ~ +5 cm above the horizontal midplane, being insensitive to the plasma shape and current profile parameters. For limiter discharges that are essentially up-down symmetric (closed circles), the neutral point of the ASDEX-Upgrade was consistent with the TSC simulation. Disruption experiments conducted by killer-pellet injection were carried out in Alcator C-Mod to identify the location of the neutral point. The disruptive plasmas initially positioned around the numerically determined neutral point (Z = + a few cm) exhibit upward- or downward-going VDEs in accordance with the TSC prediction. It thus follows that the neutral point is experimentally confirmed to widely exist as well as the JT-60U.

On the other hand, diverted discharges of the ASDEX-Upgrade (Fig. 1) exhibit a wide variety of VDE behaviors, implying that a unique neutral point does not exist in the up-down asymmetric, as it does in JT-60U and Alcator C-Mod. For the bottom-diverted configuration

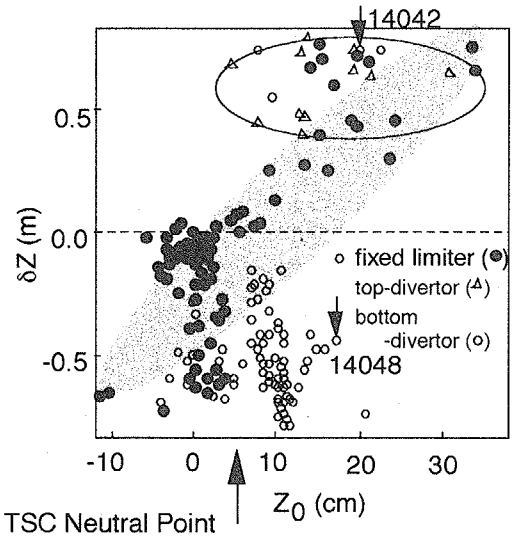

Fig. 1. Experimental excursions versus initial position. Neutral point of limiter plasmas is seen at ~5 cm above horizontal midplane as predicted by TSC simulations, whereas bottom-diverted plasmas exhibit downward (#14048) or upward VDEs (#14042).

(open circles), notice that even the discharges initially positioned considerably above the numerically determined neutral point exhibit downward-going VDEs, contrary to the TSC prediction (*e.g.* #14048). However, several exhibit upward-going VDEs in accordance with the TSC (*e.g.* #14042). Both initial equilibria of the shots #14042 and #14048 are very similar in shape (κ = 1.6, δ = 0.25) and position (Z ~ 18 cm >> the TSC neutral point : ~ 5 cm). A remarkable disparity between these two disruptions is the different change of the internal inductance, Δl_i ~ -0.7 of #14048 and ~ -0.3 of #14042, which has been often observed during the thermal quench stage prior to the plasma current quench [6].

Figure 2 obtained by the TSC simulation displays a vertical dragging effect that arises from a rapid change of the current profile of single null-diverted plasmas [5]. The newly clarified effect indicates that as the current profile becomes broad ($\Delta l_i < 0$), the plasma tends to drag itself toward divertor, whereas a current peaking ($\Delta l_i > 0$) pulls the plasma out of the divertor. Those substantially depend on a measure of the up-down asymmetry γ (= Z_l/Z_u). A value of γ = 1 denotes an up-down symmetric, double null-divertor configuration, while $\gamma > 1$ ($\gamma < 1$) denotes a bottom (top)-divertor. It thus follows that the significant change of Δl_i ~ -0.7 may drag the bottom-diverted plasma (#14048) below the neutral point to cause a downward VDE due to the following plasma current quench. Meanwhile, the small change of Δl_i ~ -0.3, being insufficient to dragging the plasma (#14042) downward, leaves the plasma much above the neutral point even after the thermal quench. Consequently, it undergoes an upward VDE. In case of the limiter or double null-divertor (γ = 1) (such as the closed circles, Fig. 1), the dragging effect is always absent, consistent with the simulation. It is also demonstrated how the dragging effect, together with that of the imbalanced attractive force that may vanish at the neutral point, can explain the precise details of VDE dynamics over the whole period of the disruptive termination in ASDEX-Upgrade.

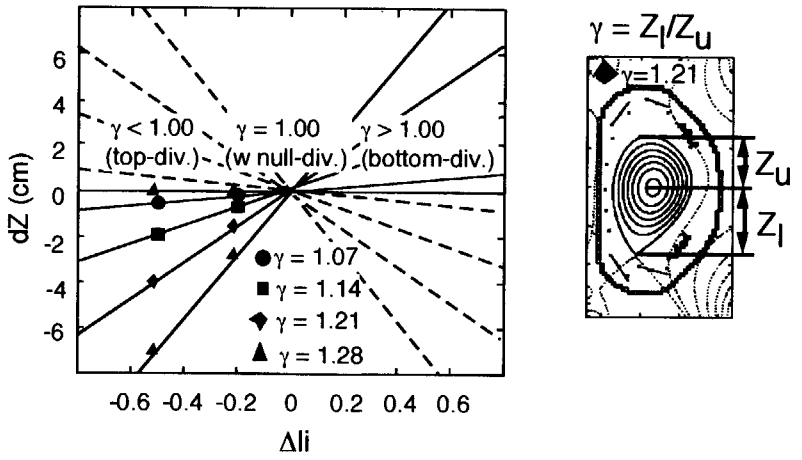

Fig. 2. Current profile changes (Δl_i) and vertical dragging effect (dZ), which substantially depends on up-down asymmetry γ (= Z_l/Z_u) of single null-divertor, and is absent in double null-divertor (γ = 1). Z_l or Z_u means respective vertical distance between magnetic axis and bottom or top edge of outermost flux surface. Dragging toward divertor at flattening ($\Delta l_i < 0$), whereas pulling out of divertor at peaking ($\Delta l_i > 0$).

It turned out that the new concept of the dragging effect strongly depends on a measure of the up-down asymmetry of the single null-diverted plasmas which closely connects with how apart a divertor coil is standing from the plasma, *e.g.* a far divertor coil of the ASDEX-Upgrade (outside the toroidal field coils) in contrast to near ones of the JT-60U and Alcator C-Mod (inside the toroidal field coils). As a consequence, it has been clarified that the dragging effect is more remarkable in the ASDEX-Upgrade than the others like the JT-60U, and that such various dragging effect brings the disrupting plasmas a diversity of VDE dynamics [7].

References

[1] Jardin, S.C., et al., J. Comput. Phys. **66**, 481 (1986).

[2] Nakamura, Y., et al., Nucl. Fusion **36**, 643 (1996).

[3] Yoshino, R., et al., Nucl. Fusion **36**, 295 (1996).

[4] Pautasso, G., Egorov, S., Finken, K.H., Gruber, O., Herrmann, A., Fuchs, C.J., Maraschek, M., Neu, G., Nakamura, Y., et al., IAEA-CN-94/EX/P4-14, Lyon, France (2002).

[5] Nakamura, Y., et al., Plasma Phys. Control. Fusion **44**, 1471 (2002).

[6] Taylor, P.L., et al., Phys. Rev. Lett. **76**, 916 (1996).

[7] Nakamura, Y., Yoshino, R., Granetz, R.S., Pautasso, G., Gruber, O. and Jardin, S.C., IAEA-CN-94/EX/P4-13, Lyon, France (2002).

7.2 Fast Plasma Shutdown Scenarios in the JT-60U Tokamak Using Intense Mixed Gas Puffing [1]

M. Bakhtiari[1)*], Y. Kawano, H. Tamai, Y. Miura, R. Yoshino, Y. Nishida[1)]
1) Energy and Environmental Science, Graduate School of Engineering, Utsunomiya University, 7-1-2 Youtoh, Utsunomiya, Tochigi 321-8585, Japan

Disruptions may result in large currents and forces in vacuum vessel, localized energy deposition on the plasma facing components from runaway electrons, and high heat fluxes due to the loss of stored energy. Terminating the discharges faster than the plasma movement at the disruption and also enhancing the radiation power to prevent concentrated heat fluxes whilst avoiding the runway electron generation are the aims of fast plasma shutdown systems in large tokamaks. Three methods have been proposed to terminate a discharge during a disruption so far; 1) injecting high-Z species into the plasma to radiate away the energy of plasma[2], 2) delivering large amounts of low-Z species into the plasma in a short time to enhance the radiation as well as the electron density [3], 3) delivering a mixture of small amounts of high-Z species and large amounts of low-Z species into the plasma [4]. In the third method the high-Z species radiate away the energy of plasma and low-Z species increase the electron density to avoid runaway electron generation and also enhance the radiation by high-Z species. We examined those three methods of plasma shutdown techniques in similar plasma conditions to compare their efficiency. The gas puff system was employed to deliver the species into the plasma. Discharges terminated by argon (high-Z) gas puffing were followed by runaway electron generation. On the other hand, intense hydrogen (low-Z) gas puffing terminated the discharges without runaway electron generation but the procedure was much slower than that by the argon gas puffing. Simultaneous puffing of small amounts of argon and large amounts of hydrogen led to terminate the discharges in a short time without runaway electron generation.

References

[1] Bakhtiari, M., et al., Nucl. Fusion **42,** 1197 (2002).
[2] Yoshino, R., et al., Plasma Phys. Control. Fusion **39,** 313 (1997)
[3] Rosenbluth, M.N., et al., Nucl. Fusion **37,** 1355 (1997).
[4] Bakhtiari M. et al Fusion Science & Technology **41,** 77 (2002).

* present address: JAERI, JFT-2M Group

7.3 A New Scheme of Plasma Shape Reconstruction Based on the CCS Method with the Axisymmetric Forward-Problem Solution of Eddy Currents for the JT-60 Equilibrium Analyses

K. Kurihara and JT-60 Control Group

1. Introduction

Magnetic measurements have been employed in plasma shape and position reconstruction as the most reliable diagnostics in the past and existing tokamaks. An accurate reconstruction requires to extract magnetic field information produced by a plasma solely. It, however, has been well recognized that eddy currents, induced in the vacuum vessel by varying fields of PF (Poloidal Field)-coils and a plasma, inevitably make an influence on magnetic sensors. In particular, fast vertical displacement of plasma column just before disruptive instability increases amounts of eddy currents. Consequently, it is necessary to estimate/compensate the magnetic field of eddy currents, to calculate precise equilibrium shape by solving an inverse problem on a quasi-stationary Maxwell equation.

On the other hand, eddy current distribution can be uniquely obtained by solving a forward problem on magnetic field diffusion under the condition that the structures and materials of the eddy-current-source conductors (e.g., a vacuum vessel) be completely known, and that the time evolution of magnetic field be completely provided.

As a reflection of these facts, we have proposed a new scheme that a forward problem (where a tentative plasma position is known, and eddy currents are unknown), and an inverse problem (where eddy currents are known, and a plasma shape is unknown) are simultaneously solved. In the application of this method to JT-60, the improvement of accuracy in shape reproduction is reported.

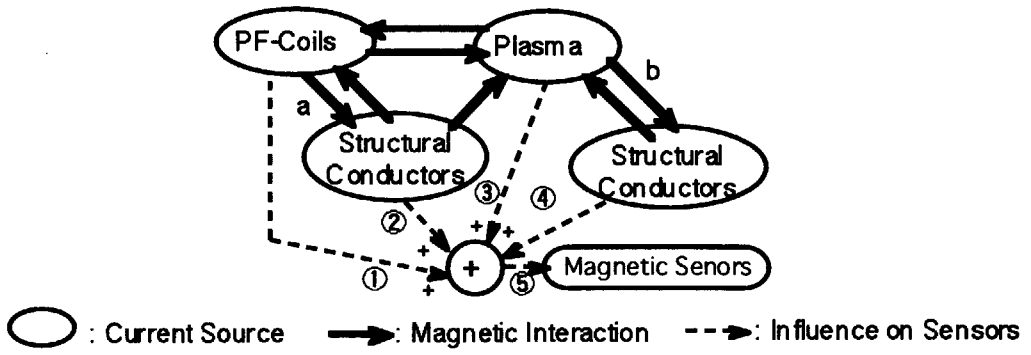

Fig. 1 Concept of Electromagnetic Interactions and Current Sources in a Tokamak

2. Problems

In the equilibrium reconstruction analyses, the current-source elements and electromagnetic interactions are shown in Fig. 1. Magnetic sensors measure the field produced by the currents flowing in the conductors, which is also shown in the same figure. Through operational experiences in JT-60, the following cases with problems have been recognized (Table 1 shows the summary.):

• Case 1: In addition to neglecting eddy currents, by subtracting only the PF-coil effect from the sensor signals, the remainders are assumed to show magnetic field produced by a plasma solely, and are employed for shape reconstruction. In a transient period, however, it has been observed that the error becomes large.

• Case 2: Many one-turn filament currents to simulate the real vacuum vessel are determined in a sense of least-squares. In most results from actual application, filament current distributions show some inconsistency with physical prediction or an ill-posed problem.

• Case 3: Through the analyses utilizing dry run of PF coils, it has been recognized that there exist eddy currents with longer time constants than those calculated under the assumption of the axisymmetric vacuum vessel. It is considered that these local eddy currents make an influence on magnetic sensors as "noise" in a certain level.

Table 1 Comparison of the new schemes with the existing analyses

<table>
<tr><th colspan="3">Current Source & Sensor</th><th colspan="2">Existing Methods of Shape Reproduction</th><th colspan="2">New Scheme of Shape Reproduction</th></tr>
<tr><td>①</td><td>PF-Coil Current</td><td>known</td><td>Employed</td><td rowspan="5">(⑤-①)is assumed to show magnetic field produced by a plasma solely.
==> The error of reproduction is large particularly in a transient period.

*Eddy current④ is identified as a lot of filament currents by IPS. But an inconsistent result cannot be avoided due to an ill-posedness.</td><td>Employed</td><td rowspan="5">Employing ①, eddy currents ② are calulated through FPS-a.

Employing ⑤-(①+②), after the plasma current center is identified, eddy currents ④ are calulated through FPS-b.

Employing [⑤-(①+②+④)] as the pure field from a plasma, the plasma shape is reconstructed through IPS.

(Again, eddy currents ④ are calulated through FPS-b. The convergence is checked)</td></tr>
<tr><td>②</td><td>Eddy Current Induced by PF-Cois</td><td>unknown</td><td>Neglected</td><td>Forward Problem Solution</td></tr>
<tr><td>③</td><td>Plasma t</td><td>unknown</td><td>Inverse Problem Solution</td><td>Inverse Problem Solution</td></tr>
<tr><td>④</td><td>Eddy Current Induced by a Change of a Plasma</td><td>unknown</td><td>Neglected or Inv. Prm Solution*</td><td>Forward Problem Solution</td></tr>
<tr><td>⑤</td><td>Magnetic Sensors (Flux loops, Pick-up Coils, etc.)</td><td>known</td><td>Employed</td><td>Employed</td></tr>
</table>

The symbols ①-⑤ and a-b correspond to the same symbols shown in Fig. 1.
IPS : Inverse Problem Solver and Solution, FPS : Forward Problem Solver and Solution.

3. A New Scheme for Shape Reconstruction

To solve the problems mentioned above, we propose a new scheme as described below. First of all, two forward solvers for eddy current have been newly developed corresponding to two causes to drive eddy current (variation of the PF coils and a plasma displacement).

• Eddy current induced by variation of the PF coil currents

We have composed the system model that can reproduce the output signal for each sensor only from the PF-coils currents input through analyses of dry run using the PF-coils in JT-60. We assume that the direct influence of the local eddy currents by way of magnetic field on the plasma equilibrium is negligible small.

• Axisymmetric eddy current induced by plasma displacement

Before plasma full shape reproduction, the weight center of plasma current is tentatively identified from magnetic measurements. After this step, one-turn voltage induced by mutual coupling with plasma displacement is calculated at the position of filament currents having the same magnetic properties with the real vacuum vessel. Finally, eddy currents in the axisymmetric geometry are calculated.

The solutions of two forward problems compensate eddy currents effects with the sensor signal, and extract the magnetic field information produced directly and purely by a plasma. After this, the CCS (Cauchy conditioned Surface) method reconstructs plasma shapes by employing those extracted data.

4. Initial Results

In application of this scheme to shape reproduction in JT-60, the accuracy of reproduction during VDE (vertical displacement event) has been improved. This leads to the effect that the time is further extended onward to the thermal/current quench phase till shape reproduction based on the CCS method [1] starts to fail due to the fluctuations in the sensor signals (induced by the 3-dimensional phenomena in a vessel). Consequently, we come to be able to investigate VDE plasmas more precisely for a longer period of time to disruption.

5. Conclusion

The new scheme is confirmed effective to improve the performance of equilibrium shape reproduction accuracy. In addition, this can also contribute more precise analyses to investigate plasma instabilities. It is, then, proposed that this new scheme be applied to real-time control in JT-60.

References

[1] Kurihara, K., Fus. Eng. Des., 51-52 (2000), 1049
Kurihara, K., Nucl. Fus., 33 (1993), 399

8. Impurities

8.1 Effects of Electron Cyclotron Heating on Impurity Transport in ITB Plasmas [1]

H. Takenaga, S. Higashijima, N. Oyama, L. G. Bruskin, Y. Koide, S. Ide, H. Shirai, Y. Sakamoto, T. Suzuki, K. W. Hill [1)], G. Rewoldt [1)], G. J. Kramer [1)], R. Nazikian [1)], T. Takizuka, T. Fujita, A. Sakasai, Y. Kamada, H. Kubo and the JT-60 Team
1) Princeton Plasma Physics Laboratory, Princeton, New Jersey, 08543-0451, U.S.A.

It is important to develop the control method for suppressing heavy impurity accumulation inside the ITB as described in 3.9. The electron cyclotron heating (ECH) is one of the candidates for the control method, because the density clamp by ECH is commonly observed not only in tokamaks but also in helical devices. In addition, a decrease of ion temperature inside the ITB is observed in JT-60U, when ECH is applied in the high β_p mode plasma. The effects of ECH on impurity transport in the ITB region are investigated in the high β_p mode and RS plasmas.

ECH is first applied inside the ITB around r/a=0.15 with Ar puffing in the high β_p mode plasma. The line averaged electron density ($\bar{n}_e$) is substantially decreased by applying ECH. The density ITB is almost lost, while the electron and ion temperature (T_e and T_i) ITBs are kept, although the T_i ITB position slightly moves inward. In a similar discharge without Ar puffing, a decrease of T_i inside the ITB is observed during ECH with small change of $\bar{n}_e$. Ar could affect the large reduction of $\bar{n}_e$ during ECH. The thermal confinement is decreased from HH_{y2}=1.0 before ECH to 0.9 during ECH. The central soft x-ray signal is drastically reduced by a factor of more than 2 when ECH is applied, indicating the Ar exhaust from the inside of the ITB. A possible mechanism for the Ar exhaust is as follows. First, the density is clamped by ECH and the density gradient becomes small. Then, Ar is exhausted due to the reduction of neoclassical inward convection velocity. Also, the Ar exhaust reduces the density. These processes could interact as a positive feedback loop for Ar exhaust. In fact, the reduction of the neoclassical inward convection velocity due to the reduction of density gradient can explain the change of measured soft x-ray profile by assuming 4 times larger diffusivity than the neoclassical value in the ITB region.

In the RS plasma, ECH is also applied inside the ITB around r/a=0.2 with Ar puffing. The density gradient is not decreased and Ar is not exhausted in the RS plasma. Although physical mechanism responsible for the density clamp has not been understood well, the density clamp has been explained by the extra outward flux induced by ECH at the deposition layer in JFT-2M [2]. In the RS discharge analyzed here, the diffusive transport in the central region is extremely large due to existence of a current hole, and the flat density profile is observed. Therefore, the extra outward flux induced by ECH might be cancelled by the large diffusive transport, and the positive feedback loop for density clamp and Ar exhaust might not work. ECH in the RS plasma without the current hole and ECH at the ITB shoulder might be effective for the Ar exhaust. The development of the density gradient control method in the RS plasma is crucial for suppression of the Ar accumulation.

[1] Takenaga, H., et al., in Fusion Energy 2002 (Proc. 19th Int. conf. Lyon, 2002) IAEA-CN-94-EX/C3-5Rb. submitted to Nucl. Fusion.
[2] Nagashima, K., et al., Nucl. Fusion **35**, 994 (1995).

8.2 Estimation of Confinement Times for Central and Edge Fuelled Helium

H. Takenaga, A. Sakasai, H. Kubo

1. Introduction

Efficient helium (He) ash exhaust is necessary to sustain burning plasma in a fusion reactor. The He exhaust characteristics have been investigated with the He fuelling in the plasma center by He neutral beam (He-NB) injection. In a high recycling ELMy H-mode plasma with a degraded confinement (H_{89P}~1.2), efficient He exhaust (τ_{He}^*/τ_E~3) was demonstrated in the JT-60U W-shaped divertor with divertor pumping from the private flux region. However, sufficient He exhaust is not demonstrated in plasmas with a high confinement such as low density/recycling ELMy H-mode plasma and reversed shear (RS) plasma with internal transport barriers (ITBs). A simple model analysis based on the He transport coefficients estimated from gas-puffing modulation experiments indicates that the He exhaust capability is not limited by the transport in the ITB region, but limited by the divertor pumping in the RS plasma [1]. In fact, τ_{He}^*/τ_E seems to be well correlated to recycling, which is closely related to divertor pumping rate, rather than the H-factor [2]. In order to show clearly that the He exhaust capability strongly depends on divertor pumping (not on core confinement), the confinement times for NB (center) and gas-puffing/recycling (edge) fuelled He are separately estimated. In section 2, the method of analysis is described. The analysis results are discussed for ELMy H-mode plasmas and RS plasmas in Section 3 and 4, respectively. Section 5 is a summary.

2. Method of Analysis

In order to separately estimate the particle confinement times for central and edge fuelled He, He particle balance for NB fuelling and gas-puffing fuelling is analyzed. For the case of NB fuelling, the He particle balance can be expressed as follows,

$$N_{He}= N_{He}^{NB} + N_{He}^{R}=\tau_{He}^{C}(S_{NB}-dN_{He}^{NB}/dt)+\tau_{He}^{E}(S_R-dN_{He}^{R}/dt), \quad (1)$$

where N_{He} is the total number of He ions, and N_{He}^{NB} and N_{He}^{R} are the number of He ions sustained by NB fuelling and recycling source, respectively. The value of N_{He} can be only measured by CXRS. τ_{He}^{C} and τ_{He}^{E} are the particle confinement times for central and edge fuelled He, respectively. S_{NB} and S_R are the He ion source rate for NB fuelling and recycling, respectively. In this analysis, τ_{He}^{E} is defined as the He confinement time including the divertor and SOL region, which means that S_R includes the He ion source in the divertor and SOL region. According to the definition of τ_{He}^{E}, N_{He} and N_{He}^{R} should include the number of He ions in the divertor and SOL region. However, the number of He ions in the divertor and SOL region is much smaller than that in the main plasma. Therefore, the number of He ions in the main plasma is only considered in this analysis. The divertor pumping rate (η) can be defined in the steady-state phase as $S_{NB}=\eta(S_{NB}+S_R)$, and then, S_R is expressed as $S_R=(1-\eta)/\eta S_{NB}$. Using this equation, eq. (1) can be rewritten in the steady-state phase as follow,

$$N_{He} =(\tau_{He}^{C}+(1-\eta)/\eta\tau_{He}^{E})S_{NB}. \quad (2)$$

For the case of gas fuelling, the He particle balance can be expressed as follows,

$$N_{He}= N_{He}^{GP} + N_{He}^{R}=\tau_{He}^{E}(S_{GP}-dN_{He}^{GP}/dt+S_R-dN_{He}^{R}/dt), \quad (3)$$

where N_{He}^{GP} is the number of He ions sustained by gas-puffing and S_{GP} is the gas-puffing rate. The He confinement time for gas-puffing is assumed to be equal to τ_{He}^{E}. The recycling source can be expressed using the divertor pumping rate in the steady-state phase as $S_R=(1-\eta)/\eta S_{GP}$.

Therefore, eq. (3) can be rewritten in the steady-state phase as $N_{He}= \tau_{He}^{E}(1+(1-\eta)/\eta)\ S_{GP}$. Since the divertor pumping rate is usually a few percent, $(1-\eta)/\eta$ is much larger than unity. Thus, N_{He} is rewritten for gas-puffing as $N_{He}\sim \tau_{He}^{E}(1-\eta)/\eta\ S_{GP}$. Here, the effective confinement time for edge fuelled He ($\tau_{He}^{E}*$) is defined as $\tau_{He}^{E}*=\tau_{He}^{E}(1-\eta)/\eta$. The value of $\tau_{He}^{E}*$ can be estimated in the steady-state phase with He gas-puffing only. By using $\tau_{He}^{E}*$, τ_{He}^{C} can be estimated in the steady-state phase with He-NB fuelling only from eq. (2).

3. Results of Analysis in ELMy H-Mode Plasmas

The analysis method described in Sec. 2 is applied to the ELMy H-mode plasmas with the plasma current (I_p) of 1.0 MA and the toroidal magnetic field (B_T) of 2.1 T. Figure 1 shows typical wave-forms with He-NB. The position of the inner strike point was changed during t=6.0-6.5 s as shown in the upper figures. The position of the inner strike point is closer to the pumping throat during t=6.5-8.0 s (small gap) compared with the position during t=4.0-6.0 s (large gap). The He-NB was injected during t=4.0-8.0 s with the D-NB heating power of 20 MW. The line averaged electron density ($\bar{n}_e$) reaches to about 70% of the Greenwald density. The density, the stored energy and the neutron yield rate are kept at constant value during t=5.0-8.0 s. The deuterium gas-puffing was applied during t=3.0-8.0 s to enhance the divertor pumping rate by producing high recycling divertor. The Dα emission intensity from the inner divertor largely increases with the large gap, indicating the recycling enhancement, and it reduces with the small gap. Although the Dα emission intensity shown in the figure does not include the emission from the inner strike point in the small gap case, the Dα emission intensity from the inner strike point in the small gap case is about half of the intensity from the inner strike point in the large gap case. The He I emission intensity in the inner divertor is also stronger than that in the outer divertor, and saturates or gradually increases with the large gap. The He I emission intensity from the inner divertor gradually decreases with the small gap. In this discharge, the He II emission intensity measured by CXRS tends to be saturated with the large gap. Time scale for saturation of the He II emission intensity is estimated to be 0.73 s. As the inner strike point moves to the pumping throat, the He II emission intensity decreases. The effective He confinement time ($\tau_{He}*=\tau_{He}^{C}+\tau_{He}^{E}*$) is estimated to be 0.57 s and 0.51 s from the He particle balance analysis with the large and small gap, respectively. The value of $\tau_{He}*$ with the large gap is smaller by about 30% than the saturation time scale for the He II emission intensity. In this discharge, the thermal energy confinement time is estimated to be

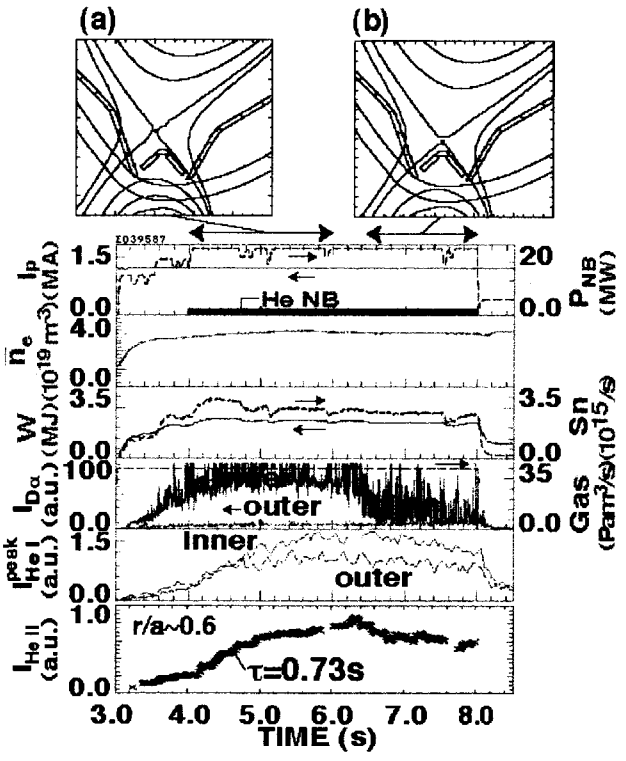

Fig. 1 Typical wave-forms of ELMy H-mode plasma with He-NB. The position of the inner strike point is changed from (a) to (b) as shown in upper figures during t=6-6.5 s.

about 0.14 s and H_{89P} is about 1.5. Thus, τ_{He}^*/τ_E is estimated to be 3.6-4.0.

In a similar discharge with He gas-puffing, τ_{He}^{E*} is estimated to be 0.28 s and 0.27 s with the large and small gap, respectively. Therefore, τ_{He}^{C} is estimated to be 0.29 s and 0.24 s with the large and small gap, respectively. The value of τ_{He}^{C} is the almost the same as τ_{He}^{E*}, indicating the similar contribution of N_{He}^{NB} and N_{He}^{R} to N_{He}. Figure 2 shows the dependence of τ_{He}^{C} and τ_{He}^{E*} on $\bar{n}_e$. For the lower density data, $\bar{n}_e$ is 50 % of the Greenwald density and H_{89P} is 1.9. For the case of He-NB, τ_{He}^* is estimated to be about 1 s from the He particle balance analysis, and τ_{He}^*/τ_E is about 5. Since the time scale of the He density increase is longer than τ_{He}^* estimated from the particle balance, more careful analysis is necessary for accurate estimation of the absolute value of τ_{He}^*. The value of τ_{He}^{C} does not strongly depend on $\bar{n}_e$ and H_{89P}. While, τ_{He}^{E*} strongly depends on $\bar{n}_e$, because the divertor recycling is enhanced in the high density region and the divertor pumping rate is higher at higher recycling. This result indicates that the low He exhaust capability in the low density discharge with a high confinement is not ascribed to the high confinement but to the low divertor pumping rate. The value of τ_{He}^{E*} is expected to be smaller for the small gap than for the large gap. However, the estimated τ_{He}^{E*} is not largely different between the large gap case and the small gap case. The deuterium pumping rate tends to depend on the outer-gap rather than the inner-gap in the both-leg pumping. The dependence of the He pumping rate on the inner-gap might be weak as well as the deuterium pumping.

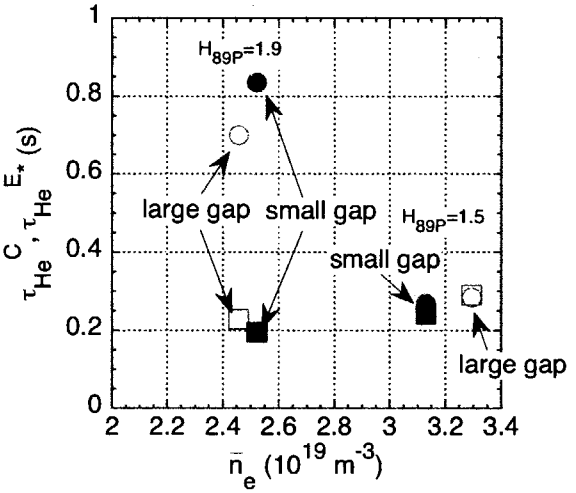

Fig. 2 τ_{He}^{C} (squares) and τ_{He}^{E*} (circles) as a function of the line averaged electron density with large gap (open symbols) and small gap (closed symbols).

4. Results of Analysis in Reversed Shear Plasmas

The same analysis method is applied to reversed shear (RS) plasmas with a strong internal transport barrier (I_p=1.3 MA and B_T=3.7 T). Figure 3 shows wave-forms of the RS plasma with He-NB. The plasma configuration is also shown in Fig. 3. Both inner and outer strike points are close to the pumping throat. The He-NB was injected from t=5.5 s after the ITB formation. The density, the stored energy and the neutron yield rate continue to increase and the steady-state phase is not obtained. The Dα emission intensity from the divertor region is one order of magnitude smaller than that in the ELMy H-mode plasma, indicating the low pumping rate due to the low recycling. On the other hand, the He I emission intensity from the divertor region is smaller only by a factor of 2 than those in the ELMy H-mode plasma. The He II emission intensity measured by CXRS inside the ITB increases during the He-NB and is not saturated. Before the He-NB injection, constant He II emission is observed. The increase of the He density inside the ITB due to the formation of the He density ITB might be balanced with the He pumping. The value of τ_{He}^* ($=N_{He}/(S_{NB}-dN_{He}/dt)$) is estimated to be 0.76 s from the He particle balance analysis. This value might be too small, because the thermal τ_E is almost the same value as τ_{He}^*. The value of τ_{He}^* estimated by an exponential fitting to the He density in the relatively steady-state phase of the RS plasma is larger by a factor of about

10 than τ_E. For accurate estimation of absolute value of τ_{He}^* from the particle balance analysis, further consideration is necessary. In the similar discharge with He gas-puffing, the steady-state phase does not obtained and the He density is not saturated.

When the He density is not steady, N_{He} in the gas-puffing case is written as $N_{He}=\tau_{He}^{E*}(S_{GP}-dN_{He}/dt)$, and the value of τ_{He}^{E*} is estimate to be 0.46 s. Similarly, for the case of He-NB, N_{He} is written as $N_{He}=(\tau_{He}^{C}+\tau_{He}^{E*})(S_{NB}-dN_{He}/dt)$ by assuming $dN_{He}/dt=dN_{He}^{NB}/dt$ or $N_{He}=(\tau_{He}^{C}S_{NB}+\tau_{He}^{E*}(S_{NB}-dN_{He}/dt))$ by assuming $dN_{He}/dt=dN_{He}^{R}/dt$. From these equations, τ_{He}^{C} is estimated to be 0.29 s and 0.21 s, although the careful consideration is necessary for the absolute value. These values are almost the same as τ_{He}^{C} in the ELMy H-mode plasma estimated in the previous section. In the RS plasma, the ITB is also observed in the He density profile. However, the ITB in the He density is weaker than that in the electron density [3]. The He confinement time in the plasmas with the ITB estimated using the He transport coefficients is not largely different from that in the plasma without the ITB [2]. The similar value of τ_{He}^{C} for both RS and ELMy H-mode plasmas is consistent with the above estimation using the He transport coefficients. The value of τ_{He}^{E*} in the RS plasma is larger than that in the high recycling ELMy H-mode plasma. The analysis results suggest that efficient He exhaust could be realized even in the high confinement RS plasma if the high recycling divertor is achieved.

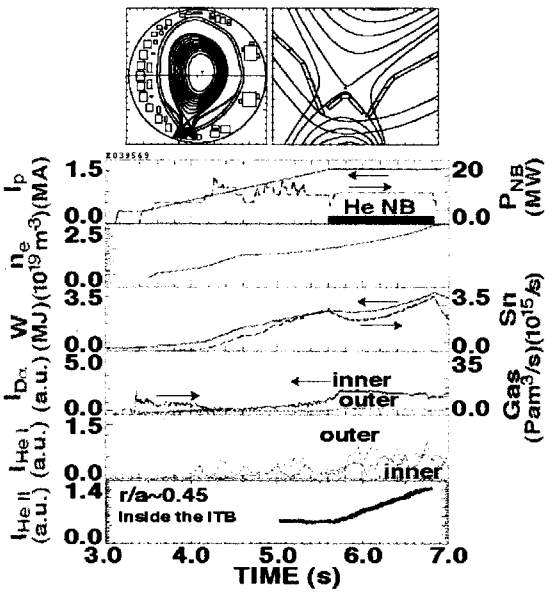

Fig. 3 Wave-forms of the RS plasma with He-NB. The plasma configuration is also shown in upper figure.

5. Summary

The particle confinement times for central and edge fuelled He are estimated using He-NB and He gas-puffing. In the ELMy H-mode plasma, the particle confinement time for central fuelled He is almost constant in the high and low density range. On the other hand, the particle confinement time for edge fuelled He is larger for the low density range. This result indicates that the low He exhaust capability in the low density discharge with a high confinement is not ascribed to the high confinement but to the low divertor pumping rate. In the RS plasma, the confinement time for central fuelled He is almost the same value as that in the ELMy H-mode plasma, although further consideration is necessary for the accurate estimation of the absolute value of the confinement times. This result suggests that the He exhaust capability is not limited by the core plasma confinement but by the divertor pumping even in the RS plasma.

References

[1] Takenaga, H. and the JT-60 Team, Phys. Plasmas **8**, 2217 (2001).

[2] Sakasai, A., et al., in Fusion Energy 2000 (Proc. 19th Int. conf. Sorrento, 2000) IAEA-CN-77-EX5/5.

[3] Takenaga, H., et al., in Fusion Energy 2002 (Proc. 19th Int. conf. Lyon, 2002) IAEA-CN-94-EX/C3-5Rb. submitted to Nucl. Fusion.

8.3 Boronization Effects using Deuterated-decaborane in JT-60U [1]

T. Nakano, S. Higashijima, H. Kubo, J. Yagyu, T. Arai, N. Asakura and K. Itami

Wall conditioning is one of keys to obtain high performance plasmas in nuclear fusion experimental devices. Boronization is one of the most effective methods in suppression of oxygen release from first walls. In the present work, boronization effects on impurities have been systematically investigated based on the database built up from about 100 discharges with identical conditions.

The database was built up from the discharges with the following conditions; the plasma current was 1.5 MA, the toroidal field was 3.0 T and the discharge had three periods, i.e. an ohmic heating (OH) period with $\overline{n_e} \sim 1.2\text{x}10^{19}\,\text{m}^{-3}$, an L-mode period with $\overline{n_e} \sim 1.5\text{x}10^{19}\,\text{m}^{-3}$ and $P_{NB} \sim 4$ MW and an H-mode period with $\overline{n_e} \sim 2.5\text{x}10^{19}\,\text{m}^{-3}$ and $P_{NB} \sim 13$ MW, where $\overline{n_e}$ and P_{NB} are a line-averaged electron density set by a feed back control system and a neutral beam heating power, respectively. The plasma shape was configured to suppress local strong plasma-wall interactions except for the strike points on the divertor plates.

In ~ 50 shots after boronization using 70 g of $B_{10}D_{14}$, the carbon content was low due to suppression of the chemical sputtering of carbon tiles while the boron content was high due to the sputtering of the boron film. In contrast to the boron and the carbon content, the oxygen content gradually increased from ~ 0.7% to ~ 1.3% in ~ 500 shots. The durability of boronization using 20 g of $B_{10}D_{14}$ is much shorter (~ 30 shots) than that of boronization using 70 g after vacuum vessel ventilation. Comparison of the boronization using 70 g and 20 g of $B_{10}D_{14}$ suggests that 20 g of $B_{10}D_{14}$ might be insufficient to obtain long durability for the surface area of JT-60U (~ 200 m^2). Since then, continual boronization using 10 - 20 g of $B_{10}D_{14}$ every ~200 shots successfully kept the oxygen content less than ~ 1%.

Figure 1 shows Z_{eff} as a function of line-averaged electron density. Due to the reduction of the carbon and the oxygen content, Z_{eff} in 50 shots after boronization lies in the lowest range of the database in the OH and the L-mode period although Z_{eff} in the H-mode period scatters.

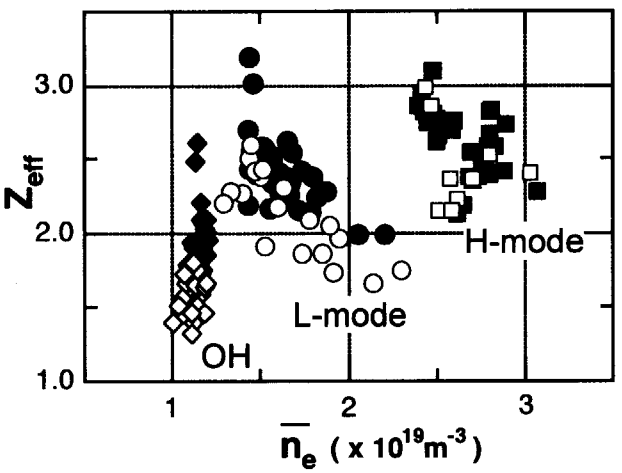

Fig.1. Z_{eff} as a function of line-averaged electron density. Open and closed symbols show Z_{eff} in 50 shots after boronization and in the other shots, respectively.

[1] Nakano, T., et al., J. Nucl. Mater. **313-316**, 149 (2003).

8.4 Estimation of the Density Ratio of Impurity Injected by Neutral Beam

T. Nakano and Y. Koide

The neutral beam heating system plays important roles in the control of plasma pressure and current distribution, resulting in high performance plasmas such as a reversed shear plasma. In most of the operation modes of the high performance plasmas, only the neutral beam and the recycling process fuel the plasmas. Since the impurity contained in the neutral beam is injected directly into the plasma, the plasma purity depends significantly on the purity of the neutral beam. In fact, to obtain the highest Q_{DT}^{eq} plasma in the world, the reduction of impurity was one of the most important issues. In the present work, the impurity density ratio in the neutral beam has been quantitatively estimated.

We observed the D_α spectrum from the neutral beam from which residual ions were removed by bending magnets after the beam passed through a neutralizer cell. Figure 1 shows the observed D_α spectrum, which consists of a stationary D_α line and Doppler-shifted D_α lines. The Doppler shift depends on the speed of the deuterium, which is determined by the mass of a deuterium ion or a deuterium molecular ion when it is accelerated. The D_α (E), D_α (E/2) and D_α (E/3) lines are emitted by a deuterium originating from D^+, D_2^+ and D_3^+, respectively. Since about 900 injections had been performed and carbon impurity seemed to reduce significantly, the main residual impurity in the ion source chamber was not carbon but oxygen [2]. Thus, the D_α (E/10) line is considered to be emitted by a deuterium originating from D_2O^+.

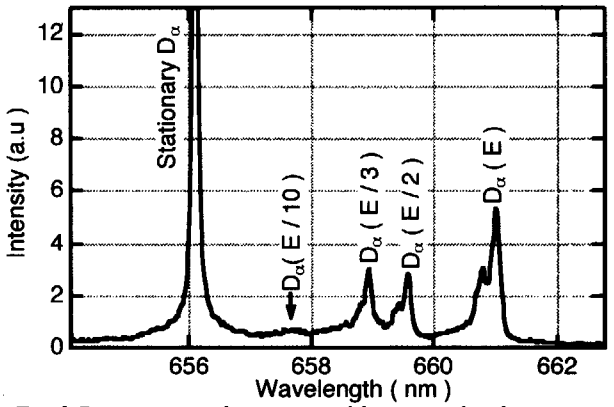

Fig.1 D_α spectrum from neutral beam in the downstream of a neuralizer cell. E is an acceleration energy.

In order to estimate the ratio of oxygen to deuterium in the neural beam, we have calculated the neutralization efficiency for D^+, D_2^+, D_3^+ and D_2O^+ in the neutralizer cell. Here, we assumed that D_2O^+ was dissociated into D^+, D_2^+ and O^+ in front of the neutralizer cell. In the calculation, the processes of D_α emission, ionization, dissociation and electron capture by a collision between deuterium and impurity beam, and D_2 gas were considered.

The above analysis resulted in the ratio of oxygen to deuterium of 0.6% - 3% in the neutral beam. It was found that the impurity ratio reduced gradually with increasing number of the beam injection. This impurity amount can dilute the plasma significantly on the assumption that most of the impurity of the neutral beam is injected into the plasma. Furthermore, we have attempted to clean the ion source chamber by Ar arc discharge in order to reduce the impurity. However, the effect of the Ar arc discharge cleaning was not clear.

[1] Okumura, Y., et al., JAERI-M 9653 (1981).

9. Divertor and SOL Plasmas

9.1 SOL Plasma Flow and Influences on Divertor Plasma

N. Asakura, H. Takenaga, S. Sakurai, G.D. Porter[1)], T.D. Rognlien[1)], M.E. Rensink[1)],
1) Lawrence Livermore National Laboratory, P.O.Box 808, Livermore , CA 94550, USA

The scrape-off layer (SOL) flow plays an important role in the plasma transport along the field lines. Determination of the SOL flow pattern has been recently advanced in JT-60U experiments. Reciprocating Mach probes were installed at the high-field-side (HFS) baffle, low-field-side (LFS) midplane and just below the X-point. Results of the SOL flow measurements and analysis were presented in 15th PSI [1] and 19th IAEA conferences [2].

1. SOL Flow Measurements at HFS and LFS [1]

Profiles of the SOL flow velocity (Mach number, M), floating potential (V_f), electron temperature (T_e) and density (n_e) were measured over wide density ranges from 1.2×10^{19} to 3.9×10^{19} m^{-3} ($\bar{n}_e/n^{GW}$ =0.23 – 0.73, where $n^{GW}=5.2\times10^{19}$ m^{-3}) in L-mode plasmas with the CW and CCW directions of B_T. Only for the ion ∇B drift direction towards the divertor (CW B_T), the SOL flow away from the divertor ("flow reversal") was observed near the separatrix both at HFS and LFS of the main plasma. Just below the X-point, the SOL flow direction (towards the divertor) was independent of B_T. These results with the different B_T directions showed that the direction of the SOL flow near the main plasma separatrix was against the ion ∇B drift.

Characteristics of HFS SOL flow profile, which were for the first time investigated, were different from those at LFS midplane. The SOL flow away from the HFS divertor with small M (= 0.1-0.2) was found at and just outside the separatrix, and width of the flow reversal (r_{mid} ~0.4 cm) was narrower than that observed at the LFS midplane (r_{mid} < 5cm). On the other hand, at the outer flux surfaces (r_{mid} > 1cm), subsonic SOL flow towards the HFS divertor (M~0.5) was produced. Parallel SOL flow may be driven from LFS to HFS on the outer flux surfaces.

2. SOL Plasma Simulation with Drift Effects [2]

Plasma flow pattern was investigated using UEDGE-code[3], where effects such as $\boldsymbol{E}\times\boldsymbol{B}$, $\boldsymbol{B}\times\nabla\boldsymbol{B}$ and diamagnetic drifts were included. Flow reversal both at HFS and LFS SOLs was produced near the separatrix of the main plasma for the case with the drift effects included. The flow reversal is mainly caused by the ion $\boldsymbol{B}\times\nabla\boldsymbol{B}$ drift, which increases ion pressure downward.

Calculated SOL flow profiles were compared to the measured ones. At the LFS midplane, the flow reversal near the separatrix (M~0.2) was smaller than the measurement (M = 0.3-0.4), and the region (r_{mid} < 3 cm) was narrower than the measurement (r_{mid} < 5 cm). At HFS SOL, Mach number of flow reversal (M~ 0.1 away from the HFS divertor) was small and it was localized near the separatrix. These simulation results qualitatively agreed with the measurements.

At the outer flux surfaces (r_{mid} >1 cm) of the HFS SOL, subsonic SOL flow (M = 0.4-0.5) was driven towards the HFS divertor, which was comparable to the measurement. However, in the simulation, the subsonic SOL flow was produced by lower T_e and higher n_e compared to the measurements. Further investigations of the impurity modeling, boundary conditions, and numerical stability are required to the SOL flow pattern near the divertor.

3. Particle Fluxes Towards HFS and LFS Divertors, and In-Out Asymmetry [1, 2]

Net particle fluxes towards the HFS and LFS divertors were investigated. Components of parallel SOL flow ($n_iV_{//} = n_iMC_s$) and E_rxB drift flow (n_iV_{drift}) for the particle flux towards the divertor are described as $n_iV_{//}\Theta$ and $n_iV_{drift}\Phi$, respectively. Here, $\Theta = B_p/B_{//}$ varies in torus (such as 0.01-0.1) and $\Phi = B_t/B_{//}$ (~1). At the HFS and LFS SOLs, $n_iV_{drift}\Phi$ was dominant near the separatrix (r_{mid} <0.5cm), and the direction was from the HFS divertor to the LFS one for the ion ∇B drift towards the divertor. At the same time, E_rxB drift flow was produced by large E_r in the private flux region under the attached divertor condition. The E_rxB drift flux was large and it contributed to plasma transport from LFS to HFS divertor.

Influences of the SOL drift flow on the total particle fluxes towards the HFS and LFS divertors, Γ_p^{HFS} and Γ_p^{LFS}, were investigated. Γ_p^{HFS} and Γ_p^{LFS} were calculated at the probe locations by integrating $n_iV_{//}\Theta$ and $n_iV_{drift}\Phi$ across SOL to r_{div} (the most outer radius where field line is connected to the divertor), $\Gamma_p^{HFS/LFS} = \int_0^{r_{div}} 2\pi R n_i [V_{//}\Theta + V_{drift}^{ExB}\Phi]\nabla\varphi \cdot dr$ (+ is towards the LFS divertor). $\Gamma_p^{HFS/LFS}$ is written as $\Gamma_{p,//}^{HFS/LFS}+\Gamma_{p,drift}^{HFS/LFS}$, where $\Gamma_{p,//}^{HFS}$ is negative value, and $\Gamma_{p,//}^{LFS}$ and $\Gamma_{p,drift}^{HFS/LFS}$ are positive values. At low $\bar{n}_e$, $\Gamma_{p,drift}^{HFS}$ was 30-50% of $|\Gamma_{p,//}^{HFS}|$, and Γ_p^{HFS} = -(1.5-3)x10^{21} s^{-1} (towards the HFS divertor). $\Gamma_{p,drift}^{LFS}$ was 50-80% of $\Gamma_{p,//}^{LFS}$, and Γ_p^{LFS} was (6-7)x10^{21} s^{-1}. As a result, Γ_p^{LFS} was larger than $|\Gamma_p^{HFS}|$: the LFS-enhanced asymmetry was mostly produced by the drift flow in SOL. On the other hand, total E_rxB drift flux at the private region was large, Γ_p^{Prv}~ -4x10^{21} s^{-1}, contributing to HFS-enhanced asymmetry.

In-out asymmetry in divertor particle flux was discussed including Γ_p^{Prv}. The total particle fluxes towards the HFS and LFS divertors were estimated as $|\Gamma_p^{HFS}|+|\Gamma_p^{Prv}|$ and $\Gamma_p^{LFS} - |\Gamma_p^{Prv}|$, respectively, assuming that a part of Γ_p^{LFS} was exhausted into the private region by diffusion and radial drifts before reaching the target plate: such particle flux would be comparable to $|\Gamma_p^{Prv}|$. Then, $|\Gamma_p^{HFS}|+|\Gamma_p^{Prv}|$ was a factor of 2-3 larger than Γ_p^{LFS}

$-|\Gamma_p^{Prv}|$. Large contribution of Γ_p^{Prv} to the HFS-enhanced asymmetry in the divertor ion flux is expected. On the other hand, when the detachment occurs at the LFS divertor at high $\bar{n}_e$, Γ_p^{Prv} disappeared and the asymmetry in Γ_p^{LFS} ($\sim\Gamma_{p,//}^{LFS}$) and $|\Gamma_p^{HFS}|$ ($\sim|\Gamma_{p,//}^{HFS}|$) becomes small or reversed. Similar HFS-enhanced asymmetries in particle recycling and neutral pressure have been generally observed [4]. When the divertor detachment occurred, such asymmetries also become small and reversed. These characteristics of the particle transport in the divertor were determined by changes in Γ_p^{HFS}, Γ_p^{LFS} and Γ_p^{Prv}.

In summary, the SOL flow measurements (at HFS, LFS and private region) and UEDGE simulation revealed the SOL flow pattern and effects of the plasma drifts. Design work including the drift effects will optimize the divertor geometry in a tokamak reactor.

References

[1] ASAKURA, N. et al., J. Nucl. Matter.313-316 (2003) 821-828.
[2] ASAKURA, N. et al., Proc. 19th IAEA Fusion Energy conf. , Lyon (2002), EX/D-3
[3] PORTER, G.D., et al., Phys. Plasma **7** (2000) 3663.
[4] ASAKURA, N., et al., Plasma Phys. Control. Fusion **44** (2002) 2101.

9.2 Fast Measurements of SOL Plasma Flow in ELMy H-mode Plasma

N. Asakura, S. Sakurai, O. Naito, K. Itami, Y. Miura, S. Higashijima,
Y. Koide, Y. Sakamoto

Transport process of ELM heat and particle fluxes responsible for the rapid plasma deposition on the divertor target was investigated. The SOL plasma flow driven along the field lines was measured in the ELMy H-mode plasma, for the first time, at the three important locations (i.e. Low-Field-Side midplane, X-point, and High-Field-Side SOL) using reciprocating Mach probes. Results of the ELM plasma measurements and analysis were presented in 8th IAEA TCM on H-mode physics and transport barriers [1].

The radial profiles of the plasma flow were determined in Type-I ELMy H-mode (I_p=1MA, B_t=2T, δ=0.32, κ=1.4, P_{NB}= 4.3MW, line-averaged density of 1.7×10^{19} m^{-3}). ELM frequency was 30-40Hz. 10 – 12 ELM events (r_{mid} <10cm) were measured during a probe reciprocation of 1 s. Just below the X-point of the LFS SOL, rapid increase in the flow velocity up to the ion sonic level (Mach number, M~1) was observed during 200-300 μs just after ELM events, and the radial width was 1.0-1.5 cm (mapping to the midplane SOL). The duration and width of the rapid plasma flow were comparable to deposition duration and width of the heat load to the outer divertor target measured with an infrared TV camera (with 250 μs time resolution).

At the same time, ion saturation current, j_s, near the X-point reached the peak in 100μs after the j_s peak at LFS midplane. The time lag between the j_s peaks was consistent with the transit time of ions from midplane to the X-point, where the connection length of 26m and acoustic speed of $C_s = 2.5\times10^5$m/s assuming edge ions and electrons are exhausted into SOL (T_i = 800eV and T_e = 600eV were measured at the edge pedestal). These results were consistent with the convective transport of the SOL plasma exhausted by ELMs. Convective heat flux to the LFS divertor target was estimated from, $q_{div}^{conv} = q_{//}^{conv}$ x field line pitch (0.04), where $q_{//}^{conv} = [5/2kT_i + 5/2kT_e + 1/2m_i(MC_s)^2]\gamma_{//}$. From the example ($j_s$ = 0.5MAm^{-2}, M = 1), q_{div}^{conv} = 80 Mwm^{-2}, which corresponds to 73% of the peak heat load (110 MWm^{-2} measured by IRTV). Such simple evaluation showed that convective transport of the SOL plasma gives large contribution to the ELM heat deposition process.

At the HFS SOL, fluctuations in V_f became large just after ELM. On the other hand, j_s starts slowly enhanced 460μs after that at LFS midplane. Time lag between the j_s peaks was 5 times longer than that between midplane and X-point, and SOL flow towards the HFS divertor was not enhanced. D_a brightness in the HFS and LFS divertors was simultaneously enhanced before the increase in j_s at the HFS SOL. The ELM heat and particle fluxes in the HFS SOL were not understood by the simple convective transport.

Reference

[1] ASAKURA, N. et al., Plasma Phys. Control. Fusion, 44 (2002) A313-321.

9.3 Fast Measurement of Divertor Plasma in ELMy H-mode

N. Asakura

1. Introduction

Investigation of rapid deposition of ELM heat and particle fluxes on the divertor target is crucial for understanding dynamics of plasma-wall interaction and erosion. Fast measurement system of the divertor Langmuir probes has been developed in 2001–2002. Eight signals of ion saturation current ($j_{//}$) or floating potential (V_f) at High-Field-Side (HFS) and Low-Field-Side (LFS) divertor targets were measured with 200 kHz sampling in 2002, June. Rapid changes in $j_{//}$ and V_f at ELM events were measured, and dynamics of ELM heat load was investigated.

2. Fast Sampling System and Experiments

Operation and data-acquisition of the Langmuir probes are preprogrammed by CAMAC and SPARC-5 workstation system. Five transient recorders of Kinetic System 4020 with 12bits-2M-memory module (KS4054) provide totally 10 channels, where 8 and 2 channels are used for monitoring probe currents and applied voltages, respectively. Maximum sampling rate is 500 kHz, and they are used typically with 50-100 kHz. Three operation modes: (1) *I_s-mode* for ion saturation current, (2) *V_f-mode* for floating potential, and (3) *V-scan-mode* for current-voltage characteristics, are selected by a remote-control-software.

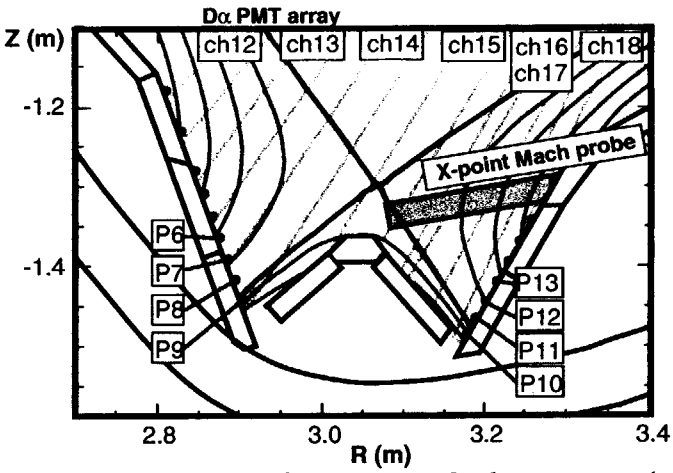

Fig. 1 Plasma configuration, probe locations, and Dα chords in the W-shaped divertor.

Measurements of the divertor plasma were performed in Type-I ELMy H-mode (I_p=1MA, B_t=2T, δ=0.32, κ=1.4, P_{NB}= 4.3MW, line-averaged electron density of 1.7×10^{19} m^{-3}). ELM frequency was 30-40Hz. Three probe operation modes were demonstrated in a series of shots: 41781 (*V-scan-mode*), 41783 (*V_f-mode*), 41784 (*I_s-mode*). Plasma configuration, viewing chords of Dα measurement and divertor probe locations are shown in Fig.1, where 8 Langmuir probes near the strike-points (P6 – P13) were used. Locations of the HFS and LFS strike-points were P8-P9 and P10-P11, respectively, according to the equilibrium calculation. Reciprocating Mach probes at the X-point and LFS midplane (as shown in Sec. 8.2) were also used to measure upstream SOL plasma profiles. Rapid deposition of heat flux to the divertor was measured by IRTV system with 4 kHz, which was not fast enough to identify accurate deposition time.

3. Changes in Ion Saturation Current and Electron Temperature

Applied voltage to the probes was scanned between −160 and 50 V with 500 Hz, and probe currents were sampled with 200 kHz (400 data for one V-scan period). Values of $j_{//}$, T_e and V_f were evaluated with interval of 2 ms, from I-V characteristics of the single probe. Both time resolution and fitting were much improved compared to the existing system (100 data for one V-scan period of 100 ms).

Time evolutions of $j_{//}$ and T_e near the HFS and LFS strike-points are shown in Fig. 2. Error bars on $j_{//}$ and T_e are large just after ELM events (I-V data was not fitted by a single probe model due to large fluctuations). After ELM events, $j_{//}$ decreases to a low level in 12-18 ms similar to Dα signals. At the LFS strike-point, $j_{//}$ (~20 kAm^{-2} at P11) between ELMs is smaller and T_e (= 50-60 eV) is higher than those at the HFS strike-point (~30 kAm^{-2} and 15-25 eV at P8). Electron pressures (n_eT_e) at HFS and LFS are comparable, assuming the same collection area of 4.2×10^{-6} m^2 for all probes (it was not a good approximation since they were used 2 years).

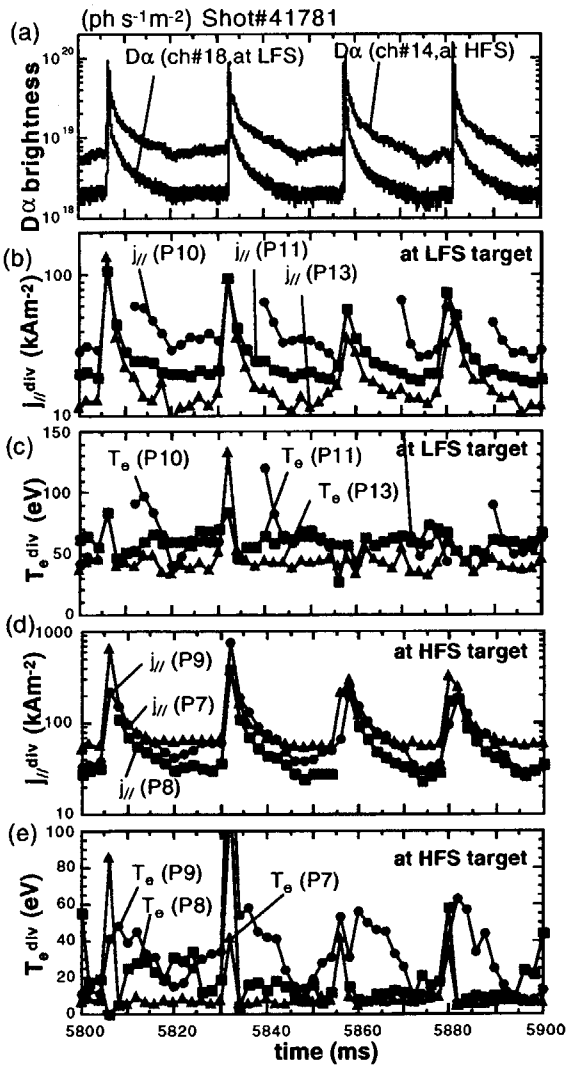

Fig.2 (a) Dα brightness, (b) $j_{//}$ and (c) T_e at LFS divertor,(d) $j_{//}$ and (e) T_e at HFS divertor.

Due to large fluctuations in probe signal at ELM (in particular, 1st frame just after ELM events), T_e has large error bar (ΔT_e larger than 50% of T_e) and data with ΔT_e larger than 100% are not shown. After the 2nd frame, values of T_e at the strike points (P8, P11) are comparable to those before ELM event: T_e recovers relatively quickly (within 2 ms). Decay time of T_e is also comparable at upstream (X-point Mach probe): less than 4 ms, i.e. 1-2 data periods.

On the other hand, at the private region, T_e at HFS (P9) and LFS (P10) increase after ELM events, and they decrease slowly (i.e. 10-15 ms) similar to $j_{//}$. Source of the high T_e plasma in the private region was not determined (diffusion or drift from the main plasma or either side of the divertor). Here, peak values of T_e at the strike-points were not determined in this experiment due to the probe separation of 2.5 cm. Thus, other possibilities such that actual strike-points are 1-1.5 cm below those of the equilibrium calculation or shift after ELM event should be also investigated.

4. Plasma Flux to the Divertor

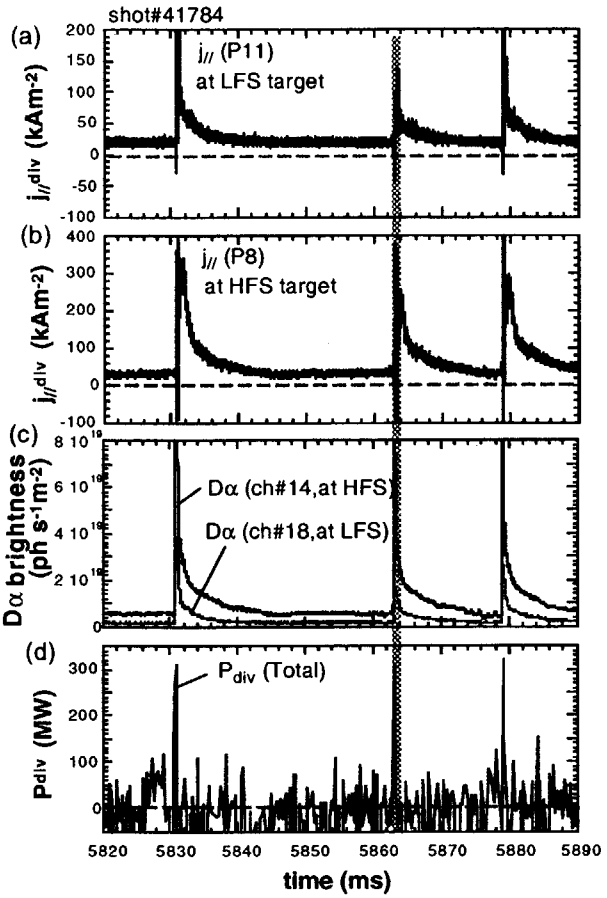

Fig.3 (a) $j_{//}$ at LFS divertor, (b) $j_{//}$ at HFS divertor, (c) Dα brightness, (d) total heat load.

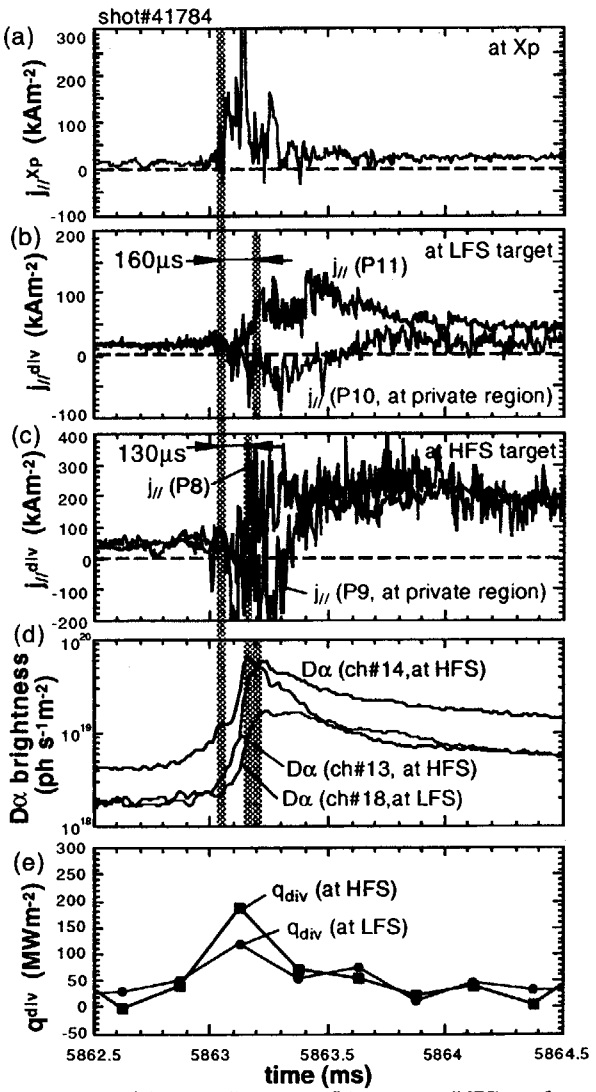

Fig.4 (a) $j_{//}$ at X-point, (b) $j_{//}$ near LFS strike-point, (c) $j_{//}$ near HFS strike-point, (d) Dα brightness, (e) peak heat flux densities at LFS and HFS divertors.

Constant voltage of −170V was applied to the probes, and $j_{//}$ was sampled with 200kHz. Rapid change in the ion flux during ELM heat deposition was investigated. Values of $j_{//}$ near the HFS and LFS strike-points and total heat load to the divertor are shown in Fig. 3. After ELM events, decay times of $j_{//}$ and Dα brightness are comparable as shown in Sec. 3. On the other hand, deposition of the heat flux is short (corresponding to one frame of ~IRTV, 250μs), and it should be noted that negative values of $j_{//}$ are observed during the ELM heat deposition to the HFS and LFS divertors.

These changes during and after ELM event (5862.5-5864.5 ms) are shown in Fig. 4. Enhancement of upstream $j_{//}$ just below X-point (by the factor of 5-8) is also shown: large ion flux reaches the X-point from 5863.04 ms to 5863.32 ms. At the same time, Mach number increases up to unity [1]. These results show that convective transport is enhanced in SOL just after ELM event. Then, $j_{//}$ at HFS (P8) and LFS (P11) divertors are enhanced by the factor of ~6 for LFS (at 5863.17 ms) and ~10 for HFS (at 5863.20 ms), suggesting that ELM ion flux simultaneously reaches the HFS and LFS divertors. Dα signals become the maximums at the same time, and the

enhancement (10 for LFS and 25 for HFS) is larger than that of $j_{//}$ since both plasma and neutral densities are increased.

Large negative $j_{//}$ is observed, in particular, at the private region of both LFS and HFS divertors: the peak values of –200 kAm^{-2} at HFS and –80 kAm^{-2} at LFS are larger than those observed at the strike-points (P8 and P11), and the durations (300 μs and 500 μs, respectively) are longer. This may be caused by deposition of fast electrons exhausted into the private region rather than thermal electric current along the field lines between the HFS and LFS divertors. However, there is no peak of the heat load profile at the private region.

5. Floating Potential at the Divertor

Rapid change in V_f during the ELM heat deposition was investigated. Time evolutions of V_f just below the X-point, HFS and LFS divertors are shown in Fig. 5. Fluctuations in V_f start at 5865.0 ms: V_f^{Xp} becomes positive (100-200 V) following negative value (-100V). Large particle flux reaches the X-point from 5865.20 ms, where $j_{//}$ is saturated since discharge occurs at the probe electrodes. V_f fluctuations start both at the HFS and LFS divertors. In particular, at the private region, V_f becomes large negative (-300~-400V at HFS) at 5865.32 ms and (–600V at LFS) at 5865.37 ms, and the negative V_f is observed during 250-300μs, which may be due to deposition of fast electrons.

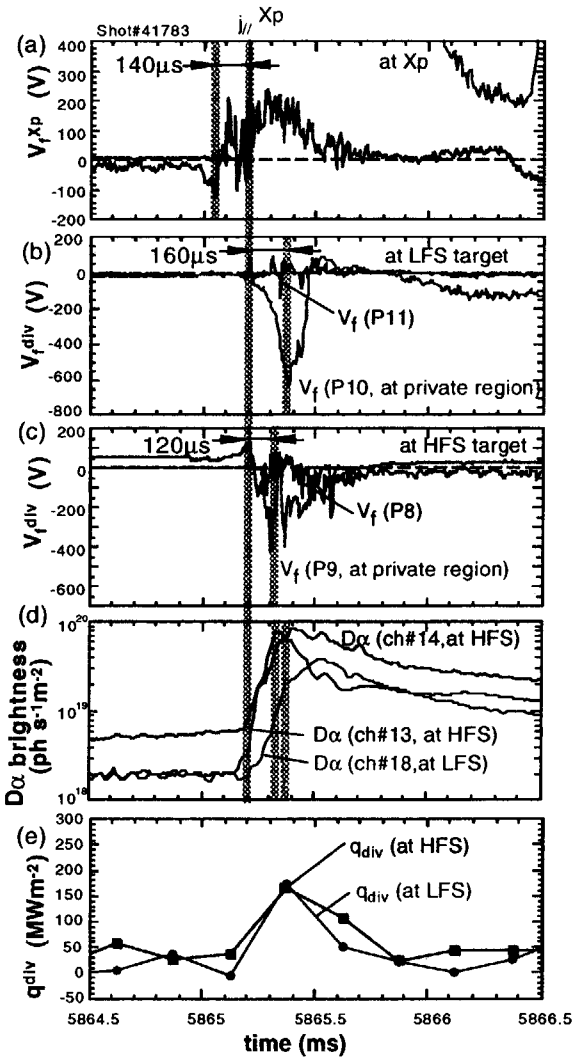

Fig.5 (a) V_f at X-point, (b) V_f near LFS strike-point, (c) V_f near HFS strike-point, (d) Dα brightness, (e) peak heat flux densities at LFS

6. Summary

Fast sampling system of the divertor Langmuir probes was developed, and dynamics of the ELM heat and particle deposition was investigated. Delay of $j_{//}$ enhancement between X-point and the divertor target was observed, suggesting the convective transport of the ELM ion flux, while $j_{//}$ at HFS and LFS divertors increased simultaneously. Strong enhancements of negative V_f and $j_{//}$ were found at the private region may be caused by deposition of the fast electrons.

References

[1] ASAKURA, N. et al., Plasma Phys. Control. Fusion, 44 (2002) A313-321.

9.4 H_2 Molecule Spectroscopy in Divertor Plasmas

H. Kubo, K. Sawada[1)], H. Takenaga, T. Nakano, S. Kobayashi[2)]
1) Shinshu University, 2) Kyoto University

1. Introduction

Most of the H^+ ions arriving at the divertor plates are eventually desorbed from the divertor plates in the form of the H_2 molecule. The H_2 molecules play an important role as a source of H^+ ions. They may also play a role as a sink of H^+ ions by molecular assisted recombination (MAR). Since excited H atoms can be produced by dissociation of H_2 molecules, the H_2 molecules can affect radiation of H atoms [1]. Thus, understanding behavior of H_2 molecules in divertor plasmas is important for divertor plasma control and H atom spectroscopy [2]. In JT-60U, H_2 molecule behavior in divertor plasmas has been studied by observation of H_2 line emission.

2. Experimental

The diagnostics for the present study are shown in Fig. 1. Using visible spectrometers with 60-ch optical fiber arrays, H Balmer lines and H_2 Fulcher (d $^3\Pi_u$ --> a $^3\Sigma_g^+$) lines were observed. Electron temperature, electron density and ion flux were measured with Langmuir probes at the divertor plates. In this paper, we will investigate the outer divertor plasmas. Figure 2 shows time evolution of the L-mode discharge to be studied in this paper. With an H_2 gas puff, the electron density increased, partial detachment of the outer divertor plasma occurred at 5.9 s, and an X-point MARFE appeared at 7.9 s. With the MARFE, the H^+-e recombination ion flux in the outer divertor was about a half of the ion flux to the outer divertor

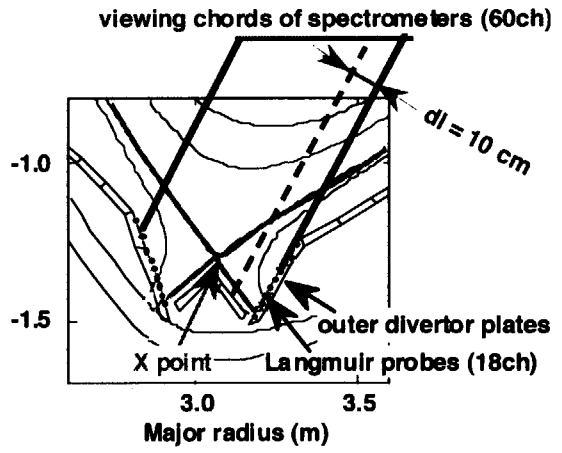

Fig. 1. Diagnostics for the present study.

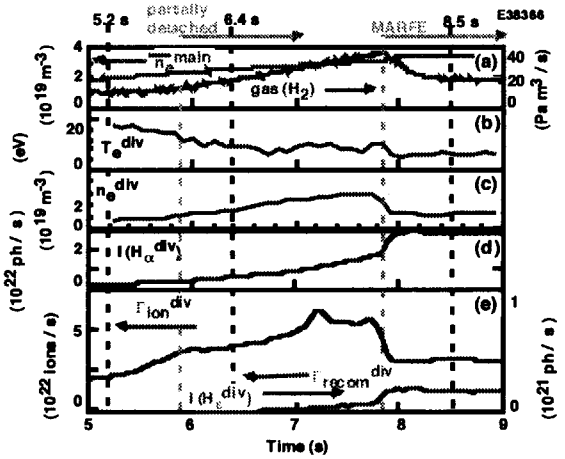

Fig. 2. Time evolution of an L-mode discharge (the plasma current: 1.5 MA, the toroidal magnetic field: 3.5 T, the NBI heating power: 4 MW). (a) Line-averaged electron density in the main plasma and H_2 gas puff rate, (b) electron temperature and (c) density measured with the Langmuir probe near the outer separatrix strike point, (d) intensity of H_α line emission from the outer divertor plasma, and (e) ion flux to the outer divertor plates measured with the Langmuir probes and intensity of H_ε line emission from the outer divertor plasma. In the column (e), the H^+-e recombination ion flux, which was derived by multiplying the H_ε line intensity by 135, can also be referred to the left scale.

plates. Details of the divertor plasma detachment and the H^+-e recombination have been analyzed in Ref. [3].

3. Results and Discussion

Figure 3 shows Fulcher lines observed near the outer divertor plates in an attached divertor plasma, where the electron temperature and density measured with the Langmuir probe near the outer separatrix strike point were 20 eV and 0.7×10^{19} m^{-3}, respectively. The Q branches with v = 0-0, 1-1 and 2-2 were identified. The vertical lines indicate the line intensities calculated on the assumption that T_{rot} (0) = 0.040 eV, T_{rot} (1) = 0.057 eV, T_{rot} (2) = 0.046 eV, n (1) / n (0) = 0.76, and n (2) / n (0) = 0.60. Here, T_{rot} (v) and n (v) are the rotational temperature and the population of the vibrational level v of the d $^3\Pi_u$ state, respectively. The T_{rot} (v) and n (v) were determined to fit the calculation to the observation. The vibrational population ratios corresponded to a vibrational temperature of ~ 1 eV.

Figure 4 (a) shows intensity of Fulcher v=1-1 Q3 line as functions of the distance from the outer divertor plates. In the attached divertor plasma (at 5.2 s), the decay length of the line intensity was ~ 1 cm, and it suggests that the H_2 molecules were localized near the divertor plates. In the detached divertor plasma with a MARFE (at 8.5 s), the decay length was ~ 4 cm, and it suggests that the H_2 molecules penetrated more deeply. Although it was expected that the molecule density and the electron density in the detached divertor plasma were higher than those in the attached divertor plasma, the intensity near the divertor plates in the detached divertor plasma was lower than that in the attached divertor plasma. It suggests that the ratio of the Fulcher line emission rate to the H_2 molecule loss rate was lower in the detached divertor plasma than in the attached divertor plasma.

The rotational temperature derived from a spectrum observed near the divertor plates was 0.04 - 0.07 eV in the detached divertor plasma (at 8.5 s). The ratios of the Q3 line intensity to the subtotal line intensity for the v=0-0, 1-1, 2-2 transitions change by less than

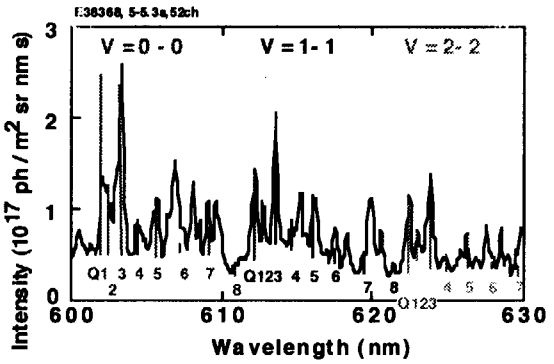

Fig. 3. Fulcher lines observed near the outer divertor plates in the attached divertor plasma (at 5.2 s of the discharge shown in Fig. 2). Calculated line intensities of Q branches of the v=0-0, 1-1, 2-2 transitions are also shown as vertical lines.

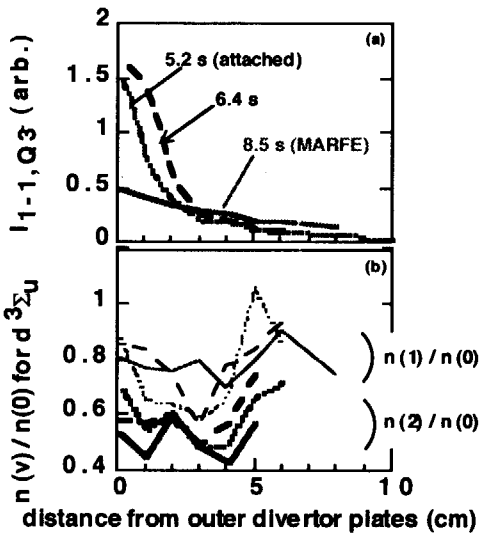

Fig. 4. (a) Intensity of Fulcher v=1-1 Q3 line ana (b) vibrational population ratios (n(1) / n(0): thin lines, n(2) / n(0): thick lines) of the d $^3\Pi_u$ state as functions of the distance from the outer divertor plates. The distance is measured as dl in Fig. 1.

10% (from 0.33 to 0.30), as the rotational temperature changes from 0.04 eV to 0.07 eV. Therefore, the Q3 line intensity was a good measure for the vibrational population. Figure 4 (b) shows the vibrational population ratios of the d $^3\Pi_u$ state, where the ratios were derived from the intensity ratios of the Q3 lines. The vibrational population ratio did not change so much with the distance from the divertor tiles. Difference between the attached and detached divertor plasmas was not seen clearly.

For the attached divertor plasma, the total intensity of the Fulcher lines were calculated with a three-dimensional neutral transport code (DEGAS2 [4]) and a collisional-radiative model code [5]. The background plasma parameters were determined using a simple divertor code from the electron temperature and density measured with the Langmuir probes. It was assumed that all the hydrogen ions that arrived at the divertor plates which were not reflected as hydrogen atoms were desorbed as hydrogen molecules. In the collisional radiative model, the vibrational levels are separately considered for the n=1 state, the electronic states for the n=2 state, and the singlet and triplet states for the n=3 state. The total intensity of Fulcher lines was calculated by assuming the statistical weight for the n=3 triplet levels. The calculated intensity is compared with the observed one in Fig. 5. Here, the measured total intensity was obtained from the measured v=1-1 Q3 line intensity on the assumption that the rotational temperature and the vibrational temperature for the d $^3\Pi_u$ state were 0.05 eV and 1 eV, respectively. This assumption was valid, as mentioned above. The measured intensity was reproduced by the calculation. Therefore, it suggests that the H_2 molecule density distribution was reproduced by the calculation for the attached divertor plasma.

Since reaction rates of the H_2 molecule depend on vibrational excitation, it is important to estimate vibrational excitation of the ground state (X $^1\Sigma_g^+$) for understanding the H_2 molecule behavior. In divertor plasmas, the coronal model is not applicable to determination of the d $^3\Pi_u$ population. However, it has recently been found that the vibrational population ratios of the d $^3\Pi_u$ state are close to the population ratios calculated by the coronal model even in such

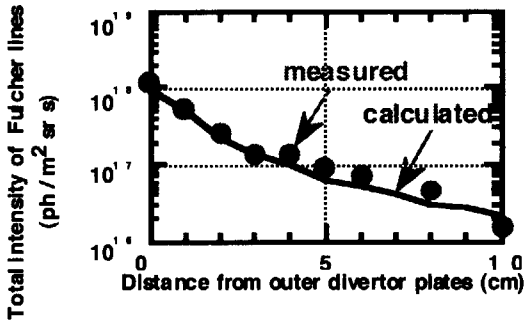

Fig. 5. Measured and calculated total intensity of Fulcher lines as functions of the distance from the outer divertor plates in the attached divertor plasma (at 5.2 s).

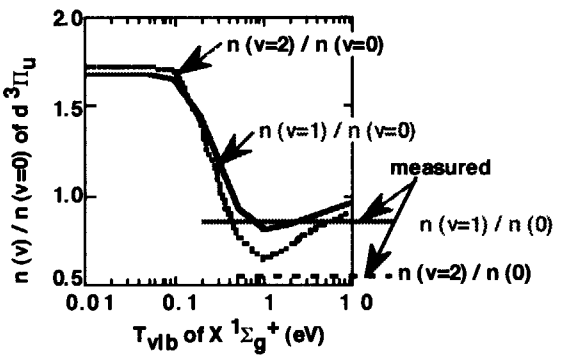

Fig. 6. Calculated population ratios of the vibrational levels of the d $^3\Pi_u$ state as functions of the vibration temperature of the X $^1\Sigma_g^+$ state. The measured population ratios are also shown as horizontal lines.

a case since the potential wells associated with the most important internal states all have rather similar shapes [6]. Then, vibrational population ratios of the X $^1\Sigma_g^+$ state can roughly be estimated from the measured population ratios of the vibrational levels of the d $^3\Pi_u$ state using the Franck-Condon factors between the X $^1\Sigma_g^+$ and the d $^3\Pi_u$ state [7]. Figure 6 shows the calculated population ratios of the vibrational levels of the d $^3\Pi_u$ state as functions of the vibrational temperature of the X $^1\Sigma_g^+$ state. Here, the population ratios were calculated by the coronal model. Comparison between the calculated ratios and the measured ones, which are shown as horizontal lines in Fig. 6, suggests that the vibrational temperature of the X $^1\Sigma_g^+$ state was ~ 1eV in both the attached and the detached divertor plasma. At the vibrational temperature of 1 eV, the ratio of the v=5 level population to the v=0 level population is ~ 0.1. The reaction rates of the MAR can increase drastically (by more than one order), as the v increases from 0 to 5. Therefore, it suggests that the vibrational excitation enhanced the MAR.

For further quantitative analysis, a Monte-Carlo neutral transport code considering the vibrational excitation is under development. In addition, further information on spatial distribution of the temperature and the density is required for investigation of H_2 molecule behavior in detached divertor plasmas.

4. Summary

In JT-60U, H_2 molecule behavior in divertor plasmas was studied by observation of H_2 Fulcher lines. The decay lengths of the line intensity in an attached and a detached divertor plasma with a MARFE were ~ 1 cm and ~ 4 cm, respectively. It suggests that H_2 molecules penetrate more deeply in the detached divertor plasma with a MARFE than in the attached divertor plasma. The measured intensity in the attached divertor plasma was reproduced by a calculation with a neutral transport and a collisional-radiative model code. It suggests that the H_2 molecule density distribution was reproduced by the calculation for the attached divertor plasma. In both the attached and the detached divertor plasma, the vibrational temperature of the ground state was estimated to be ~ 1 eV.

References

[1] Kubo H., et al., Plasma Phys. Control. Fusion **40** 1115, (1998).

[2] Kubo H., in "ATOMIC AND MOLECULAR DATA AND THEIR APPLICATIONS", edited by D. R. Schultz, et al., American Institute of Physics, New York, 161 (2002).

[3] Kubo, H. et al., in "Review of JT-60U Experimental Results in 2000", JAERI-Review 2002-022, 118 (2002).

[4] Stotler, D. P., et al., Contrib. Plasma Phys. **34** 392, (1994).

[5] Sawada, K., et al., J. Appl. Phys. **78** 2913, (1995).

[6] Greenland, P. T., Contrib. Plasma Phys. **42** 608, (2002).

[7] Fantz, U., et al., Plasma Phys. Control. Fusion **40** 2023, (1998).

9.5 2D Distribution of Divertor Radiation in JT-60U [1]

S. Konoshima, H. Tamai, Y. Miura, S. Higashijima, H. Kubo, S. Sakurai,
K. Shimizu, T. Takizuka, Y. Koide T. Hatae and H. Takenaga

Two-dimensional (2D) reconstruction software was developed for bolometer signals of the JT-60U tokamak. Radiative divertor plasma with emissivity of $10MWm^{-3}$ was found previously to extend 10 cm from the target plates [2]. When the density is increased further by larger gas puffing, the emissivity imbalance between both divertor legs becomes less significant. The radiative zones move upward along the divertor legs, redistribute uniformly over the whole divertor region without peaks and eventually merge into a single bright peak near the X-point at density around 5.2×10^{19} m^{-3}, or 83 % of the Greenwald density (toroidal field 3.6T, plasma current 1.4MA), called X-point MARFE (multifaceted asymmetric radiation from edge). The diameter of a half-maximum of the MARFE is about 10 cm with an emissivity more than 20 MWm^{-3}. No radiation is observed near the target plate, indicating the divertor plasma is detached fully from the walls. Total radiated power at the divertor is found to saturate when the power flow from the core plasma, Psol, is approximately equal to the radiated power at the divertor. Here Psol is defined as a remaining power, which is not dissipated by the core radiation. Deuterium fuelling gives a faster rate of rise of the divertor radiation relative to the core, while argon seeded discharges are characterized by a large increase of the core radiation which results in early saturation of the divertor radiation.

References

[1] 15th PSI Conf. (2002), to be published in J. Nucl. Mater. **313-316C** (2003) 888.
[2] Konoshima S., Leonard A. W., Ishijima T., et al., Plasma Phys. Control. Fusion **43** (2001) 959.

9.6 Measurement of Ion Temperature in Divertor Plasmas [1]

T. Nakano, H. Kubo, S. Higashijima, N. Asakura and K. Shimizu

The information on the spatial distribution of ion (deuteron) temperature in divertor plasma is essential to understand the divertor plasma. However, the ion temperature has not been experimentally investigated in detail because of difficulties of the direct measurement. In this work, the ion temperature has been inferred from the Doppler broadening of a carbon ion spectral line.

The spectral line of C IV ($n = 6 - 7$, λ : 772.6 nm) was used for the present measurement because of the following two reasons. For the ion temperature measurement with carbon spectral line, the carbon ion is required to be heated up to the ion temperature by ion collision. Since this heating time becomes short with increasing carbon ion charge, spectral lines from highly charged carbon ions are preferred. The other reason is the advantage in the measurement : a visible (near-infrared) optical system can be used for this spectral line, resulting in the measurement of spatial distribution and absolute intensity with ease.

The ion temperature was measured in the attached divertor plasma with $n_e \sim 2.5$ and $\sim 0.5 \times 10^{19} m^{-3}$ and $T_e \sim 15$ and ~ 80 eV at the inner and the outer strike point, respectively. The figure shows the spectrum observed along the viewing chord near the X-point. The spectral line could not be reproduced by one Doppler broadening component but by two. The temperature of the broad component corresponded to $\sim$ 118 eV while the temperature of the narrow one corresponded to $\sim$ 26 eV.

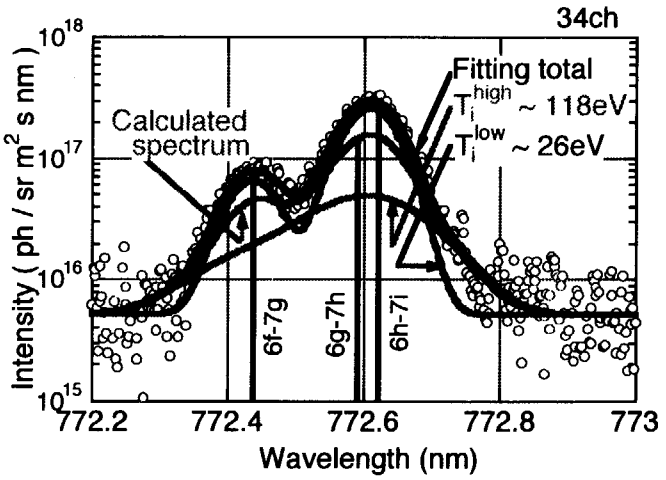

Fig. Comparison of the observed and the calculated π component spectra of C IV (n = 6 – 7) along the viewing chord near the X-point.

In analysis of the spectral line, the following steps were taken. First, the two-dimensional distribution of plasma parameters was determined by a plasma transport code [2]. Second, on the background plasma calculated in the first step, the two-dimensional distribution of impurity parameters was determined by an impurity transport code [3]. Third, the population density of C IV ($n = 7$) was determined by a collisional-radiative model. Forth, the spectrum was synthesized using a spectral width and an emission intensity, respectively, calculated from the ion temperature and the population density. Fifth, the synthesized spectra were summed along a viewing chord. Finally, the spectrum calculated by the above procedure was compared with the observed spectrum.

In the figure, the observed and the calculated spectrum are compared. The above analysis indicated that the temperature of the broad component reflected the ion temperature in the common flux plasma, and that the temperature of the narrow component reflected the ion temperature in the private plasma. For the common flux plasma, the measurement of the temperature and the intensity was in fair agreement with the simulation. For the private plasma, on the other hand, although the temperature agreed well, the simulation underestimated the intensity by a factor of ~ 2. This underestimation resulted in the discrepancy between the observed and the calculated spectrum. Similar results were obtained from the other viewing chords. Further investigation of the carbon ion transport in the private plasmas is needed.

We have attempted to measure an ion temperature with the spectral line of C IV ($n = 6 - 7$) in divertor plasmas. From the spectrum, two ion temperatures were inferred, i.e., a broad and a narrow component. In order to interpret this result, the observed spectrum was compared with the spectrum calculated by a plasma transport code, an impurity transport code and a collisional-radiative model. This analysis indicated that the temperature of a broad and a narrow component reflected the ion temperature in the common flux plasma and the private plasma, respectively. The comparison resulted in good agreement between the measurement and the simulation for both of the temperature and the intensity of the broad component. However, for the narrow component, the simulation underestimated the intensity although the temperature agreed well.

[1] Nakano, T., et al., submitted to J. Plasma Fusion Res. (2003).
[2] Shimizu, K., et al., J. Nucl. Mater. **196-198** 476 (1992).
[3] Shimizu, K., et al., J. Nucl. Mater. **220-222** 410 (1995).

9.7 Feedback Control of Divertor Plasma Density using Divertor Interferometer

H. Takenaga, N. Oyama, S. Kokusen, S. Sakata, T. Fukuda

1. Introduction

Active control of the divertor plasma is important for optimization of the divertor performance. In JT-60U, feedback control of the divertor radiation loss power or its fraction to the NB heating power and the divertor neutral pressure is demonstrated using the divertor gas-puffing [1, 2]. Since the divertor plasma density is expected to respond quickly to the divertor gas-puffing, the feedback control of the divertor plasma density has been developed using the divertor mm-wave interferometer [3] to expand the divertor plasma controllability. In this report, first demonstration of the feedback control for the divertor plasma density and results of the trial for independent control of divertor and main plasma densities are presented. The feedback control system is described in section 2. The feedback control of the divertor plasma density is demonstrated in section 3. Possibility of the independent control for the divertor and main plasma densities is discussed in section 4, followed by a summary in section 5.

2. Feedback Control System

Figure 1 shows schematic drawing of the feedback control system for the divertor plasma density together with fuelling to the main plasma. The line integrated divertor plasma density is measured using the mm-wave interferometer with a frequency of 183 GHz. A cut-off density is calculated to be 4.8×10^{20} m^{-3}. The measuring chord passes horizontally under the X-point as shown in Fig. 1. The phase shift (ϕ) between signal and reference waves is detected with analogue phase detector, and the line integrated density is calculated from $\sin(\phi)$ and $\cos(\phi)$ in the real time processor. The divertor gas-puffing rate (Q_{div}) is determined using proportional and differential gains (α_p and α_d) as $Q_{div}=\alpha_p(n_el^{sig}-n_el^{ref})+\alpha_d\Delta(n_el^{sig}-n_el^{ref})/\Delta t$, where n_el^{sig} is the measured line integrated divertor plasma density and n_el^{ref} is the preprogrammed reference value. The divertor gas-puffing is applied from bottoms of W-shape configuration as shown in Fig. 1. Fuelling to the main plasma such as main gas-puffing, NB injection and high-field-side (HFS) midplane pellet injection are used for the study of the independent control for the divertor and main plasma densities. The geometries of these fuellings are also shown in Fig. 1.

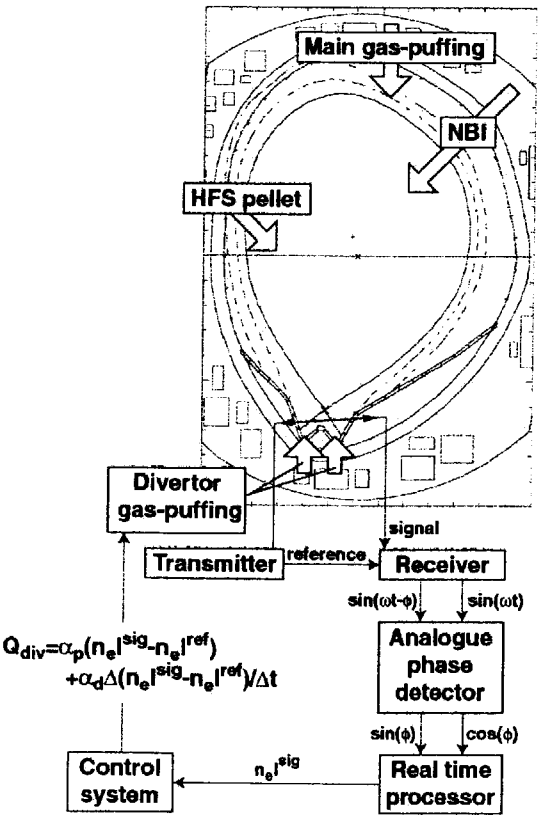

Fig. 1 Schematic drawing of feedback control system of divertor plasma density.

3. Demonstration of Feedback Control for Divertor Plasma Density

The feedback control of the divertor plasma density is demonstrated in hydrogen OH plasma. Figure 2 shows typical wave-forms with the plasma current of I_p=1.2 MA and the toroidal magnetic field of B_T=3.5 T, where α_p and α_d are set to be 1.5×10^{-13} and 3×10^{-15}, respectively. The feedback control is applied from t=3 s to t=10 s. The reference value is set to be 3×10^{18} m^{-2} during t=5-7 s and 5×10^{18} m^{-2} during t=9-10 s. It can be seen from this figure that the divertor plasma density is well controlled by the feedback control system. In this discharge, the oscillation of the divertor plasma density disappears by optimizing α_p and α_d. When α_p and α_d are set to be 2×10^{-13} and 4×10^{-15}, respectively, the oscillation of the divertor plasma density is observed in the range of $n_e l^{div}>4\times10^{18}$ m^{-2}.

In the discharge shown in Fig. 2, the main plasma density is lower than 25% of the Greenwald density. The difference between the measured divertor density and the reference seems to be smaller in the low density region compared with the feedback control of the divertor radiation loss power and the divertor neutral pressure. However, in the high density region, the oscillation of the divertor plasma density still appears. The oscillation in the high density region could be ascribed to the non-linear dependence of the divertor plasma density on the divertor gas-puffing rate. Further optimization of α_p and α_d is necessary in the high density region considering the non-linear dependence.

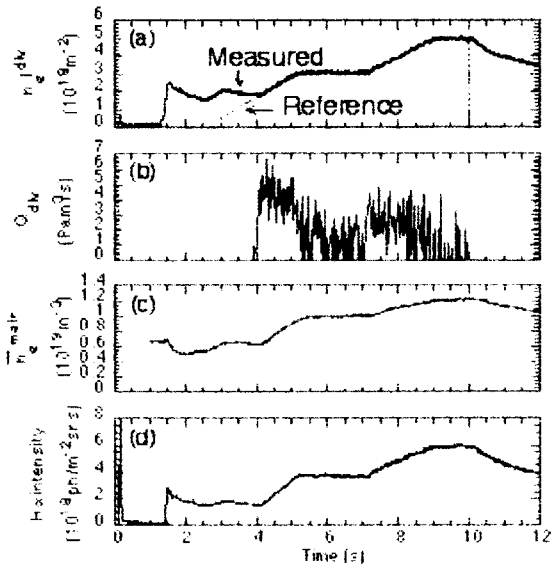

Fig. 2 Typical wave-forms of feedback control for divertor plasma density : (a) line integrated divertor plasma density for measurement and reference, (b) divertor gas-puffing rate, (c) main plasma density and (d) Hα emission intensity.

4. Independent Density Control for Divertor and Main Plasmas

In the steady-state phase, the densities in the main and divertor plasmas (n_e^{main} and n_e^{div}) are expressed as follows,

$$n_e^{main}=(S_{main}\tau_p^{main}+S_{div}\tau_p^{edge})/V^{main} \quad (1)$$

$$n_e^{div}=(S_{main}+S_{div})\tau_p^{div}/V^{div} \quad (2)$$

where S_{main} and S_{div} are the particle source for the main and divertor plasmas, respectively. S_{div} includes the recycling source and divertor gas-puffing. τ_p^{main} and τ_p^{edge} are the effective particle confinement times of the main plasma for the particle source in the main and divertor plasmas, respectively. τ_p^{div} is the effective particle confinement time in the divertor plasma. V^{main} and V^{div} are the volume of the main and divertor plasmas, respectively. In order to control the divertor plasma density independently from the main plasma density, fuelling for the main plasma with a larger τ_p^{main} is effective. In this section, possibility of the independent density control is discussed using the particle source for the main plasma such as main gas-puffing, NB fuelling and pellet injection. The plasma parameter scan is also effective for the independent control through the change of the effective particle confinement times. Here, the plasma current is scanned for a trial of the independent density control.

4.1 Main Gas-puffing

The independent density control is first tried by combining the divertor and main gas-puffing as shown in Fig. 3 with I_p=1.2 MA and B_T=3.5 T. In this discharge, the main gas-puffing is applied from t=6.5 s with a puffing rate of Q_{main}=3 Pam^3/s. The divertor gas-puffing rate is decreased during the main gas-puffing. The increasing rate of the main plasma density seems to be slightly large during the main gas-puffing, indicating that τ_p^{main} for the main gas-puffing is not largely different from τ_p^{edge}. The relationship between the divertor and main plasma densities is not largely changed with the main gas-puffing. The particle confinement time ($\tau_p=(S_{main}\tau_p^{main}+S_{div}\tau_p^{edge})/(S_{main}+S_{div})$) including the divertor and SOL regions is roughly estimated to be 54 ms before (t=6.25 s) and 51 ms during (t=7.25 s) the main gas-puffing. These values indicate difficulty of sufficient independent density control by using the main gas-puffing, because different τ_p is necessary for the independent density control.

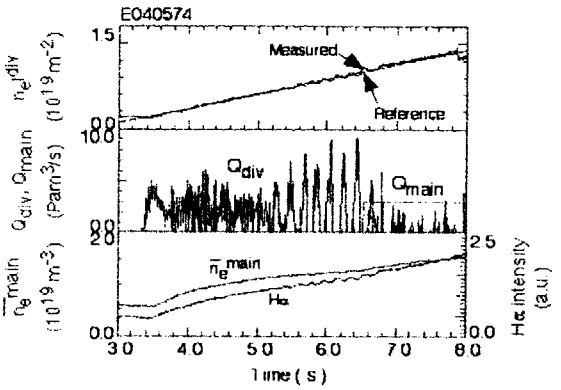

Fig. 3 Wave-forms of feedback control for divertor plasma density with main gas-puffing.

4.2 Neutral Beam Injection

As an alternative approach, the independent control of main and divertor densities have also undertaken using NB with I_p=1.2 MA and B_T=3.5 T. The result is shown in Fig. 4. In this discharge, NB is injected during t=6.5-9.0 s with a heating power of 1.2-3.6 MW. During the NB phase, the main plasma density slightly decreases. On the other hand, the divertor plasma density is increased by enhancement of the recycling, although the fuelling rate of the NB at t=7-8 s (3.5×10^{20} /s) is smaller than the divertor gas-puffing rate averaged during t=6-6.5 s (1.7×10^{21} /s). The recycling coefficient becomes large probably due to heat load onto the divertor plates during the NB phase. The value of τ_p is reduced from 47 ms before (t=6.25 s) to 31 ms during (t=7.8 s) the NB injection. Therefore, the main plasma density does not increase even with the particle source in the main plasma due to NB injection, although the divertor plasma density increases due to the enhancement of the recycling. This result indicates possibility of the independent density control by changing τ_p.

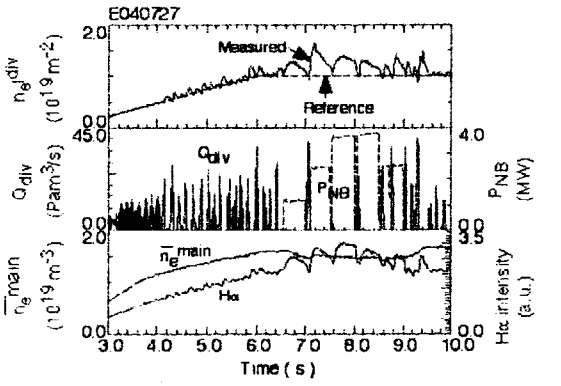

Fig. 4 Wave-forms of feedback control for divertor plasma density with NB.

4.3 Pellet Injection

In order to fuel to the main plasma without the degradation of τ_p, pellet injection is used as shown in Fig. 5. The pellet is injected from the HFS midplane at t=5.72 s into deuterium

plasma during the feedback control of the divertor plasma density with a constant reference value at I_p=1.2 MA and B_T=3.5 T. Both main and divertor plasma densities are increased by the pellet injection, and the divertor gas-puffing is stopped during t=5.8-6.2 s. The main plasma density is transiently increased to 1.5×10^{19} m^{-3} by the pellet injection with $n_e l^{div}=6\times10^{18}$ m^{-2}. The main plasma density is 25% higher than that with the divertor gas-puffing with the same divertor density. The pellet injection is one of the methods for independent density control.

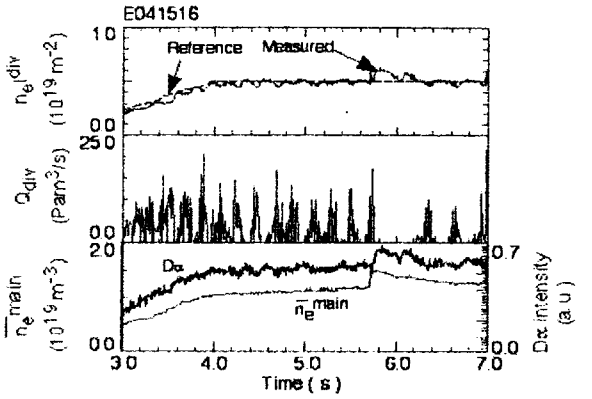

Fig. 5 Wave-forms of feedback control for divertor plasma density with pellet injection.

4.4 Plasma Current Scan

Finally, the independent density control is tried by I_p scan. In the discharge shown in Fig. 6, I_p is scanned from 0.8 MA to 1.5 MA with B_T=3 T during the feedback control of the divertor plasma density with a constant reference value. The main plasma density increases with I_p, while the divertor plasma density is well controlled to the constant reference value. The main plasma density is changed by more than 50% (from 0.9×10^{19} m^{-3} to 1.4×10^{19} m^{-3}) with a constant divertor plasma density. However, τ_p is changed only by 16% (from 61 ms at t=5.25 s to 71 ms at t=11.75 s) during I_p scan. The main plasma density increases more than increase of τ_p due to enhancement of recycling. The recycling is higher by 38% with I_p=1.5 MA (t=11.75 s) than that with I_p=0.8 MA (t=5.25 s). Therefore, the independent density control is achieved not only by the change of τ_p but also the change of τ_p^{div}.

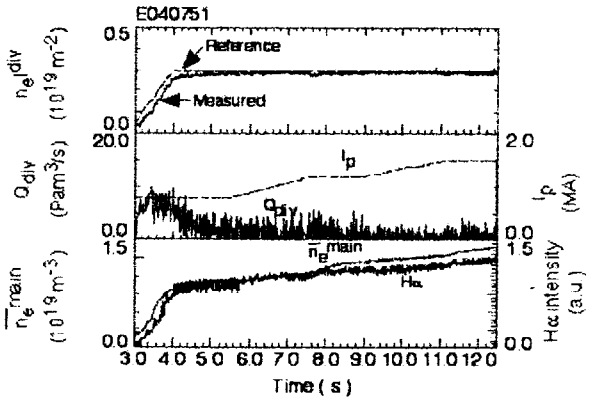

Fig. 6 Wave-forms of feedback control for divertor plasma density with I_p scan.

5. Summary

The divertor density feedback control is first demonstrated using the divertor mm-wave interferometer. Good controllability is achieved in the low density region. Sufficient independent density control is not achieved with the main gas-puffing. However, NB, pellet injection and plasma current scan change the relationship between the divertor and main plasma densities, indicating possibility of the independent density control for the divertor and main plasmas.

References

[1] Tamai, H., et al., Fusion Eng. Des. **39-40**, 163 (1998).
[2] Tamai, H., et al., J. Nucl. Mater. **266-269**, 1219 (1999).
[3] Takenaga, H., et. al., Rev. Sci. Instrum **69**, 3181 (1998).

10. Plasma Facing Materials and Detritiation

10.1 Tritium Distribution in the Plasma-facing Wall of JT-60U [1,2]

K. Masaki, K. Sugiyama[1)] T. Tanabe[1)], Y. Gotoh, K. Tobita, Y. Miyo,
A. Kaminaga, K. Kodama , T. Arai, N. Miya
1) Center for Integrated Research in Science and Engineering, Nagoya University, Japan

In the recent work at JT-60U, detailed analyses of the tritium in the carbon-based plasma-facing wall were performed using imaging plate (IP) technique [3] and full combustion method. A high tritium level was observed at the dome top tiles in the private region and the outer baffle tiles. The tritium concentrations in the dome top and the outer baffle tiles were 60 kBq/cm^2 and 20 kBq/cm^2, respectively. The tritium level in the divertor target tiles was lowest (0.2 kBq/cm^2) in the divertor region. In scanning electron microscope analyses, thick deposition layers (~ 60μm) were found on the inner divertor target tiles, while the deposition layer was not obviously observed on the dome top and the outer divertor target tiles [4]. These results showed no correlation between the deposition layers and the tritium retention in JT-60U. In the full toroidal IP measurements of the dome top tiles, the tritium was distributed periodically, and it was correlated to the toroidal field (TF) coil positions, i.e. TF ripple. On the other hand, although the tritium level in other first wall region was lower than the divertor region, the tritium level in the outside midplane first wall tiles was higher than the level in the inside first wall tiles.

An important mechanism of energetic ion losses is the ripple transport, which is caused by the TF ripple. In JT-60U, the tritons with the initial energy of 1MeV are produced by the DD nuclear reaction. To assess the energetic triton loss, a simulation using an orbit following Monte-Calro code was performed taking into account the ripple transport. The simulation result showed that 31% of the produced tritons were lost and implanted into the wall. The triton deposition distribution was consistent with the tritium distribution obtained by IP and full combustion measurements. Moreover, a high surface temperature of above 500°C of the divertor target tiles could cause thermal release of the retained tritium in the tiles. These results indicate that the tritium distribution on the plasma-facing wall of JT-60U reflects the distribution of the energetic tritons impinging on the wall with a slight modification due to the surface temperature rise. According to the simulation, the tritons were implanted deeply into the wall with high energy of up to 1MeV.

References

[1] Masaki, K., et al., 15th PSI, Gifu, Japan, (2002), J. Nucl. Mater., in press.
[2] Tanabe, T., et al., 19th IAEA Fusion Energy Conference, Lyon, France, (2002), to be published in Nuclear Fusion.
[3] Tanabe, T., et al., Fusion and Science Technol. **41**, 877 (2002).
[4] Gotoh, Y., et al., 15th PSI, Gifu, Japan, (2002), J. Nucl. Mater., in press.

10.2 The Depth Profiles of Deuterium and Hydrogen in Graphite Tiles Exposed to Deuterium Plasma Discharges of JT-60U

Y.Hirohata[1], Y.Oya[2], H.Yoshida[1], Y.Morimoto[3], H.Kodama[3], K.Kizu[4], J.Yagyu[4], Y.Gotoh[4], K.Masaki[4], T.Arai[4], K.Okuno[3], N.Miya[4], T.Hino[1], S.Tanaka[2] and T.Tanabe[5]

1) Hokkaido University, 2) The University of Tokyo, 3) Shizuoka University, 4) JAERI, Naka, 5) Nagoya University

1. Introduction

It is a very important issue to evaluate retention properties of tritium and deuterium in in-vessel components from a viewpoint of safety for a fusion reactor. There have been many investigations of the retention properties of hydrogen isotopes in in-vessel components of current devices. Based on these investigations and laboratory works, the tritium inventory in ITER has been evaluated. Quite recently, plasma-facing graphite tiles used in JT-60U have become available for various investigations. Tritium retention in the graphite tiles was analyzed by the tritium imaging plate (IP) technique [1]. Larger tritium level was found at the dome top unit or the "private region", mainly due to the implantation of high-energy tritium produced by D-D reaction [1,2]. However, the retention of other hydrogen isotopes, i.e. hydrogen and deuterium, has not been clarified yet.

In this study, the depth profiles of hydrogen and deuterium retained in the graphite tiles placed in the JT-60U W-shaped divertor were investigated by secondary ion mass spectrometry (SIMS). These tiles were exposed to deuterium and hydrogen discharges from June 1997 to October 1998.

2. Experiments

Figure 1 shows the cross sectional view of the JT-60U W-shaped divertor. All tiles received 3600 shots of deuterium discharges. After each of two deuterium discharge periods, a hydrogen discharge experiment, of totally 700 shots, was carried out for deterioration of tritium before vent. Thirteen thermocouples were installed in the divertor region, monitoring the tile temperatures during the discharge experiments. The position of each thermocouple was 6 mm under the tile surface. For this study, samples (5mm×10mm×1mm) were cut from the tiles just above the thermocouples. Four samples (ID1~ID4) from the inner divertor tiles, three samples (OD1~OD3) from the outer divertor tiles, four samples from the baffle plates (BP1, BP11, BP2, BP3) and nine samples (DM1~DM9) from the dome units were prepared.

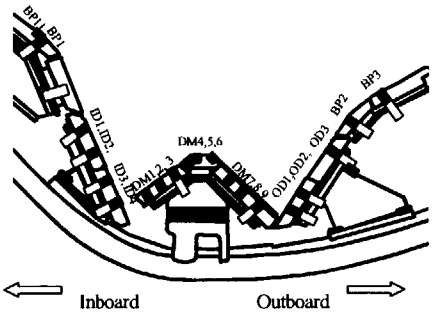

Fig.1 Cross sectional view of the divertor region of the JT-60U W- shaped divertor.

Depth profiles of hydrogen, deuterium, boron and oxygen retained in the graphite tiles were analyzed by SIMS using Cesium primary ions (Cs^+) for sputtering. The sputtering rate was approximately 1 μm/hr. The signal intensities of hydrogen isotopes, boron, and oxygen were normalized by that of ^{12}C for comparison. In order to compare the concentration of retained

hydrogen (deuterium) in the tile, time-integration of intensity ratios of H/^{12}C and D/^{12}C were obtained within the sputtering time of 6000 seconds, corresponding to the depth of 1.7 μm. Theses values are named as ΣH/^{12}C and ΣD/^{12}C.

3. Results and Discussion

Figure 2 shows the depth profiles of H/^{12}C (a) and D/^{12}C (b) signal intensity ratios in the outer divertor tiles and the inner baffle plate (BP11). On the outer divertor, erosion with a maximum depth of about 20 μm was found [3]. The H/^{12}C ratio near the surface was approximately one order of magnitude larger than that of D/^{12}C in all the samples, and the ratio approached to that of the bulk CFC (0.01~0.03). These results indicate that the deuterium near surface region was replaced by hydrogen. Spectroscopic measurement during the H discharges clearly showed the replacement of retained D by H [4]. In addition, surface deuterium could also be replaced by hydrogen through isotopic exchange with water molecules in the atmosphere after removal of the tile from the vacuum vessel. The depth profiles of the H/^{12}C ratios were almost the same for all the samples as shown in Fig. 2(a). On the other hand, the D/^{12}C ratios were very different among the tiles. In the outer divertor tiles, the smallest ΣD/^{12}C value observed in OD2 was 0.01. The strike point was usually located between OD1 and OD2. At OD2, the tile temperature was high and the frequency when separatrix strike located was largest among the outer divertor tiles. The maximum D/^{12}C ratio in the BP11 sample was observed at a depth of 750 nm. The D/^{12}C ratio in the BP11 sample slowly decreased with the depth, but the ratio was still at least several times larger than those of the outer divertor tiles. At the inner baffle plates (BP1) and outer baffle plates(BP3), high deuterium retention was also observed. The ΣD/^{12}C and the Σ(H+D)/^{12}C values from BP1 were 0.94 and 1.32, respectively, which were the largest values in all the measured samples.

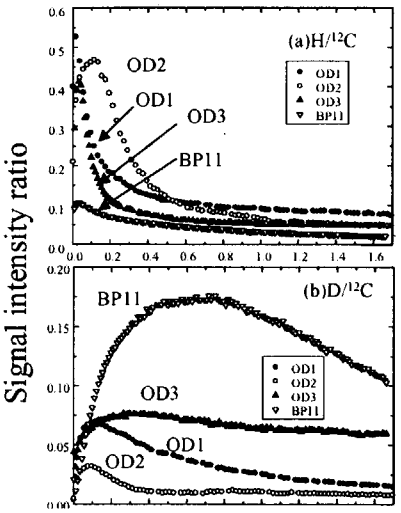

Fig.2 Depth profiles of H/^{12}C (a) and D/^{12}C(b) signal intensity ratios in the outer divertor tiles (OD1, OD2, OD3 samples) and the inner baffle plate (BP11 sample)

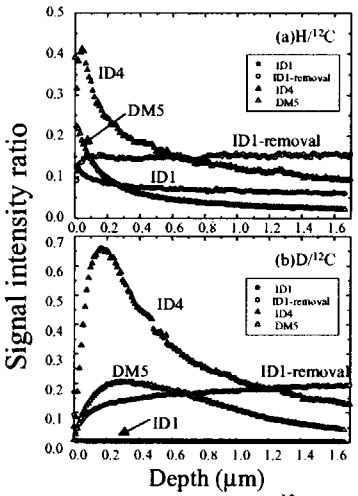

Fig.3 Depth profiles of H/^{12}C (a) and D/^{12}C(b) signal intensity ratios in the inner divertor tiles (ID1, ID4 samples) and the dome top tile (DM5 sample)

Figure 3 compares the depth profiles of H/^{12}C (a) and D/^{12}C (b) signal intensity ratios in the inner divertor tiles (ID1, ID4) and the dome top tile (DM5). From the observation of the cross section of these tiles, thick and continuous redeposition layers with the thicknesses from several to a few tens of microns were observed on the surface of all inner divertor tiles except for ID4[3]. In contrast, on the dome top and the outer dome wing tiles as well as ID4, no remarkable redeposition layers were found. Since the thickness of the redeposition layers were larger than 1.7 μm, the depth profiles of

ID1 means that of the redeposition layer. The D/^{12}C ratio of the redeposition layer(ID1) was very small, 0.003, only two orders of magnitude larger than that of the bulk CFC (~10^{-5}). Similar results were obtained in ID2 and 3 with thick redeposition layer. In order to understand these small-integrated intensity ratios in the redeposition layers, the redeposition layer of ID1 was mechanically eliminated. The depth profiles of H/^{12}C and D/^{12}C of ID1 after removal the redeposition layer (ID1-removal) are also shown in Fig.3. Both intensity ratios of ID1-removal were different from those of ID1. The ΣD/^{12}C value of ID1-removal was 0.2, approximately 70 times larger than that before. From this result, it was clear that the layer with large concentration of hydrogen and deuterium existed under the redeposition layer. It is suggested that thermal contact of the redeposition layer to the tile surface was so poor that the surface temperatures of the redeposition layer was much higher than that measured by the thermocouples, resulting in the small H/^{12}C and D/^{12}C ratios in the redeposition layers on the inner divertor tiles. The largest H/^{12}C and D/^{12}C ratios in the inner divertor were observed at ID4 (near the inner slot), where no redeposition layer was found. The ΣD/^{12}C value was large, 0.33, two orders of magnitude larger than other ID samples. Similar tendency in the ΣH/^{12}C value was also observed. The strike point in the inner divertor region was located mainly between ID2 and ID4. In the case of ID4, the temperature measured by the thermocouple during discharge was lower than 340 °C (see Fig.4). The ID4 sample was irradiated with high-flux hydrogen (deuterium) ions, when separatrix strike point was located on the sample. The sample was irradiated with high-flux hydrogen(deuterium) particles. The high fluxes of particles and the low temperature may have been the reason why the D/^{12}C value in ID4 became large. The depth profiles of H/^{12}C and D/^{12}C of the dome top tile (DM5) were very similar to those of ID4. The maximum D/^{12}C ratio of DM5 was observed at a depth of 0.2 μm which was deeper than that of ID4. Further explanations for the deep penetration of deuterium in the dome region probably at the lower operation temperatures will still be needed.

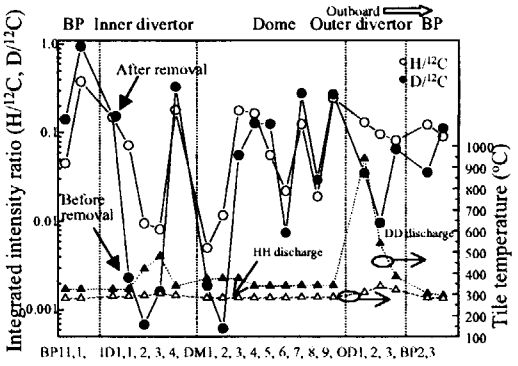

Fig.4 Integrated intensity ratios of D/^{12}C (●) and H/^{12}C(○)of all measured samples. The maximum temperature rise of the tile during deuterium discharges (▲) and the average temperature of the tile during hydrogen discharges (△) are also plotted.

Figure 4 summarizes the integrated intensity ratios, ΣD/^{12}C and ΣH/^{12}C, which were obtained within the depth of 1.7 μm. In this figure, the maximum temperature rise of each tile during deuterium discharges [5] and the average temperature during hydrogen discharge measured by the thermocouples are also plotted. The surface temperatures of the tiles should be higher than those measured by thermocouples, and are very different from the positions. Largest temperature difference was 500°C at divertor target tile, 30°C at other tile e.g., dome and baffle tiles. A large difference was observed in the divertor tiles, i.e. the erosion mainly occurred in the outer divertor tiles, whereas the redeposition mainly occurred in the inner divertor tiles. This difference strongly affects the Σ(H+D)/^{12}C values. Described above, the Σ(H+D)/^{12}C values of the inner divertor tiles with thick redeposition layers (ID1~ID3) were those of the redeposition layers. We can see that the

$\Sigma D/^{12}C$ and $\Sigma H/^{12}C$ values of the samples with redeposition layers ($\Sigma D/^{12}C$ values = 0.0007~0.002, $\Sigma H/^{12}C$ values = 0.008~0.07) were considerably smaller than that of the samples without the layers.

In the cases of ID4 without the redeposition layer and ID1 after the removal of the redeposition layer, the $\Sigma D/^{12}C$ values were larger than those of the outer divertor tiles. The reason is that the temperatures of the inner divertor tiles during deuterium discharges were lower than those of the outer divertor tiles. The $\Sigma(H+D)/^{12}C$ values were affected not only by the temperatures of the tiles, but also by the fluxes and energies of hydrogen isotopes ions and charge exchange particles. Therefore, if the average temperature of the tile becomes low at the strike point, the $\Sigma(H+D)/^{12}C$ value might be large similar to ID4. In the outer divertor tiles, the smallest $\Sigma D/^{12}C$ value was observed at OD2. The reason may be that in the last 100 shots of hydrogen discharge period, separatrix strike point was more frequently located around the OD2 position. The $\Sigma(H+D)/^{12}C$ values in the outer divertor tiles and the outer baffle plate generally increased with distance away from the center of the frequency distribution of strike point. The reason may be that the temperature of the tile and the distance from the plasma both decreased. In the dome unit, the $\Sigma D/^{12}C$ and the $\Sigma H/^{12}C$ values were largely different among the analyzed positions. There does not appear to be any relationship between the temperature and the $\Sigma(H+D)/^{12}C$ value. Larger $\Sigma(H+D)/^{12}C$ values were observed at the inner side of the dome tiles (DM3~DM5). It is assumed that laminar and globular depositions may exist partially on the inner dome wing tile[3]. Similar reason may be applied to the baffle plates.

4. Conclusions

The depth profiles of deuterium and hydrogen of the tiles placed in the divertor region of JT-60U were investigated by SIMS. The signal intensity ratio of $H/^{12}C$ or $D^{12}C$ varied with the position of the tiles. In the case of the outer divertor tiles, where the erosion mainly occurred, the minimum point of the integrated intensity ratio, $(H+D)/^{12}C$ roughly correlated with the strike point position in the last hydrogen discharge periods. In the case of the redeposition layer of the inner divertor tiles, the integrated intensity ratios of $(H+D)/^{12}C$ were very small. In the case of the dome tiles and the baffle plates, the $(H+D)/^{12}C$ ratios were very large. The $D/^{12}C$ and $H/^{12}C$ integrated intensity ratios roughly increased with the decrease of the maximum temperature of the tile during the deuterium discharge, and the average temperature during the hydrogen discharge.

The present profiles of hydrogen isotopes are well correlated to the flux of ion and/or charge exchange neutral and the exist of the re-deposition layer and the temperature of the tiles.

Reference

[1] Tanabe, T., et.al., Fusion Sic. & Tech. **41**, 877(2002).
[2] Masaki, K., et.al., J.Nucl.Mater., **313-316**, 514(2003).
[3] Gotoh, Y., et.al., J.Nucl.Mater., **313-316**, 370(2003).
[4] Higashijima S. and the JT-60U Team, J. Plasma and Fusion Research, **75**, 1297 (1999).
[5] Masaki, K, et.al., Proc. 20th Symposium on Fusion Technology, France, Marseille, 67 (1998)

10.3 Study of Chemical States of Graphite Tiles exposed to Deuterium Plasma by XPS

Y.Oya[1], Y.Morimoto[2], Y.Hirohata[3], H.Kodama[2], H.Yoshida[3], K.Kizu[4], J.Yagyu[4], Y.Gotoh[4], K.Masaki[4], K.Okuno[2], N.Miya[4], T.Hino[3], S.Tanaka[1] and T.Tanabe[5]
1) The University of Tokyo, 2) Shizuoka University, 3) Hokkaido University, 4) JAERI, 5) Nagoya University

1. Introduction

Understanding of tritium and deuterium behaviors in in-vessel components is one of the most critical issues for a future fusion reactor on a viewpoint of safety evaluation. Quite recently, plasma-facing graphite tiles used in JT-60U at Japan Atomic Energy Research Institute (JAERI) has become available for various investigations. Tritium retention in graphite tiles used in JT-60U was analyzed by the tritium imaging plate technique, and the highest tritium level was found at the center of the dome top unit or the private region and the outer baffle plates, where the plasma did not hit but the distance from the plasma was the shortest [1]. However, the chemical form of the hydrogen isotopes were not clarified sufficiently and it is important to understand the behavior and the chemical states of the hydrogen isotopes in plasma-facing materials.

In this study, the chemical states of carbon, oxygen and boron in the graphite tiles of the dome top unit used for ~3600 shots of deuterium plasma discharges, followed by ~700 shots of hydrogen plasma discharges for about one year operation in JT-60U, have been investigated by X-ray photoelectron spectroscopy (XPS). The experimental results for XPS are also discussed with those for secondary ion mass spectroscopy (SIMS) taken from the previous study [2].

2. Experimental

Figure 1 depicts the cross section of the JT-60U W-shaped divertor. Thirteen thermocouples were installed in the divertor region, monitoring the tile temperatures during the discharge experiments. The position of each thermocouple was 6 mm under the tile surface. The graphite tiles investigated in this study were carbon fiber composite (CFC:PCC-2S) for the dome top. All tiles were exposed to ~3600 shots of

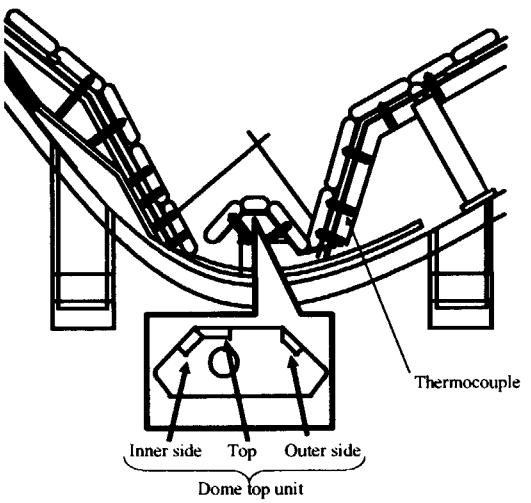

Fig.1 Cross section of divertor region in JT-60U

deuterium discharges for the June 1997 – October 1998 experimental period. During the deuterium plasma discharges, the vacuum vessel was evacuated from the inner divertor slot with cryopumps. Boronization was performed two times during that experimental period [3,4]. After the deuterium-plasma periods, 700 shots of hydrogen discharges were carried out to remove the surface tritium. The samples were cut from the tiles with the thickness of about 1mm.

The chemical states of graphite, boron and oxygen from the samples were studied by XPS (ULVAC-PHI ESCA5500MC system), using a Mg-Kα 400 W X-ray source and a hemispherical electron analyzer. The depth profile was also analyzed by Ar ion (Ar^+) sputtering with an energy of 4.0 keV and a fluence range of 2.93×10^{21} - 1.54×10^{23} m^{-2}.

3. Results and discussion

Figure 2 shows the photoelectron spectra of C 1s, B 1s and O 1s, respectively. The peak top position of the tile before Ar sputtering was clearly different from the standard peak position and shifted to a higher binding energy side. After Ar^+ ion sputtering with the fluence of more than 2.93×10^{21} m^{-2}, which corresponds to a sputtered depth of about 40 nm, estimated from the sputtering yield [5], the spectra were shifted toward the standard C 1s position. It was reported that the binding energy of C 1s for amorphous hydrogenated carbon (a-C:H) and CO are 284.9~285.5 eV and 286.4~286.8 eV, respectively [6]. This result indicates that hydrocarbons were formed only on the surface (about 40 nm) of the tile. In the case of B 1s, the peak from the tile before Ar^+ ion sputtering was shifted to a higher binding energy of 193 eV, indicating that boron oxide was formed on the surface of the tile. After the Ar^+ ion sputtering of 2.93×10^{21} m^{-2}, the B 1s peak was shifted to a lower binding energy and divided into two peaks, B(Oxide) and B(Carbide) or B 1s. The O 1s peak was also weakened by the Ar^+ sputtering. It

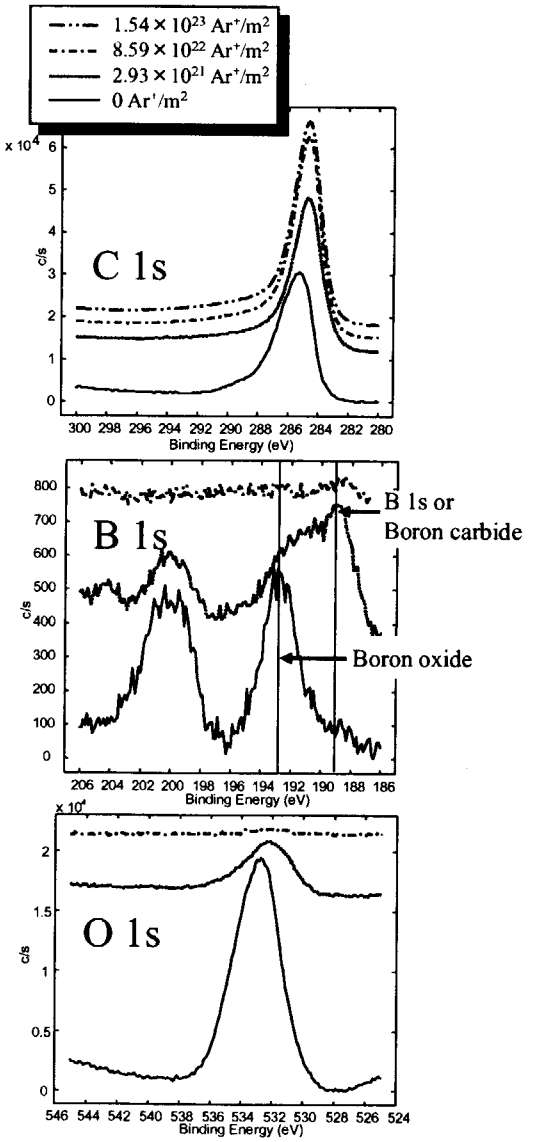

Fig.2 Photoelectron spectra of C 1s, B 1s and O 1s from the center of the dome top unit by XPS

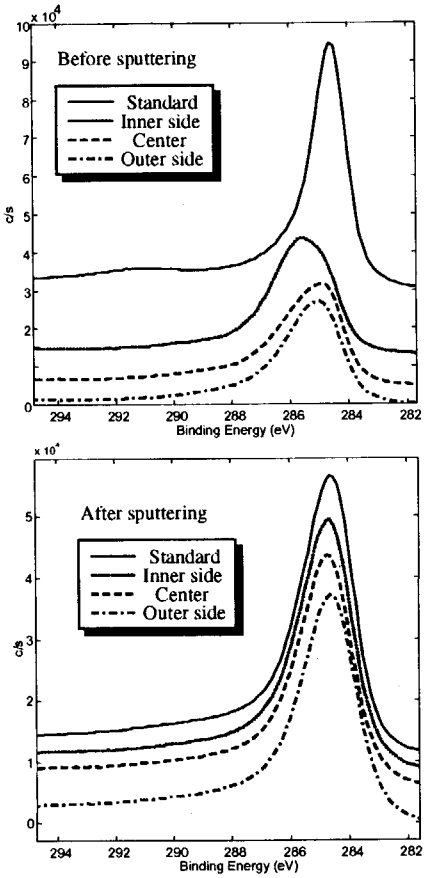

Fig.3 Photoelectron spectra of C 1s from the inner side, the center and the outer side of the dome top unit before and after Ar^+ ion sputtering by XPS.

indicates that the oxygen is combined with boron mainly.

The photoelectron spectra of C 1s from the inner side, the center and the outer side of the dome top unit by XPS were shown in Fig.3. The back side of the center of the dome top unit tile was used as standard, of which the binding energy was 284.57 eV. The peak top position of the inner side of the dome top unit was clearly different from the standard and shifted to a high binding energy than 285.56eV. In the center of the dome top unit, the shoulder peak was also observed in higher binding energy. After the Ar^+ ion sputtering, which fluence was $2.93\times10^{21}m^{-2}$, the spectra of all the dome unit tile were shifted to the lower energy side. However, the peaks at the inner side as well as at the center of the dome top tile were still shifted to the higher binding energy side (less than 0.1 eV) of the standard. Those positive shifts show existences of hydrogen (deuterium) implantation layers in the subsurface layers. The larger positive shift on the inner side of the dome top tile shows existences of thin hydrocarbon absorption layers and re-deposition layers (thickness <1㎛). This experimental result can be correlated with the fact that re-deposition layers were observed on the inner targets rather than on the outer targets in the W-shaped divertor region[7].

It was also reported that large amount of hydrogen isotopes were retained in the inner side of the dome top unit by SIMS and the concentration was decreased as it goes to the outer side[2,8]. These results are consistent with the experimental results by XPS. In this dome region, only the temperature of dome wing was measured and these temperatures were less than 400 ℃. Those facts indicate that distribution of the retained hydrogen (deuterium) in the dome top region would depend not only on the distributions of flux and energies of the incomming hydrogen (deuterium) but also on those of the flux and energies of incoming impurity species especially hydrocarbons.

4. Conclusion

The chemical states of carbon, boron and oxygen in the tiles used for deuterium and hydrogen plasma operation in JT-60U were studied by XPS. It was found that the

binding energies of C-1s on the surface of all the tiles were shifted to higher energies compares with the standard CFC sample, and this result indicates that hydrogenated carbon layers were formed on the surface region (～40nm) of the tiles. The boron also existed on the surface with the chemical form of boron oxide from the experimental results of B 1s and O 1s spectra.

The chemical states of carbon from the inner side, the center and the outer side of the dome top unit were also studied by XPS. It was found that large peak shift was observed in the inner side of the dome top unit. It indicates that the hydrocarbon absorption layer and re-deposition layer exist mostly on the inner side of the dome top unit compared with the outer side.

These experimental results were compared with those by SIMS. It was found that the large amount of hydrogen isotopes were retained in the inner side of the dome top unit by SIMS and the concentration was decreased as it goes to the outer side. These results were consistent with the experimental results by XPS and it can be said that the amount of deuterium would depend not only on the distributions of flux and energies of the incomming hydrogen (deuterium) but also on those of the flux and energies of incoming impurity species especially hydrocarbons.

References

[1] Tanabe, T., et al., Fusion Sci & Tech. **41**, 877 (2002).

[2] Hirohata, Y., et al., Physica Scripta, in press.

[3] Yagyu, J., et al., to be published in Proc. of the IEEE 19th Symposium on Fusion Engineering, Atlantic City, (2002).

[4] Yagyu, J., et al., J. Nucl. Mater. **241-243**, 579 (1997).

[5] Kanaya, K. et.al, Jpn J.Appl.Phys. **12**, 1297 (1973)

[6] Moulder, J.F., et al., Handbook of X-ray Photoelectron Spectroscopy, Physical Electronics, Eden Prairie, (1992).

[7[Gotoh, Y., et al., J. Nucl. Mater., in press.

[8] Oya, Y., et al., J. Nucl. Mater., in press.

10.4 Erosion and Re-deposition on the Graphite and CFC Tiles used in the W-shaped Divertor [1]

Y. Gotoh, J. Yagyu, K. Masaki, Y. Miyo, A. Kaminaga,
K. Kodama, T. Arai, T. Tanabe[1)], N. Miya
1) Nagoya University, CIRSE, Furo-cho, Chikusa-ku, Nagoya-shi, Aichi, 464-8603, Japan

Studies on erosion and re-deposition on the divertor plates are of primary importance for lifetime estimation of the divertor target plates, elucidation of carbon impurity behavior, and estimation of hydrogen isotope inventory in the divertor region.

Erosion and re-deposition on graphite and carbon fiber composite (CFC) tiles sampled from the W-shaped divertor with the inner-side pumping slot [2] have been studied. Those tiles were used in the operation periods of June 1997 - October 1998. Totally 4300 tokamak discharges (3700 deuterium discharges and 700 hydrogen discharges) and two times boronization have been performed. Erosion depths at the tile front faces were measured in poloidal direction using a dial gauge. Re-deposition layer thicknesses were estimated from cross-sectional images of deposition layers taken using a scanning electron microscope (SEM), in both the poloidal and the toroidal directions on the tiles.

Continuous re-deposition layers were not found on the dome top nor on the outer dome wing, whereas re-deposition layers of ~20μm thickness were found on the mid zone of the inner dome wing. On the outer divertor target, erosion was dominant: the maximum erosion depth was ~20μm. On the inner target, re-deposition was dominant: the maximum thickness was ~60μm. The SEM observations showed that microstructures of the thinner re-deposition layers below ~30μm were rather porous and columnar, whereas those of the over-layers of the thicker layers (>~30μm) were laminar - columnar multi-layered structures. The laminar structures were explained through the higher deposition temperatures at the strike point due to the lower thermal conductivity of the porous columnar under-layers. For both the inner and the outer target, poloidal distributions of the erosion depth and the re-deposition layer thickness were well correlated with the poloidal distributions of the time-integrated strike point positions on the targets, which were weighted with total power of neutral beam injection. For the inner target, the re-deposition layers were much thinner in areas shadowed from divertor plasmas by the edges of the neighboring tiles along the magnetic field lines, compared to those formed in the un-shadowed area.

X-ray photoelectron spectroscopy revealed that the re-deposition layers on the inner target were composed of C, B (3 - 4 %), and others: O, Fe, Cr, Ni (<0.6 %). Boron atoms were mostly bound to C atoms, but some of them precipitated as boron.

Reference

[1] Gotoh, Y., et al., J. Nucl. Mater., in press.
[2] Takenaga, H., et al., Fusion Science and Technol. **42**, 327 (2002).

10.5 Tritium Degassing Operation using Cleaning Discharges

S. Higashijima, H. Nakamura, T. Horikawa, A. Kaminaga, A. Oikawa, M. Seki, T. Arai, W. Shu, T. Umehara, T. Nakano, N. Oyama, N. Asakura, H. Kubo, S. Konishi, Y. Miura, N. Miya, M. Nishi, M. Nishikawa[1)], T. Tanabe[2)]
1) Kyushu University, 2) Nagoya University

1. Introduction

Tritium removal from the vacuum vessel is a crucial issue in a tokamak reactor with the carbon-based first wall such as ITER because tritium is tightly contained in the carbon deposits on the first wall and tritium inventory can restrict its operation from the point of view of the safety [1].

Working gas is usually deuterium in tokamak discharges of JT-60U, and tritium is generated by D-D reaction. This tritium with high energy of ~1 MeV is mainly escaped from the main plasma without energy loss due to the toroidal ripple loss, and the tritium is injected into the deep position (~μm) of the carbon tiles in JT-60U [2]. More than a half of the tritium is finally retained in the carbon tiles [3].

We have executed cleaning discharges and investigated tritium concentration and chemical species to establish an efficient technique for tritium removal. The execution of cleaning discharges is independent of tokamak discharges, and they are attractive in shortening the time to obtain the clean tokamak discharges. Data of chemical species including tritium in the exhausted gas are necessary for the design of the plant to recycle tritium.

In this paper, an overview of the tritium degassing operation is reported. The cleaning discharges in this experiment and the experimental procedure are explained in section 2. In section 3, we indicate results and discussion. The summary is shown in section 4.

2. Cleaning Discharges of JT-60U [4]

Before tritium degassing operation using cleaning discharges, tokamak operation has been carried out until June, 2002. The detailed operating conditions were as follows; working gas was deuterium, static pressure of the vacuum vessel was kept at ~1×10^{-5} Pa, baking temperature was 300 °C and NB injection using deuterium with beam energy of ~90 keV was applied. After this usual tokamak operation, pumping system was stopped and the vacuum vessel was filled with dry nitrogen gas at the atmosphere pressure for four months.

The tritium degassing operation was executed for six weeks from October to December, 2002. Working gas was helium, argon and hydrogen, and they were basically used in order of He, Ar and H_2 in a week because physical sputtering is enhanced in heavier atom such as Ar, and hydrogen is not only chemically activated but also has an effect of isotope exchange. Tritium was measured when these gases were flowed to the vacuum vessel. Gas flow, Taylor

discharge cleaning (TDC), and electron cyclotron resonance discharge cleaning (ECRDC) and glow discharge cleaning (GDC) were applied in this order. Baking of the vacuum vessel up to 300 °C was applied at the same time with the above cleaning discharges, and the temperature of the vacuum vessel was room temperature in the 1st, 2nd and 6th week, and 150 °C in the 3rd week, 250 ℃ in the 4th week and 300 °C in the 5th week.

ECRDC is formed by an injection of the electron cyclotron resonance radiofrequency wave from the lower hybrid radiofrequency (LHRF) injection system. Radiofrequency wave of a klystron with three frequencies of 1.74 GHz, 2.00 GHz and 2.23 GHz was injected to a toroidal magnetic field of ~0.07 T, and the resonance positions are 2.98 m, 3.32 m and 3.81 m, respectively. The pressure of the vacuum vessel was ~$3x10^{-2}$ Pa in the He case, ~$6x10^{-3}$ Pa in the Ar case, and $1x10^{-2}$ Pa in the H_2 case. Two types of ECRDC were explored; the one was an injection of continuous wave with low power less than 40 kW (CW injection), and the other was a pulse injection with a discharge interval of ~7 s, a pulse length of ~70 ms and high power up to 500 kW (TDC-like injection). With a mm-wave interferometer, the line-averaged electron density was measured to be ~$1x10^{16}$ m^{-3} in the two types of ECRDC. The detailed explanation of ECR system is shown in section 12.4.

In TDC, short pulse tokamak discharges are repeated periodically. This is an effective cleaning discharge in the first wall near the null point in the plasma initiation by repeating the ignition of tokamak discharge. The typical discharge conditions of JT-60U TDC are as follows; plasma current ~50 kA, toroidal magnetic field 0.73 T, discharge duration 20 ms, repetition time of the discharge 3 ~ 5 s. The pulsed gas puffing was carried out just before the discharge, and the puffing rate was 0.5 Pa m^3/s in the He case, 0.22 Pa m^3/s in the Ar case, and 0.1 Pa m^3/s in the H_2 case. The line-averaged electron density was 1.0 ~$1.5x10^{18}$ m^{-3}.

GDC is carried out by applying a high voltage with six anodes inside the vacuum vessel (cathode). Two large anodes and a small anode were used in this gas degassing operation. The large anodes are stainless steel plates (224 mm square) covered with carbon tiles with pre-ignition electrodes. The small anode consists of a piece of the first wall carbon tiles that are electrically isolated from the vacuum vessel. In the He case, the applied voltage was ~200 V, the total current was 7 A, and the pressure in the vacuum vessel was $3.0x10^{-1}$ Pa. In the Ar case, the applied voltage was ~450 V, the total current was 6 A, and the pressure was $2.0x10^{-2}$ Pa. In the H_2 case, the applied voltage was ~340 V, the total current was 7 A, and the pressure was $3.0x10^{-1}$ Pa. The line-averaged electron density was lower than detection limit (~$2x10^{15}$ m^{-3}). GDC can also clean up the inside of ports of NB injection and diagnostics where tokamak plasmas with the toroidal magnetic field are not interactive.

3. Results and discussion

Fig. 1 shows a summary of tritium removal. Amount of removed tritium in the 1st week was small because it took a time to investigate the operational window of ECR discharges and

the discharge duration was short. Although the temperature of the vacuum vessel was gradually increased from the room temperature to 300 °C, the amount of removed tritium in a week was almost constant. This means that the tritium already has been removed by cleaning discharges in the previous week and the amount of removed tritium in a week was smaller than the expected one. The total amount of removed tritium was ~73 MBq and smaller than the predicted retained tritium (about several hundreds GBq) in the first wall. Since the tritium exists in the deep position (~μm) of the carbon tiles, it suggests that cleaning discharges can only remove the tritium on the surface of the first wall. The amount of removed tritium was reduced in the 6th week in comparison with one in the 2nd week, and we confirmed that the tritium degassing operation using cleaning discharges was effective in tritium removal.

Table 1 shows the amount of removed tritium in the 4th week (250 °C). In the case of gas flow, we observed tritium removal, but the amount was small. A large amount of the tritium was removed in GDC due to a long duration of the discharge. The time behavior of tritium removal was different between the cleaning discharges. The initial maximum value monotonically decreased in glow discharge. The time behavior strongly depended on the shot history in ECR and Taylor discharges. The amount of removed tritium was smaller in the discharges of pulsed ECR wave injection (TDC-like injection) than in Taylor discharges because of the low injected power. In the case of the noble gas, an efficiency of tritium removal, defined as the removed tritium over the discharge duration, was higher in glow discharges than in ECR and Taylor discharges. This is attributed to an effect of ion bombardment with higher energy (several hundred eV) in glow discharge than in the others. On the other hand, in the case of the hydrogen, the efficiency was almost the same in all the cleaning discharges. Hydrogen was most effective in tritium removal among all the gases, and this can be attributed to chemical reactions such as isotope exchange. Chemical species of removed tritium was mainly elemental form (HT and DT), and the contents of water vapor (HTO and DTO) and hydrocarbon were small.

4. Summary

In the tritium degassing operation of JT-60U, the cleaning discharges were carried out to establish an efficient technique for tritium removal. Hydrogen was the most efficient gas and glow discharge was effective in the tritium removal, but it is found that the cleaning discharges can only remove the tritium on the surface of the first wall. Chemical species of removed tritium was mainly elemental form.

References

[1] Federici G. et al., Nucl. Fusion **41**, 1967 (2001).

[2] Tanabe T. et al., J. Nucl. Mater. **313-316**, 478 (2003).

[3] Miya N. et al., Fusion Tech. **16**, 507 (1994).

[4] Higashijima S. et al., J. Plasma Fusion Res. **75**, 1297 (1999) (in Japanese).

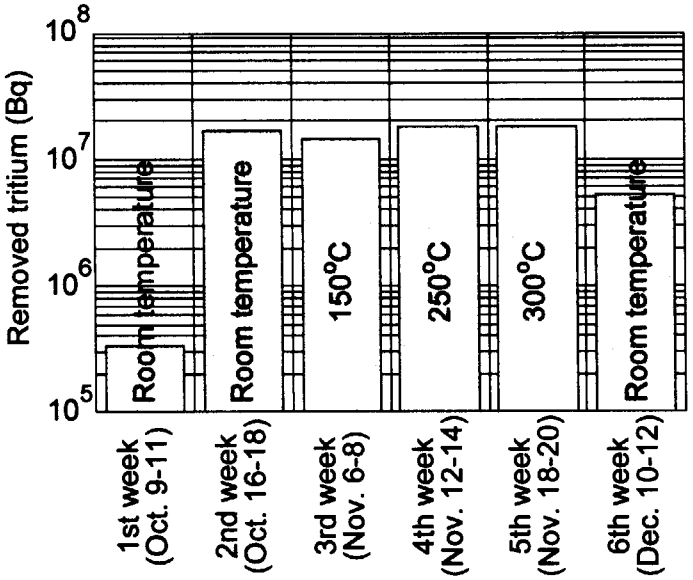

Fig. 1. Amount of removed tritium in this tritium degassing operation. Temperature of the vacuum vessel: room temperature in the 1st, 2nd and 6th week, and 150 °C in the 3rd week, 250 °C in the 4th week and 300 °C in the 5th week.

Table 1. Amount of removed tritium in the 4th week (250 °C).

Day	Removed T	Cleaning discharge (duration time)	Removed T	Average degassing rate (Bq/s)
12-Nov-02	3.0 MBq	He gas flow (30min)	80 kBq	44.4
		He-GDC (1h57min)	1.2 MBq	170.9
		He-ECRDC (31min) (CW)	30 kBq	16.1
		He-TDC (10min)	57 kBq	95.0
		Baking (24h)	1.72 MBq	19.9
13-Nov-02	3.3 MBq	Ar gas flow (12min)	13 kBq	18.1
		Ar-GDC (1h49min)	1 MBq	152.9
		Ar-TDC (10min)	5 kBq	8.3
		H_2-TDC (50min)	1.4 MBq	466.7
		Baking (24h)	0.86 MBq	10.0
14-Nov-02	11.8 MBq	H_2 gas flow (33min)	48 kBq	24.2
		H_2-ECRDC (1h6min) (Pulsed injection)	0.42 MBq	106.1
		H_2-ECRDC (1h9min) (CW)	2.1 MBq	507.2
		H_2-GDC (5h4min)	8.7 MBq	477.0
		Baking (24h)	0.52 MBq	6.0
Total amount of the week	18.1 MBq			

10.6 Detritiation Characteristics by Glow Discharge Cleaning in JT-60U

H. Nakamura, S. Higashijima, K. Isobe, A. Kaminaga, T. Horikawa, S. Konishi, T. Tanabe

1. Introduction

In the fusion reactor such as ITER, the tritium inventory reduction in the vacuum vessel during the plasma operation is required for the reason of safety issues [1]. Although several tritium recovery methods have been proposed in ITER such as oxygen baking or laser ablation [2], those methods disturb the plasma operation due to water formation or requirement of venting the vacuum vessel. In JT-60U, the application of the wall conditioning discharge, which can be performed easily and frequently during plasma operation to the surface tritium inventory reduction has been investigated. Detritiation experiment using Glow Discharge Cleaning (GDC), Taylor Discharge Cleaning (TDC), and Electron Cyclotron Resonance Discharge Cleaning (ECRDC) was carried out. The system configuration of tritium measurement is shown in 11.16, and the detritiation experiment is outlined in 10.5. The GDC was most effective in detritiation from the first wall surface among the three discharge methods. In this report, detritiation performance of the GDC are shown in detail and the mechanism of detritiation is discussed.

2. Results and Discussions

2.1. Detritiation Characteristics of GDC

Figure 1 shows the time evolution of the tritium concentration in the JT-60U exhaust gas during H_2-GDC at various wall temperatures. As seen in Fig. 1, the tritium concentrations show sharp peaks just after start of GDC, and then it shows slow decay curves. The decay curves can not be expressed by a simple exponential function of time.

From bubbler measurement, it was found that the major part of tritium in the exhaust gas was hydrogen form and the rest was a little hydrocarbon (<10%) and little vapor (<1%).

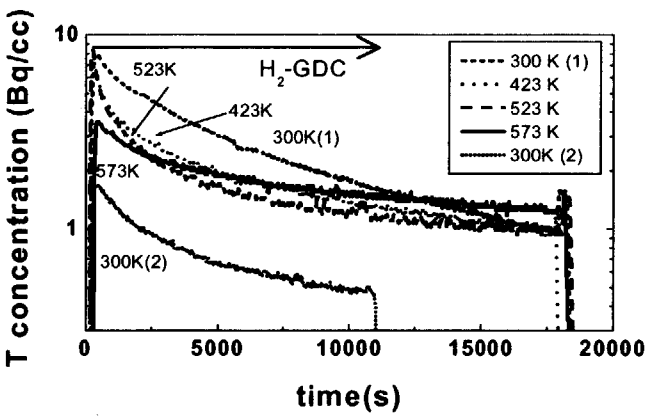

Fig. 1 Time evolution of tritium concentration in JT-60U exhaust gas during H_2-GDC at various wall temperatures at a H_2 pressure of 0.3 Pa, a total current of 3A, and a discharge voltage of 340-350 V. Here, detritiation experiment was carried out in order of 300K(1), 423K, 523 K, 573K and 300K (2).

2. 2. Mechanism of Detritiation of GDC

When it is assumed that the detritiation process is expressed by a first order reaction of the surface tritium concentration $C_T(t)$, time dependence of the tritium concentration in the exhaust gas $C(t)$ can be expressed by the following equation.

$$C(t) = -\frac{dC_T(t)}{dt}\frac{S}{F} = kC_T(t)\frac{S}{F} \quad , \tag{1}$$

Here, k, S and F are a rate constant of surface reaction, the surface area of detritiation area of the vacuum vessel and flow rate of exhaust gas, respectively. By solving Eq. (1), $C(t)$ can be derived as,

$$C(t) = \frac{A}{\tau}\exp\left(-\frac{t}{\tau}\right) \quad , \tag{2}$$

here, $A=C_{T0}S/F$, $\tau=1/k$ and C_{T0} is $C(0)$. From Eq. (2), $C(t)$ can be expressed with a simple exponential function of time. However, the observed decay curves shown in Fig.1 seem to contain multiple exponential functions and a time independent factor. Then, the decay curve of the tritium concentration is expressed by the following equation.

$$C(t) = C_0 + \sum_i^n \frac{A_i}{\tau_i}\exp\left(-\frac{t}{\tau_i}\right) \quad , \tag{3}$$

Here, C_0, A_i and τ_i mean a constant, pre-exponential factor and time constant for detritiation process i, respectively. A_i and τ_i also correspond to the maximum detritiation amount and the 1/rate of the process i. Figure 2 shows fitting result of the decay curve obtained in the case of the H_2 GDC at 300K using Eq. (3). By assuming two time dependent detritiation processes, i.e. the process 1 with a short time constant τ_1 and the process 2 with a long time constant τ_2, the experimental result can be reproduced as shown in Fig. 2. Since the tritium concentration attributed to the process 1 attenuates in short time, the tritium exhaust is mainly dominated by the process 2 and C_0.

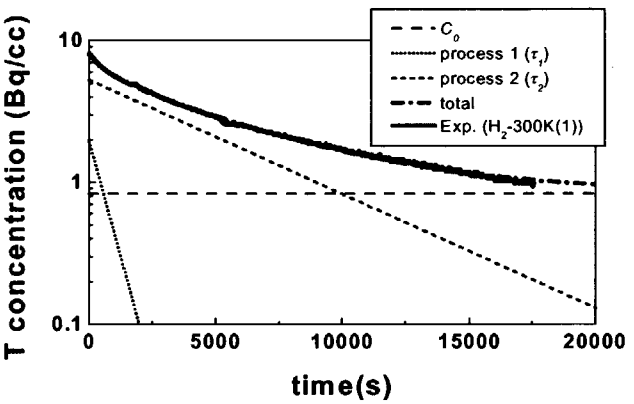

Fig. 2 An example of fitting result of the decay curve using Eq.(3). Here, the decay curve is the result of H_2 GDC at 300 K before the wall baking.

Figure 3 (a) ~ (e) show temperature dependence of C_0, time constants τ_1, τ_2 and pre-exponential factors A_1, A_2 for the H_2 and the He GDC. Here, τ_1 and τ_2 are shown in Arrenius relation in Fig. 3 (b) and (d), respectively.

The time independent factor C_0 for H_2 is about 3 times larger than that for He as shown in

Fig. 3 (a). It means that detritiation rate of the H_2 GDC is superior to the He GDC in case of long discharge duration.

The detritiation process 1 consists of τ_1 of 10^2~10^3 seconds and A_1 of 10^3~10^4 Bq/cc/s as seen in Fig. 3 (b) and (c), and the detritiation process 2 consists of τ_2 of 10^3~10^4 seconds and A_2 of ~10^3 Bq/cc/s for He and 8,000~30,000 Bq/cc/s for H_2 as seen in Fig. 3 (d) and (e). For the detritiation process 1, τ_1 for He and H_2 are shorter than τ_2 and near to the time constant of vacuum pump system (~120 s) at higher wall temperature. It means that the detritiation reaction ceases in a short time after start of the discharge. Additionally, the A_1 for He and H_2 are small and are not always to decrease with the experimental order as shown in Fig. 3 (c). Because derived results mean that the binding energy of tritium with the wall surface removed by the process 1 could be small and the removable tritium can vary in the experimental conditions, the detritiation mechanism of the process 1 could be attributed to the physical sputtering of molecules adsorbed on the surface by the glow discharge for both He and H_2.

On the other hand, the detritiation process 2 for He GDC is estimated to the physical sputtering of tritium inside of the first wall by the ion bombardment.

Longer τ_2, which mean higher binding energy of tritium with the material, also support the explanation.

The A_2 for the H_2 GDC is greater than

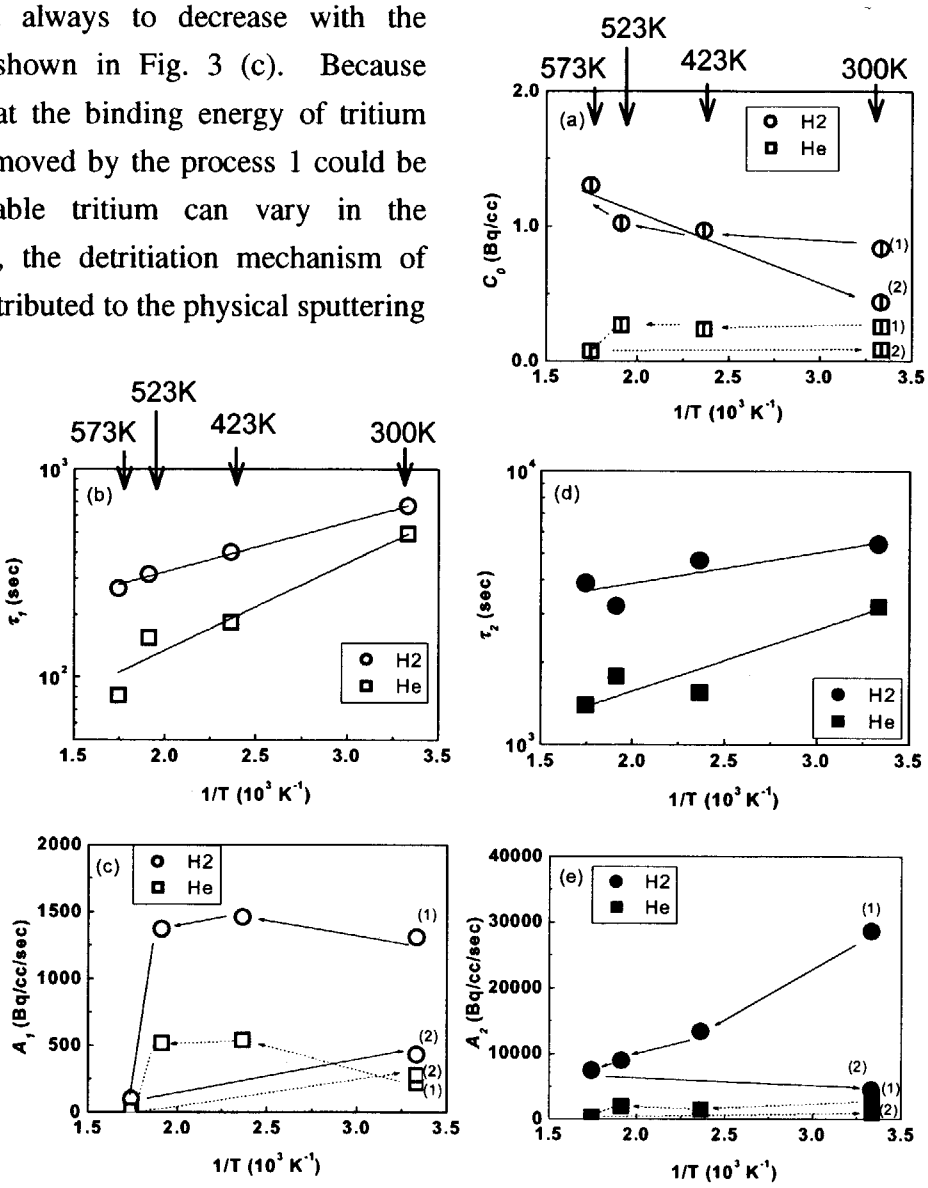

Fig. 3 Temperature dependence of C_0, time constants τ_1, τ_2 and pre-exponential factors A_1, A_2 derived from the decay curves shown in Fig. 1 using Eq. (3). Here, (1) and (2) mean before and after the wall baking. (a) C_0, (b) τ_1, (c) τ_2, (d) A_1 and (e) A_2

that for He by 5-10 times, and it decreases with experimental order as shown in Fig. 3 (e). Since such irreversible decrease of the A_2 means the decrease of the surface tritium concentration with the experimental order, it means that the process 2 of H_2 GDC can remove tritium on the first wall surface of JT-60U certainly. The experimental results that detritiation process 2 of the H_2 GDC has larger detritiation capacity (A_2) and tritium is removed as elemental form (HT) as mentioned in 2.1, suggests that the detritiation process 2 can be attributed to the chemical effects induced by the discharge such as isotope exchange or surface recombination.

The analysis suggests that detritiation mechanisms of the He and the H_2 GDC were the physical sputter and discharge induced chemical reactions at the surface. The C_0 process might be attributed to the implantation effect of hydrogen into the first wall and the diffusion process of tritium from deeper area of the first wall and of hydrogen in the implantation area of the first wall.

In the DT machine, tritium exists in the near-surface region of the first wall such as the re-deposited layer. Because the removal characteristics of near-surface hydrogen isotopes, i.e., deuterium in JT-60U, becomes quite important to simulate the detritiation behavior in the DT machine, the deuterium removal behavior during the discharge cleaning in JT-60U will be investigated in a future work.

3. Summary

By analyzing the detritiation behavior of the GDC with the first order surface reaction cleaning model, detritiation mechanism can be classified into three processes with the different time constants for the He and the H_2 GDC. It was suggested that detritiation processes in the He discharge could be attributed to the physical sputter of tritium adsorbed on the surface and tritium trapped inside the near-surface region. In the H_2 discharge, the process could be attributed to the physical sputter of tritium on the adsorbed on the surface tritium and discharge induced chemical reaction. Observed higher detritiation rate for the H_2 GDC could be explained by the discharge-induced chemical effect such as the isotope exchange reaction.

References

[1] Federicci G., et al., Fusion Eng. Des. **39-40** 445, (1998).

[2] Shu. W., et al., J. Plasma and Fusion Research **76** 1021, (2000).

10.7 Exhaust Gas Composition in Discharge Cleaning of JT-60U

T. Horikawa, A. Kaminaga, H. Nakamura, S. Higashijima, S. Konishi

1. Introduction

Exhaust gas composition in discharge cleaning is an important information for the study of tritium removal process and the design of a tritium processing plant for the fusion reactor such as ITER. In this report, the result of the measurement of exhaust gas composition during the discharge cleaning experiment of JT-60U is shown and the observed gas species and their time-dependent release behavior are discussed.

2. Observed Gas Species

Exhaust gas composition in discharge cleaning (Electron Cyclotron Resonance Discharge Cleaning : ECRDC, Taylor Discharge Cleaning : TDC, Glow Discharge Cleaning : GDC) of JT-60U was analyzed by micro gas chromatograph. Gas species observed in the exhaust gas are listed in Table 1.

Table 1. Gas species observed in exhaust gas during cleaning. (a) at room temperature, (b) at 150 ℃, (c) at 250 ℃ and (d) at 300 ℃. BG level is the meaning of background level.

(a) room temperature

working gas	He	Ar	H_2	remarks
gas flow	–	–		
ECRDC	–	–		
TDC	–	hydrogen		
GDC	hydrogen	hydrogen methane acetylene and/or ethylene helium	methane	

(b) 150 ℃

working gas	He	Ar	H_2	remarks
gas flow	–	–		
ECRDC	–		methane acetylene and/or ethylene CO2*	*after discharge finished.
TDC	hydrogen	hydrogen	methane acetylene and/or ethylene	
GDC	hydrogen methane acetylene and/or ethylene	hydrogen methane acetylene and/or ethylene helium	methane acetylene and/or ethylene	

(c) 250 ℃

working gas	He	Ar	H_2	remarks
gas flow	hydrogen (BG level)	hydrogen (BG level)		
ECRDC	hydrogen		methane acetylene and/or ethylene ethane*	*rare case
TDC		hydrogen	methane acetylene and/or ethylene	
GDC	hydrogen methane acetylene and/or ethylene ethane	hydrogen methane acetylene and/or ethylene helium	methane acetylene and/or ethylene ethane	

(d) 300 ℃

working gas	He	Ar	H_2	remarks
gas flow	hydrogen (BG level)	hydrogen (BG level)		
ECRDC	hydrogen	hydrogen methane* acetylene and/or ethylene*	methane acetylene and/or ethylene ethane**	*next of H_2-ECRDC **rare case
TDC	hydrogen	hydrogen	methane acetylene and/or ethylene	
GDC	hydrogen methane acetylene and/or ethylene	hydrogen methane acetylene and/or ethylene helium	methane acetylene and/or ethylene ethane	

Hydrogen, hydrocarbons and so on other than the working gas injected for discharge were observed. When the working gas is hydrogen, hydrogen gas released from the first wall can not be separated from the working gas. Therefore, it is not written in Table 1. Since the peaks of acetylene and ethylene could not clearly be separated on the chromatogram, the observed peak might be acetylene's, ethylene's, or the both.

Many species were observed at the high temperature. More gas species were observed in GDC than in other discharge cleaning. The hydrogen release rate of GDC was larger than those of ECRDC and TDC. When the working gas is hydrogen, hydrocarbons can be produced by reaction of hydrogen with carbon such as the graphite tiles of the first wall or carbon particles deposited to the wall surface.

3. Time-Dependent Release Behavior of Gas Species

Time-dependent release behavior of hydrogen during He-GDC and Ar-GDC are shown in Fig. 1. In the He-GDC and Ar-GDC, the hydrogen concentration in the exhaust gas decreased exponentially as shown in Fig. 1 (a) and (b). The concentration dropped quickly first and then decreased slowly. For example, in the He-GDC at 150-300 ℃, the time constant is 300−1000 s in the early phase, and is 5000−6000 s about sixty minutes after the start of the discharge. The hydrogen release rate may be able to be expressed by combination of two exponential functions as the tritium release rate [1]. Release behavior of hydrogen from the first wall has some relation with that of tritium. However for further discussion, it is needed to clarify the initial distributions of hydrogen and tritium near the surface of the first wall, since the distributions effect the release behavior. Experiment history influences release behavior. After a discharge with hydrogen the hydrogen absorbed can also influence the behavior during the next discharge cleaning, as mentioned later.

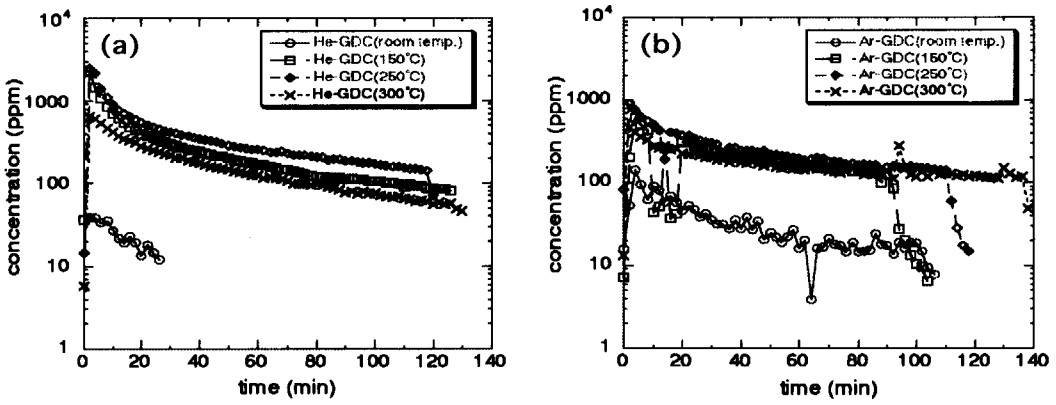

Fig. 1. Time evolution of the hydrogen concentration in the exhaust gas during (a) He-GDC and (b) Ar-GDC.

Time-dependent release behaviors of other gas species during He-GDC, Ar-GDC and H_2-GDC at 250 ℃ are shown in Fig. 2. In the He-GDC and Ar-GDC, as shown in Fig. 2 (a) and (b) the concentrations of hydrocarbons decreased quickly. In the Ar-GDC, helium concentration also dropped fast as shown in Fig. 2 (b). These gas species are considered to be produced and adsorbed to the wall surface in the preceding discharges. On the other hand, in the H_2-GDC, as shown in Fig. 2 (c), the concentrations of hydrocarbons became constant It seems that the production and the release of hydrocarbons balances after several hours from the start of discharge.

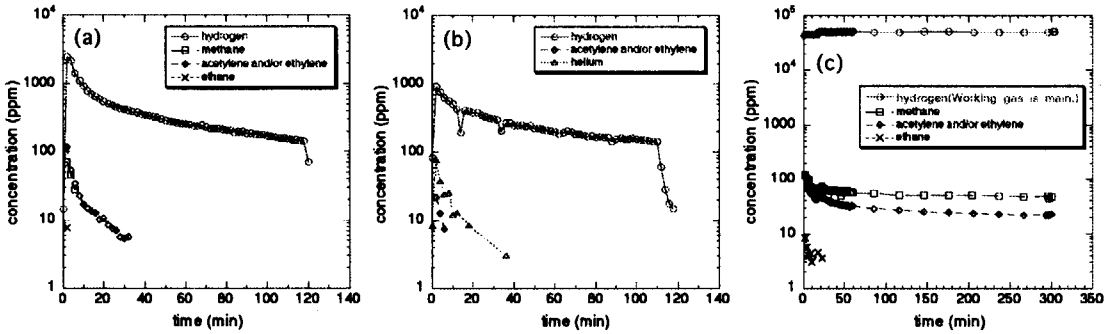

Fig. 2. Time evolution of the concentration of hydrocarbons and other gas species in the exhaust gas during (a) He-GDC, (b) Ar-GDC and H_2-GDC.

Time-dependent release behaviors of hydrocarbons (methane and acetylene and/or ethylene) during the H_2-GDC at baking temperatures of 150, 250 and 300 ℃ are shown in Fig. 3. When the baking temperature is 150 ℃ and 250 ℃, the concentrations of hydrocarbons decreased first and became constant. On the other hand at 300 ℃, it increased slowly. This difference of behaviors is considered to be caused by the difference of initial amounts of hydrocarbons adsorbed to the wall surface. Release rates of hydrocarbons after

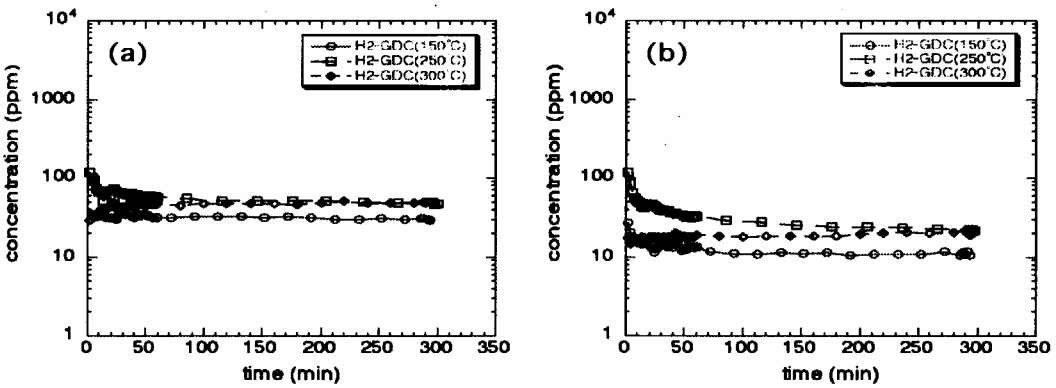

Fig. 3. Time evolution of the concentrations of hydrocarbons in exhaust gas during H_2-GDC. (a) methane and (b) acetylene and/or ethylene.

long-run discharge increase with the baking temperature, and then saturate at ～250 ℃.The saturated concentrations of hydrocarbons are about 50 ppm for methane, 20 ppm for acetylene and/or ethylene and a few ppm for ethane.

Time-dependent release behaviors of gas species during H_2-ECRDC and Ar-ECRDC are shown in Fig. 4. In the ECRDC, interesting behavior was observed during the discharge. As shown in Fig. 4 (a), the concentration of hydrogen injected as the working gas dropped sharply at the beginning of the discharge, and then it rose but did not recover the first concentration. When the discharge finished, the hydrogen concentration quickly recovered to the first level having a small rebound. As the working gas was continuously supplied into the vacuum vessel during the discharge, a portion of the deducted concentration of hydrogen is thought to adsorb to the first wall. Similar behavior of hydrogen gas was also observed in the Ar-ECRDC as shown in Fig. 4 (b). The concentration of hydrogen rose slightly when the discharge started, but it decreased during the discharge. When the discharge finished, it rebounded. The hydrogen gas desorbed by the discharge is seemed to be taken back to the wall. This behavior was not observed during GDC and TDC.

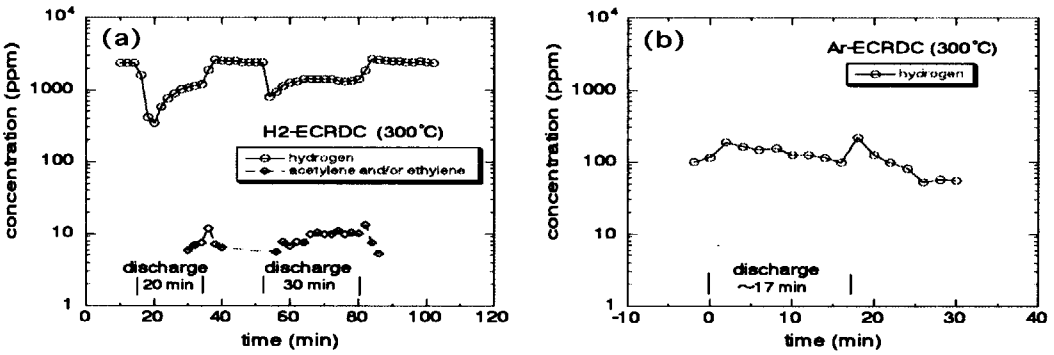

Fig. 4. Time evolution of the concentrations of hydrogen and acetylene and/or ethylene in the exhaust gas during (a) H_2-ECRDC and (b) Ar-ECRDC.

4. Summary

The number of gas species and their concentration in exhaust gas tended to increase as the baking temperature was up. The concentration of hydrogen during GDC was larger than those during ECRDC and TDC. When the working gas is hydrogen, it is thought that hydrocarbons were produced by the reaction of hydrogen with carbon such as the graphite tiles of the first wall or carbon particles deposited to the wall surface.

Reference

[1] Nakamura, H., et al., 10.6 in this volume.

11. Diagnostics

11.1 Application of Nonlinear Optics for Drastic Improvement of YAG Laser Performance on JT-60U Thomson Scattering System

M. Nakatsuka[1)], Hidetsugu Yoshida[1)], H. Fujita[1)], T. Hatae, S. Kitamura,
T. Sakuma, T. Hamano
1) Institute of Laser Engineering, Osaka University

1. Introduction

The specification of the laser, such as Nd^{3+}:YAG solid-state laser (YAG laser), shows a high peak power, high repetition rate and good beam quality for tight focus in the stable operation. At JT-60U, JAERI, the YAG laser system for Thomson scattering diagnostics delivered routinely 1.0-1.5 J of 30 ns pulse width in 30 Hz repetition to average power of 30-40 W [1]. The beam pattern was affected seriously in its near field by the thermally induced effects in YAG laser rods in a serial arrangement due to strong pumping to achieve its maximum gain. The thermal effects, such as thermal lens and depolarization, suppressed the average power level because of the off-axis ray trajectory with aberration and resulting polarizing losses in the laser rods.

The stimulated-Brillouin-scattering phase conjugation mirror (SBS-PCM)[2-5] which is one of nonlinear optics is well known to compensate the phase front aberration induced in dielectric optical components. Recently, it was first demonstrated that a single cell SBS-PCM of the closed type enabled the incident power to reach a 100 W level because of the use of materials with small absorption coefficients such as heavy fluorocarbons [6]. Also, a single-line YAG laser system using this SBS-PCM have achieved a 2.6-J output energy at 50 Hz drive [7].

In this paper, a drastic improvement of the laser performance by using SBS-PCM is described. An average output power of 205 W at 50 Hz was achieved with a total energy of more than 4.1 J by a new layout that consisted of two-line YAG amplifier system.

2. Experimental Results

Figure 1 shows the 2-line YAG laser/amplifier system with SBS-PCMs at 50 Hz repetition rate used as the Thomson scattering light source at JT-60U. The laser oscillator was a linearly polarized, single-frequency, TEM_{00} Nd^{3+}:YAG Q-switched laser. The output pulse was 30-mJ in energy of quasi-Gaussian pulse shape, and had about 30-ns FWHM pulse width at a 50 Hz repetition rate. The oscillator beam was amplified up to 100-mJ energy by a double-pass pre-amplifier arrangement with the combination of a Faraday rotator (FR) and a high reflectance mirror. The output from pre-amplifier was divided at the

thin film polarizer (POL) into perpendicularly polarized parts onto two chains. One beam of s-polarization fraction reflected by the POL-3 was rotated to p-polarization component by a half-wave plate (HWP) and was then amplified by serial amplifier arrangement. Another p-polarization beam was image-relayed to amplifiers head at a distance of 4.5 m. Each chain consists of a MOPA (Master Oscillator Power Amplifier) scheme with a 14 mm^{ϕ} × 65 mm^{l} Nd^{3+}:YAG amplifiers and a 12 mm^{ϕ} × 65 mm^{l} amplifiers. The one-pass amplified output beam was focused onto a point of 200 mm inside a 300-mm-long SBS-PCM by a lens of 200 mm focal length. Each PCM had used different material as an SBS liquid medium, Fluorinert FC-72 and -75, manufactured by 3M Company. After passing amplifiers again, the initial beam quality was almost compensated by SBS-PCM. The amplified pulse was rotated again by an angle of 45 degree after passing the Faraday rotator a second time. A thin-film polarizer realized output coupling by a 90-degree rotation carried out by a Faraday rotator. The interference between two beams was prevented by using different SBS substances of different Brillouin frequency. The Brillouin frequency shift of FC-72 and -75 are 1.15±0.05 and 1.35±0.05 GHz at a 1064-nm wavelength, respectively.

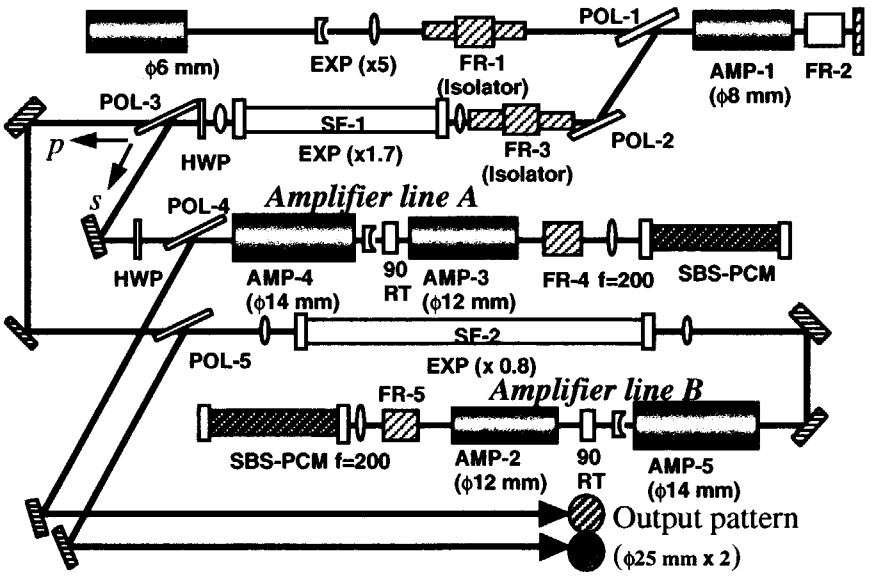

Fig.1 Optical layouts of YAG laser system.

The measured SBS reflectivity of each line is shown in Fig. 2 that was defined as the ratio of the reflected energy from SBS mirror to the energy incident to the PCM cell. A maximum intrinsic SBS reflectivity of approximately 95% was obtained at a 1.5-J incident energy. The transmitted power was only 3.75 W at a 75 W input power. The SBS reflectivity in a repetitive rate operation was almost similar to that in the single-shot operation. No optical damage was observed in all optic components during the experiment.

We have measured the pulse shape of combined beam to prevent the beat wave generation. Using an intracavity etalon in the oscillator, the laser line width was reduced to

less 200 MHz (FWHM) to achieve a coherence length of about 1.5 m. The separation between two beams must need over 3 m corresponding to 2 ns to avoid two-beam interference. Figure 3 shows the output pulse shape at the optical path difference in two beams of 13 ns. It was shown that the two-SBS-PCM system using different SBS materials did not generate the beat structure in a combined pulse because two beams were left each other 4.25-m intervals longer than the coherent length.

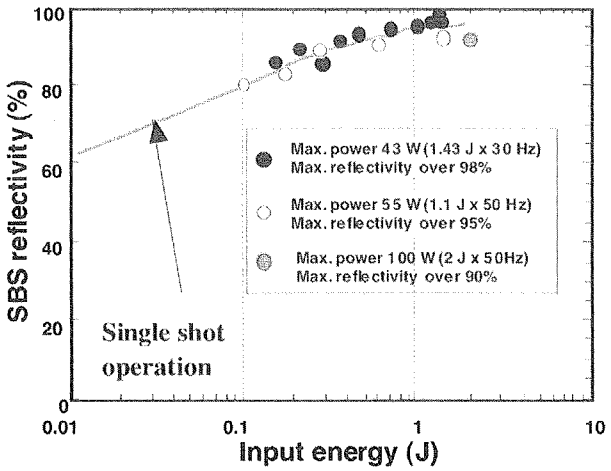

Fig.2 SBS reflectivity as a function of input energy.

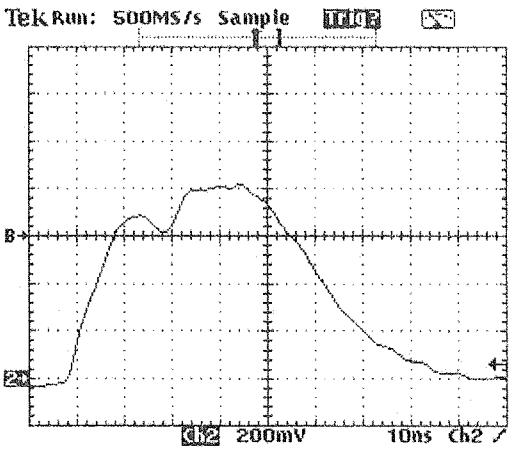

Fig.3 Typical pulse shape of combined pulse.

The most interesting parameter of the SBS-PCM is the fidelity of the reflected and amplified beam. The near field (NFP) and far field (FFP) patterns of the single-pass and double-pass amplified pulse with SBS-PCM are shown in Fig. 4. At the single-pass operation, the depolarization of NFP occurs orientation of the indicatrix of a thermally stressed rod. The spot size of single-pass amplified beam was reduced to a full angle divergence of 5 times the diffraction-limited value. On the other hand, the NFP of double-pass amplified pulse using an SBS-PCM shows a good flattop pattern as a result of the spatial filtering effect of SBS process. Birefringence effect appeared at single-pass amplification was seen clearly because the laser beam passed through the 45 degree Faraday rotator. The reflection from the SBS-PCM was initiated at the beam waist in a SBS cell so that the diffracted fraction of high spatial frequency of the incident beam felt a weak reflectance, resulting in the spatial filtering of the beam. The focal spot size of only 1.5

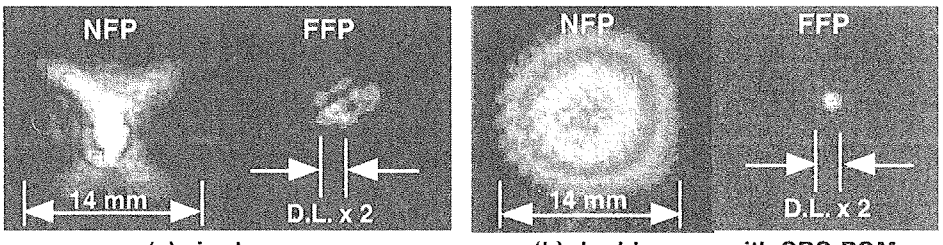

Fig.4 Typical NFP and FFP of (a) single-pass and (b) double-pass amplification.

times the diffraction-limited value shown in the figure was similar to the incident beam characteristics.

The maximum two-pulse energies reached 4.1 J in a 30-ns pulse width at a repetition rate of 50 Hz. The system developed here demonstrated successfully a maximum output power of 205 W at two average operation amplifiers that was 7 times larger than the original system.

3. Conclusion

An improvement was achieved in the output beam power/quality of two-stage YAG laser system by using the SBS-PCM. An average output power of 205 W was achieved at 50 Hz with total pulse energy of 4.1 J by 2-line YAG amplifier system.

In the meantime, Nonlinear optics is one of the fields to apply the power photonics using a high peak power laser. Its principle was invented far from now, but there have not been many examples in the industrial application as shown here. The pulse compression by nonlinear optics [8] is also interested at the high peak power laser application for diagnostics. The stimulated Brillouin scattering and Raman scattering are applicable for such process. The pulse compression is achievable from several tens nanosecond pulse to sub nanosecond pulse with an efficiency over 80%. The investigation is needed on the material search and efficiency recovering for more shorter pulse compression.

In conclusion, the nonlinear optics and power photonics are very useful to apply the energetic pulse generation and compression into the plasma diagnostics tool for magnetic confinement fusion research.

References

[1] Hatae T., Nagashima A., et al., Rev. Sci. Instru. **70**, 772 (1999).

[2] Yoshida H., Fujita H., Nakatsuka M., and Yoshida K., Optical Eng. **36**, 2557 (1997).

[3] Yoshida H., Fujita H., Nakatsuka M., and Yoshida K., Jpn. J. Appl. Phys. **38**, L521 (1999).

[4] Yoshida H., Fujita H., Yoshida K., and Yamanaka T., Jpn. J. Optics **26**, 31 (1997) (In Japanese).

[5] Yoshida H., Ohkubo A., Fujita H., and Nakatsuka M., Jpn. Rev. Laser Eng. **29**, 109 (2001) (In Japanese).

[6] Yoshida H., Kmetik V., Fujita H., Nakatsuka M., Yamanaka T., and Yoshida K., Appl. Opt. **36**, 3739 (1997).

[7] Yoshida H., Nakatsuka M., Hatae T., Kitamura S., and Kashiwabara T., Jpn. J. Appl. Phys. **42** (2003)(in press).

[8] KmetikV., Fiedorowicz H., Andeev A. A., Witte K. J., Daido H., Fujita H., Nakatsuka M., and Yamanaka T., Appl. Opt. **37**, 7085 (1998).

11.2 Double pass Thomson Scattering Diagnostics using SBS Phase Conjugation Mirror in JT-60U

T. Hatae, M. Nakatsuka[1)], Hidetsugu Yoshida[1)], O. Naito, S. Kitamura,
T. Sakuma, T. Hamano, and Y. Tsukahara
1) Institute of Laser Engineering, Osaka university

1. Introduction

Thomson scattering diagnostics is one of the standard diagnostics for electron temperature and density measurement in magnetic fusion devices. Since the Thomson scattering light is very weak, increasing in scattered light improves the measurement accuracy. Increasing the incident laser energy is the most effective way in order to increase the scattered light without degrading the measurement accuracy. Possible methods to increase the laser energy and scattered light are as follows: (1) bundle the beams from more than one laser device into a single path[1]. (2) improve the existing laser to get higher energy output[2]. (3) make an incident laser beam go back and forth in the plasma to double a scattered energy.

This paper focuses on items (3). A high performance phase conjugation mirror by stimulated Brillouin scattering (SBS-PCM) using a liquid fluorocarbon was introduced into the existing YAG laser Thomson scattering system at JT-60U[3]. A double pass Thomson scattering method with SBS-PCM was first demonstrated[4].

2. High performance phase conjugation mirror

A phase conjugation mirror by stimulated Brillouin scattering (SBS-PCM) [5] generates a reflecting wave whose shape of spatial wave front is the same as that of incident wave front and its direction of propagation is perfectly reverse. The SBS-PCM compensates a wave front distortion that occurs when a laser beam propagates through optically non-uniform medium due to thermally induced aberration in high power amplifying rods of solid-state lasers. An SBS cell for SBS-PCM including a liquid SBS medium is a stainless steel pipe (length=300mm, bore=30mm) with AR-coated windows at both ends. A liquid fluorocarbon (the trade name is 3M Fluorinert, FC-75) filtered by a membrane filter (0.025 μm) is used as an SBS medium [6]. To operate the SBS cell as a reflective SBS-PCM, the incident laser beam was focused with a plano-convex lens (f=150mm or 200mm). Figure 1 shows the reflectivity of SBS-PCM compared with other results. It found that our SBS-PCM performed a high reflectivity of more than 90% at high laser energy input of 2-J with a repetition rate of 50Hz (average power is 100W).

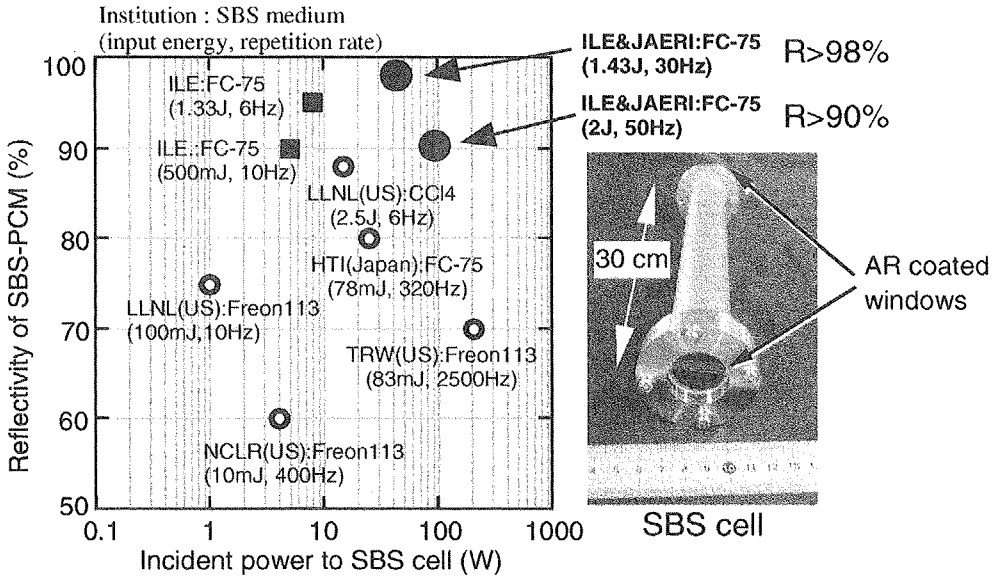

Fig.1. Reflectivity of SBS-PCM compared with conventional results and the picture of SBS cell

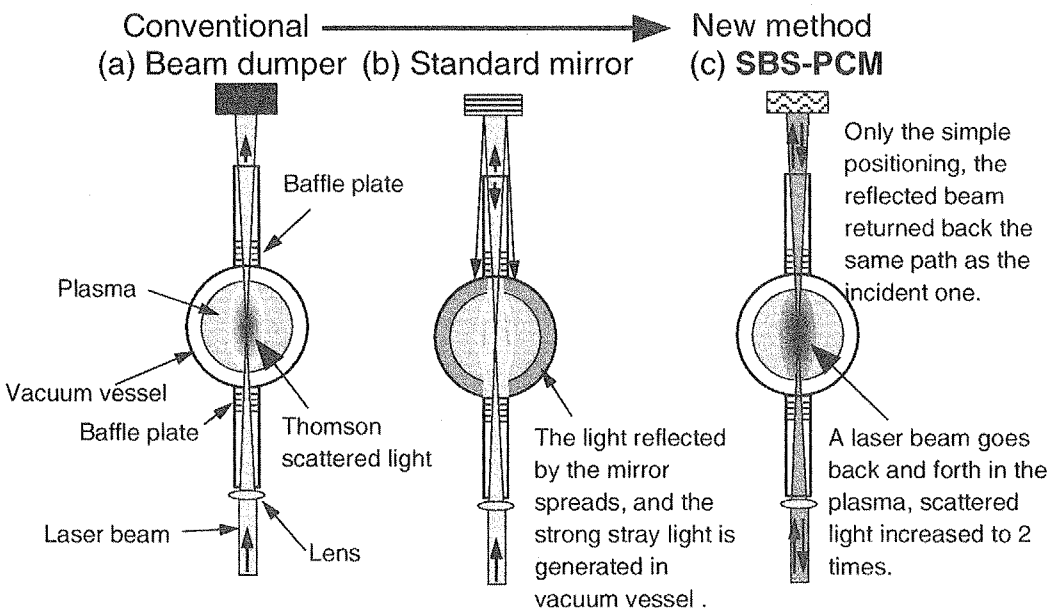

Fig.2 Conventional method and newly proposed double path Thomson scattering with SBS-PCM

3. Double pass Thomson scattering method using SBS-PCM

In the conventional Thomson scattering system, the laser beam which pass through a plasma is very small energy loss, and most part of the strong energy is still remain in the passed beam. Since the laser beam should be terminated safely, the beam is absorbed by beam damper. Accordingly, the most part of laser energy is abandoned in the conventional system (Fig.2(a)). On the other hand, if a flat mirror which is replaced with beam dumper is used to reuse the passed beam, the reflected light spreads, and the spread light hit the vacuum vessel and produce strong stray light. In this case, it is difficult to measure the Thomson scattered light due to the existence of the strong stray light (Fig.2(b)). Furthermore, if a concave mirror

in place of the flat mirror, very severe beam alignment is frequently required to reduce a stray light.

For the application of SBS-PCM, we have newly proposed a double pass Thomson scattering method with SBS-PCM as shown in Fig.2(c)[4]. In this new optical design, a laser beam passing through the plasma is reflected by the SBS-PCM in place of a beam dumper, and a reflected beam returned back through exactly the same path as the incident one by the phase conjugation effect, and passed through the plasma again. As we mentioned before, if a conventional mirror is used for this purpose, very severe beam alignment is frequently required to reduce a stray light. However, it is completely unnecessary for such alignment in the case of SBS-PCM. After an initial simple positioning, the SBS-PCM is alignment-free. By this new method, we obtain two times larger scattered light intensity with an alignment-free operation in contrast with a conventional single path design.

Schematic of the double pass Thomson scattering with SBS-PCM in JT-60U is shown in Fig.3. The beam propagates the distance of 153 m (both way). A Faraday isolator easily removed the laser beam returning back to the laser system. The input power to SBS cell was about 100W (2J, 50Hz). Note that double pass amplifiers with SBS-PCM [2] is not installed in the laser system to get high reflectivity of SBS-PCM. From the first measurement using the double pass scattering, the scattered light intensity became 1.6 times larger and relative error reduced to 2/3 of that for single path scattering as shown in Fig.4[4]. Almost the same ohmic plasmas were produced to compare the double pass Thomson scattering with that of single pass in the first measurement. To simplify the evaluation of T_e and n_e, only ~90° scattering data were used, because spectra of both forward and back scattering are the same shape. For the evaluation for non-90° scattering, it needs further consideration.

The amount of scattered light by a returned laser beam is affected by followings: a laser quality (quality of single longitudinal mode structure), small depolarization due to propagation with standard mirrors and transmission loss. If the laser quality and depolarization could be improved, the amount of double pass scattered light would be increased to about 2 times. On the other hand, the double path scattering also increased the amount of stray light to 1.6 times of that for single path. Since the stray light in JT-60U has been always kept at a low level compared with scattered light, and blocking ratio of interference filters for stray light is high (10^{-5}-10^{-4}), the increased stray light has not influenced the measurement of scattered spectra.

4. Conclusion

A double pass Thomson scattering method with SBS-PCM demonstrated for the first time and the scattered light increased 1.6 times larger than the conventional measurement. It is possible to extend this idea to a multi-path scattering scheme in which laser beam goes back and forth in the plasma many times. This approaches promise us precision Thomson scattering

diagnostics with higher accuracy in JT-60U.

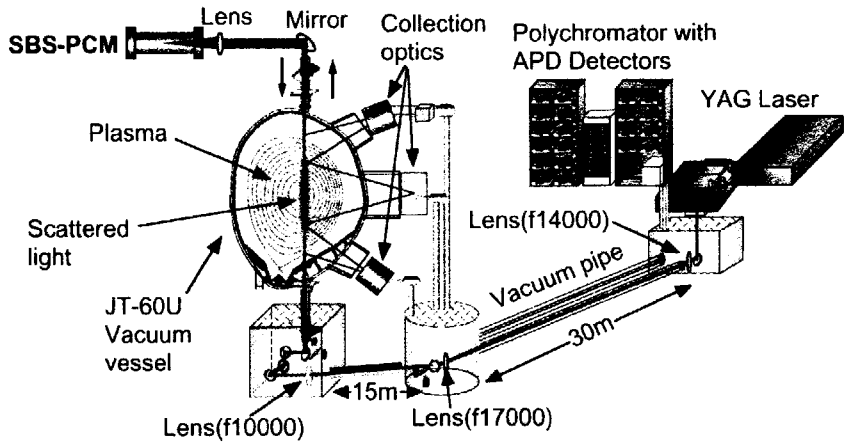

Fig.3 Schematic of the double pass Thomson scattering with SBS-PCM in JT-60U

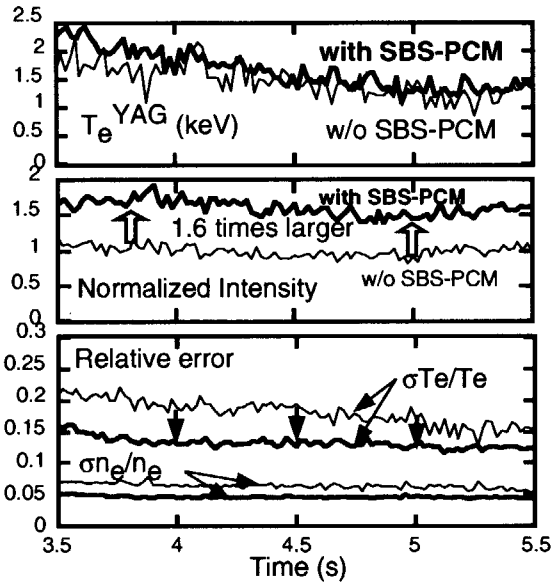

Fig.4
Preliminary results from the double pass Thomson scattering with SBS-PCM.
Upper: Time evolutions of electron temperature with/without SBS-PCM.
Middle: Time evolutions of Normalized intensity. The intensity corresponds to amount of Thomson scattered light.
Lower: Time evolutions of relative error for T_e and n_e.
Thick trace shows in case with SBS-PCM. Thin trace shows in case without SBS-PCM.

References

[1] Stockdale R.E., Carlstrom T.N., Hsieh C.L., et al., Rev. Sci. Instrum. **66**, 490 (1995).

[2] Nakatsuka M., Yoshida Hidetsugu, Fujita H., Hatae T., et al, "Application of Nonlinear Optics for Drastic Improvement of YAG Laser Performance on JT-60U Thomson scattering system", ibid.

[3] Hatae T., Nagashima A., et al., Rev. Sci. Instru. **70**, 772 (1999).

[4] Hatae T., Nakatsuka M., Yoshida Hidetsugu, et al., 29th EPS Conference on Plasma Phys. and Contr. Fusion Montreux, 17-21 June 2002 ECA Vol. **26B**, P-2.125 (2002).

[5] Zel'dovich B.Ya., Pilipetsky N.F., Shkunov V.V., "Principles of Phase Conjugation", Springer Series in Optical Sciences 42, Springer-Verlag, (1985)

[6] Yoshida Hidetsugu, Kmetic V., Fujita H., Nakatsuka M., Yamanaka T., and Yoshida K., Appl. Opt. **36**, 3739 (1997).

11.3 Very High Electron Temperature Diagnostics using Combined Ruby and YAG Laser Thomson Scattering System in JT-60U

T. Hatae, O. Naito, T. Sakuma, S. Kitamura, and T. Hamano

1. Introduction

The JT-60U Thomson scattering system consists of the Ruby laser system [1-6] and the YAG laser system [7]. Each system has been operated independently for multi-pulse and multi-point measurement of plasma from lower T_e edge region to higher T_e core region. Both systems of Ruby and YAG were designed and optimized for electron temperature region less than 20keV.

In recent intense electron heating experiments using electron cyclotron heating (ECH) with gyrotron[8], it seems that central T_e rises above ~15 keV. However, error bars are relatively large (~100% of T_e), it is difficult to measure the very high T_e beyond ~15 keV with high accuracy because the electron temperature region exceeds that of the original design. Since JT-60U is equipped with another electron heating tool, i.e. negative ion based neutral beam injector (N-NBI), it is expected that the central T_e is increased higher than ~20 keV by ECH and N-NBI. Accordingly, very high T_e measurement system with high accuracy is needed.

In the case of very high T_e measurement, since Thomson scattered spectrum is relatively broadened and the peak of the spectrum is shifted to shorter wavelength due to the relativistic effect, consideration of the wavelength of the laser as probe beam and kind of detector is also important. Fortunately, JT-60U has two kind of Thomson scattering system, i.e. Ruby laser system and YAG laser system. To examine the combined performance of the Ruby laser and YAG laser systems for getting higher accuracy at very high T_e provides a starting point for very high T_e measurement. This paper describes the performance of the measurement for very high T_e using combined Ruby laser system and YAG laser system.

2. Individual property of Ruby laser system and YAG laser system

In the Ruby laser system, a Littrow type spectrometer is used, where the number of wavelength channels is six. Slit functions of the spectrometer is shown in Fig.1(a). Central wavelength of each channel are 678, 670, 632, 592, 533 and 447 nm. Scattered light at each wavelength channel is detected by Photomultiplier tubes. We use the term "PMT" to refer to the detection system for the Ruby laser system. On the other hand, an interference type polychromator which has 6 wavelength channels is used in the YAG laser system. Filter functions of the polychromator is also shown in Fig.1(a). Central values of each wavelength channel are 1064 nm (band width of interference filter $\Delta\lambda$=3nm), 1058 nm ($\Delta\lambda$=6nm), 1048

nm ($\Delta\lambda$=15nm), 1023 nm ($\Delta\lambda$=35nm), 958 nm ($\Delta\lambda$=94nm) and 791nm ($\Delta\lambda$=240nm). Scattered light is detected by silicon avalanche photodiode. We use the term "APD" to refer to the detection system for the YAG laser system. Thomson scattering spectra (T_e =1, 10, 30, 50 keV) for Ruby laser (λ=694.3nm) and YAG laser (λ=1064nm) are shown in Fig.1(b) and (c), respectively.

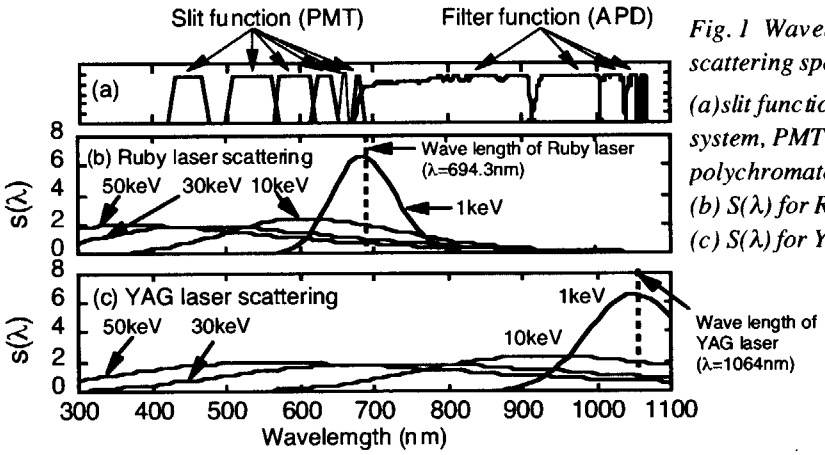

Fig. 1 Wavelength channels with Thomson scattering spectrum S(λ) at T_e =1,10,30,50keV. (a)slit function of spectrometer (Ruby laser system, PMT) and filter function of polychromator (YAG laser system, APD). (b) S(λ) for Ruby laser (λ=694.3nm). (c) S(λ) for YAG laser (λ=1064nm).

Generally the electron temperature is evaluated using short wavelength side of the scattered spectrum (blue side) in existing systems. However, T_e is evaluated using long wavelength side (red side) in the case of very high T_e measurement. Simulated performance of the measurement with PMT for Ruby laser system and APD for YAG laser system are shown in Fig.2(a) and (b), respectively. Since the intense electron heating experiments are done in low n_e target plasma, value of n_e is fixed to 5×10^{18}m^{-3} in the simulation. For other input parameter for the simulation, Ruby laser energy of 10 J, YAG laser energy of 2 J were used. Relative error in both PMT and APD increases when T_e is beyond 10 keV. Relative error in APD is larger than that in PMT. This is caused by the difference of effective sensitivity and photon noise characteristics.

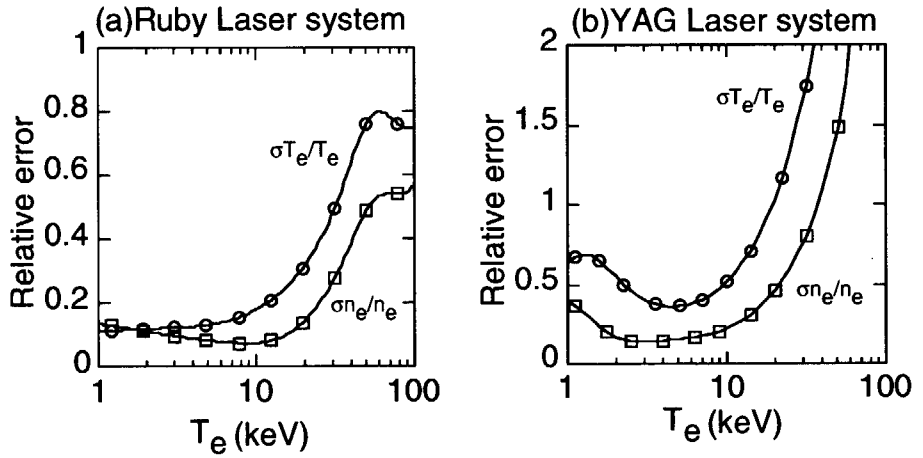

Fig. 2 Performance of the measurement with original systems. (a) Ruby laser system with PMT, (b) YAG laser system with APD. Open circle and square symbols indicate relative error for T_e and n_e, respectively.

3. Combined performance of Ruby laser and YAG laser system

To examine the measurement performance in the very high T_e region, the simulation is focused on different laser wavelength and a combination of detection systems (PMT+APD). Using both PMT and APD simultaneously, it is possible that 11 wavelength channels cover the wide range (~700 nm) from the visible to near infrared. Combined performance of PMT and APD were examined in each case of Ruby laser (Fig.3(a)) and YAG laser scattering (Fig.3(b)). In the case of Ruby laser scattering, the error is not improved well in the very high T_e region. The cause is that APD does not work effectively because the peak wavelength of scattered spectrum is in less than 500nm and the spectral intensity of near infrared region is weak. However, it is found that the combined system in the YAG laser scattering is well optimized at T_e ~ 20keV and relative error is reduced significantly compared with the original system. In the YAG laser scattering at T_e ~ 20keV, since the peak wavelength of scattered spectrum is shifted to 820nm, PMT measures the scattered spectrum of the shorter wavelength side (visible region) and APD measures the that of longer wavelength side (near infrared region). It seems that measurement of both side of shorter and longer wavelength side on the wide scatted spectrum leads the improvement of accuracy in very high T_e region.

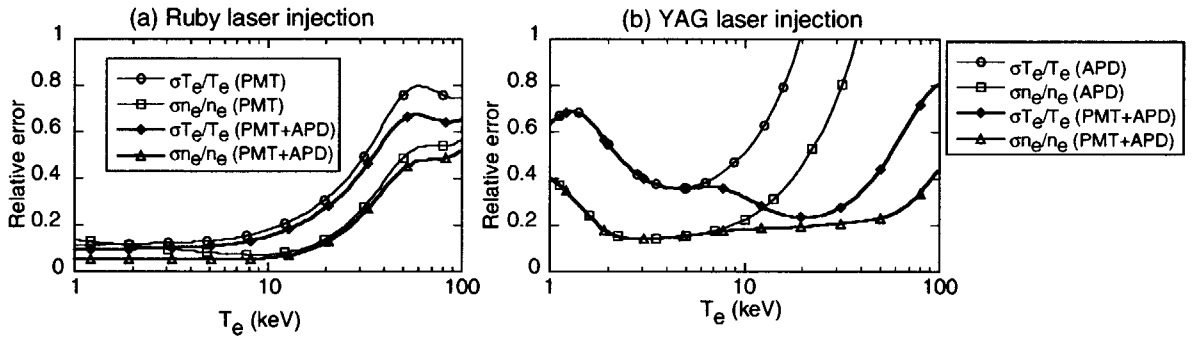

Fig. 3 Difference of relative error in each case of "PMT or APD only" and "combined PMT and APD". (a) Ruby laser injection. (b) YAG laser injection.

4. Preliminary measurement with combined PMT and APD detection system

We have attempted to measure very high T_e plasma using combined PMT and APD system with YAG laser (λ=1064nm) in an intense electron heating experiment (E040689, I_p=1.2MA, B_t=3.8T). Since PMT and APD observed independent spatial position, spatially adjacent points or points mapped on the same magnetic surface was chosen and combined. As a preliminary observation, Fig.4 shows scattered signals from 12 wavelength channels with PMT and APD detection system. The spatial position corresponds to ρ~0.2. After EC wave injection (t=5.8 s), an ITB was established and center T_e rapidly increased in the discharge, and center T_e reached up to 25 keV (measured by ECE diagnostics). *S/N* ratio of PMT detection system is poorer than that of APD at this point in time, and an improvement of *S/N* ratio is needed. However, it is recognized PMT scattered signals in visible light region (λ=632nm, 592nm) increase after EC wave injection. By using combined detection system, we verified that the scattered spectrum observed very high temperature plasma extended to the visible region. The future

direction of this study will be improvement of S/N ratio in visible channel and evaluation of electron temperature with combined detection system.

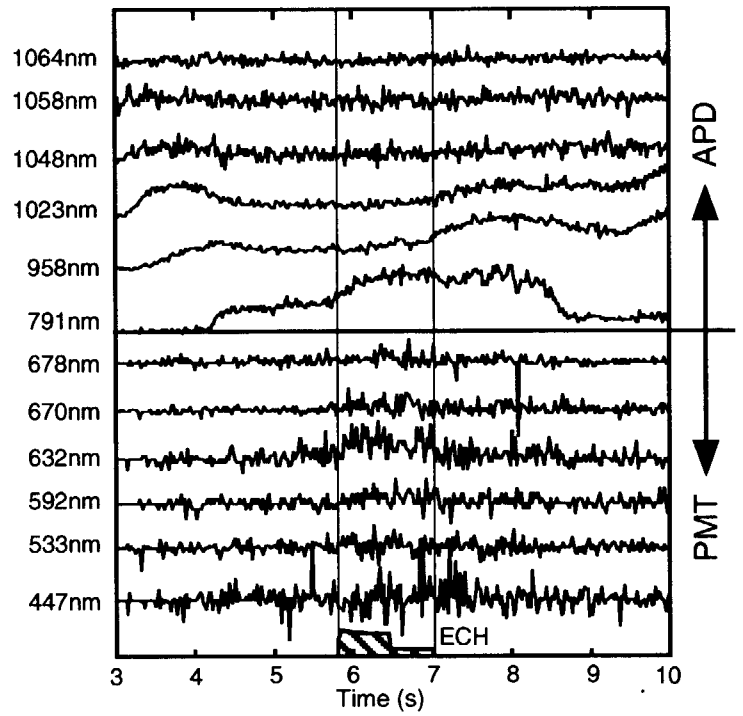

Fig. 4 Preliminary results with combined detection system (PMT+APD). Time evolution of 12 wavelength channel are shown. Data from APD detection system correspond to upper 6 wave forms, and PMT data

5. Conclusion

To improve the measurement performance in very high T_e over ~15 keV, we have tried combined operation of existing Ruby laser system and YAG laser system. From simulations, it was found that the combined system for YAG laser scattering is well optimized at T_e ~ 20keV and relative error is reduced significantly compared with original system. Results indicate that it is possible to improve the accuracy of very high T_e measurement by the combined PMT and APD systems.

References

[1] Yoshida Hidetoshi, et al., Rev. Sci. Instrum. **70**, 851 (1999) .

[2] Yoshida Hidetoshi, et al., Rev. Sci. Instrum. **70**, 747 (1999).

[3] Yoshida Hidetoshi, et al., Rev. Sci. Instrum. **68** 1152 (1997).

[4] Yoshida Hidetoshi, et al., Rev. Sci. Instrum. **68**, 256 (1997).

[5] Yoshida Hidetoshi, et al., Rev. Sci. Instrum. **66**, 143 (1995).

[6] Naito O., et al., Rev. Sci. Instrum. **70**, 3780 (1999).

[7] Hatae T. et al., Rev. Sci. Instrum. **70**, 772 (1999).

[8] Ikeda Y., et al., Proc. 12th Joint workshop on ECE and ECRH, Aix-en Provence, May 13-16 2002, "Formation of high electron temperature plasmas in ECH experiments on JT-60U tokamak", (2002)

11.4 First Application of Diamond Window for Infrared Laser Diagnostics in Fusion Plasmas [1]

Y. Kawano, S. Chiba, and A. Inoue

The diamond is a suitable material for vacuum windows in optical diagnostics with its excellencies of hardness, high heat conductivity, low thermal expansion, and flat transparency from visible to microwave range except of some absorption band [2]. In addition to them, the Verdét constant, a coefficient of Faraday rotation, of the diamond is much smaller (~1/20) than that of the zinc selenide (ZnSe) which is conventionally used at infrared range. On JT-60U, the CVD diamond plate has been first applied as a vacuum window for infrared laser diagnostics in fusion devices. Two vacuum flange sets with two CVD diamond plates (55 mm in diameter, 1.2 mm in thickness) in each set have been installed at two tangential ports for the CO_2 laser interferometer / polarimeter. We have confirmed that there are no problems to use the CVD diamond plate as a vacuum window in interferometry. In polarimetery, the Faraday rotation component that arises at vacuum windows, which becomes a background offset in a measured signal, has substantially reduced to be negligible as expected. Consequently, the feasibility of the diamond vacuum window for optical diagnostics has been demonstrated accompanied with the improvement of polarimetry signal.

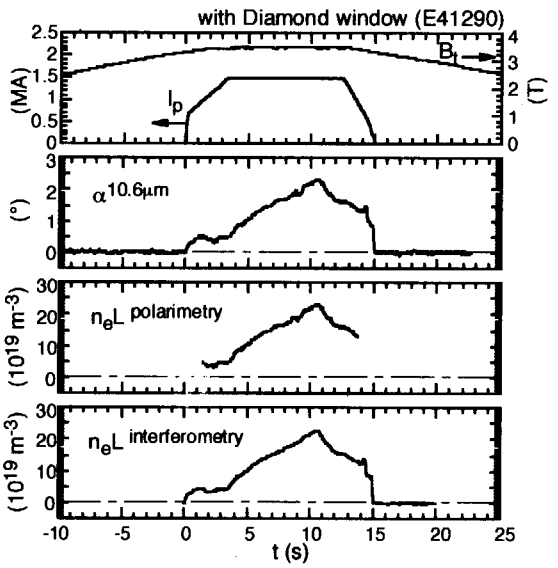

Fig.1 Typical waveforms of the CO_2 laser interferometer/polarimeter using diamond windows. The Faraday rotation component at vacuum windows, which should be seen in the second column before and after a plasma discharge, is not clear or negligible.

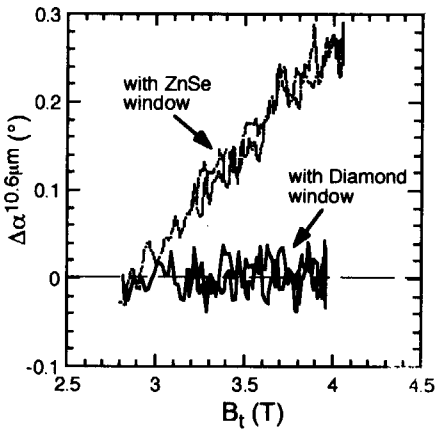

Fig.2 Comparison betweem the Faraday rotation angles measured by the 10.6-μm polarimeter $\Delta\alpha^{10.6\mu m}$ using diamond windows (1.2-mm thick, 4 plates) and ZnSe windows (10-mm thick, 4 plates). The data were taken without plasma dischares, hence traces are attributed to the Faraday rotation components at vacuum windows. The substantial reduction of the Faraday rotation components at vacuum windows is shown for the case with diamond windows.

[1] Y. Kawano, S. Chiba, and A. Inoue, to be submitted to Rev. Sci. Instrum.

[2] Y. Kawano, S. Chiba, and A. Inoue, JAER-Research **99-048**, 97 (1999).

11.5 Heterodyne O-mode Reflectometer on the JT-60U Tokamak [1]

N. Oyama and K. Shinohara

In fusion research, the presence of a transport barrier in the plasma is a key to improving its confinement. Transport barriers at the edge and/or core regions, i.e., the edge transport barrier (ETB) and internal transport barrier (ITB), have been observed in many fusion devices. However, the relation between anomalous transport and fluctuations has not been fully understood yet. In JT-60U, the Broadband O-mode reflectometer showed the reduction of the density fluctuation at the L-H transition [2], and the X-mode core correlation reflectometer successfully measured the correlation length of reflected wave [3, 4]. But, the frequency range of the X-mode system is optimized for a toroidal magnetic field, B_T, from 3.3 to 4.0 T under normal density profiles. Therefore, the X-mode system cannot measure in lower B_T discharges less than 3.0T due to the disappearance of the cutoff layer. Since the cutoff layer depends only on the electron density using O-mode propagation, on the other hand, the reflectometer system can be applied to the density fluctuation measurement independently of B_T. In order to measure the density fluctuation not only at the ETB region but also at the ITB region, in addition to the X-mode system, a three channel heterodyne O-mode reflectometer has been developed for density fluctuation measurements.

The reflectometer system consists of one fixed channel with a frequency of 34 GHz and two selectable frequency channels with frequencies in the range of 34–40 and 48–50 GHz, which correspond to cutoff densities of 1.4×10^{19} m^{-3}, $(1.4–2.0)\times10^{19}$ m^{-3} and $(2.8–3.1)\times10^{19}$ m^{-3}, respectively. Using these frequencies, the reflectometer system can measure the change of fluctuation amplitude, fluctuation coherence, and movement of the cutoff layer, at the ETB and/or ITB. Since the quadrature phase detector enables us to analyze both phase and amplitude of the reflected signal, the applicable experimental condition of the system has been spread as compared with the conventional system with digital phase detector. Thanks to the conventional configuration of the reflectometer system with quadrature phase detector and remote control system, the reliability of the system is high enough as a standard diagnostic for density fluctuation measurements on JT-60U. The capabilities of the system are also illustrated for three experimental results: the reduction of the density fluctuation at the ETB, change of correlation function at the ITB in reversed shear plasmas, and fast turbulence burst at the onset of multifaceted asymmetric radiation from the edge (MARFE).

Reference

[1] Oyama, N. and Shinohara, K., Rev. Sci. Instrum **73**, 1169 (2002).
[2] Fukuda, T., *et al.*, Rev. Sci. Instrum. **61**, 3524 (1990).
[3] Nazikian, R., *et al.*, in Fusion Energy 1998 (Proc. 17th Int. Conf, Yokohama, 1998) post deadline.
[4] Shinohara, K., *et al.*, Rev. Sci. Instrum **70**, 4246 (1999).

11.6 Singular Value Decomposition Analysis of Multichannel Electron Cyclotron Emission Signals of Tokamak Plasma [1]

A. Isayama, N. Iwama[1)], Y. Hosoda[2)], S. Satake[3)], N. Isei, S. Ishida and M. Sato
1) School of Informatics, Daido Institute of Technology
2) Department of Information Science, Fukui University
3) Department of Electronics and Informatics, Toyama Kenritsu University

In a multichannel diagnostic system, a set of data obtained in one discharge can be expressed as a matrix which possesses the i-th time sample of the j-th channel as its (i, j) element. The matrix is analogous to a two-dimensional image and provided with various kinds of matrix operation. One is the singular value decomposition (SVD), and in this paper we applied the SVD to ECE signals measured with the grating polychromator.

The singular value decomposition of an mxn matrix A ($m \geq n$) is unique in practical aspect and expressed as $A=U\Sigma V^T$. Here, U and V are $m \times n$ and $n \times n$ orthonormal matrices, respectively. And $\Sigma=\mathrm{diag}(\sigma_i)$ is a diagonal matrix and has the n singular values σ_i in descending order such that $\sigma_1 \geq \sigma_2 \geq \ldots \geq \sigma_n > 0$. From the expanded form $A=\sum_{i=1}^{n} \sigma_i \mathbf{u}_i \mathbf{v}_i^T$, it can be seen that a set of multichannel signal data is expressed as a weighted sum of the images $\mathbf{u}_i \mathbf{v}_i^T$ ($1 \leq i \leq n$), which are orthonormal bases in the sense of image analysis. Here $\mathbf{u}_i$ and $\mathbf{v}_i$ are the i-th column vectors of U and V, respectively. Since the contribution of the base $\mathbf{u}_i \mathbf{v}_i^T$ to the matrix A becomes smaller with the coefficient σ_i, it can be considered that the principal feature of the multichannel signal will be contained in the terms $\sigma_i \mathbf{u}_i \mathbf{v}_i^T$ with small i, and that the large-i terms may be noise dominant.

It is found that the SVD-based time-space spectral analysis is useful with respect to ECE signals of the grating polychromator for the purpose of tokamak plasma diagnostics. The results show that the SVD analysis can well separate the perturbative component of electron temperature from the equilibrium component in space-time profile. In particular, the topo can clearly reveal the spatial extent and magnitude of an instability like the tearing mode, whose time-space display is not useful because of the oscillation rapid in time and localized in space. An additional utility may be found in filtering of noisy waveforms of ECE with conserving the sharp time profiles, for example, to detect small signals like a precursor of instability.

References

[1] Isayama A, *et al.*, Jpn. J. Appl. Phys. **42**, L329 (2003).

11.7 Maximum Entropy Estimation of Electron Cyclotron Emission Spectra from Incomplete Interferograms in ELMy H-mode Tokamak Experiment [1]

A. Isayama, N. Iwama[1)], T. Showa[2)], Y. Hosoda[3)], N. Isei, S. Ishida and M. Sato
1) School of Informatics, Daido Institute of Technology
2) Department of Electronics and Informatics, Toyama Kenritsu University
3) Department of Information Science, Fukui University

In ELMy H-mode phase, the signal waveform of a Fourier transform spectrometer (FTS) is corrupted in a complicated manner by the ELM-originated external noise. The nonthermal emission pulses appear with various amplitudes at unpredictable locations and can also induce a very large bias of the objective interferogram of ECE. This large disturbance gives a serious effect to the FTS measurement of electron temperature, which makes use of the whole signal record during one period of mirror scan. A method was proposed and examined for saving the FTS from this difficulty.

The procedure of differentiating the signal waveform is simple and useful for selectively enhancing the pulses. The fourth-order differential is preferable for the automatic detection of the pulses which appear in such amplitude that the electron temperature profile measurement is affected. The highpass filtering is also useful for restoring the interferograms except the data missing at pulse locations. Applied to the restored interferograms which may be incomplete with missing observations, the nonparametric maximum entropy method (MEM) for spectral analysis is effective. Unless the data are lost in the zero path-difference (ZPD) region, the MEM can give a close approximation to the FFT spectral estimation, which is well established as the standard for ECE diagnostics. When the missing in the ZPD region is compensated either by using the previous scan data of FTS or by the extension to maximum cross entropy method (MCEM), the spectral estimation is good enough. The MCEM is implemented by appropriating the reference spectrum in only two parameters, that is, the frequency width and the height of rectangular spectrum.

The whole proposed method was examined on long series of interferograms which were observed in the discharge experiments. The result was satisfactory from the standpoint of plasma measurement. The radial profile of electron temperature was well pursued in time evolution even during the ELMy H-mode phase. The profiles agreed well with those obtained by the grating polychromator. The generalized cross validation (GCV), which is approximated for the nonlinear regularization of MEM, was used to determine an adequate value of the regularization parameter for the purpose of getting reliable spectra without excessive smoothing during the whole observation of discharge. The Newton-Raphson method to get a spectral solution gave a good convergence after ~10 iterations, which lead to improvement of the numerical accuracy. The computing time was short enough for the practical purpose of tokamak experiment. A tool of data analysis has been implemented for the ECE diagnostics in high confinement mode experiment.

References

[1] Isayama A, et al., Jpn. J. Appl. Phys., in press

11.8 Collective Thomson Scattering Based on CO_2 Laser for Ion Energy Spectrum Measurement in JT-60U[1]

T. Kondoh, Y. Miura, S. Lee*,
R. K. Richards[1)], D. P. Hutchinson[1)], C. A. Bennett[1)]
1) Oak Ridge National Laboratory, Oak Ridge, Tennessee 37831

Diagnostics for the measurement of fusion-generated alpha particles are important for the understanding of their contribution to plasma heating and plasma instabilities. However, effective measurement methods have not yet been established. A collective Thomson scattering (CTS) diagnostic is a very attractive technique to measure the energy distribution and spatial profile of thermal and fast ions including alpha-particles.

A CTS diagnostic system based on a pulsed CO_2 laser has been developed and brought into operation to establish a measurement technique for ion temperature and the energy spectrum of fast ions [2-8]. The pulsed CO_2 laser (wavelength 10.6μm, beam energy 15 J, pulse width 1μs) and a heterodyne receiver were installed on the JT-60U tokamak. Calculation of the scattered power spectrum from high temperature (ion temperature $T_i \approx 10$ keV) plasmas in JT-60U shows that good (~ 18) S/N values are expected for the bulk-ion temperature measurement. Calibration of the heterodyne receiver system has been carried out using a large area (12 cm × 12 cm) blackbody radiation source. Commissioning of the CTS system by injecting the CO_2 laser into the plasmas has been accomplished. At the present stage, scattered signals have not yet been detected due to electrical noise originating from the pulsed laser discharge and stray signal coming from mode impurities in the pulsed laser. However, by reduction of the electrical noise and stray light, the scattered spectrum will be obtained.

References

[1] Kondoh, T., et al., Rev. Sci. Instrum., **74**, 1642 (2003).
[2] Kondoh, T, et al., J. of Plasma and Fusion Res., **76**, 883 (2000) (in Japanese).
[3] Lee, S., et al., Rev. Sci. Instrum., **71**, 4445 (2000).
[4] Lee, S., et al., Rev. Sci. Instrum., **71**, 3718 (2000).
[5] Kondoh, T., et al., Rev. Sci. Instrum., **72**, 1143 (2001).
[6] Lee, S., et al., J. of Plasma and Fusion Res., **77**, 919 (2001) (in Japanese).
[7] Lee, S., et al., Transactions of Fusion Technology, **39**, No. 1T, 151 (2001)
[8] Lee, S., et al., Jpn. J. Appl. Phys., **41**, 6574 (2002).

*Present address; High Energy Accelerator Research Organization, Ibaraki, 305-0801, Japan

11.9 Spatial Profile Measurement Method of Absolute Detection Efficiency of the Infrared Heterodyne Receiver for the CO_2 Laser Collective Thomson Scattering System in JT-60U [1]

S. Lee*, T. Kondoh, Y. Miura

In order to examine the feasibility of collective Thomson scattering (CTS) diagnostic technique, a CO2 laser CTS system has been installed on JT-60U. Since the small angle of CTS system, the optical beam alignment is essential to such measurement. The sample volume is determined by the cross section of the beam waist and actual field-of-view of the quantum well infrared photo (QWIP) receiver. In this paper, we present an effective observation method for the field of view of the infrared heterodyne receiver and results of experiments using a large homogeneous blackbody (12 cm×12 cm) radiation source for the JT-60U CTS system.

It was initially predicted that the viewing shape, width and sensitivity would correspond to the beam profile of the local oscillator (LO) and QWIP diode mixer. The divergence of the field of view of the heterodyne receiver is also important because the scattered beam passes through a long distance (~70 m) in JT-60U. The viewing profile was measured vertically, horizontally and at a 45-degree angle at the location 15 m separate from the QWIP detector. It could be confirmed that the field of view has a circular profile. The radial profile after Abel inversion is also presented. A Gaussian profile was a good fit to the sensitivity of the field of view. The measured $1/e^2$ field of view diameter at 15 m was about 40 mm. The smallest receiver viewing spot size of 15 mm was measured close to the QWIP detector. This result is consistent with the spot size of both the local beam (ϕ~15 mm) and sensitive area of the QWIP detector.

The viewing area and divergence of the field of view were investigated with this method. The spot size could be narrowed to 0.74 mrad by adjusting the focal length of the local oscillator. The scattering beam loss due to the spread of the field of view was practically suppressed in this setup.

Refecrence

[1] Lee, S., et al., Jpn. J. Appl. Phys., **41**, 6574 (2002).

*Present address; High Energy Accelerator Research Organization, Ibaraki, 305-0801, Japan

11.10 Development of Advanced Collective Thomson Scattering for Impurity Concentration, Helium Ash Density and D/T Ratio Measurements [1]

S. Lee*, T. Kondoh, Y. Miura

The diagnostics of the concentration of impurities in the main plasma is one of the most important measurement in the International Thermonuclear Experimental Reactor (ITER). In order to solve the above diagnosis issue, advanced method using a pulsed CO_2 laser collective Thomson scattering (CTS) is examined. The conceptual design of this technique and calculation results of the scattered spectrum associated with the impurities in the ITER plasma are described. The procedure of proof-of-principle in JT-60U and LHD plasmas is also proposed.

The components of the scattered wave vector are determined by the scattering geometry and the magnetic field, where $k_{\perp}=k\sin(\phi)$, and $k_{\parallel}=k\cos(\phi)$, with ϕ being the angle between the direction of the scattered wave vector and the magnetic field. The expected scattered power spectrum from pure deuterium and include argon (0.12%), beryllium (2%) plasmas in ITER were calculated. We assume that the Plasma parameters are; magnetic field, BT=5.3T, electron density, and deuterium ion density, $n_e=n_D=2\times10^{20}m^{-3}$, electron and ion temperature $T_e=T_i=20keV$. In the condition of the scattered wave vector must be nearly perpendicular to the magnetic field direction, the spectral density function exhibits the characteristic modulation at the ion cyclotron frequency. The modulation occur at the deuterium cyclotron frequency of 40.4MHz and the spectrum extends to approximately 1 GHz. Although the spectrum becomes more complicated with impurity ions, components of main plasma and impurities can be distinguished because the two ion species have different Doppler widths and the impurity modulations are larger at the lower frequencies.

The diagnostic technique proposed in this article shows that the pulsed CO_2 laser CTS system can measure the concentration of impurities of D-T burning plasmas. A calculation was also performed to evaluate the possibility of $k\perp\mathbf{B}$ scattering method for different magnetic field angles.

Reference

[1] Lee, S., et al., J. of Plasma and Fusion Res., **77**, 919 (2001).

*Present address; High Energy Accelerator Research Organization, Ibaraki, 305-0801, Japan

11.11 Collective Thomson Scattering Diagnostic for Fast Ion and Deuterium to Tritium Ratio Measurement in Open Magnetic Systems [1]

S. Lee*, T. Kondoh, R, Yoshino, T. Cho[1)], M. Hirata[1)] and Y. Miura

1) Plasma Research Center, University of Tsukuba, Tsukuba, Ibaraki, 305-8577, Japan

An advanced diagnostic technique to measure the ion temperature and fast ions in open magnetic field systems is described. The method for the determination of deuterium to tritium ratio and the helium ash density in DT burning plasmas is also proposed. The measurement is made by small angle collective Thomson scattering (CTS) using a high power pulsed CO_2 laser and heterodyne receiver system.

The calculation shows that the contribution from ions is much larger than that from electrons. The scattered power from alpha particles covers the frequency range from 3 to 12 GHz. The component of scattered laser power nearly perpendicular to the magnetic field giving rise to ion cyclotron modulation of the scattered spectrum. Spectrum from pure deuterium and from D-T mixed plasma show the possibility of fuel ratio measurement. The scattered spectrum of D-T plasmas with thermalized helium ash is also calculated. We assume that the velocity distribution of electron and bulk are Maxwellian, and the magnetic field is 3.0 T. The scattering angle θ=0.3 deg, and magnetic angle ϕ=89.8 deg are also assumed. The modulation occurs at the deuterium cyclotron frequency of 22.9 MHz and the spectrum extends to approximately 300 MHz.

The diagnostic technique proposed in this article shows that the pulsed CO_2 laser collective Thomson scattering system can be used to measure the ion temperature and the fast ion of D-T burning plasmas in tandem mirror devices. A calculation was also performed to evaluate the possibility of a proof of principle of CTS diagnostics in tandem mirror (GAMMA 10). This calculation is the first demonstration of a diagnostic technique that will be capable of axial profile measurements of ion temperature, confined alpha particle, fuel ratio and helium ash density in open ended fusion plasmas.

Reference

[1] Lee, S., et al., Transactions of Fusion Technology, **39**, No. 1T, 151 (2001)

*Present address; High Energy Accelerator Research Organization, Ibaraki, 305-0801, Japan

11.12 Development of Fast Charge Exchange Recombination Spectroscopy using Interference Filter Method in JT-60U[1]

S. Kobayashi[1)], A. Sakasai, Y. Koide, Y. Sakamoto, Y. Kamada, T. Hatae, N. Oyama, Y. Miura

1) Institute of Advanced Energy, Kyoto Univ. Gokasho, Uji 611-0011, Japan

Measurement of ion temperature, rotation velocity and electric field plays a key role in understanding the property of the improved confinement or the mechanism of collapse phenomenon in fusion plasma; for example, transition of H-mode, formation of internal transport barrier (ITB), minor collapse and disruption. Since these events have a time scale of some hundreds microseconds, the diagnostic systems are required to have a high time resolution enough to observe the evolution of such fast phenomena.

A filter method with three wavelength channels has been applied to the CXRS diagnostics aiming at the measurement of the ion temperature and rotation with a high time resolution [2]. Since the data size of the measured spectral profile is small and the ion temperature and rotation velocity can be determined by the intensity ratios of each channel without complicated nonlinear least squares fitting, the filter CXRS system of three wavelength channels has an advantage that can be easily applied to the real-time measurement or feedback control of the temperature or rotation. To obtain better signal to noise ratio, the optical system of the filter CXRS system has been improved. The alignment between the collection optics and the photomultiplier was optimized because the first dynode of the photomultiplier was not on its axis. As a result, the rapid change in the temperature and rotation could be observed with the minimum time resolution of 0.8 ms in the minor collapse in the reversed shear discharge on JT-60U, which is about 20 times higher than that by the standard CXRS system with the CCD detector in JT-60U [3].

Another filter CXRS system with seven filters was newly developed for obtaining a detailed spectral profile of CXR emission with fast sampling speed. Through the measurement of an H-mode plasma with giant (Type I) edge localized modes (ELMs), it was found that the ion temperature near the separatrix increased slightly just before the ELM event and it recovered rapidly.

Reference

[1] Kobayashi, S., et al., to be published in J. of Plasma and Fus. Res.

[2] Koog, J. S. et al., Rev. Sci. Inst. **70**, 372 (1999)

[3] Koide, Y. et al., Rev. Sci. Inst. **72**, 119 (2001)

11.13 Remark on Apparent Increase in Ion Temperature in CXRS Measurement due to Large Velocity Gradient

Y. Koide

1. Introduction

In a series of high-Q_{DT} experiment in October, locally high ion temperature at the ITB shoulder was estimated with the toroidal CXRS system [1]. Figure 1 shows an example where the central temperature is ~20keV with a flat profile while temperature at the ITB shoulder (channel 8) is extremely high (~24keV).

In this paper, the cause for this locally high ion temperature is investigated from the viewpoint of reliability of CXRS measurement.

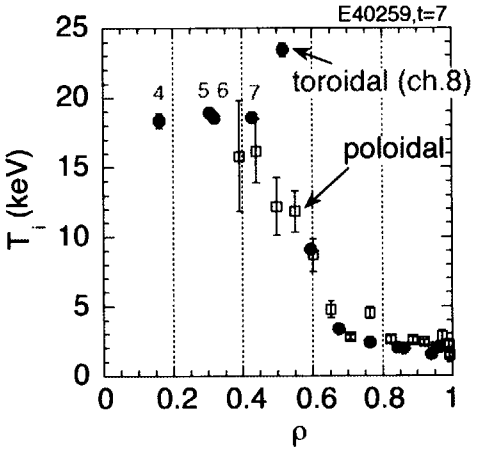

Fig. 1. Ion temperature profile from toroidal and poloidal CXRS systems.

2. Considerations

2.1. Spectral Line Shape

There was no detectable deformation nor any contamination by other lines in the spectrum for the channel 8 in Fig. 1 (Fig. 2).

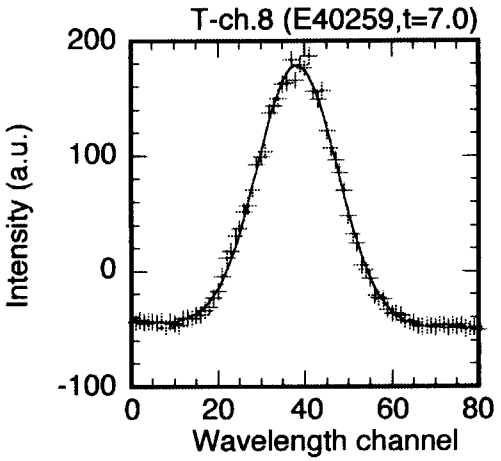

Fig. 2. Charge exchange recombination spectrum for channel 8 in Fig. 1.

2.2. Comparison with Poloidal CXRS System

The poloidal CXRS system shows the ion temperature at the ITB is ~15keV without no substantial local increase within its error bar (Fig. 1), which contradicts with the ion temperature profile from the toroidal system.

2.3 Heating Profile

Figure 3 shows the deposited heating power profile of each plasma species. There is no localized heating power which may produce local temperature increase in the region of ~6cm width as seen in the toroidal system measurement.

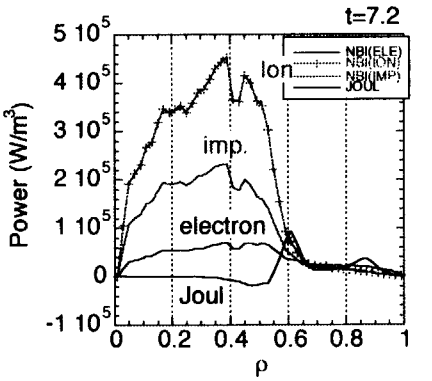

Fig. 3. Deposited heating power profile to each plasma species

2.4 Energy Dependence of Emission Rate

Apparent Doppler broadening can be produced due to the energy dependence of the emission cross section [2]; the effect is substantial when ion temperature is high and the angle between the line of sight and neutral beam (δ) is near a right angle. Apparent temperature also depends on the energy composition of neutral beams (E, E/2 and E/3) contained in the emission volume. Figure 4 shows (a) the angle for some of toroidal channels (δ for channel 8 is ~5.5 degree) and (b) apparent temperature against true temperature. In figure 4(b), for simplicity, two extreme cases of (i) no beam attenuation for all of energy components (designated as E3) and of (ii) full attenuation of E/2 and E/3 energy components (designated as E) are shown; results for two cases of δ=0 and 10 degrees are compared. The experimental condition falls on the in-between of the two cases of energy components and of the two cases for δ. Since the results show that the overestimation is at most 1keV, the locally high ion temperature in Fig. 1 cannot be explained.

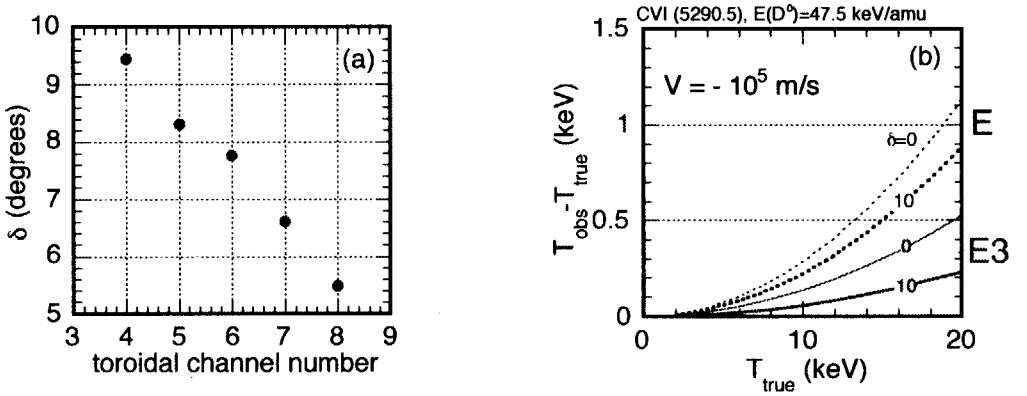

Fig. 4. (a) Angle between the line of sight and neutral beam for some of toroidal channels and (b) apparent temperature against true temperature.

2.5. Gradient of Toroidal Rotation Velocity

The emission volume of CXRS measurement is defined by the intersection of the neutral beam and the field of view of the fiber optics; the cross section of the volume, which mainly determines the spatial resolution, is ~6cm in diameter for the toroidal system. When pressure gradient increases significantly due to ITB formation, a steep gradient of toroidal rotation velocity is often formed in the ITB region (Fig. 5). If the scale length of the velocity gradient becomes shorter than the spatial resolution, measured spectrum will consist of a set of Maxwellians with

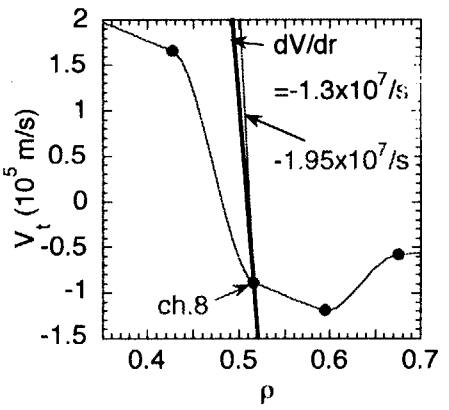

Fig. 5. Toroidal rotation velocity profile. Symbols: measured rotation velocity, thick and thin lines: gradients required for the two cases (see the text) to produce the apparent ion temperature of 24keV shown in Fig. 1.

continuously varying Doppler shift. The significance of this effect was calculated, and the required steep velocity gradient to produce the apparent local increase shown in Fig. 1 was estimated in the following.

Maxwellian distribution function of CVI ions in parallel to the magnetic line of force which is measured by toroidal system is expressed as,

$$f_{//}(\lambda,r)=\frac{n_c(r)}{\sqrt{2\pi T_i(r)}}\exp\left[-\frac{\{\lambda-\lambda_0(1+V_t(r)/c)\}^2}{2T_i(r)/m_c\cdot(\lambda_0/c)^2}\right],$$

where $n_c(r)$ is measured carbon density and $T_i(r)$ is ion temperature profile with neglecting the data point of channel 8. The region of one spatial point is divided into 6 sections where each section has different velocity as shown in Fig. 6(a). Considering the signal weight due to the surface area of each section, measured spectrum of section 2, 4 and 6 are plotted with symbols in Fig. 6(b), where weights for section 1 and 7 are zero due to zero surface area. Here it was assumed that T_i of channel 8 was 20keV (same as the central temperature) and that velocity gradient was $\nabla V_t=-1.3\times10^7$/s (shown with a thick solid line in Fig. 5), the background of which will be shown later. A thick solid line in Fig. 6(b) shows the normalized sum of the contribution from each section and a thin line normalized spectrum from the central section, i.e. section 4; the former corresponds to measured spectrum and the latter local spectrum at the center of the spatial point. It should be noted that observed spectrum (a thick line) has wider FWHM than the local one (a thin line) by more than 10%, which leads to overestimate of ion temperature by 21%. In other words, the assumption of large toroidal velocity gradient can explain the local increase in T_i from 20keV to 24keV shown in Fig. 1. On the other hand, if we adopt 13keV for channel 8 based on the poloidal measurement, $\nabla V_t=-1.95\times10^7$/s (shown with a thin solid line in Fig. 5) is required for the overestimation as 24keV (Fig. 7).

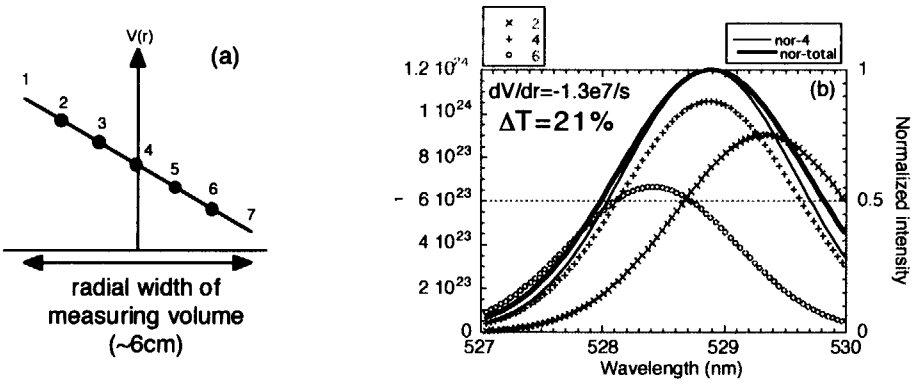

Fig. 6. (a) Model toroidal rotation velocity profile which varies spatially within a spatial region of channel 8, (b) spectrum contributed from each section (symbols) and reconstructed spectrum (a thick line). $\nabla V_t=-1.3\times10^7$ / s and T_i (channel 8)=20keV.

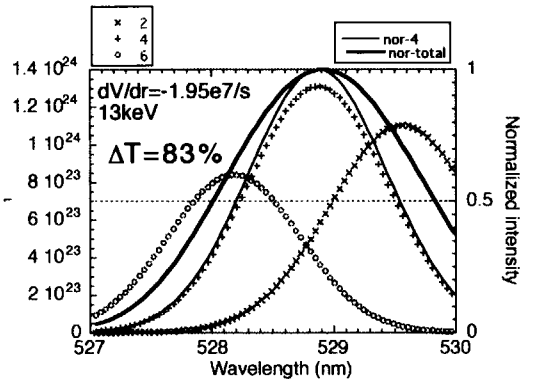

Fig. 7. Spectrum contributed from each section (symbols) and reconstructed spectrum (a thick line). $\nabla V_t = -1.95 \times 10^7$ / s and T_i (channel 8)=13keV.

3. Future Work

It was shown that steep velocity gradient beyond the spatial resolution such as $\nabla V_t = -1.3 \times 10^7$/s and $\nabla V_t = -1.95 \times 10^7$/s can explain the locally increased ion temperature shown in Fig.1 as an overestimation. According to the spatial gradient, however, extrapolated velocity at $\rho \sim 0.55$ reaches $V_t = -5.1 \times 10^5$m/s and -7.2×10^5m/s, respectively; these values correspond to 28% and 47% of sound speed ($= \sqrt{(T_e + \gamma_i T_i)/m_D}$), respectively. Since plasma flow with such subsonic speed is believed to affect the MHD equilibrium, we must investigate whether the deduced gradient is physically reasonable or not.

References

[1] Y. Koide et al., Rev. Sci. Instrum. **72**, 119 (2001).

[2] M. von Hellermann et al., Plasma Phys. Control. Fusion **37**, 71 (1995).

11.14 Neutron Emission Profile Measurement on JT-60U

M. Ishikawa[1], T. Nishitani, A. Morioka, M. Takechi, K. Shinohara, M. Shimada,
Y. Miura, M. Nagami, Yu A Kaschuck[2]

1) Plasma Research Center, University of Tsukuba, Tsukuba-shi 305-8877, Japan
2) Troitsk Institute of Innovating and Fusion Reserch (TRINITI) Troitsk, Moscow redion 142092, Russia

Neutron diagnostics is one of the most important diagnostics for control of burning plasmas for future fusion devices like ITER. Above all, a measurement of neutron profile is of great importance for the knowledge of the profile of fusion power and the source of alpha particles. Therefore establishment of a measurement method of neutron profile is highly desirable.

We have been measured neutron emission profile of JT-60 plasma using a fan-shaped six channel neutron collimator array (2.6m×1.3m×1.6m), which views a poloidal cross section through the plasma and is located about 5 m away from the plasma center. At the beginning, NE213 organic liquid scintillators were employed as neutron detectors because of their good time resolution and well-known efficiency. However, since such organic scintillators detect gamma-rays as well as neutrons, precise investigation of neutron behavior was difficult.

In order to resolve above problem, we installed Stilbene neutron detector developed by TRINITI laboratory in Russia on the JT-60U Tokamak to measure the neutron emission profile for the first time [1]. Stilbene neutron detector is a detector which combines Stilbene crystal scintillator with a neutron-gamma pulse shape discrimination circuit, with a very compact size. For the application of this detector to JT-60U experiments, the calibration using neutron and gamma sources and the performance test on Fusion Neutron Source (FNS) [2] in JAERI Tokai were conducted. In these tests, good gamma-ray suppression of Stilbene neutron detector was verified in the count range of $10^2 \sim 10^5$ cps. under existence of background gamma-rays. Also by using MCNP (Monte Carlo Code for Neutron and Photon Transport) [3], the effect of shielding and scattering of neutrons for vacuum vessel and the neutron collimator array was evaluated.

Using Stilbene neutron detector, neutron emission profile measurement was preformed in JT-60U DD experiments. The neutron emission profile obtained is in a reasonable agreement with calculated profile using TOPICS code [4]. Therefore, measurements of neutron emission profile become available routinely in JT-60U.

References

[1] Ishikawa, M., et al., Rev. Sci. Instrum., **73**, 4237 (2002)
[2] Nakamura, T., et al., Proc. Int. Ion Eng.ongress-ISIAT **83**, 567 (1983)
[3] Briesmeister, J. F., (Ed.), LA-12625-M, Los Alamos National Laboratory (1997)
[4] Nishitani, T., et al., Nucl. Fusion **34**, 1069 (1994)

11.15 Reciprocating Mach Probe System for High-Field-Side SOL Measurement

N. Asakura, S. Sakurai, K. Masaki, R. Yoshino

1. Introduction

Scrape-off layer (SOL) flow plays an important role in the plasma transport along the field lines, and determination of the SOL flow velocity and direction is crucial for particle control in edge and divertor. New reciprocating Mach probe system was installed at the high-field-side (HFS) baffle in 2001, and profiles of the SOL flow velocity (Mach number, M), floating potential (V_f), electron temperature (T_e) were measured, for the first time, at the HFS SOL. The Mach probe system and operation are described in this section. Experimental results in high-density L-mode and ELMy H-mode plasmas were summarized in Sec. 8.1 and 8.2.

2. System Description

Inner reciprocating Mach probe system (IMPS) was installed at U-1 diagnostics port of P-2 toroidal section, as shown in Fig.1. Basic components of the system are similar to the midplane reciprocating probe [1], and X-point reciprocating Mach probe. Probe head with 5 electrodes is inserted into the SOL plasma above the inner (HFS) baffle as shown in Fig. 2. The IMPS performs a vertical scan of 34 cm in 0.6s and 0.5 s during the insertion and extraction, respectively. Laser displacement gauge (KEYENCE, LK-500) provides high spatial resolution of 1 mm with a time response of 1 ms.

All drive components and vacuum boundaries are located below the JT-60 machine support. Drive components of the IMPS consist of a compact pneumatic cylinder and steel springs (SUP10). They are mounted on a movable probe-system support. Since hold position of the probe-system

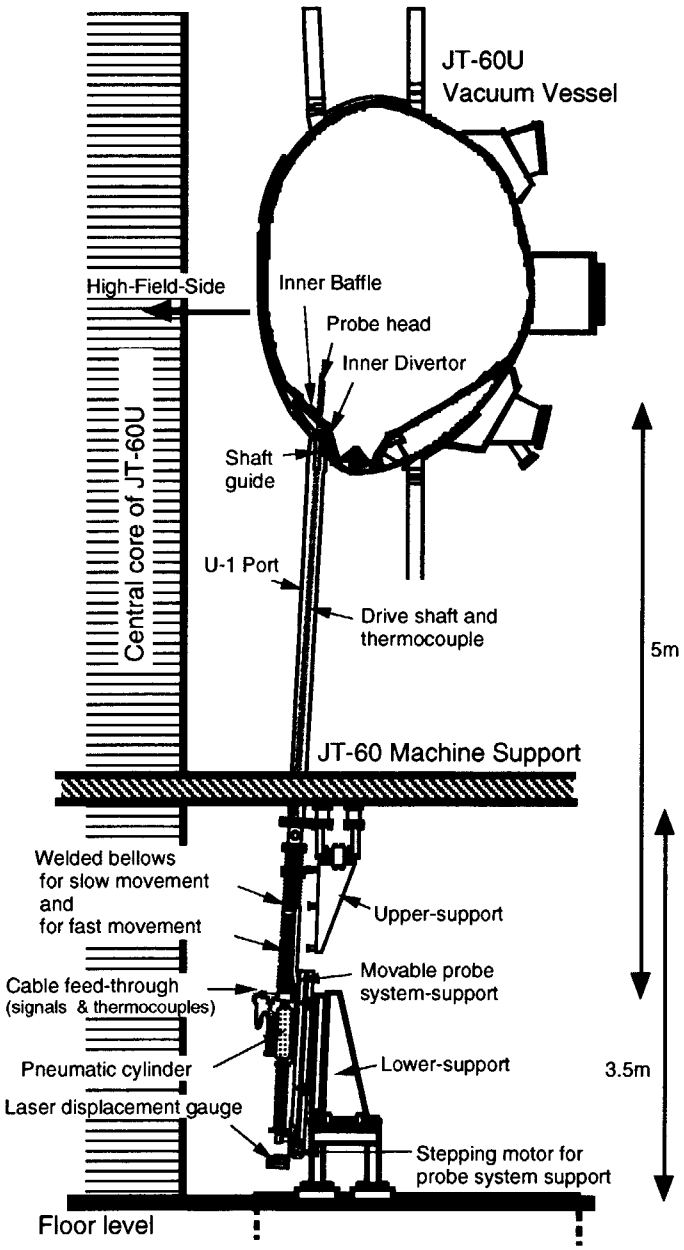

Fig.1 Inner reciprocating probe system and JT-60 vacuum vessel.

support is varied by a stepping-motor, the initial position of the probe head (as shown in Fig. 2) is chosen from the surface of the HFS baffle to 19 cm below, depending on the plasma configuration.

Drive shaft is 4.5 m in length and 30 mm in the diameter, which consists of three circular pipes (SUS304) and was incorporated during the installation. One set of Si_3N_4 ball bearings mechanically contacts to a guide cylinder, and electrically isolates the drive shaft from the JT-60 vacuum vessel (the guide cylinder is also insulated from the vacuum vessel). Vibration of the probe head during the probe insertion is minimized less than 1 mm. A collimator with 40mm hole

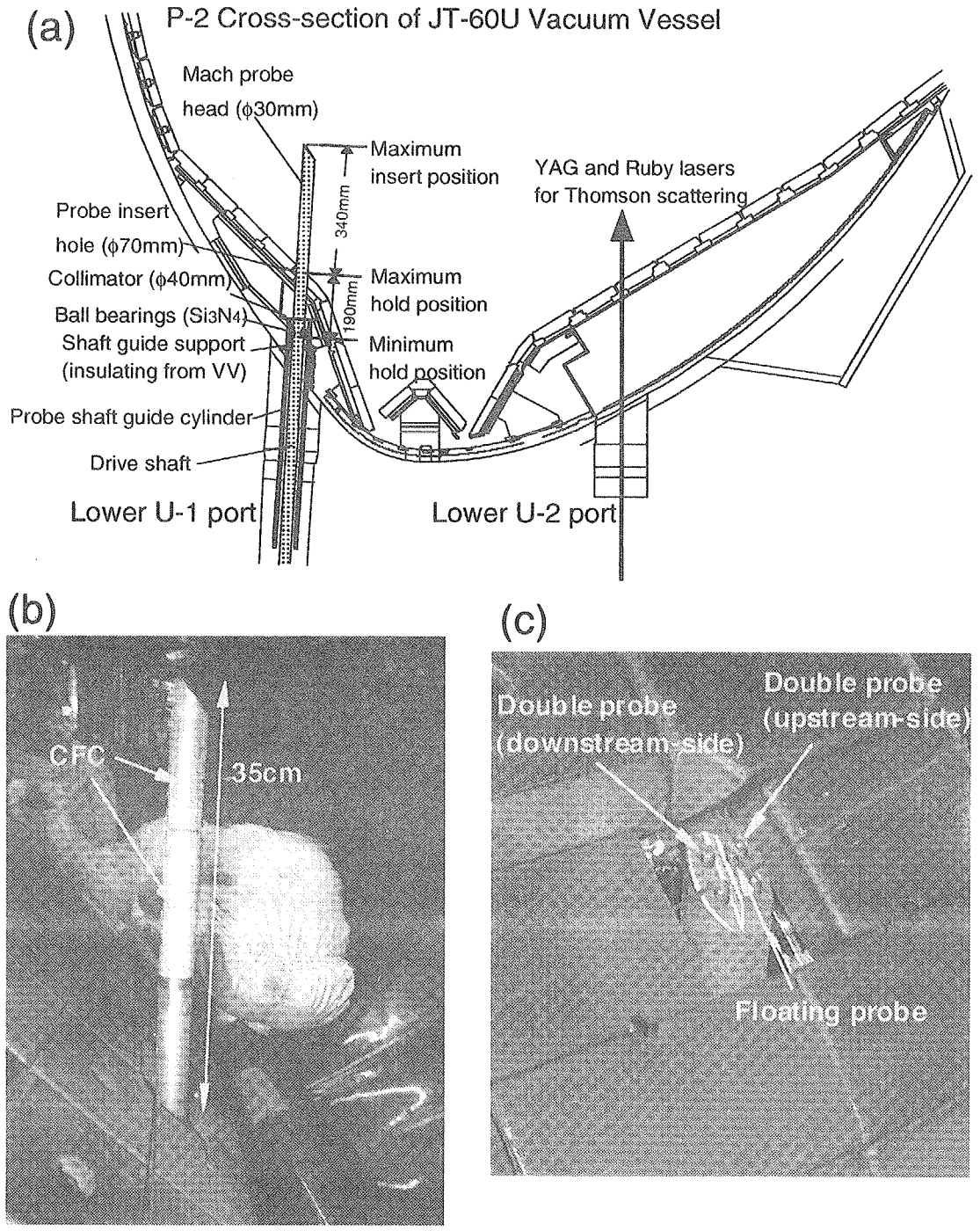

Fig.2 (a) JT-60 W-shaped divertor and inner Mach probe location, (b) Maximum insert position of IMP, (c) Probe electrodes at Maximum hold position

in diameter minimizes neutral back flow from under-baffle to the main chamber.

Carbon fiber composite (CX-2002U) is used for probe head and five electrodes as shown in Fig. 2(b) and (c). Each probe electrode is 4mm in diameter with its spherical apex protruding 1.5 mm into the plasma. Two sets of double-probe measurements provide ion saturation current (j_s) and T_e at upstream- and downstream-side of the field lines. The Mach number of the SOL plasma flow is evaluated from ratio of j_s^{up} and j_s^{down} using Hutchinson's formula [2], $M = M_c \, ln \, (j_s^{up} / j_s^{down})$, where a value of 0.35 is used for M_c. It is deduced from the fluid equations, which are valid under the experimental conditions of the SOL plasma, i.e. the ions are collisional. One electrode at the top measures V_f. Plasma potential, V_p, and radial electric field, E_r, are calculated from $V_p = V_f + 2.75T_e^{up}$ and its differentiation, respectively.

3. Probe Operation

Operation and data acquisition of IMPS are preprogrammed by a CAMAC system and a microcomputer (Apple, Macintosh Quadra 800). The probe reciprocation is initiated by a trigger signal from the programmable clock, which opens the solenoid valve for pneumatic cylinder, triggers a function generator and starts data sampling.

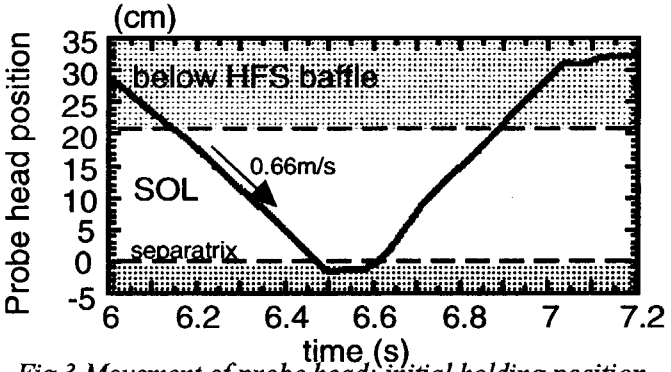

Fig.3 Movement of probe head: initial holding position is 11cm below the HFS baffle surface.

Movement of the probe head is shown in Fig. 3, where spatial resolution (1 mm for fast sampling rate of 1 ms) and noise of the Laser displacement gauge are several times better than a standard potentiometer. During the forward movement, the velocity is almost constant (0.66 m/s). In order to minimize vibrations of the probe head at transition from forward- to backward-movement (~6.5 s), components (a mechanical air dumper, a slow leak-valve in the pneumatic cylinder and position of the optical sensor to trigger the backward-solenoid valve) are adjusted.

Applied voltage to the double probe is a triangle waveform with 200 V and a typical frequency of 500 Hz (2 ms period), which corresponds to special resolution of 1.3 mm. Probe signals for I-V characteristic fit (V-scan-mode) are sampled with a frequency of 200 kHz (400 data for one V-scan period). Double probe analysis was described in Ref. [1].

4. Measurements of Mach Number and Ion Flux

Figure 4 (a) shows one example of j_s profiles in L-mode plasma (I_p=1.6MA, B_t=3.4T, δ=0.33, κ=1.4, P_{NB}= 4.3MW, line-averaged electron density of 1.5×10^{19} m^{-3}). j_s^{up} decreases gradually and it is found that the SOL plasma extends to a surface of the HFS baffle even in relatively low-density plasma. On the other hand, j_s^{down} decreases largely outside the separatrix: the Mach

number is increased. j_s^{down} decreased largely again at outer flux surfaces (r > 15 cm) since connection length of downstream-side probe becomes very short (i.e. field-lines are connected to the HFS baffle). Profile of the Mach number is shown in Fig. 4 (b): the SOL flow velocity at the outer flux surfaces is subsonic level (~0.4), and SOL flow away from the HFS divertor is observed at and just outside separatrix. Here, Mach numbers at r > 15 cm would be overestimated when $M_c = 0.35$ in Ref.2. SOL flow pattern was discussed in Sec. 8.1, and flow reversal is caused by an influence of the plasma drifts.

Figure 5 shows j_s^{up} profile in ELMy H-mode plasma (I_p=1MA, B_t=2T, δ=0.32, κ=1.4, P_{NB}=4.3MW, line-averaged electron density of 1.7×10^{19} m^{-3}). Circle symbols (fit data in V-scan-mode) and square symbols (ELM peaks in I_s-mode) show that ion flux profile becomes flat just after ELMs, and that large particle flux reaches the HFS baffle. This suggests that diffusion of the SOL plasma to the outer flux surfaces such as 20-25 cm is largely enhanced, and it is recovered in ~10 ms.

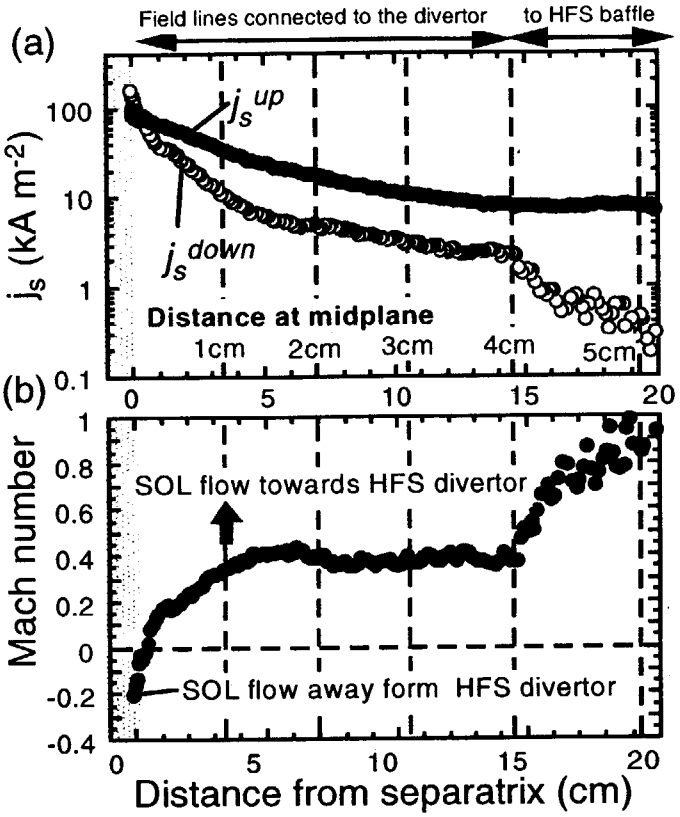

Fig.4 Profiles of (a) ion saturation current at upstream and downstream-sides, (b) Mach numbers.

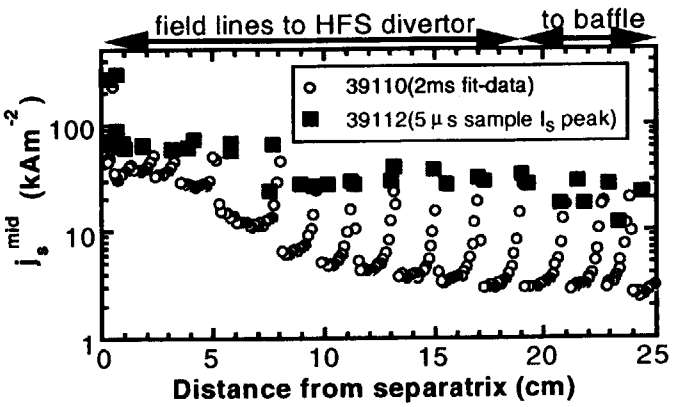

Fig.5 Profile of ion saturation current at upstream-side in ELMy H-mode plasma.

5. Summary

The high-field-side reciprocating Mach probe system was installed, and SOL profiles of the Mach number, T_e, n_e and V_f were measured, for the first time, in the divertor tokamak. New experiment results greatly contributed to progress the edge and divertor study.

References

[1] Asakura, N. et al., Rev. Sci. Instrum., 66 (1995) 5428-5432.
[2] Hutchinson,I.H. Phys. Rev., A37 (1988) 4358.

11.16 Tritium and Gas Species Measurement System in JT-60U Exhaust Gas

A. Kaminaga, H. Nakamura, S. Higashijima, T. Horikawa, S. Konishi

1. Introduction

Tritium removal characteristics from the first wall of the large tokamak device is quite important in the viewpoint of not only the tritium control of JT-60U but also the optimization of tritium removal for future fusion device. Therefore, it is desired to obtain the tritium behavior in the vacuum vessel from the generation by the nuclear reaction to emission from the graphite tiles or co-deposit layer. In the JT-60U, deuterium plasma experiments have been carried out since 1991. During the deuterium plasma experiment, a triton and a neutron are generated by the D(d,n)T reaction. A part of generated tritium is evacuated and exhausted to the outside of the vacuum vessel with the vacuum system, and the rest remains in the vacuum vessel. On the basis of previous investigations [1,2], it has been revealed that most of tritium generated by the DD reaction remains in the first-wall graphite tiles, because high-energy tritium generated by the DD reaction are directly implanted into the deep (~μm) area of the first wall. Although distribution and state of tritium on/in the JT-60U first-wall graphite tiles has been investigated extensively using imaging plates, surface analysis and thermal desorption, tritium behavior in the vacuum vessel of JT-60U such as evacuation characteristics or release characteristics from the co-deposition or first wall is still unknown. In such viewpoint, tritium measurement of exhaust gas of JT-60U and tritium removal from the first wall by the discharge cleaning such as Glow Discharge Cleaning (GDC) or Taylor Discharge cleaning (TDC) and Electron Cyclotron Resonance Discharge Cleaning (ECRDC) was planned. Prior to the tritium measurement, equipment for tritium measurement and hydrogen-isotope gas species measurement has been installed at the vacuum system of the JT-60U. This report presents the specification of the measurement system of tritium and gas species and initial results of the performance verification test.

2. Specification of the Exhaust Gas Measurement System

2.1 Overview of Exhaust Gas Measurement

The vacuum pumping system of JT-60U consists of Turbo Molecular Pumps(TMP), Mechanical Booster Pumps(MBP) and dry vacuum pumps (DVP). Figure 1 shows a flow sheet of the JT-60U vacuum pumping system. The tritium measurement system and the gas species measurement system are shown in Fig. 2; the flow sheet of ion chamber, bubbler system and GC system connected from B in Fig. 1. A residual gas analyzer (RGA) and a gas chromatography (GC) are prepared for the gas species measurement, and an ion chamber and

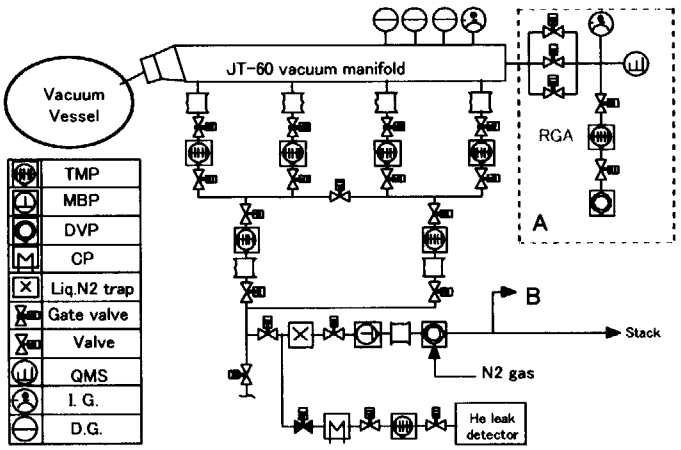

Fig.1 Flow sheet of the JT-60U vacuum pump system

a water bubbler system with hot catalysts are prepared for the tritium measurement. The RGA is installed in a manifold of the vacuum system (A in Fig.1), and the ion chamber, bubbler system and GC are installed at the down stream of the vacuum system by bypassing the exhaust line (B in Fig.1). Specifications of the tritium and gas species measurement system are summarized in Table 1.

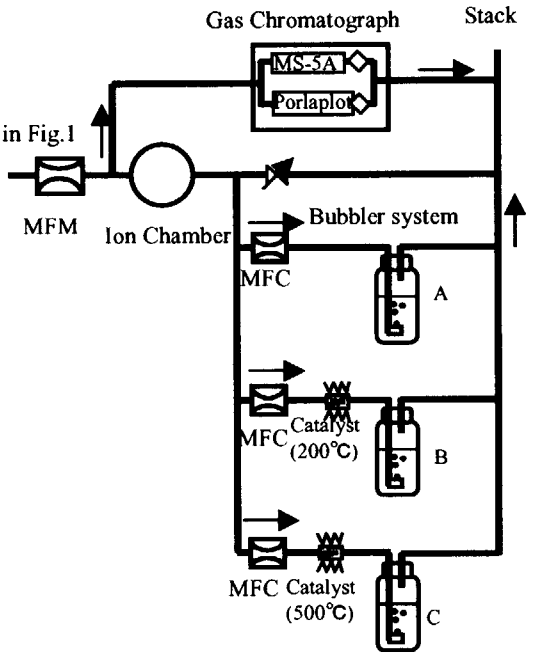

Fig.2 Flow sheet of tritium and gas species measurement system
MFC: Mass Flow controller
Bubbler A: vapor tritium collection, Bubbler B: vaporand hydrogen tritium collection, and Bubbler C: All tritium collection.

Table 1 Specifications of tritium and gas species measurement system

	Tritium measurement		Gas species measurement	
	Ion chamber (I.C.)	Water bubbler	RGA	GC
Maker/model	Aloka/MGR133	JAERI	Ulvac/MSQ-400	Agilent/G2890A
Object	All tritium	Chemical species of tritium	Mass of gas	Gas species
Method	βray detection (ion chamber)	βray detection (LSC*)	Mass analysis (M/e=1-400)	TCD after gas chromatography
Specification	I.C. volume 3 L	Heated Catalyst** (200°C,500°C)		Molecular Sieve (10m) Porlaplot Q (8m)
Detection limit	0.05 Bq/cc	0.3Bq (LSC)	5E-12 Pa(N_2)	1 ppm (H_2)

* LSC: Liquid scintillation counter, ** catalysts: popcalite

2.2 Tritium Measurement System

The ion chamber (Aloka-MGR133) measures the tritium concentration in the exhaust gas, and the bubbler system measures the chemical species of tritium (vapor, hydrogen and hydrocarbons) in the exhaust gas. The detection limit of the tritium for the ion chamber and the bubbler system is 0.06Bq/cc and 0.008Bq/cc for 1-hour measurement, respectively.

2.3 Gas Species Measurement System

The RGA (ULVAC-MSQ400) measures the mass numbers of the residual gases, and this system can control the gas flow from the vacuum vessel to the RGA by selecting 3 orifices of different diameters. The detection limit of the RGA is almost $5x10^{-12}$ Pa for N_2. The GC (Agilent-G2890A) system measures the gas species in the exhaust gas with a combination of a Thermal Conductivity Detector (TCD) and two columns: Molecular sieve-5A (5m) with Ar gas carrier for H_2, He and hydrocarbons and Porlaplot Q (8m) with He gas carrier for H_2O, CO and CO_2. The detection limit of this GC system is almost 1 ppm in the H_2 gas

3. Preliminary Result of JT-60U Exhaust Gas Measurement

The performance verification test of the gas species measurement and the tritium measurement system was carried out during DD discharge experiment.

3.1 Tritium Measurement

Figure3 shows the tritium concentration in the exhaust gas of JT-60U during the deuterium plasma experiment measured with the ion chamber. Significant increase of tritium concentration was observed by the discharges. Each peak corresponds to the individual shot such as deuterium tokamak discharge, He-TDC and He-GDC. Tritium concentration increases rapidly for about 2 minutes after the discharge, and decreases slowly. Since the time constant of the ion chamber is about 50 seconds, it is shown that the tritium release behavior in each discharge can be measured.

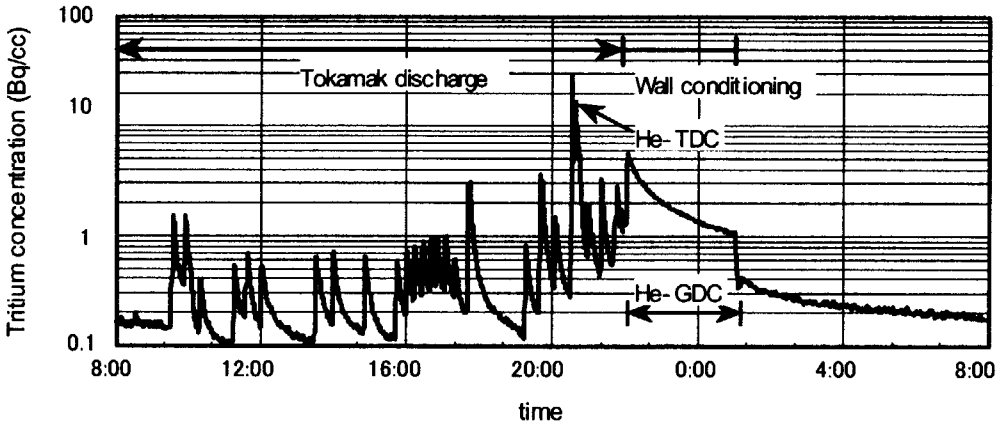

Fig.3 Tritium concentration change during deuterium plasma experiment

3.2 Gas Species Measurement

Figure 4 shows an example of gas analysis in the vacuum vessel measured with the RGA and tritium concentration in the exhaust gas during a plasma experiment. The time constant of the RGA measurement is almost 30 seconds. Clear correlation between the tritium concentration in the exhaust gas and the RGA signals of the residual gases in the vacuum vessel has been confirmed as shown in Fig. 4. Therefore, the chemical form of tritium in the

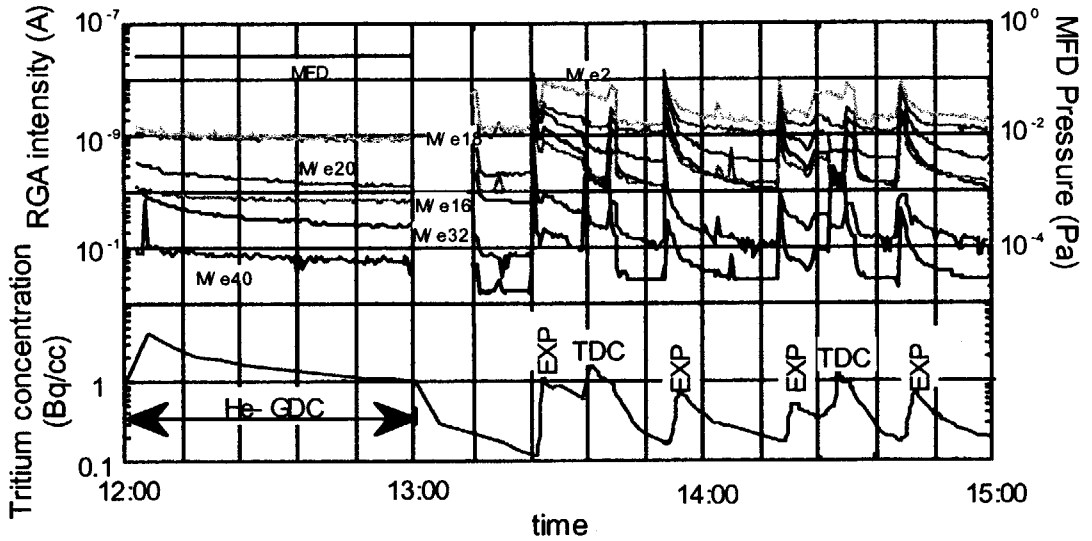

Fig.4 Comparison between RGA intensity and tritium concentration during deuterium plasma experiment.

exhaust gas can be identified by the RGA measurement.

The chemical species were also measured with the GC. An example of the GC measurement during a tokamak discharge experiment is shown in Fig. 5. The result indicates most of the exhaust gas at a tokamak discharge is hydrogen isotopes, and it contains a little amount of He and few hydrocarbons. On the basis of the results of RGA and GC, it was confirmed the capability of gas species analysis. It gives useful information for identification of the chemical form of tritium.

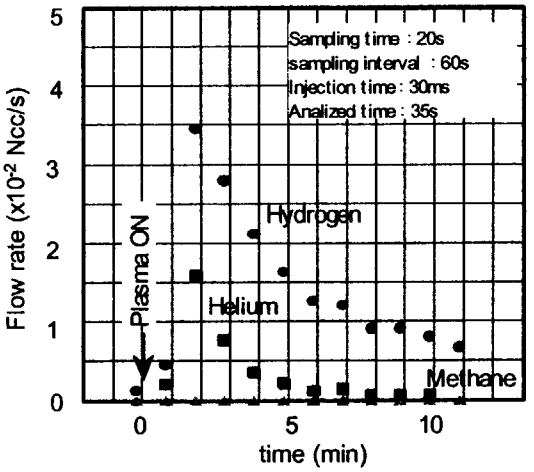

Fig.5 Gas species in the exhaust gas measured with GC after deuterium tokamak discharge

4. Summary

Tritium and chemical composition measurement system has been installed in the JT-60U vacuum system to measure the tritium exhaust amount and chemical form of tritium in the exhaust gas during JT-60U operation such as tokamak experiments or wall conditioning.

Performance of the system was tested. The detection limit and the time constant of the system were derived. Using the equipment, the tritium removal by discharge cleaning such as TDC, GDC and ECRDC will be investigated.

Reference

[1] Masaki K. et al., Fusion Eng. Des. **31** 181, (1996).

[2] Tanabe T. et al., Fusion Science & Technol. **40** 877, (2002).

12. Heating Systems

12.1 Improvement of Beam Performance in Negative-Ion Based NBI System for JT-60U

N.Umeda, T.Yamamoto, M.Kawai, L.Grisham and JT-60 NBI team

Injection performance of negative-ion based NBI system for JT-60U has been improved. Previously the pulse duration was limited up to 2 seconds with injection power of 5 MW because of high heat load and subsequent temperature rise of the NBI port limiter. The size of the narrowest NBI port limiter which is located at 22 m far from the ion source is 46 cm height and 50 cm width, while the size of beam extraction area is 110 cm height and 45cm width. Therefore it is important to improve the beam focusing.

The beam profile was measured at 3.5 m downstream from the ion source by using a target plate and an IR camera. From the measurement it was found that the beamlets of the segment edge were deflected 14 mrad outward. There were small grooves with 5 mm in depth and 40 mm in width at the down streamside of the extractor grid segments. These grooves generated electric field distortion. To make the distorted electric field uniform, copper bars were embedded in the grooves. As a result, the deflection angle of the edge beamlets was reduced to 6 mrad outward. It seemed that the beamlet is deflected by space charge effect of beamlet-beamlet interaction [2]. To correct this deflection, the thickness of the copper bar was increased to generate the electric field to steer the beamlets inward to the each segment. The suitable height of the bar was estimated by using a three-dimensional beam trajectory code and 1.5 mm height was selected. The beamlet deflection by beamlet-beamlet interaction was corrected completely.

Figure 1 shows temperature rise of the beam limiter at the NBI port. The heat loads on the limiter with the flat bar and 1.5 mm extruded bar were decreased to less than 60% and 70% of the original one, respectively. The injection port of N-NBI for JT-60U is so narrow that even slight beam deflection largely affects. This improvement enabled the long pulse injection at high beam power and the continuous injection of 2.6 MW at 355 keV has achieved for 10 seconds.

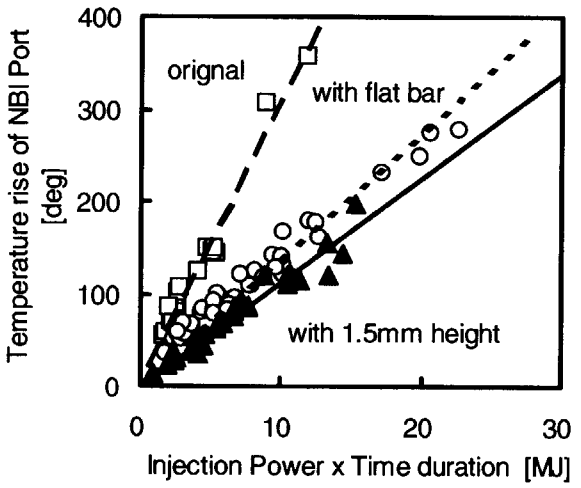

Fig.1 Temperature rise of the beam limiter at NBI port

References

[1] Umeda, N ., et al, Proc.19th IAEA Fusion Energy Conf. Lyon,(2002) CT-6Rd

[2] Okumura,Y., et al., Proc. 18th IAEA Fusion Energy Conf. Sorento, (2000) FTP1/18R
http://www.iaea.org/programmes/ripc/physics/fec2000/html/node317.htm

12.2 Operational Progress of the ECRF System in JT-60U

T. Fujii, Y. Ikeda, M. Seki, S. Moriyama, M. Shinozaki, T. Terakado, K. Yokokura, M. Shimono, S. Hiranai, K. Anno, M. Isaka, K. Igarashi, K. Ishii, H. Sato and the JT-60 team

1. Introduction

It is one of key issues for attaining higher plasma performance in a large tokamak to control MHD instabilities and a current profile by local heating or current drive. For such a purpose, we started to develop a high power electron cyclotron range of frequency (ECRF) system for JT-60U, whose objective specifications were the injected power of 3 MW at 110 GHz corresponding to the toroidal magnetic field of 3.8 T. It, however, is very difficult to develop the high power ECRF system, especially a high power source gyrotron. On the basis of rapid progress in research and development of the gyrotron for ITER, the first one unit of the JT-60U ECRF system was constructed in December 1998. Its operation was started in 1999, and the second and third units were constructed in March 2000 [1, 2].

2. Increase of injected power

The ECRF system was completed as shown in Fig. 1 when the fourth unit had been constructed in March 2001. Each unit consists of a 1 MW gyrotron and a 60 m-long transmission line. The line has corrugated waveguides of diameter 31.75 mm and nine bends including a pair of polarizers are used and is evacuated at 10^{-4} - 10^{-3} Pa to avoid rf breakdown. There are two quasi-optical antennas composed by focus and steerable mirrors. Antenna A is connected with three lines and antenna B with the fourth line. Both antennas can control the poroidal angle of the EC beam while only antenna B can control the toroidal angle.

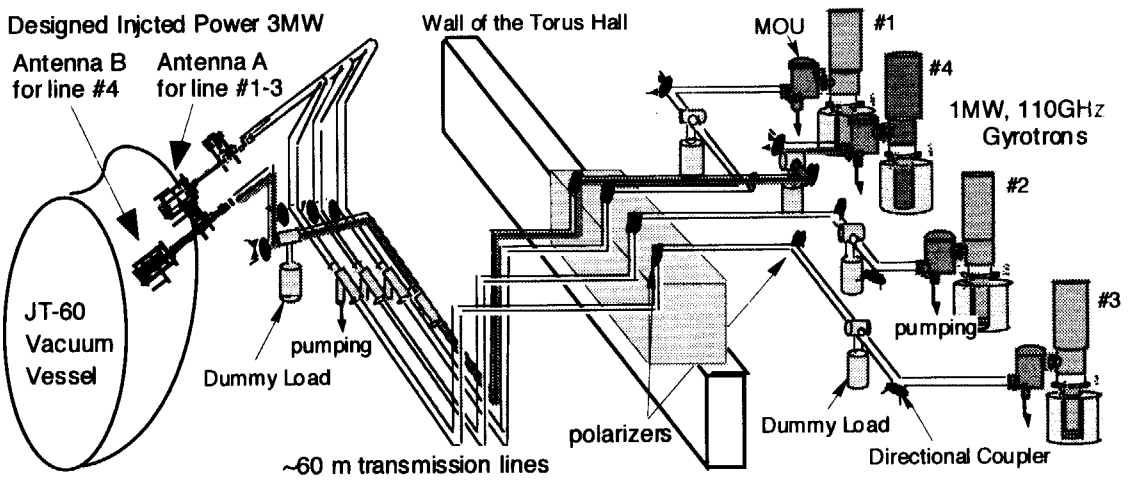

Fig. 1 Outline of the high power ECRF system in JT-60U

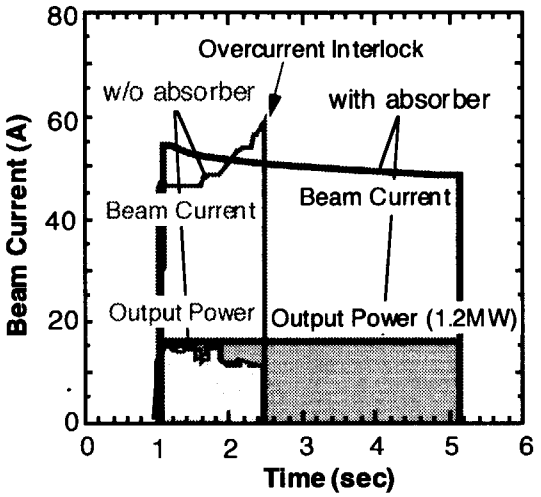

Fig. 2 Improvement in performance by rf absorber built in the gyrotorn.

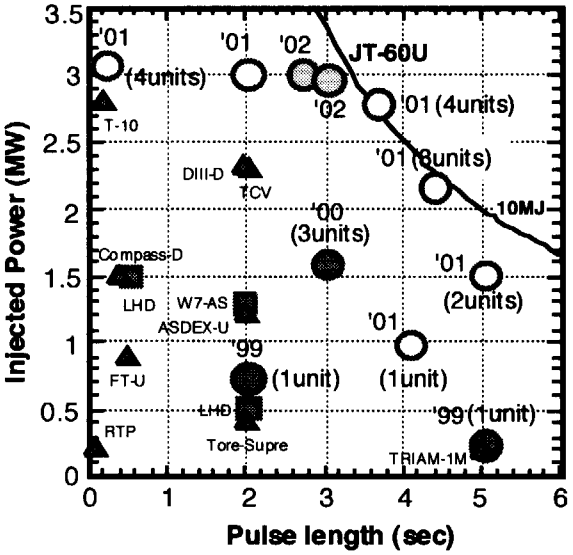

Fig. 3 Injected power as a function of pulse length achieved in ECRF systems in the world.

The power injection performance is progressed by conditioning and improving the gyrotrons and the rf lines in parallel with operation. The first progress is to improve the gyrotron performance at a high power level of 1MW. We found a difficulty in extending pulse length to more than 1 s, because the beam current in gyrotron increased with anomalous heating of the cathode by unnecessary rf wave modes due to the parasitic oscillation, and the overcurrent interlock worked as shown in Fig. 2 [3, 4]. We have improved the gyrotron by setting rf absorber in the beam tunnel because these waves are generated near the cavity and go down to the cathode through the beam tunnel. The absorber suppresses these waves and makes the beam current steady or gradually decreasing. Then, the pulse length is successfully increased at the high power greater than 1 MW and the output power reaches to 1.2 MW [4]. The second is the improvement in the transmission lines. Its designed transmission efficiency is 80% that is the highest level at these high frequencies, because the matching optics unit (MOU) is designed to have a high transmission efficiency of 95%. The measured efficiencies were from 60% to 75% at first, but they are improved to be from 70% to 80% by realignment of the waveguides and adjustment of the MOU. As a result of these improvements, the injected power and the pulse length are extended to 1.5 MW for 5 s, 2.8 MW for 3.6 s and 3 MW for 2.7 s as shown in Fig. 3, which are the highest values in a range of 80-170 GHz. In long pulse operation up to 5 s, the temperature rise of the components in the transmission line is not so large without water-cooling. Then it will be no serious issue even in longer pulse operation with full water-cooling. This is an encouraging result towards the steady state operation.

3. Establishment of feedback-control of injected EC beam angle

Another progress of the ECRF system is with regard to the performance of the EC

beam control by two antennas. Both antennas can inject the EC beams with an oblique toroidal injection angle for the current drive so as to couple the fundamental O-mode from the low field side, which is the same scheme for EC current drive in ITER. They can originally control a poloidal injection angle of the EC beams by the steerable mirrors [2]. We have improved them for feedback-control of the injection angle according to one of measured plasma parameters. Figure 4 shows the block diagram of the feedback control. For example, the fluctuation of the electron temperature by a neoclassical tearing mode (NTM) is measured by the electron cyclotron emission (ECE) diagnostics and then the NTM location is identified. This location data is fed to the ECH computer via the JT-60 real time processor every 10 ms, and the injection angle is changed by smoothed location data so as to aim at the NTM location. Indeed, we have succeeded in the NTM stabilization by this feedback control [5].

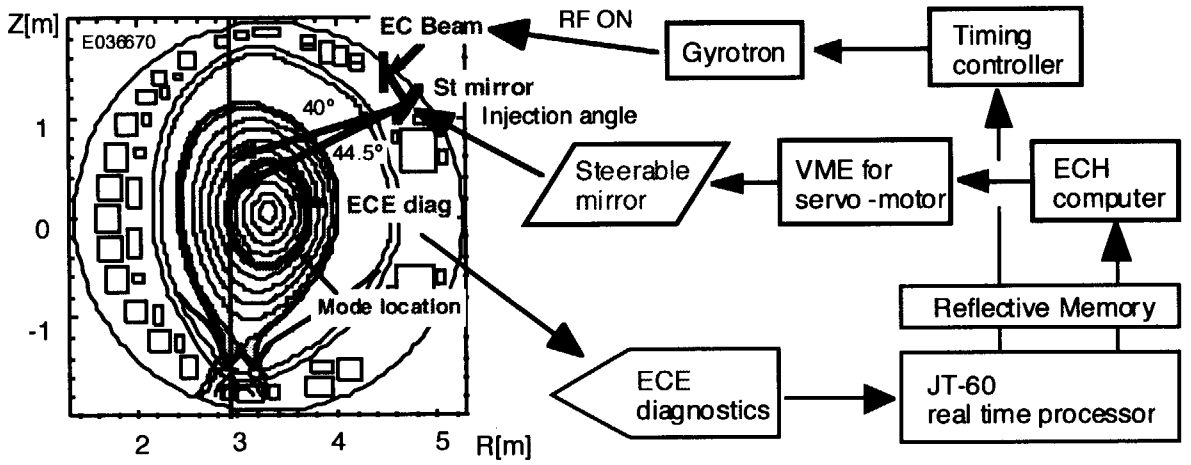

Fig.4 Block diagram of the feedback control of the poloidal injection angle in the NTM stbilization.

4. Summary

The ECRF system in JT-60U has been completed in 2001. We have achieved the highest injected power of 3 MW with the improved gyrotrons which have rf absorber for suppressing the parasitic oscillation. We have established the feedback control of the poloidal injection angle of the EC beam. Then we have succeeded in the NTM stabilization by this feedback control.

References

[1] Ikeda, Y., et al., Fusion Eng. and Design **53,** 351 (2001).

[2] Moriyama, S., et al., Proc. 14th Topical Conf. Radio Freq. Power in Plasmas, 322 (2001).

[3] Ikeda, Y., et al., Fusion Science and Technology 42, 435 (2002).

[4] Kajiwara, K., et al., to be published in Fusion Eng. and Design.

[5] Isayama, A., et al., 19th IAEA Fusion Energy Conference, IAEA-CN-94/EX/C2-2, 2002.

12.3 Optimization of Polarization for ECRF System in JT-60U

S. Moriyama, K. Takahashi

1. Introduction

Polarization of an incident EC wave should be optimized to excite a pure o/x mode wave in a plasma that is necessary for an efficient EC heating or current drive. A pair of polarizer (a polarization rotator and a circular polarizer) is equipped in the transmission line, and the rotation angles of the grooved mirrors are controlled to attain the required polarization (polarization angle and ellipticity). The polarization for the co-injection of the unit #1 and #4 had already been optimized. Further optimization was done by plasma heating experiments in 2002. A purpose of this experiment was to improve the o-mode purity (o-purity) for the unit #2, #3 and to attain optimum polarization for the new function of perpendicular/counter-injection of #4. Prior to the experiment, an electric field of the rf wave at the end of the waveguide near the antenna was measured at the low power level as a function of the rotation angle of the polarizers. The maps of the polarization and of the o-mode purity on the plane of the rotary mirror angles were calculated using the measured data.

2. Experimental Result

Figure 1 shows the map of the o-purity for the counter-injection of unit #4 as a result of the low power measurement. Using the maps, the rotary mirrors were set at the predicted angles corresponding to the local peak of o-purity. The increment rates of electron temperature normalized by EC power, $\Delta Te/\Delta t/P_{EC}$ were compared at a few angles around the predicted angle related to the local peak in the map to obtain the optimum. The injection angle was -20° in the toroidal direction and the poloidal angle was set for on-axis heating. Figure 2 shows the measured $\Delta Te/\Delta t/P_{EC}$ and predicted o-purity. Error bars came from accuracy of P_{EC}, $\Delta Te/\Delta t$ measurement and range of target n_e. High $\Delta Te/\Delta t/P_{EC}$ was observed with the predicted polarization. More data is needed to determine the optimum, precisely. However, $\Delta Te/\Delta t/P_{EC}$ is at the same level as unit #1 which was already optimized and the o-purity was estimated 90-95%. For the perpendicular (0°) injection, $\Delta Te/\Delta t/P_{EC}$ was at the same level as unit #1 at the predicted polarization. For the unit #2, improvement in $\Delta Te/\Delta t/P_{EC}$ with the measured polarization, which was determined using the map similar to Fig.1, was small. It is consistent with the calculation. For the unit #3, improvement (5-20%) in $\Delta Te/\Delta t/P_{EC}$ with the measured polarization was observed.

3. Summary

New polarizer sets to obtain higher o-purity were attained for the unit #3 and #4, as a result of the low power measurement and the plasma heating experiments.

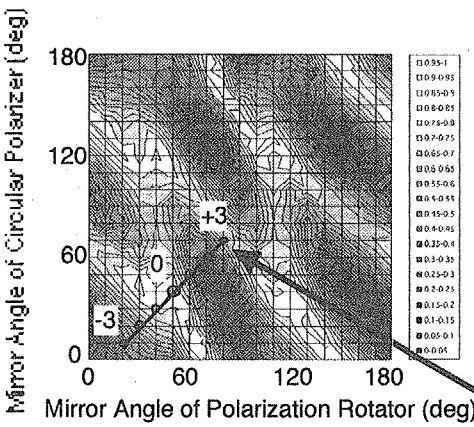

Figure 1 Calculated map of o-mode purity.

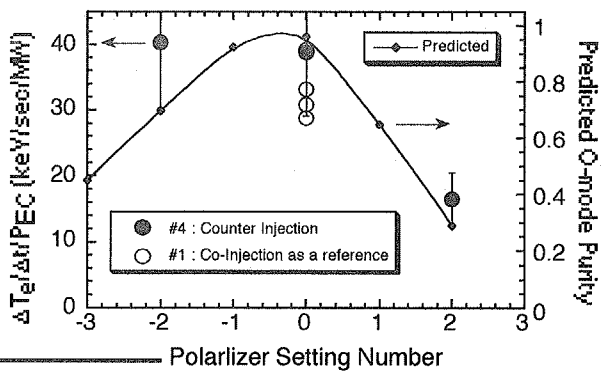

Figure 2 Increment rates of electron temperature normalized by EC power.

12.4 Optimization of LHRF System for ECR Discharge Cleaning

M. Seki, S. Higashijima, K. Anno, K. Igarashi, K. Ishii,
M. Shimono, M. Takahashi, M. Terakado

In future steady state fusion devices with super conducting toroidal coils such as ITER, conditioning of the first wall by Taylor discharge cleaning (TDC) and/or glow discharge cleaning (GDC) is difficult. Therefore electron cyclotron resonance (ECR) discharge cleaning (DC) is an influential candidate for a method of wall conditioning to reduce impurities from the first wall even with toroidal magnetic field [1]. The ECR DC has been performed using 2GHz-LHRF system in JT-60U as shown in Fig. 1. As a result, the effect of ECR DC for tritium removal is found to be at the same level to GDC with H_2 gas.

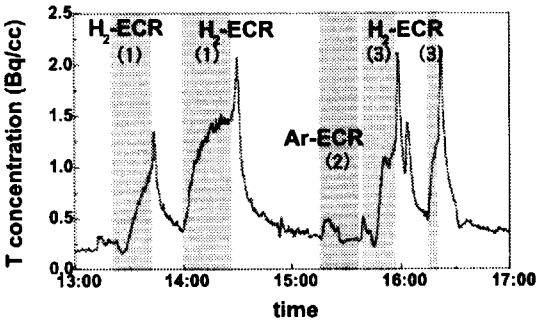

Fig.1.Time evolution of the tritium concentration during ECR DC with H_2 and Ar

The JT-60U LHRF was originally used to drive plasma current up to 3.5 MA, so that main power sources such as klystron were designed to generate a high rf power around 1 MW during 10 sec. For the low power-long pulse operation to perform ECR DC, the LHRF system, especially the 1MW-2GHz klystron, was optimized as follows. At first a beam current for the klystron was decreased from ~20 A to ~5 A for continuos operation with a high voltage Direct Current Generator (DCG) in the power supply system. And cavity positions of the klystron were optimized to yield output power of 30-40 kW using the low beam current up to 5A as illustrated in Fig. 2. Temperatures in the whole LHRF system were monitored during ~45 min-operation for ECR DC, and no problems were observed.

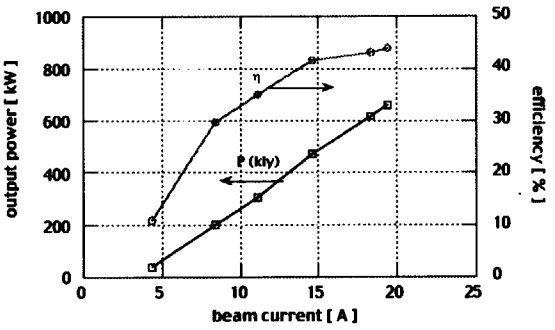

Fig.2. Output power and efficiency as a function of beam current.

References

[1] Ushigusa, K., Seki, M., *et al.*, Fusion Engineering and Design **45**,137 (1999).

Acknowledgments

The authors wish to acknowledge dedicated efforts of the members of Japan Atomic Energy Research Institute in support of the JT-60 program. They also wish to express their gratitude for domestic and international collaborations for the JT-60 experiments.

This is a blank page.

国際単位系 (SI) と換算表

表 1　SI基本単位および補助単位

量	名称	記号
長さ	メートル	m
質量	キログラム	kg
時間	秒	s
電流	アンペア	A
熱力学温度	ケルビン	K
物質量	モル	mol
光度	カンデラ	cd
平面角	ラジアン	rad
立体角	ステラジアン	sr

表 2　SIと併用される単位

名称	記号
分，時，日	min，h，d
度，分，秒	°，′，″
リットル	l，L
トン	t
電子ボルト	eV
原子質量単位	u

1 eV = 1.60218 × 10^{-19} J

1 u = 1.66054 × 10^{-27} kg

表 5　SI接頭語

倍数	接頭語	記号
10^{18}	エクサ	E
10^{15}	ペタ	P
10^{12}	テラ	T
10^{9}	ギガ	G
10^{6}	メガ	M
10^{3}	キロ	k
10^{2}	ヘクト	h
10^{1}	デカ	da
10^{-1}	デシ	d
10^{-2}	センチ	c
10^{-3}	ミリ	m
10^{-6}	マイクロ	μ
10^{-9}	ナノ	n
10^{-12}	ピコ	p
10^{-15}	フェムト	f
10^{-18}	アト	a

表 3　固有の名称をもつSI組立単位

量	名称	記号	他のSI単位による表現
周波数	ヘルツ	Hz	s^{-1}
力	ニュートン	N	$m \cdot kg/s^2$
圧力，応力	パスカル	Pa	N/m^2
エネルギー，仕事，熱量	ジュール	J	N·m
工率，放射束	ワット	W	J/s
電気量，電荷	クーロン	C	A·s
電位，電圧，起電力	ボルト	V	W/A
静電容量	ファラド	F	C/V
電気抵抗	オーム	Ω	V/A
コンダクタンス	ジーメンス	S	A/V
磁束	ウェーバ	Wb	V·s
磁束密度	テスラ	T	Wb/m^2
インダクタンス	ヘンリー	H	Wb/A
セルシウス温度	セルシウス度	℃	
光束	ルーメン	lm	cd·sr
照度	ルクス	lx	lm/m^2
放射能	ベクレル	Bq	s^{-1}
吸収線量	グレイ	Gy	J/kg
線量当量	シーベルト	Sv	J/kg

表 4　SIと共に暫定的に維持される単位

名称	記号
オングストローム	Å
バーン	b
バール	bar
ガル	Gal
キュリー	Ci
レントゲン	R
ラド	rad
レム	rem

1 Å = 0.1 nm = 10^{-10} m

1 b = 100 fm^2 = 10^{-28} m^2

1 bar = 0.1 MPa = 10^5 Pa

1 Gal = 1 cm/s^2 = 10^{-2} m/s^2

1 Ci = 3.7 × 10^{10} Bq

1 R = 2.58 × 10^{-4} C/kg

1 rad = 1 cGy = 10^{-2} Gy

1 rem = 1 cSv = 10^{-2} Sv

（注）

1. 表1－5は「国際単位系」第5版，国際度量衡局 1985年刊行による。ただし，1 eVおよび1 uの値はCODATAの1986年推奨値によった。
2. 表4には海里，ノット，アール，ヘクタールも含まれているが日常の単位なのでここでは省略した。
3. barは，JISでは流体の圧力を表わす場合に限り表2のカテゴリーに分類されている。
4. EC閣僚理事会指令ではbar，barnおよび「血圧の単位」mmHgを表2のカテゴリーに入れている。

換　算　表

力	N(=10^5 dyn)	kgf	lbf
	1	0.101972	0.224809
	9.80665	1	2.20462
	4.44822	0.453592	1

粘度　1 Pa·s(N·s/m^2) = 10 P(ポアズ)(g/(cm·s))

動粘度　1 m^2/s = 10^4 St(ストークス)(cm^2/s)

圧力	MPa(=10 bar)	kgf/cm^2	atm	mmHg(Torr)	lbf/in^2(psi)
	1	10.1972	9.86923	7.50062 × 10^3	145.038
	0.0980665	1	0.967841	735.559	14.2233
	0.101325	1.03323	1	760	14.6959
	1.33322 × 10^{-4}	1.35951 × 10^{-3}	1.31579 × 10^{-3}	1	1.93368 × 10^{-2}
	6.89476 × 10^{-3}	7.03070 × 10^{-2}	6.80460 × 10^{-2}	51.7149	1

エネルギー・仕事・熱量	J(=10^7 erg)	kgf·m	kW·h	cal(計量法)	Btu	ft·lbf	eV
	1	0.101972	2.77778 × 10^{-7}	0.238889	9.47813 × 10^{-4}	0.737562	6.24150 × 10^{18}
	9.80665	1	2.72407 × 10^{-6}	2.34270	9.29487 × 10^{-3}	7.23301	6.12082 × 10^{19}
	3.6 × 10^6	3.67098 × 10^5	1	8.59999 × 10^5	3412.13	2.65522 × 10^6	2.24694 × 10^{25}
	4.18605	0.426858	1.16279 × 10^{-6}	1	3.96759 × 10^{-3}	3.08747	2.61272 × 10^{19}
	1055.06	107.586	2.93072 × 10^{-4}	252.042	1	778.172	6.58515 × 10^{21}
	1.35582	0.138255	3.76616 × 10^{-7}	0.323890	1.28506 × 10^{-3}	1	8.46233 × 10^{18}
	1.60218 × 10^{-19}	1.63377 × 10^{-20}	4.45050 × 10^{-26}	3.82743 × 10^{-20}	1.51857 × 10^{-22}	1.18171 × 10^{-19}	1

1 cal = 4.18605 J (計量法)

= 4.184 J (熱化学)

= 4.1855 J (15 °C)

= 4.1868 J (国際蒸気表)

仕事率　1 PS (仏馬力)

= 75 kgf·m/s

= 735.499 W

放射能	Bq	Ci
	1	2.70270 × 10^{-11}
	3.7 × 10^{10}	1

吸収線量	Gy	rad
	1	100
	0.01	1

照射線量	C/kg	R
	1	3876
	2.58 × 10^{-4}	1

線量当量	Sv	rem
	1	100
	0.01	1

(86年12月26日現在)

Review of JT-60U Experimental Results in 2001 and 2002